SCUOLA DI DOTTORATO
UNIVERSITA' DEGLI STUDI DI MILANO-BICOCCA

Dipartimento di / Department of Biotechnology and Biosciences
Dottorato di Ricerca in / PhD program: Life Sciences
Ciclo / Cycle: XXIX Cycle
Morphofunctional curriculum

FOSTERING CELL TRANSFORMATION ASSAY IN CARCINOGENICITY ASSESSMENT: TOWARD *IN VITRO-IN SILICO* BRIDGING

Cognome / Surname: Callegaro
Nome / Name: Giulia
Matricola / Registration number: 722365

Tutore / Tutor: Chiara Urani[1]
Cotutore / Co-tutor: Federico M. Stefanini[2]
Coordinatore / Coordinator: Marco Vanoni

[1]Department of Earth
and Environmental Sciences
University of Milano-Bicocca
Milan, Italy

[2]Department of Statistics,
Computer Science and Applications
University of Florence
Florence, Italy

ANNO ACCADEMICO / ACADEMIC YEAR: 2015-2016

Assessment committee:

Prof. Paolo Tortora

Department of Biotechnology and Biosciences, University of Milano-Bicocca, Piazza della Scienza 2, 20126 Milan, Italy.

Prof. Chiara Urani

Department of Earth and Environmental Sciences, University of Milano-Bicocca, Piazza della Scienza, 1, 20126, Milan, Italy.

Prof. Paolo Paoli

Department of Experimental and Clinical Biomedical Sciences "Mario Serio", University of Firenze, Viale Morgagni 50, 50134 Florence, Italy.

Prof. Elena Papaleo

Danish Cancer Society Research Centre, Computational Biology Laboratory, Unit of Statistics, Bioinformatics and Registry Copenhagen, Denmark.

Reviewers:

Prof. Bas Blaauboer

Inst. for Risk Assessment Sciences (IRAS), Utrecht University, Utrecht, Netherlands.

Federica Madia

Systems Toxicology Unit, European Union Reference Laboratory for alternatives to animal testing (EURL ECVAM), Institute for Health and Consumer Protection of the European Commission's Joint Research Centre (IHCP-JRC).

Prof. Gareth Jenkins

Institute of Life Science, Singleton Park, Swansea University, Swansea, UK.

Fostering Cell Transformation Assay in carcinogenicity assessment: toward in vitro-in silico bridging

Keywords: Carcinogenicity testing; Cell Transformation Assay; *Foci*; Image analysis; Molecular pathways; Statistical image descriptors

Contents

Abstract

The evaluation of the carcinogenic potential to humans relies at regulatory level on the two-year rodent bioassays (OECD TG451), which are extremely costly in terms of time and animals used, and whose predictive value towards humans has been questioned. The Cell Transformation Assays (CTAs) are the most advanced *in vitro* methods to identify the chemical carcinogenicity potential, in terms of standardization and validation, and reproduce key stages of *in vivo* transformation. The endpoint is the formation of transformed colonies (or *foci*) upon treatment with a carcinogen, which are visually scored by stereomicroscopy, using defined morphological features. These assays offer several advantages in comparison to the *in vivo* bioassays in rodents, and are used by industry and academia as screening methods for carcinogenicity testing and as a tool for mechanistic studies. Even though OECD Guidance Documents on CTAs have been recently published, further improvements are considered important to enhance the use of the assay. We developed two approaches aiming to: *i*) increase throughput and reliability of the scoring process, by developing algorithms and statistical methods designed to quantitatively characterize foci morphological features and *ii*) increase the understanding of *in vitro* transformation mechanisms, through the molecular characterization of transformed cells from foci, and from initial phases of transformation. A database of digital images of *foci* from CTAs performed by the European Union Reference Laboratory for alternatives to animal testing (EURL ECVAM, Joint Research Centre, JRC), in the prevalidation study, and by the Agenzia Regionale per la protezione dell'Ambiente, Emilia Romagna (ARPA-ER), were acquired and *foci* regions were isolated from the background through an originally developed algorithm. Statistical image descriptors defining the morphological features recognized during visual scoring were developed to cover size, multilayer growth, spindle-shape, invasiveness, and degree of heterogeneity of *foci*. Statistical models were developed to automatically classify *foci*,

supporting the phase of visual scoring. In addition, exploiting fitted parametric models using defined statistical descriptors, it was possible to estimate the effects of concentrations of tested carcinogens on *foci* morphologies. To disclose the mechanisms of *in vitro* transformation, it is crucial to evaluate the process through a temporal approach. Cells from initial phases of exposure to carcinogen and from transformed *foci* were collected to perform transcriptomic and biochemical analyses of signalling cascades. We exploited this system to study mechanisms involved in cadmium-induced transformation, hence cadmium is an established human carcinogen, but whose mechanisms of action are still not fully understood. During *in vitro* transformation many processes are involved and non-unique ways to the establishment of transformed cells can be covered. Indeed, we demonstrated that upon the same stimulus, *foci* characterised by different phenotypes can be induced, and different phenotypes correspond indeed to a specific biochemical/molecular cell clone fingerprint. This approach provides a tool for mechanistic studies and it will allow the comprehension of the links between transformed phenotype of *foci* and the biochemical fingerprint. An increased mechanistic understanding of *in vitro* transformation could support an integrated approach based on quantitative scoring of *foci* and molecular fingerprinting. This advancement will also meet specific recommendations of EURL ECVAM in view of future broader acceptance of these assays.

Riassunto

La valutazione del potenziale carcinogeno delle sostanze chimiche si basa, a livello regolatorio, sul saggio di cancerogenesi sui roditori (OECD, TG 451). La loro diffusa applicabilità è però messa in discussione a causa delle lunghe tempistiche e dei costi associati alla loro esecuzione, e dal potenzialmente limitato valore predittivo verso l'uomo. I Cell Transformation Assays (CTA) sono tra i metodi *in vitro* più avanzati e standardizzati a livello regolatorio. I CTA riproducono passaggi chiave della trasformazione *in vivo*; si basano sulla formazione, in seguito al trattamento con un sospetto carcinogeno, di colonie trasformate (o foci), classificate al microscopio da un esperto sulla base di caratteristiche morfologiche standard. I CTA sono impiegati sia per la valutazione del rischio sia nell'ambito della ricerca; tuttavia, per consentirne un maggior utilizzo, alcuni miglioramenti sono auspicabili. Nel presente lavoro sono stati sviluppati due approcci allo scopo di potenziare i saggi CTA. Il primo ha lo scopo di ottimizzare la fase di riconoscimento dei *foci* trasformati sulla base di caratteristiche morfologiche, spesso affetta da soggettività. Questo obiettivo è stato raggiunto sviluppando algoritmi e metodi statistici per definire in modo quantitativo le caratteristiche morfologiche dei *foci*. Il secondo approccio ha come obiettivo il miglioramento della comprensione dei meccanismi coinvolti nella trasformazione *in vitro*, attraverso la caratterizzazione biochimica e molecolare di cellule isolate da *foci* e durante fasi iniziali della trasformazione. E' stato acquisito un database di immagini di *foci* ottenuti tramite saggi CTA condotti da EURL ECVAM (JRC), nell'ambito dello studio di prevalidazione, e da ARPA-ER. Sono stati sviluppati: 1) un algoritmo di segmentazione capace di isolare la regione del *focus* dal monostrato circostante; 2) descrittori statistici delle immagini dei *foci*, allo scopo di riassumere le caratteristiche di dimensione, crescita multistrato, invasività e grado di eterogeneità dei *foci*, e spindle-shape delle cellule. I descrittori statistici così definiti sono stati impiegati per costruire modelli di classificazione dei *foci*, allo

scopo di fornire supporto alla classificazione operata dall'esperto. Inoltre è stato possibile studiare l'effetto esercitato dalla concentrazione di due carcinogeni sulla morfologia dei *foci* trasformati, come catturata dai descrittori statistici introdotti. Allo scopo di migliorare la comprensione dei meccanismi di cancerogenesi *in vitro*, sono state valutate diverse fasi temporali del processo. Campioni provenienti dalle fasi iniziali del processo di trasformazione e da *foci* trasformati sono stati analizzati tramite tecniche di biochimica e trascrittomica. Il saggio CTA è un metodo utilizzato ampiamente in accademia per studiare i meccanismi di azione della cancerogenesi chimica; abbiamo sfruttato questa configurazione sperimentale per analizzare i processi coinvolti nella cancerogenesi *in vitro* indotta da cadmio, cancerogeno umano i cui meccanismi di azione sono ancora non completamente noti. Abbiamo dimostrato che nelle fasi iniziali a seguito di trattamento con cadmio sono coinvolti processi riguardanti l'omeostasi degli ioni Cd^{2+}, Zn^{2+} e Ca^{2+}, alterazioni del citoscheletro e della segnalazione cellulare. A partire da questi processi di difesa, possono essere intraprese vie non univoche per completare la trasformazione: a fronte dello stesso stimolo possono originarsi *foci* caratterizzati da diversi fenotipi, che sottendono a diversi profili biochimici/molecolari. L'inclusione nei saggi CTA di una valutazione oggettiva delle caratteristiche morfologiche e della corrispondenza tra il fenotipo dei *foci* trasformati e le caratteristiche molecolari alla base del processo di trasformazione, rappresenta un significativo avanzamento nella valutazione della cancerogenesi *in vitro*, componente di un più generale approccio integrato alla valutazione del danno.

Preface

This thesis was submitted to the PhD School of Science, University of Milano-Bicocca, as the final fulfillment of the requirements to obtain the PhD degree. The work presented was carried out in the years 2014-2017 in the laboratory of Prof. Chiara Urani at the Department of Department of Earth and Environmental Sciences, University of Milano-Bicocca, Italy and under the supervision of Prof. Federico M. Stefanini, University of Florence, Italy. I additionally spent three extremely experiencing months in the laboratory of Prof. Bob van de Water at the Leiden Academic Centre for Drug Research, Division of Toxicology (LACDR, Leiden University, The Netherlands), during the Summer of 2015. As a results of the collaboration a poster for The Society of Toxicology (SOT) congress 2016 (New Orleans, Louisiana, USA) was presented, and a poster for SOT congress 2017 (Baltimore, Maryland, USA) was accepted. The thesis is a direct continuation of my Master's thesis titled *"The Cell Transformation Assay for chemical carcinogenicity assessment: formulation and analysis of statistical image descriptors"* which was carried out under the supervision of Prof. Chiara Urani and Prof. Federico M. Stefanini and defended in 2013. The paper resulting from my Master's work, published in *Toxicology in Vitro* (Elsevier) in 2013, is highly relevant and frequently referred to in this thesis and it has therefore been included as Chapter 3.

List of Abbreviations

A 2-Acetylaminofluorene

ACC Accuracy

AO Adverse Outcome

AOP Adverse Outcome Pathway

ARPA-ER Agenzia Regionale per la protezione dell'Ambiente, Emilia Romagna

AUC Area Under the Curve

BP Biological Process

BD Boundary Index

BIC Bayesian Information Criteria

B[a]P Benzo[a]Pyrene

C Concentration

CC Cellular Component

CTA In vitro Cell Transformation Assay

DEG Differentially Expressed Gene

DMSO Dimethylsulfoxide

EC European Commission

ED Equivalent Diameter

EFP Perimeter of the circle with equivalent area

EFSA European Food and Safety Authority

EGF Epidermal growth factor

EGFR Epidermal growth factor receptor

EMA European Medicine Agency

EURL ECVAM European Union Reference Laboratory for alternatives to animal testing

FDA Food and Drug Administration

FN False negative

FPO False positive

FP Focus perimeter

GO Gene Ontology

GST Glutathione S-transferase

HB Anthracene

HD Heterogeneity Detector

HTS High-Throughput Screening

IARC International Agency of Research on Cancer

IATA Integrated Approach to Testing Assessment

ICH International Conference on Harmonisation of Technical Requirements for Registration of Pharmaceuticals for Human Use

ITS Integrated Testing Strategies

JRC Joint Research Centre

KE Key Event

LSD Line Segment Detector

MAPK Ras/Raf/mitogen-activated protein kinase

MCA 3-methylcholanthrene

MD Median

MIE Molecular Initiating Event

MF Molecular Function

MT Metallothionein

NGTxC Non-genotoxic carcinogens

OECD Organization of the Economic Co-Operation and Developement

PBPK (modelling) Physiologically based pharmacokinetic modelling

PBS Phosphate buffered saline

PD Petri dish

PI3K Phosphoinositide-3-kinase

(Q)SAR (Quantitative) structure-activity relationships

RCB Rodent Cancer Bioassay

RCE Relative cloning efficiency

REACH Registration, Evaluation and Authorisation of CHemicals

ROC Receiver Operating Characteristic curve

ROI Region of Interest

ROS Reactive Oxygen Species

SD Multicellular-Spindle Detector

SE Standard error

SHE Syrian Hamster Embryo

SNS Sensitivity

SPC Specificity

TB o-Toluidine

TF Transformation Frequency

TN True Negative

TP True Positive

TG Testing Guideline

TPA 12-O-tetradecanoylphorbol-13-acetate

WPD Weighted Perimeter Difference

1

Introduction

The first Chapter introduces the framework of the project, that falls into the field of carcinogenicity testing. First, chemical carcinogenicity is briefly introduced, insisting on the properties of the carcinogens relevant for their testing for safety issues; then the regulatory testing requirements and state of art of the carcinogenicity testing are presented. Finally, the project is outlined and the thesis overview is proposed.

Contents

1.1 Chemical Carcinogenesis

1.1.1 Preamble

Cancer. Cancers figure among the leading cause of morbidity and mortality worldwide, with approximately 14 million new cases and 8.2 million cancer related deaths in 2012. It is expected that annual cancer cases will rise from 14 million in 2012 to 22 within the next 2 decades (Stewart and Wild, 2014). Cancer arises from a single cell in a multistage process, typically a progression from pre-cancerous lesions to fully malignant phenotypes. Cancer development is associated and influenced by interactions between individual genetic factors and environmental factors. Indeed, most cancers are associated with risks from environmental, lifestyle, or behavioural exposures: among them, exposure to chemicals is one of the most relevant (Stewart and Wild, 2014).

For these reasons the evaluation of chemical carcinogenicity, defined as the ability for a chemical substance or a mixture of chemical substances to induce cancer or increase its incidence, has become a leading task in public health risk assessment research throughout the last decades. In particular, regulators are asked to set appropriate standards for exposure in the workplace, home, and clinic, along with classifying carcinogens to which the population may be exposed.

The carcinogenic risk and the cancer hazard. Some important definitions need to be specified when discussing about chemical carcinogenicity. An agent is considered of cancer hazard if it is capable to cause cancer under some circumstances, while the risk measures the probability that cancer will occur, taking into account the level of exposure to the agent. In addition, the carcinogenic

potential defines a qualitative descriptor of carcinogenicity, while the carcinogenic potency is related to the extent of carcinogenicity activity, hence a quantitative descriptor (IARC, 2006).

First descriptions of cancer hazard associated to chemical exposures are historically linked to the field of occupational exposure. Starting from the early quantitative observations of Sir Percival Pott in 1775, describing occurrence of scrotum cancer in chimney sweeps in England, discoveries in this growing field led to the first experimental induction of tumours in animal models by Yamagiwa and Ichikawa (1915).

In recent times, considering the increasing amount of compounds of health safety concerns, the need to collect data regarding cancer hazard of compounds in a comprehensive fashion, became an essential aspect of hazard identification and risk assessment. The International Agency of Research on Cancer (IARC) programme, opened in 1969 by Lorenzo Tomatis (1929-2007) and colleagues, answered to this need. The programme concerns the evaluation of the carcinogenic hazard of chemicals to humans involving the production of critically evaluated monographs on individual chemicals. The programme also includes the evaluation of carcinogenic hazard associated with exposures to complex mixtures, pharmaceutical, lifestyle factors and biological and physical agents, as well as occupational exposure. Agents are finally categorized by IARC into groups, reflecting the strength of evidence derived from studies in humans and in experimental animals, and from mechanistic and other relevant data (IARC, 2006). The three groups are:

- Group 1: the agent is carcinogenic to humans. This category is used when there is sufficient evidence of carcinogenicity in humans. 199 agents belong to this category, e.g. benzo[a]Pyrene and cadmium and its compounds.
- Group 2A: the agent is probably carcinogenic to humans. This category is used when there is limited evidence of carcinogenicity in humans and sufficient evidence of carcinogenicity in experimental animals. The agents listed in this category are

81, among them DDT (4,4'-Dichlorodiphenyltrichloroethane) and consumption of red meat.

- Group 2B: the agent is possibly carcinogenic to humans. This category is used for agents for which there is limited evidence of carcinogenicity in humans and less than sufficient evidence of carcinogenicity in experimental animals. The agents listed in this category are 292, among them gasoline and chloroform.
- Group 3: the agent is not classifiable as to its carcinogenicity to humans. This category is used most commonly for agents for which the evidence of carcinogenicity is inadequate in humans and inadequate or limited in experimental animals. The agents listed in this category are 505, among them caffeine and paracetamol.
- Group 4: the agent is probably not carcinogenic to humans. This category is used for agents for which there is evidence suggesting lack of carcinogenicity in humans and in experimental animals. Only one agent is listed in this category, caprolactam.

An efficient and comprehensive evaluation of carcinogenic hazard associated with a compound needs to consider different sources of data that could be relevant to the final judgement and subsequent setting of safety threshold. In particular epidemiological studies, cancer bioassays in experimental animals as well as mechanistic and other relevant data must be organized and produced.

Current needs for carcinogenicity testing. Cancer hazard can derive from exposure to substances belonging to different sectors: industrial chemicals, biocides, pharmaceuticals, pesticides, cosmetics, veterinary medicines. For each sectors, the different regulations set out recommended data-driven decision pathways to determine whether carcinogenicity studies should be conducted (Madia et al., 2016).

Chemical risk assessment The European Commission (EC) proposed the REACH (Registration, Evaluation and Authorisation of CHemicals) system to evaluate the toxicity of both

existing and new chemical substances. This system is based on a top-down approach to toxicity testing, in which the degree of toxicity information required is dictated primarily by the production volume (tonnage). Carcinogenicity testing requires Rodent Cancer Bioassays (RCBs), described in more details in paragraph 1.2.1. Consequently, very large numbers of laboratory animals could be needed in response to the REACH system, causing ethical, scientific and logistic problems that would be incompatible with the time-schedule envisaged for testing (Combes et al., 2006; Paules et al., 2011). The EC has emphasised the need to minimise animal use:

> The Commission, Member States, industry and other stakeholders should continue to contribute to the promotion of alternative test methods on an international and national level including computer supported methodologies, *in vitro* methodologies, as appropriate, those based on toxicogenomics, and other relevant methodologies (European Union, 2006).

In addition, note that different stakeholders participate to regulatory testing, and, as a consequence, different concerns need to be considered. Regulatory hazard assessors aim at avoiding the occurrence of the false negatives in toxicity, and in particular carcinogenicity, prediction. While industrial safety assessors particularly care about avoiding as much as possible false positive prediction. Consequently, the identification of assays for toxicity testing needs of carefully considering both perspectives (Benigni, 2014).

Pharmaceutical development and drug discovery The European Medicines Agency (EMA) and its international counterparts as the United States Food and Drug Administration (FDA) are the drug-regulatory agency entitled of approve safety and effective drugs for human use. When considering needs of the pharmaceutical and drugs industry in carcinogenicity testing, some aspects must be highlighted. Firstly, the human exposure

to drugs is an intrinsic consequence considered in the drug design process. The way and the span of exposure, the time of residence as well as the possibility of accumulation in the patient and interference with other drugs are characteristics known and desired since the very early phases of drug development. Nonetheless, some side effects and possible toxic effects are unknown, and tests are needed to ensure human safety. Carcinogenicity testing in pharma, unlike other endpoints, can not be assessed in the course of clinical trials, because of long latency period of most human cancers. In addition, even retrospective epidemiologic studies lack of sensitivity because of confounding factors e.g. multiple drug exposure (Bourcier et al., 2015).

Biocidal/Pesticides products and Veterinary medicines
Legislation requires carcinogenicity studies for all new active substances in biocidal and pesticides products, with specific exceptions depending on the sector (European Union, 2012; 2013a,b; Madia et al., 2016). Veterinary medicine are tested for the carcinogenicity endpoint as the human counterparts, but possible residues of veterinary drugs need to be tested whether the animals provide food to human consumers (Food and Drug Administration, 2006). Biocidal/pesticides product and veterinary medicines can be of public health concern as they may end up in food or feed.

Cosmetic Ingredients and Products The Cosmetic Regulation prohibits the placing on the market of cosmetic products containing ingredients, which have been tested on animals. At the moment, the decision of the carcinogenic potential of cosmetic ingredients may be made on the outcome of *in vitro* mutagenicity tests (European Union, 2009).

Although regulatory and theoretical requirements for carcinogenicity testing of substances vary according to product sector and regulatory jurisdiction, the need of highly specific, low cost, rapid and reliable assays is shared, and requires an urgent answer.

1.1.2 Description of chemical carcinogenesis

Chemical carcinogenesis is defined as the ability of a chemical substance or a mixture of chemical substances to induce cancer or increase its incidence. A description of chemical carcinogenensis is therefore linked to both cancer features, and to chemical characteristics.

The Hallmarks of Cancer. Several evidences indicate that tumorigenesis is a multistep process, whose main three steps are initiation, promotion and progression. These steps reflect genetic alterations, e.g. loss of tumour suppressor genes or activation of oncogenes, that drive the progressive transformation of normal human cells into highly malignant derivatives.

The inherent complexity in defining carcinogenesis and cancer is due to the vast catalogue of cancer genotypes that can be found, as well as different tissues that can be targeted. Nevertheless, in the last two decades, great efforts for understanding the biological mechanisms underlying cancer onset and progression led to the assembling of the various characteristics of specific tumours into main alterations of cell physiology, the Hallmarks of Cancer. Initially six hallmarks were described in 2000: self-sufficiency in growth signals, insensitivity to growth-inhibitory (antigrowth) signals, evasion of programmed cell death (apoptosis), limitless replicative potential, sustained angiogenesis, and tissue invasion and metastasis (Hanahan and Weinberg, 2000). To this set, further hallmarks have been added, including dysregulation of cell metabolism and avoidance of immune destruction. Genetic instability and chronic inflammation underlie these hallmarks, as do epigenetic perturbation mechanisms, particularly changes in DNA methylation (Moggs et al., 2004; Thomson et al., 2014; Miousse et al., 2015). See Figure 1.1 as a graphical representation of the above listed hallmarks. Each of these physiologic changes represents the successful breaching of an anticancer

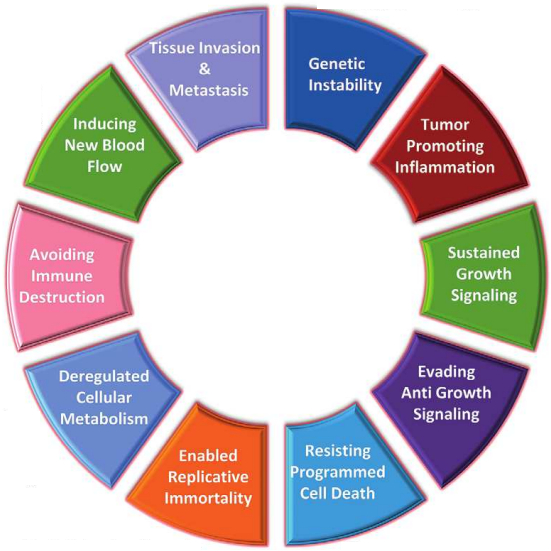

Figure 1.1: The Hallmarks of Cancer. Adapted and modified from Jacobs et al., 2016.

defense mechanism and the novel capabilities acquired during tumour development.

In recent times, the need to provide transparent mechanistic explanations and reduce uncertainty for complex toxicological endpoints, led to the definition of the Adverse Outcome Pathway (AOP) concept (OECD, 2013). AOPs delineate the documented plausible and testable processes by which a chemical induces molecular perturbations (Molecular Initiating Event, MIE) and the associated biological responses that describe how the molecular perturbations cause effects at the subcellular, cellular, tissue, organ, whole animal and population levels of observation. More precisely, it refers to a set of pathways, that would proceed from the MIE, where a chemical interacts with the biological target, through key events (KEs) of biological activities, ultimately culminate in the adverse outcome (AO) (OECD, 2013). As carcinogenicity can be considered as an adverse outcome, a so defined formalization of carcinogenicity could

provide improvements in the understanding the whole mechanisms, as well as insights into the specific mode of actions of different chemicals. Obviously, an AOP for carcinogenicity is not so easy to be formalized, considered the high degree of complexity of the process and the several mechanisms involved (Benigni, 2014).

Carcinogens Characteristics. Human carcinogens can be divided, as a first general approximation, into two broad categories: genotoxic and non-genotoxic carcinogens.

Genotoxic mechanisms cause initiation of the transformation process, and are characterized by direct interaction with DNA through the formation of covalent bonds, resulting in DNA-carcinogen complexes. More in detail, testing for genotoxicity includes mutagenicity, but also checking for DNA damage, which may or may not result in permanent alterations in the structure or information content in a cell or its progeny. On the contrary, mutagenicity results in events that alter the DNA and/or chromosomal structure and that are passed to subsequent generations.
Mutations potentially leading to carcinogenesis, include the following alterations: (1) changes in a single base pair, partial, single or multiple genes, or chromosomes; (2) breaks in chromosomes that result in the stable (transmissible) deletion, duplication or rearrangement of chromosome segments; (3) a change (gain or loss) in chromosome number (i.e. aneuploidy) resulting in cells that have not an exact multiple of the haploid number; and, (4) mitotic recombination (OECD, 2015a).

Non-genotoxic carcinogens (NGTxC), on the contrary, do not involve direct interaction of a compound with DNA, but act through secondary mechanisms, that comprise (Jacobs et al., 2016):

- epigenetic changes; the term "epigenetic" indicates the full spectrum of transcriptional regulatory processes that appear to mediate environmental influences and change a cellular state to reflect past and current (chemical) exposures (Greally and Jacobs, 2013). In particular epigenetic changes comprehend

changes in chromatin (DNA methylation and/or histone modifications) and non-coding RNAs, including microRNAs;

- peroxisome proliferation;
- immune suppression;
- receptor-mediated endocrine modulation;
- inhibition of intercellular communication;
- induction of tissue-specific toxicity;
- inflammatory responses;
- disruption of cellular signaling or structures by changing the rate of either cell proliferation or of processes that increase the risk of genetic error;
- disruption of certain negative cell feedback signals that can enhance proliferative signaling;
- long term mutations in tumour suppressor genes that allow cells to evade growth suppression and contact inhibition.

Some of these mechanisms are not purely non-genotoxic but are shared also by the mode of action of genotoxic carcinogens. In addition, some mechanisms are not exclusive for the adverse outcome of cancer. A relevant example is oxidative stress, one of the mechanisms through which environmental pollutants may induce cell damage, triggering an inflammatory response which may evolve into chronic inflammation as a consequence of enduring exposure. Both genotoxic as non-genotoxic carcinogens can act through oxidative stress; in addition oxidative stress can be related to other adverse outcomes.

A remarkable attempt to a further systematic evaluation and categorization of carcinogens was recently proposed by Smith and colleagues (2016), following the debate emerged during two workshops organized by IARC in 2012. The authors acknowledged the absence of a systematic method to identify mechanistic data for the decision makers in cancer hazard identification; moreover chemical carcinogens characteristics and similarities across different categories were recognized to be not well defined.

Table 1.1: The 10 key characteristics of chemical carcinogens (Smith et al., 2016).

	Characteristic of a chemical carcinogen
1	Is electrophilic or can be metabolically activated to electrophilies
2	Is genotoxic
3	Alters DNA repair or causes genomic instability
4	Induces epigenetic alterations
5	Induces oxidative stress
6	Induces chronic inflammation
7	Is immunosuppressive
8	Modulates receptor-mediated effects
9	Causes immortalization
10	Alters cell proliferation, cell death or nutrient supply

Starting from the hallmarks of cancer, a systematic organization of chemical properties that trigger cancer can be performed. A recent computational toxicology study has shown that chemicals that alter the targets or pathways among the hallmarks of cancer are likely to be carcinogenic (Kleinstreuer et al., 2013). For chemical carcinogens, 10 key characteristics were defined, as properties that human carcinogens commonly show (with at least two of them always present) and can encompass many different types of mechanistic endpoints. The 10 characteristics are shown in Table 1.1.

The 10 characteristics range from chemical and direct effects (electrophilicity and genotoxicity) to secondary effects (epigenetic alterations, oxidative stress), finally to systemic and multicellular alterations (alterations to cell proliferation, cell death, nutrient supply, immunosuppression).

An additional description is needed for a particular class of carcinogens, metal compounds, since the mechanisms of actions of one of them, cadmium, are object of study in this thesis. Metals are small compounds, and play a multifaced role in cellular homeostasis, since some of them are essential for cellular metabolisms and functions. They interact in a complex pattern with macromolecules, metabolic and signal transduction pathways and genetic processes.

The physiochemical form which they interact with biological systems can be determinant for their effects: they can be found as free ions, complexes, particles or poorly solubles compounds. Especially for the free ion form, the charge and the ion radius of the metal are pivotal in determining their effect.

With the exception of chromium(VI), metals are weak mutagens in mammals: hence, they cause their carcinogenic effect mainly through non-genotoxic mechanisms. Despite singularities characterizing each metal, they share some mode of actions and general mechanisms:

Induction of oxidative stress. Metals can generate, through various mechanisms, Reactive Oxygen Species (ROS), that can trigger oxidative stress targeting important biomolecules (DNA, proteins, lipids), and/or interfering with the energetic metabolism (Lee et al., 2012).

Interference with DNA repair. DNA repair consists in four systems, base excision, mismatch, nucleotide excision, recombinational repair, all of them possible targets of metal interference. Inhibition of repair and persistent DNA damage result in genomic instability, which is deleterious especially under conditions of accelerated cell proliferations and/or impaired apoptosis (Hartwig, 2013).

Deregulation of cell proliferation. Metals can deregulate cell proliferation both by affecting expression of growth stimulating factors, through epigenetic mechanisms and/or induction of specific genes, as well as inactivating growth control mechanisms. The latter can be triggered, for example, by the interaction with tumour suppressor proteins as p53, or by the inactivation of apoptotic processes resulting in adaptation to the cytotoxicity of the metals (Beyersmann and Hartwig, 2008).

1.2 Carcinogenicity Testing

The goal of human risk assessment is to decide whether a given level of exposure to a particular chemical or substance is acceptable to human health, and to provide risk management measures based on an evaluation and prediction of the effects of that exposure on human health. Within this framework, the assessment of possible carcinogenic properties of drugs, cosmetics, industrial chemicals, and environmental exposures is of relevant importance (Paules et al., 2011).

1.2.1 State of the Art

Regulatory requirements for carcinogenicity testing of chemicals vary from legislation to legislation and region to region; however, the standard approach is based on a combination of genotoxicity tests and rodent cancer bioassays (RCBs).

Genotoxicity tests. The purpose of genotoxicity testing is to identify substances that can cause genetic alterations in somatic and/or germ cells.
Two types of genetic toxicology studies are considered important: 1) those measuring direct, irreversible damage to the DNA that is transmissible to the next cell generation, (i.e. mutagenicity); and 2) those measuring early, potentially reversible effects to DNA or on mechanisms involved in the preservation of the integrity of the genome, genotoxicity (Organization of the Economic Co-Operation and Developement, OECD, 2015a).
In addition, both *in vitro* and *in vivo* genotoxicity tests are available: positive *in vitro* assays lead to *in vivo* assays, and if these are also

positive, *in vivo* mammalian testing can be recommended (Jacobs et al., 2016).

A plethora of genotoxicity assays have been developed and validated for testing purpose; the most relevant ones and their relative Testing Guidelines (TG) are here presented:

***In vitro* genotoxicity testing.** These methods include tests for evaluating gene mutations (Bacterial Reverse Mutation Test, TG 471; *in vitro* mammalian cell gene mutation tests using the *hprt* or *xprt* genes, TG 476; *in vitro* mammalian cell gene mutation tests using the thymidine kinase gene, TG 490).
Chromosomal aberration can also be evaluated, taking advantage of the *in vitro* mammalian chromosomal aberration test (TG 473), while chromosomal breaks and aneuploidy can be assessed thanks to the *in vitro* mammalian cell micronucleus test (TG 487).

***In vivo* genetic toxicology tests.** Several *in vivo* genotoxicity assays have been developed, both aiming at evaluating gene mutations (TG 488: Transgenic rodent somatic and germ cell gene mutation assays) as well as chromosomal damage (Mammalian bone marrow chromosomal aberration test, TG 475; Mammalian erythrocyte micronucleus test, TG 474; Rodent dominant lethal assay, TG 478; Mammalian spermatogonial chromosomal aberration test, TG 483; Mouse heritable translocation assay, TG 485).
Indicator tests are also available (Unscheduled DNA synthesis test with mammalian liver cells *in vivo*, TG 486; *In vivo* mammalian alkaline comet assay, TG 489), but they are not able to assess the mutagenic consequences of the unrepaired genetic damage.

Even though these assays are able to provide valuable information for genotoxicity testing, it is clear that they are of little value for compounds that do not involve any direct interaction with DNA, as non-genotoxic carcinogens (NGTxC). There are no OECD approved

in vitro screening methods for the detection NGTxC, but the assessment of their carcinogenic properties is addressed through the RCB *in vivo* tests.

***In vivo* Bioassays.** In order to assess the genotoxicity and carcinogenicity of a chemical compound, several steps may be requested. Firstly, compounds are screened through the *in vitro* genotoxicity tests; if they are positive, the *in vivo* genotoxicity tests are performed to further clarify the *in vitro* results. Finally, if any of the *in vivo* genotoxicity tests are positive, RCBs may be requested, which allow the detection of NGTxC.

RCB was proposed for the first time in 1949 by the FDA, and the standardization of the testing approaches was not put into place until the end of '70s.

RCBs are detailed and described in two internationally accepted guidelines published by the OECD, the Test Guideline 451 (OECD, 2009a), and the Test Guideline 453 (OECD, 2009b). In addition, a scientific report prepared by the European Food and Safety Authority (EFSA) is available, in order to support the establishment of protocols for chronic toxicity and/or carcinogenicity studies in rodent with whole food/feed (EFSA, 2013). The RCBs are based on daily administration of the test substance in graduated doses, to several groups of animals, for the majority of their life span (approximately 2 years). The animals are closely observed for signs of toxicity and the development of neoplastic lesions.

In the OECD Test Guideline 451, carcinogenicity testing in rodents is detailed. The preferred rodent species is the rat, although other rodent species (e.g. mouse), can be used. The usage of non-rodent mammal species may be considered if indicated as particularly relevant for the compound tested. The test compound is normally administrated orally to groups consisting of 50 animals of each sex, for each concentration of the compound. At least three doses should be tested, the highest chosen to identify target organs, simultaneously avoiding suffering, severe toxicity, morbidity, or death. A control

group should be tested as well. Animals are weighted, and their food and water consumption are measured along all the duration of the study; all the animals should be subjected to a full necropsy, and fixed and stained samples examined by microscopy.

The OECD Test Guideline 453 describes the combined chronic toxicity/ carcinogenicity test, consisting of two parallel phases, the 1-year chronic phase, and the 2-years carcinogenicity study. The latter is defined by the same criteria detailed in TG 451.

In general, recommendations detailed in TG 451 and TG 453 are valid for a broad range of substances, including pesticides and industrial chemicals, but some details and requirements may differ for pharmaceuticals. For more specifics, the International Conference on Harmonisation of Technical Requirements for Registration of Pharmaceuticals for Human Use is the reference document (ICH, 1997).

1.2.1.1 Problems of *in vivo* bioassays

The genetic toxicology battery was designed to be very sensitive in predicting chemical carcinogenicity, but this comes at the cost of very low specificity. For instance, 50% of non-carcinogens among pharmaceulticals have at least one genotoxicity test positive (Hoffmann and Hartung, 2006; Snyder, 2009; Paules et al., 2011). Furthermore, the battery of genotoxicity assays, fails in detecting NGTxC. It has been estimated that 10-20% of the recognized human carcinogens classified as Class 1 by IARC act by NGTx mechanisms (Hernández et al., 2009).

RCBs are the standard comprehensive *in vivo* tests for the detection of carcinogens, including those acting *via* NGTx mechanisms, but in some cases they are not performed (Jacobs et al., 2016) and there is a wide consensus of their several limitations:

- they are associated with high costs, high animal burden and a long time frame. These criticisms were highlighted since the

forward-looking observations of Goldberg and Frazier (1989), and from then stressed by the regulatory bodies (OECD, 2007), and the European Commission (European Union, 2006).

- Other concerns related to RCBs are due to their limited accuracy (detection limit of approximately 10 %, see Cohen and Ellwein, 1990), and limited predictability, resulting from a high rate of false positive. This high incidence of tumours in bioassays, could be due to the overwhelming of physiological defences, and the unnatural elevation of cell division rates during *ad libitum* feeding studies (Knight et al., 2006a). This consequently leads to the following point.
- RCBs have been questioned concerning human relevance: uncertainty is associated with the extrapolation to humans (Knight et al., 2006a,b). This could be due to a combination of several factors, including the variable stress caused by handling and restraint, the stressful routes of administration common to carcinogenicity bioassays, and their effects on hormonal regulation, immune status and predisposition to carcinogenesis. In addition, differences in rates of absorption and transport mechanisms between test routes of administration and other important human routes of exposure, could be responsible of a different response between rodents and humans.
- Concerns on RCBs have been raised regarding age-related tumour incidence, with many tumours arising only after 18-24 months of exposure (Paules et al., 2011).
- Finally, they lack of mechanistic information. RCBs rely on the observation of effects on a phenomenological level (tumours formation) and do neither provide information on the mechanism of action nor on the dynamics of the biological reaction to the exposure (d'Yvoire et al., 2012).

In addition, some context-dependent issues need to be highlighted. According to the 7th Amendment to the EU Cosmetics Directive 76/768/EEC, in Europe, the RCBs and the more routinely used *in*

vivo genotoxicity tests have been banned for cosmetics since 2009. This caused a profound impact on the ability to evaluate and conduct a quantitative risk assessment for potential carcinogenicity of new cosmetic ingredients and set a challenge to find/develop alternative tests for both genotoxic and non-genotoxic carcinogens (Adler et al., 2011; d'Yvoire et al., 2012).

In the pharmaceutical field, some other considerations are needed. Even though also in this field the RCB is considered as the "gold standard", it clearly has pitfalls. The studies are lengthy and expensive, even considering the overall cost of drug development. Nonetheless, most animal experiments have a limited sample size, and they are more likely to report higher estimates of effect than studies with larger numbers of animals. In addition, animal models are questioned for their ability to mimic human pathophysiology. Doses exceeding those likely to be used clinically are often tested; the high dose in a cancer bioassay is often a maximally tolerated dose. Exposing animals to maximally tolerated doses can alter biological processes that are not relevant at clinical exposures and can produce artifacts, necessitating careful interpretation of positive tumour results. Finally, rodent bioassays can result in drug-induced tumours that arise by mechanisms of questionable relevance to human risk (Meer et al., 2012; Bourcier et al., 2015).

The inadequacy of *in vivo* models, not only for carcinogenicity studies but for toxicity testing in general, gave the stimulus to the introduction of a different paradigm for toxicity testing, enucleated by Smyth (1978) in the concept of *Alternative Methods to animal testing*, defined as:

> All procedures that can completely replace the need of animal experiments, reduce the number of animals required, or diminish the amount of pain or distress suffered by animals in meeting the essential needs of man an other animals.

This definition implies another concept, condensed in the acronym 3Rs, introduced by Russel and Burch in their revolutionary book

"The Principles of Humane Experimental Technique" (1959). The concept of 3Rs refers to the need to improve the design, conduct and analysis of research using animals; in particular are recommended methods that:

- Replace or avoid the use of animals;
- Reduce the number of animals used in the experiments;
- Refine the conditions of animals in the experiments, e.g. minimise the pain, suffering, distress or lasting harm that may be experienced by the animals.

Alternative Methods includes *in vitro* methods, as well as non-testing methods such as *in silico* analyses ([Q]SAR and Read Across techniques), Physiologically Based Pharmacokinetic (PBPK) modeling and epidemiology studies. The concept of Alternative Methods has gained importance in all areas of scientific research (e.g. Goldberg and Fraizer, 1989; Annys et al., 2014) and regulatory bodies solicit the usage and the development of alternative methods to animal research, when possible (e.g. European Union, 2006).

In conclusions, alternatives to the current paradigm *in vitro-in vivo* genotoxicity tests followed by RCBs, are necessary, in order to assess quickly and in a reliable way natural and/or anthropogenic chemicals, already in use and in future production.

1.2.2 Alternative methods: historical background

Cell Transformation Assays. Neoplastic transformation *in vitro* is a progressive event analogous of *in vivo* carcinogenesis (Barrett and Ts'o, 1978). Following this principle, cell transformation has been defined as the induction of certain phenotypic alterations in cultured cells that are characteristic of tumorigenic cells (Barrett and Ts'o, 1978). The stepwise process of *in vitro* transformation leads to several cellular alterations, including:

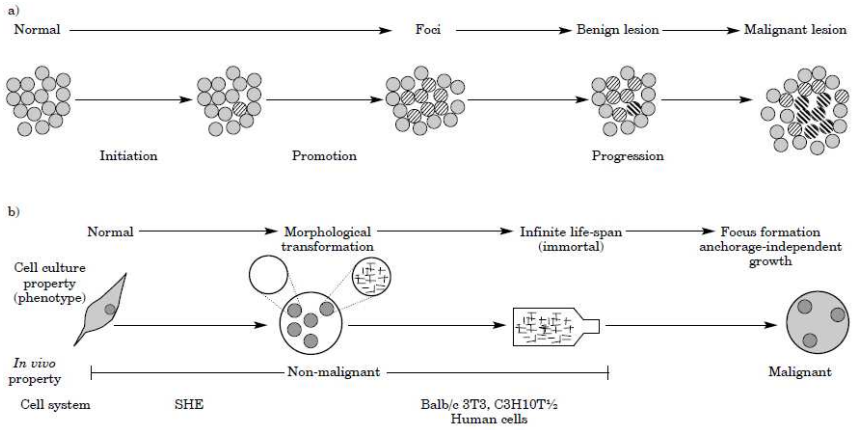

Figure 1.2: *In vivo* (a) and *in vitro* (b) steps of transformation. This figure is adapted from Combes et al. (1999).

- the acquisition of infinite life-span (immortalization);
- changes in morphology (e.g. spindle-shape morphology);
- changes in growth pattern (e.g. criss-cross and multilayered growth of the cultured cells);
- aneuploid and genetic instability;
- anchorange-independent growth (e.g. colony formation in soft agar);
- the ability to induce tumours *in vivo* (Berwald and Sachs, 1963; 1965).

Accordingly, the Cell Transformation Assay exploits these concepts as it was developed to mimic the multistage nature of carcinogenesis (Yamasaki, 1995). See Figure 1.2 as a graphical representation of the similarities of the *in vivo* and *in vitro* transformation processes.

The cultured cells suitable to study *in vitro* transformation must have a low incidence of spontaneous transformation rate and be sensitive to the neoplastic transformation by exposure to a carcinogen.
The main systems used are based on rodent cell lines: BALB/c 3T3 and C3H10T1/2 cells, immortalized fibroblasts of rodent origin, and

Syrian Hamster Embryo (SHE), that are primary cells (DiPaolo et al., 1972; Landolph, 1985; LeBoeuf et al., 1999). Recently, Bhas 42 cells were established as a clone by the transfection with the *v-Ha-ras* gene into mouse BALB/c 3T3 A31-1-1 cells and their subsequent selection based on their sensitivity to 12-O-tetradecanoylphorbol-13-acetate (TPA) (Sasaki et al., 2015).
Thanks to their promising properties, CTAs gained the attention of the regulatory agencies: in 2007 the OECD published a Detailed Review Paper on Cell Transformation Assays for detection of chemical carcinogens (OECD, 2007), and in 2012 and 2013 the European Union Reference Laboratory for alternatives to animal testing (EURL ECVAM) published two Recommendations for Cell Transformation Assays, using BALB/c 3T3, SHE and Bhas 42 systems (EURL ECVAM, 2012; 2013). In addition, OECD recently published two Guidance documents for SHE and Bhas 42 CTAs (OECD, 2015b; 2016). For an overview of the performances of the several protocols of CTA, see Figure 1.3, displaying in a graphical representation the information detailed by EURL ECVAM (2012), OECD (2007) and Sakai and collegues (2010).

Ideally, human-cell based systems would be clearly preferable to the rodent-cell based systems for cell transformation assays (Combes et al., 1999; Maurici et al., 2005). Despite this, no progress has been made in this respect.

All the system protocols share the same endpoint: the formation of colonies/*foci* of transformed cells upon treatment in culture with a suspected carcinogen. The transformed cells acquire phenotypic alterations typical of malignant cells and have the ability to form invasive tumours in susceptible animals (Kakunaga, 1973; Reznikoff et al., 1973; Barrett and Ts'o, 1978). In this regard, CTAs have a clear biological connection with cancer.

The here presented work is focusing in particular on two protocols of CTA, using BALB/c 3T3 and C3H10T1/2 cell lines: for this reason a quick overview is provided and graphically depicted in Figure 1.4 just on these two systems. Both protocols share a cytotoxicity test

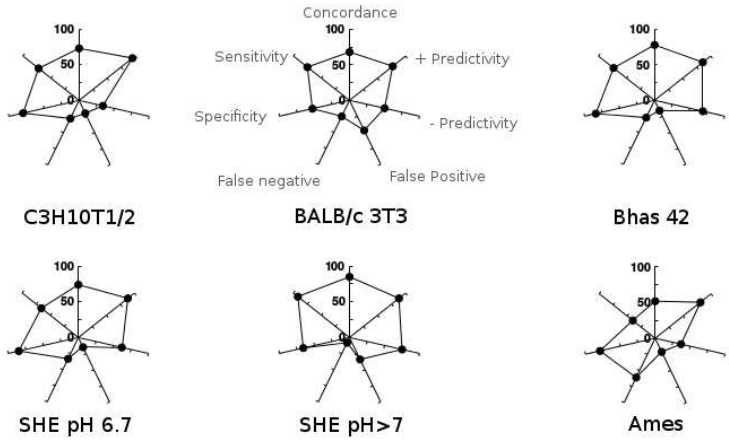

Figure 1.3: Performances of CTA based on different cellular systems. Performances of CTAs based on different cellular systems are displayed in radar-charts, where at each axis corresponds one parameter of classification, namely, concordance, sensitivity, specificity, positive and negative instances predictivity, and false positive and negative. These data are detailed in EURL ECVAM, 2012; OECD, 2007 and Sakai et al., 2010.

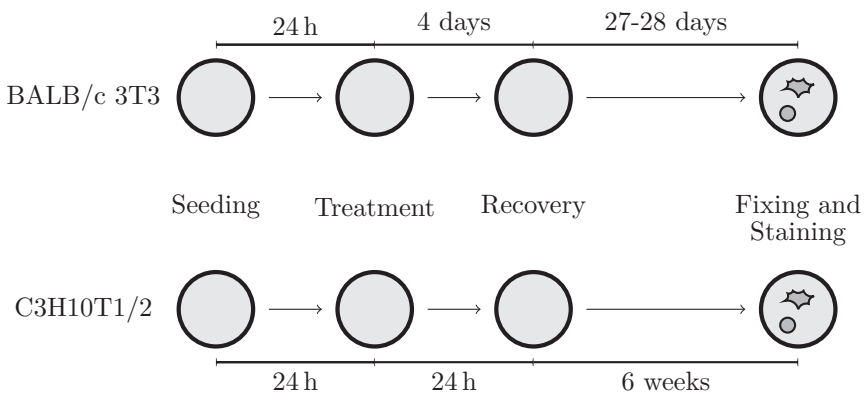

Figure 1.4: CTA protocol in brief, using BALB/c 3T3 and C3H10T1/2 systems.

or dose-range finding phase (not shown in Figure 1.4), followed by the transformation assay. A cytotoxicity test is carried out prior and/or in parallel to the transformation assays to select the optimal range of test chemical concentrations for the transformation assays and to evaluate cytotoxicity of each treatment. The transformation assays must test at least five doses (BALB/c 3T3 CTA) and positive and negative controls must be tested as well. Positive controls are usually 3-methylcholanthrene (MCA) and TPA as tumour promoter, while negative controls should comprise also the vehicle compound. Preferred vessels are 100-mm Petri dish, 10 for each group tested (BALB/c 3T3 CTA). For both cell systems, so called two-step CTAs can be performed, in order to test the initiation or promotion activity of the analysed compound. Firstly, cells are treated with the initiating agent as in the standard transformation assay. Initiating agents most often employed are 3-methylcholanthrene (MCA) or N-methyl-N'-nitro-N-nitrosoguanidine (MNNG). Following removal of the medium containing the initiating agent, cells are refilled with fresh normal medium for 3 days (BALB/c 3T3) or 24 to 48 hours (C3H10T1/2). The medium is removed and replaced with medium containing the promoting agent. Investigation of the timing of promoter addition may be required to determine an optimal response (OECD, 2007).

The transformation assay starts with the seeding at low density ($2 * 10^4$ cells/100-mm dish for BALB/c 3T3 and 800 cells/100-mm dish for C3H10T1/2 system), followed after one day by the treatment with the suspected carcinogen. The treatment with the compound can last 1-2 day for C3H10T1/2 CTA to 4 days for BALB/c 3T3 CTA and it is followed by a long recovery phase when medium is changed regularly. After 27-28 days (BALB/c 3T3) or 6 weeks (C3H10T1/2) dishes are methanol-fixed and Giemsa-stained for final microscope observation. Transformed colonies called *foci* are visually scored using a stereomicroscope following coded morphological criteria. Three types of *foci* have been distinguished (I, II, III), although it is likely that a continuum of focal phenotypes exists (Landolph, 1985).

Type I *foci*, which are more tightly packed than the normal monolayer of cells and only slightly basophilic, are not scored since they do not give rise to neoplastic growths upon injection into irradiated mice. Type II *foci* display massive piling up into virtually opaque multilayers, the cells are moderately polar and criss-crossing is not pronounced. Type III *foci* are highly polar, fibroblastic, multilayered, criss-crossed arrays of densely stained cells. Invasive misoriented cellular projections radiating into the surrounding density-inhibited confluent monolayer of nontransformed cells are sometimes seen in Type III *foci*. Type II and Type III *foci* are scored as positive in C3H10T1/2 CTA, while just Type III *foci* are scored as positive in BALB/C 3T3 CTA. The relevant data scored at the end of C3H10T1/2 CTA is the fraction of dishes in a treatment group with one or several *foci* and the number of Type II and Type III *foci* in the total number of dishes counted for each group. While for BALB/c 3T3 CTA the number of Type III *foci* per dish is counted. More details about the single protocols of specific cell lines are provided in each Chapter.

CTA's current users are academia, and the chemical, agro-chemical, cosmetic, pharmaceutical and tobacco industries, that are interested to these assays for several purposes:

- to provide useful ancillary information when the biological significance of the bioassay result is uncertain (e.g. in pharmaceutical industry);
- to clarify *in vitro* genotoxic positive results by weight of evidence (e.g. in chemical and cosmetic industries);
- to screen for non-genotoxic carcinogens (e.g. in agro-chemical industry);
- to demonstrate differences and similarities across a chemical class (e.g. in chemical companies within REACH);
- to screen for efficacy of chemopreventive agents (in pharmaceutical industry);
- to investigate tumour promotion activity (e.g. in agro-chemical and chemical industries);

- for mechanistic studies of carcinogenicity (e.g. in academia and industry).

Moreover, in the pharmaceutical testing framework, data from CTAs can be useful at the compound selection stage (ICH, 1997). In addition, CTAs are indicated as alternative for genotoxocity/carcinogenicity testing for cosmetics (Adler et al., 2011).

Nevertheless, some concerns related to CTAs have been raised in literature and by the regulatory agencies (OECD, 2007; EURL ECVAM, 2012; Combes, 2012; Creton et al., 2012; Vasseur and Lasne, 2012), that gave the impulse to research devoted to CTAs improvement. Major concerns lie in:

1. Reproducibility of results between laboratories.

2. The subjective nature of scoring transformed *foci*, relying on a judgement of the operator using coded morphological criteria.

3. The lack of understanding of the molecular mechanisms underlying *in vitro* transformation. CTAs have not been developed based on a theoretical correlation between carcinogenesis and a particular mode of action of tested carcinogens.

4. The CTA ability to assess carcinogenicity of chemicals in humans.

For point number (1), many efforts were undergone to standardize the protocols, and to increase their reproducibility (Matthews, 1993; Colacci et al., 2011). In particular, prevalidation studies were performed to evaluate the reproducibility inter- and intra-laboratories and that finally led to standardized protocols (Tanaka et al., 2012; Sasaki et al., 2012a; Maire et al., 2012a,b). Point number (4) can be addressed by the usage of CTA in a tiered or an integrated approach, as further detailed in the next paragraph. Points number (2) and (3) will widely be discussed in the next paragraph and in several Chapters of this thesis.

1.2.3 Alternative methods: recent advancements

1.2.3.1 Improvements of CTA and integrations

Considering CTAs undoubted relevance and advantages, research has been done to improve weak points of CTAs and to suggest novel applications for their usage.

CTAs have been applied to the assessment of the carcinogenicity potential of environmental samples and contaminants (e.g. Perocco et al., 1993; Breheny et al., 2005; Colacci et al., 2014), of mixtures (e.g. Mascolo et al., 2010; Rodríguez-Sastre et al., 2014) and even for radiations (Balcer-Kubiczek et al., 1996). In addition, improvements to the protocols in order to gain rapidity and accuracy in the assessment have been proposed (Plöttner et al., 2013). CTAs have also been used to analyse chemopreventive properties of chemicals (Poburski and Thierbach, 2016).

Many other studies were focusing on the two main improvements needed for a complete regulatory acceptance. CTAs have been questioned for the lack of understanding of the molecular mechanisms underlying the transformation (point number (3) listed in paragraph 1.2.2). Questions have been raised as to how the CTAs are able to detect chemical carcinogens that operate by a wide variety of mechanisms of action, both genotoxic and non-genotoxic (e.g. immune suppression, hormonal disequilibrium) and that can demonstrate species, gender and/or tissue specificity. Many studies focused then on the mechanisms underlying CTA's ability to detect chemicals promoting carcinogenesis, by genotoxic mechanisms as well as by non-genotoxic mechanisms (Landolph et al., 2002; Verma et al., 2004; Clemens et al., 2005; Ao et al., 2010; Rohrbeck et al., 2010; Priya et al., 2013; Vaccari et al., 2015).

Studies were devoted to analyse the process of *in vitro* transformation focusing on the final tumorigenicity in the BALB/c 3T3 system

(Keshava, 2000) and senescence by-pass in SHE system (Pickles et al., 2016). Cell systems used for CTA were also transfected to further dissect the mechanisms of chemical induced transformation, for example analysing the response of constitutively initiated cells (Teegarden et al., 1990; Sasaki et al., 2015).
Most of these studies have the additional value to exploit CTAs to study unknown mechanisms of *in vitro* carcinogenesis induced by a compound, or by a mixture of compounds. CTAs have been employed in *in vitro* carcinogenicity investigations for over three decades (OECD, 2007). In particular, C3H10T1/2 CTA was remarkably exploited for mechanistic studies, hence it is considered a model useful to elucidate molecular mechanisms of cell transformation at the genomic and transcriptomic level (Vasseur and Lasne, 2012).

Finally, research was focused on the improvements of the final phase of the CTA protocol, namely visual scoring of the transformed morphologies. This phase relies on the ability of a trained expert to classify transformed colonies/*foci* into positive instances (finally registered for the *in vitro* carcinogenicity assessment) and negative instances. This classification is based on coded morphological criteria (Landolph, 1985; Sasaki et al., 2012b). Transformed cells belonging to *foci*:

- are deeply basophilic stained;
- acquire a spindle shape;
- grow into multilayers (piling up of cells);
- are randomly oriented at the edge of the *focus*;
- are invasive into the background monolayer.

Even though this method of classification is widely accepted and supported by specifically designed photo catalogues (Sasaki et al., 2012b; Maire et al., 2012c; Bohnenberger et al., 2012; OECD, 2016), expert-driven classification by visual scoring is inherently subjective and sometimes it also leaves the scoring of *foci* doubtful. Actually there is a continuous distribution of transformed morphologies, rather

than a clear categorization into classes, as demonstrated by the occurrence of mixed and intermediate morphologies, difficult to assign into a defined Type (Landolph, 1985). Specifically, intermediate *foci* show a transition degree of coded morphological criteria, hence they are not clearly assignable into a Type; while mixed *foci* are composed partly of areas that are, e.g. Type I-like and partly that are Type II-like (Landolph, 1985; Sasaki et al., 2012b).
This concern has been addressed analysing transformed colonies (SHE CTA) using attenuated total reflection Fourier-transform infrared (ATR-FTIR) spectroscopy, in order to couple the information of transformed morphology with biomarkers of transformation (Ahmadzai et al., 2015).
As a notable alternative, image analysis of transformed colonies seems a very promising road to overcome the subjectivity issues (Poth, 2009). To this end, research has been lead to classify transformed morphology relying on black-box measurements, as well as based on selected features measurements (Ridder et al., 1997; Urani et al., 2009; Procaccianti et al., 2011). More details about techniques available and recent advancements are provided in Chapters of Part I of this thesis.

As a final remark, CTAs predictivity of human carcinogens was questioned (Combes, 2012; point number (4) listed in paragraph 1.2.2). However, especially for a complex adverse outcome such as carcinogenicity, no *in vitro*/*in silico* method should be considered standalone, but combined in an integrated approach (Annys et al., 2014; Leist et al., 2014). As an example, Benigni and collegues (Benigni et al., 2013) showed that a tiered approach consisting in Ames and SHE CTA assays, combined with structure-activity (SA) was able to identify almost all IARC human carcinogens, consisting in genotoxic and non-genotoxic carcinogens.
As widely suggested in the literature, *in vitro* methods such as CTA should be considered as a part of an Integrated Approach to Testing Assessment (IATA) or in tiered approach taking advantage of *in silico* methods as well as statistical methods (Jaworska and Hoffmann,

2010; Pfuhler et al., 2010; De Wever et al., 2012; Stefanini, 2013; Rovida, 2014; Jacobs et al., 2016).

1.2.3.2 Toxicogenomics programmes

The introduction of genomic technologies *circa* 15 years ago, gave the stimulus to exploit these methods for the application to toxicology. With the help of genomic techniques, global perturbations by chemicals in cells and organisms can by analysed though bioinformatic tools in an unbiased way, by considering variations in genes, transcripts, proteins and metabolites. This knowledge can be used for elucidating the mode of action of compounds, prediction of toxic properties, for cross-species and *in vitro-in vivo* comparison. Predominantly, transcriptomics (gene expression analyses at the level of mRNA) has received most attention and has proven to be promising. The incorporation of genomic approaches into hazard assessment paradigm could improve carcinogenicity testing, being these methods able to provide insights into carcinogenic mechanisms (Ellinger-Ziegelbauer et al., 2009; Guyton et al., 2009; Waters et al., 2010). Even though derived toxicogenomic *in vivo* and *in vitro* datasets exhibit significant variability, common features emerge with respect of molecular pathways: systems biology approaches could bridge *in vitro* e and *in vivo* preclinical assays with human relevant mechanisms (Paules et al., 2011).

To improve this paradigm, large datasets of compounds need to be tested: impetus to this research has been given by specific research programmes such as ToxCast/Tox21 (Krewski et al., 2009; Kavlock et al., 2012; Tice et al., 2013). ToxCast, an abbreviation for Toxicity Forecaster, is a project aiming at generating profiles of chemicals through High-Throughput Screening (HTS) techniques. To this end, ToxCast is supported by Tox21, aiming at the development of innovative test methods for human safety.

With the support of toxicogenomic platforms, many applications

for toxicity testing begin achievable. Become achievable to set up panels of Cell Reporter Assays, e.g. for genotoxicity (Hendriks et al., 2013), as well as select biomarkers reflecting the effects and the responses induced by specific compounds, e.g. metals (Koedrith and Seo, 2011). Tissue-specific and omic-performing *in vitro* approaches to recognize carcinogens can be developed (e.g. carcinoGENOMICS project, Rieswijk et al., 2016), with a particular attention to the biotransformation properties of selected cell lines (Khoury et al., 2016).

Finally, interlaboratory reproducibility of these methods needs to be further tested, in order to increase their robustness and to consider them for regulatory purpose (Herwig et al., 2016).

1.2.3.3 Non-testing methods

Non-testing methods include (quantitative) structure-activity relationships ([Q]SARs) and the formation of chemical categories to facilitate the application of read-across between similar chemicals.

To date, hundreds of QSAR models have been published in the literature for predicting genotoxicity and carcinogenicity. The most common test used for modelling is the gene mutation test in bacteria: it was shown that it has a high positive predictivity on genotoxic chemical carcinogens (around 80%, Benigni and Bossa, 2011). On the contrary, QSARs for non-genotoxic carcinogenicity are still in an early stage of development. Nonetheless, several commercial as well as free software are available for predicting genotoxicity as well as carcinogenicity (Benfenati et al., 2009; Fjodorova et al., 2010; Serafimova et al., 2010).
In general, [Q]SAR models allow to organize and explore data in a very convenient way. They will be even more relevant in case of an increased availability of data, arising, for instance, from the Tox-Cast initiative.

Read-across is based on a grouping approach of family related chemicals, more robust than the traditional substance-by-substance evaluation. Nonetheless, a limitation of these methods is that their reproducibility can be low, because the definition of the similar compounds and their number is not standardised. Several softwares are available to help building categories and fill data gaps related with genotoxicity and carcinogenicity (Serafimova et al., 2010). Still, the experience on the use of read-across methods for carcinogenicity is limited.
An extensive review of these methods, in particular in the cosmetic context, is available in Adler et al., 2011.

Other non-testing methods relevant to reach a quantitative and predictive toxicology are the physiologically based pharmacokinetic (PBPK) modeling and PBPK/pharmacodynamic (PBPK/PD) modeling. PBPK models allow to achieve a mechanistic representation of a compound in biological systems: these models combine information on the compound of interest with independent prior knowledge on the physiology and biology at the organism level. Since PBPK models explicitly consider different organs and tissues, it is possible to obtain the quantitative characterization of concentration–time profiles in the respective compartments. With PBPK modeling it is possible to estimate the exposure to the compound at the site of action, which may be difficult or impossible to measure experimentally (Kuepfer et al., 2016). Interesting advancements in the carcinogenicity testing area resulted from the integration between PBPK/PD modeling and QSAR in predicting the carcinogenic potential of chemicals and chemical mixtures. Toxicological interactions that are relevant to carcinogenicity may be linked for different chemicals in a chemical mixture via PBPK/PD modeling, while QSAR modeling may be used to extrapolate to other chemicals that are structurally similar to the components of a chemical mixture under study (Yang et al., 1998).

1.2.4 *In vitro* carcinogenicity debated points and needs

The development of alternative methods and the refinement of the existing ones are a mandatory issue, given the growing body of evidence showing that Rodent Cancer Bioassays (RCBs) are insufficient and not enough reliable for the carcinogenicity assessment of the increasing amount of chemicals of health concerns.

Nevertheless, such alternative methods, as well as the integration among them, need to be at least as accurate as RCBs to be considered for regulatory purpose. In addition, there are some issues related to their development and improvement that can be envisaged:

Non-genotoxic carcinogens indentification. The current genotoxicity test battery is not able to identify non-genotoxic carcinogens (NGTxC), detectable only by the RCBs, that are not always requested. Therefore NGTxC might remain unidentified, causing a severe underestimation of human health risk. In fact, 10-20% of recognized human carcinogens classified as Group 1 by IARC act *via* NGTxC mechanisms. As a consequence, it is essential that robust alternative methods address non-genotoxic modes of action (Jacobs et al., 2016).

Mimic the multistep process or rely on mechanistic-based assays. Carcinogenicity testing can be addressed both by developing methods able to mimic the multistep process of *in vivo* carcinogenesis, as in CTAs, or by developing assays based on specific mechanisms, e.g. genotoxic mechanisms. More likely, there is not a winning method, but integrations of the two kind of approaches will assure the highest level of information. In addition, improvements of the method, e.g. providing a mechanistic explanation of *in vitro* transformation process occurring in CTAs, would lead to a significantly enhanced assay.

Metabolic activation. It is widely recognized that several com-

pounds undergo bioactivation though several enzymes pathways *in vivo* (Cohen and Arnold, 2011). Hence, the presence of a valid and human-resembling system for metabolic transformation in an alternative method for carcinogenicity testing is an issue to be considered. This is relevant for both multistage assays as CTA (Combes, 2012), as well for mechanistic-based assays such as those relying on toxicogenomics (Khoury et al., 2016).

Addressing human relevance. The alternative methods should be designed and/or improved enabling the assessment of the relevance of observed findings for human health and diseases (Paules et al., 2011). This aim can be achieved deriving assays from human *in vitro* cellular models, but also incorporating different assays into integrated approaches, considering also non-human based *in vitro* assays, in order to obtain an overall better prediction of human health (Benigni et al., 2013). This consideration naturally leads to the following point.

Integration of models in approaches. Combining assays into a tiered approach (Benigni, 2014), as well as designing structured strategies for testing assessment, e.g. IATA (Rovida, 2014; Jacobs et al., 2016), could improve overall carcinogenicity testing performances and assist regulatory decision makers. Carcinogenicity assessment is applied to chemical compounds with a variety of usages and occurrences, from drugs to environmental contaminants, that need to be tested in different stages of their production/development. In addition, complexity is increased by the different conceptualization of mechanisms underlying the carcinogenesis process, e.g. chemical carcinogens may act *via* several diverse mechanisms. For these reasons, it is unlikely that there would be a "winning" method universally accepted as a replacement of animal testing in carcinogenicity, whereas a cooperative network of different methods is preferred.

1.3 Bibliography

Adler, S., D. Basketter, S. Creton, O. Pelkonen, et al. (2011). "Alternative (non-animal) methods for cosmetics testing: current status and future prospects-2010". In: *Archives of Toxicology* 85.5, pp. 367–485.

Ahmadzai, A. A., J. Trevisan, W. Pang, M. J. Riding, et al. (2015). "Classification of agents using Syrian hamster embryo (SHE) cell transformation assay (CTA) with ATR-FTIR spectroscopy and multivariate analysis". In: *Mutagenesis* 30.5, pp. 603–12.

Annys, E., R. Billington, R. Clayton, K.-D. Bremm, et al. (2014). "Advancing the 3Rs in regulatory toxicology – Carcinogenicity testing: Scope for harmonisation and advancing the 3Rs in regulated sectors of the European Union". In: *Regulatory Toxicology and Pharmacology* 69.2, pp. 234–242.

Ao, L., J.-y. Liu, W.-b. Liu, L.-h. Gao, et al. (2010). "Comparison of gene expression profiles in BALB/c 3T3 transformed foci exposed to tumor promoting agents". In: *Toxicology in Vitro* 24.2, pp. 430–438.

Balcer-Kubiczek, E. K., X. F. Zhang, G. H. Harrison, W. A. McCready, et al. (1996). "Rodent cell transformation and immediate early gene expression following 60-Hz magnetic field exposure." In: *Environmental Health Perspectives* 104.11, pp. 1188–1198.

Barrett, J. C. and P. O. Ts'o (1978). "Evidence for the progressive nature of neoplastic transformation in vitro." In: *Proceedings of the National Academy of Sciences of the United States of America* 75.8, pp. 3761–3765.

Benfenati, E., R. Benigni, D. M. Demarini, C. Helma, et al. (2009). "Predictive models for carcinogenicity and mutagenicity: frameworks, state-of-the-art, and perspectives". In: *Journal of Environmental Science and Health. Part C, Environmental Carcinogenesis & Ecotoxicology Reviews* 27.2, pp. 57–90.

Benigni, R. (2014). "Predicting the carcinogenicity of chemicals with alternative approaches: recent advances". In: *Expert Opinion on Drug Metabolism & Toxicology* 10.9, pp. 1199–1208.

Benigni, R. and C. Bossa (2011). "Alternative strategies for carcinogenicity assessment: an efficient and simplified approach based on in vitro mutagenicity and cell transformation assays". In: *Mutagenesis* 26.3, pp. 455–460.

Benigni, R., C. Bossa, and O. Tcheremenskaia (2013). "In vitro cell transformation assays for an integrated, alternative assessment of carcinogenicity: a data-based analysis". In: *Mutagenesis* 28.1, pp. 107–116.

Berwald, Y. and L. Sachs (1963). "In Vitro Cell Transformation with Chemical Carcinogens". In: *Nature* 200, pp. 1182–1184.

– (1965). “In Vitro Transformation of Normal Cells to Tumor Cells by Carcinogenic Hydrocarbons”. In: *Journal of the National Cancer Institute* 35.4, pp. 641–661.

Beyersmann, D. and A. Hartwig (2008). “Carcinogenic metal compounds: recent insight into molecular and cellular mechanisms”. In: *Archives of Toxicology* 82.8, pp. 493–512.

Bohnenberger, S., S. W. Bruce, T. Kunkelmann, K. Pant, et al. (2012). “Photo catalogue for the classification of cell colonies in the Syrian hamster embryo (SHE) cell transformation assay at pH 6.7”. In: *Mutation Research* 744.1, pp. 82–96.

Bourcier, T., T. McGovern, L. Stavitskaya, N. Kruhlak, and D. Jacobson-Kram (2015). “Improving Prediction of Carcinogenicity to Reduce, Refine, and Replace the Use of Experimental Animals”. In: *Journal of the American Association for Laboratory Animal Science : JAALAS* 54.2, pp. 163–169.

Breheny, D., H. Zhang, and E. D. Massey (2005). “Application of a two-stage Syrian hamster embryo cell transformation assay to cigarette smoke particulate matter”. In: *Mutation Research/Fundamental and Molecular Mechanisms of Mutagenesis* 572.1, pp. 45–57.

Clemens, F., R. Verma, J. Ramnath, and J. R. Landolph (2005). “Amplification of the Ect2 proto-oncogene and over-expression of Ect2 mRNA and protein in nickel compound and methylcholanthrene-transformed 10T1/2 mouse fibroblast cell lines”. In: *Toxicology and Applied Pharmacology*. Molecular Biomarkers - 21st Century Tools for 21st Century Problems in Toxicology 206.2, pp. 138–149.

Cohen, S. M. and L. B. Ellwein (1990). “Proliferative and genotoxic cellular effects in 2-acetylaminofluorene bladder and liver carcinogenesis: biological modeling of the ED01 study”. In: *Toxicology and Applied Pharmacology* 104.1, pp. 79–93.

Cohen, S. M. and L. L. Arnold (2011). “Chemical Carcinogenesis”. In: *Toxicological Sciences* 120 (Suppl 1), S76–S92.

Colacci, A., M. G. Mascolo, S. Perdichizzi, D. Quercioli, et al. (2011). “Different sensitivity of BALB/c 3T3 cell clones in the response to carcinogens”. In: *Toxicology in Vitro* 25.6, pp. 1183–1190.

Colacci, A., M. Vaccari, M. Mascolo, S. Perdichizzi, et al. (2014). “The use of SHE cell transformation assay to predict the transforming potential of non genotoxic carcinogens”. In: *ALTEX Proceedings, 9th World Congress on Alternatives and Animal Use in the Life Science* 3, p. 141.

Combes, R. (2012). “Cell transformation assays: are we barking up the wrong tree?” In: *Alternatives to laboratory animals: ATLA* 40.2, pp. 115–130.

Combes, R., M. Balls, and R. Curren (1999). “Cell Transformation Assay as Predictor of human carcinogenicity, ECVAM Workshop Report 39”. In: *Alternatives to laboratory animals: ATLA* 27, pp. 745–767.

Combes, R., M. Barratt, and M. Balls (2006). "An overall strategy for the testing of chemicals for human hazard and risk assessment under the EU REACH system". In: *Alternatives to laboratory animals: ATLA* 34 (Suppl 1), pp. 15–27.

Creton, S., M. J. Aardema, P. L. Carmichael, J. S. Harvey, et al. (2012). "Cell transformation assays for prediction of carcinogenic potential: state of the science and future research needs". In: *Mutagenesis* 27.1, pp. 93–101.

De Wever, B., H. W. Fuchs, M. Gaca, C. Krul, et al. (2012). "Implementation challenges for designing integrated in vitro testing strategies (ITS) aiming at reducing and replacing animal experimentation". In: *Toxicology in Vitro* 26.3, pp. 526–534.

DiPaolo, J. A., K. Takano, and N. C. Popescu (1972). "Quantitation of chemically induced neoplastic transformation of BALB-3T3 cloned cell lines". In: *Cancer research* 32.12, pp. 2686–2695.

d'Yvoire, M. B., S. Bremer, S. Casati, M. Ceridono, et al. (2012). "ECVAM and new technologies for toxicity testing". In: *New Technologies for Toxicity Testing*. Springer, pp. 154–180.

EFSA (2013). "Considerations on the applicability of OECD TG 453 to whole food/feed testing". In: *EFSA Journal* 11.7.

Ellinger-Ziegelbauer, H., J. Aubrecht, J. C. Kleinjans, and H.-J. Ahr (2009). "Application of toxicogenomics to study mechanisms of genotoxicity and carcinogenicity". In: *Toxicology Letters*. Toxicogenomics and Clinical Toxicology 186.1, pp. 36–44.

EURL ECVAM (2012). *EURL-ECVAM -Recommendation on three Cell Transformation Assays*.

– (2013). *EURL ECVAM Recommendation Bhas-CTA 2013*.

European Union (2006). *REGULATION (EC) No 1907/2006 OF THE EUROPEAN PARLIAMENT AND OF THE COUNCIL of 18 December 2006 concerning the Registration, Evaluation, Authorisation and Restriction of Chemicals (REACH), establishing a European Chemicals Agency, amending Directive 1999/4*.

– (2009). *Regulation (EC) No 1223/2009 of the European Parliament and of the Council of 30 November 2009 on cosmetic products*.

– (2012). *Regulation (EU) No 528/2012 of the European Parliament and of the Council of 22 May 2012 concerning the making available on the market and use of biocidal products*.

– (2013a). *COMMISSION REGULATION (EU) No 284/2013 of 1 March 2013 setting out the data requirements for plant protection products, in accordance with Regulation (EC) No 1107/2009 of the European Parliament and of the Council concerning the placing of plant protection*.

– (2013b). *Regulation (EU) No 283/2013 setting out the data requirements for active substances, in accordance with Regulation (EC) No 1107/2009 of*

the European Parliament and of the Council concerning the placing of plant protection products on the market.

Fjodorova, N., M. Vracko, M. Novic, A. Roncaglioni, and E. Benfenati (2010). "New public QSAR model for carcinogenicity". In: *Chem Cent J* 4 (Suppl 1), S3.

Food and Drug Administration (2006). *Studies to evaluate the safety of residues of veterinary drugs in human food: carcinogenicity testing VICH GL28*.

Goldberg, A. M. and J. M. Fraizer (1989). "Alternatives to animals in toxicity testing". In: *Scientific American* 261.2, pp. 24–30.

Greally, J. M. and M. N. Jacobs (2013). "In vitro and in vivo testing methods of epigenomic endpoints for evaluating endocrine disruptors". In: *ALTEX-Alternatives to Animal Experimentation* 30.4, pp. 445–471.

Guyton, K. Z., A. D. Kyle, J. Aubrecht, V. J. Cogliano, et al. (2009). "Improving prediction of chemical carcinogenicity by considering multiple mechanisms and applying toxicogenomic approaches". In: *Mutation Research/Reviews in Mutation Research* 681.2, pp. 230–240.

Hanahan, D. and R. A. Weinberg (2000). "The hallmarks of cancer". In: *Cell* 100.1, pp. 57–70.

Hartwig, A. (2013). "Metal interaction with redox regulation: an integrating concept in metal carcinogenesis?" In: *Free Radical Biology and Medicine* 55, pp. 63–72.

Hendriks, G., B. van de Water, W. Schoonen, and H. Vrieling (2013). "Cellular-signaling pathways unveil the carcinogenic potential of chemicals". In: *Journal of Applied Toxicology* 33.6, pp. 399–409.

Hernández, L. G., H. van Steeg, M. Luijten, and J. van Benthem (2009). "Mechanisms of non-genotoxic carcinogens and importance of a weight of evidence approach". In: *Mutation Research/Reviews in Mutation Research* 682.2, pp. 94–109.

Herwig, R., H. Gmuender, R. Corvi, K. M. Bloch, et al. (2016). "Inter-laboratory study of human in vitro toxicogenomics-based tests as alternative methods for evaluating chemical carcinogenicity: a bioinformatics perspective". In: *Archives of Toxicology* 90.9, pp. 2215–2229.

Hoffmann, S. and T. Hartung (2006). "Toward an evidence-based toxicology". In: *Human & Experimental Toxicology* 25.9, pp. 497–513.

IARC (2006). *IARC Monographs on the Evaluation of Carcinogenic Risks to Humans*.

ICH (1997). *ICH Harmonized Tripartite Guideline - Testing for Carcinogenicity of Pharmacauticals S1B*.

Jacobs, M. N., A. Colacci, K. Louekari, M. Luijten, et al. (2016). "International regulatory needs for development of an IATA for non-genotoxic carcinogenic chemical substances". In: *ALTEX-Alternatives to Animal Experimentation* 33.4, pp. 359–392.

Jaworska, J. and S. Hoffmann (2010). "Integrated Testing Strategy (ITS) - Opportunities to better use existing data and guide future testing in toxicology". In: *ALTEX-Alternatives to Animal Experimentation* 27.4, pp. 231–242.

Kakunaga, T. (1973). "A quantitative system for assay of malignant transformation by chemical carcinogens using a clone derived from BALB-3T3". In: *International journal of cancer* 12.2, pp. 463–473.

Kavlock, R., K. Chandler, K. Houck, S. Hunter, et al. (2012). "Update on EPA's ToxCast Program: Providing High Throughput Decision Support Tools for Chemical Risk Management". In: *Chemical Research in Toxicology* 25.7, pp. 1287–1302.

Keshava, N. (2000). "Tumorigenicity of morphologically distinct transformed foci induced by 3-methylcholanthrene in BALB/c-3T3 cells". In: *Mutation Research/Fundamental and Molecular Mechanisms of Mutagenesis* 447.2, pp. 281–286.

Khoury, L., D. Zalko, and M. Audebert (2016). "Evaluation of four human cell lines with distinct biotransformation properties for genotoxic screening". In: *Mutagenesis* 31.1, pp. 83–96.

Kleinstreuer, N. C., D. J. Dix, K. A. Houck, R. J. Kavlock, et al. (2013). "In Vitro Perturbations of Targets in Cancer Hallmark Processes Predict Rodent Chemical Carcinogenesis". In: *Toxicological Sciences* 131.1, pp. 40–55.

Knight, A., J. Bailey, and J. Balcombe (2006b). "Animal carcinogenicity studies: 1. Poor human predictivity". In: *Alternatives to laboratory animals: ATLA* 34.1, pp. 19–27.

– (2006a). "Animal carcinogenicity studies: 2. Obstacles to extrapolation of data to humans". In: *Alternatives to laboratory animals: ATLA* 34.1, pp. 29–38.

Koedrith, P. and Y. R. Seo (2011). "Advances in carcinogenic metal toxicity and potential molecular markers". In: *International Journal of Molecular Sciences* 12.12, pp. 9576–9595.

Krewski, D., M. E. Andersen, E. Mantus, and L. Zeise (2009). "Toxicity Testing in the 21st Century: Implications for Human Health Risk Assessment". In: *Risk Analysis* 29.4, pp. 474–479.

Kuepfer, L., C. Niederalt, T. Wendl, J.-F. Schlender, et al. (2016). "Applied Concepts in PBPK Modeling: How to Build a PBPK/PD Model". In: *CPT: Pharmacometrics & Systems Pharmacology* 5.10, pp. 516–531.

Landolph, J. R. (1985). "Chemical transformation in C3H 10T1/2 Cl 8 mouse embryo fibroblasts: historical background, assessment of the transformation assay, and evolution and optimization of the transformation assay protocol". In: *IARC scientific publications* 67, pp. 185–203.

Landolph, J. R., A. Verma, J. Ramnath, and F. Clemens (2002). "Molecular biology of deregulated gene expression in transformed C3H/10T1/2 mouse embryo cell lines induced by specific insoluble carcinogenic nickel compounds." In: *Environmental Health Perspectives* 110 (Suppl 5), pp. 845–850.

LeBoeuf, R. A., K. A. Kerckaert, M. J. Aardema, and R. J. Isfort (1999). "Use of Syrian hamster embryo and BALB/c 3T3 cell transformation for assessing the carcinogenic potential of chemicals". In: *IARC scientific publications* 146, pp. 409–425.

Lee, J.-C., Y.-O. Son, P. Pratheeshkumar, and X. Shi (2012). "Oxidative stress and metal carcinogenesis". In: *Free Radical Biology and Medicine* 53.4, pp. 742–757.

Leist, M., N. Hasiwa, C. Rovida, M. Daneshian, et al. (2014). "Consensus report on the future of animal-free systemic toxicity testing". In: *ALTEX* 31.3, pp. 341–356.

Madia, F., A. Worth, and C. Raffaella (2016). *Analysis of carcinogenicity testing for regulatory purposes in the European Union*. ENG. Publications Office of the European Union.

Maire, M.-A., K. Pant, P. Phrakonkham, A. Poth, et al. (2012a). "Recommended protocol for the Syrian hamster embryo (SHE) cell transformation assay". In: *Mutation Research* 744.1, pp. 76–81.

Maire, M.-A., K. Pant, A. Poth, K.-R. Schwind, et al. (2012b). "Prevalidation study of the Syrian hamster embryo (SHE) cell transformation assay at pH 7.0 for assessment of carcinogenic potential of chemicals". In: *Mutation Research* 744.1, pp. 64–75.

Maire, M.-A., C. Rast, and P. Vasseur (2012c). "Photo catalogue for the classification of cell colonies in the Syrian hamster embryo (SHE) cell transformation assay at pH 7.0". In: *Mutation Research/Genetic Toxicology and Environmental Mutagenesis*. International Prevalidation Study on Cell Transformation Assays 744.1, pp. 97–110.

Mascolo, M. G., S. Perdichizzi, F. Rotondo, E. Morandi, et al. (2010). "BALB/c 3T3 cell transformation assay for the prediction of carcinogenic potential of chemicals and environmental mixtures". In: *Toxicology in Vitro* 24.4, pp. 1292–1300.

Matthews, E. J. (1993). "Transformation of BALB/c-3T3 cells: I. Investigation of experimental parameters that influence detection of spontaneous transformation." In: *Environmental Health Perspectives* 101 (Suppl 2), pp. 277–291.

Maurici, D., M. Aardema, and R. Corvi (2005). "Carcinogenicity". In: *Alternatives to laboratory animals: ATLA* 33.1, pp. 177–182.

Meer, P. J. K. van, M. Kooijman, C. C. Gispen-de Wied, E. H. M. Moors, and H. Schellekens (2012). "The ability of animal studies to detect serious post marketing adverse events is limited". In: *Regulatory Toxicology and Pharmacology* 64.3, pp. 345–349.

Miousse, I. R., R. Currie, K. Datta, H. Ellinger-Ziegelbauer, et al. (2015). "Importance of investigating epigenetic alterations for industry and regulators:

An appraisal of current efforts by the Health and Environmental Sciences Institute". In: *Toxicology* 335, pp. 11–19.

Moggs, J. G., J. I. Goodman, J. E. Trosko, and R. A. Roberts (2004). "Epigenetics and cancer: implications for drug discovery and safety assessment". In: *Toxicology and Applied Pharmacology* 196.3, pp. 422–430.

OECD (2007). *Detailed Review Paper on Cell Transformation Assays for detection of chemical carcinogens - series on testing and assessment Number 31.*

– (2009a). *Test Guideline 451 – Carcinogenicity studies. OECD Guidelines for the Testing of Chemicals.*

– (2009b). *Test Guideline 453 - Combined Chronic Toxicity/Carcinogenicity Studies. OECD Guidelines for the Testing of Chemicals.*

– (2013). *Guidance Document for developing and assessing Adverse Outcome Pathways (AOPs) - Series on Testing and Assessment No. 184.*

– (2015a). *Genetic Toxicology Guidance Document.*

– (2015b). *Guidance Document on the in vitro Syrian Hamster Embryo (SHE) Cell Transformation Assay - Series on Testing & Assessment No. 214.*

– (2016). *Guidance Document on the in vitro Bhas 42 Cell Transformation Assay - Series on Testing & Assessment No. 231.*

Paules, R. S., J. Aubrecht, R. Corvi, B. Garthoff, and J. C. Kleinjans (2011). "Moving forward in human cancer risk assessment". In: *Environmental health perspectives* 119.6, pp. 739–743.

Perocco, P., A. Colacci, and S. Grilli (1993). "In vitro cytotoxic and cell transforming activities exerted by the pesticides cyanazine, dithianon, diflubenzuron, procymidone, and vinclozolin on BALB/c 3T3 cells". In: *Environmental and Molecular Mutagenesis* 21.1, pp. 81–86.

Pfuhler, S., A. Kirst, M. Aardema, N. Banduhn, et al. (2010). "A tiered approach to the use of alternatives to animal testing for the safety assessment of cosmetics: Genotoxicity. A COLIPA analysis". In: *Regulatory Toxicology and Pharmacology* 57.2, pp. 315–324.

Pickles, J. C., K. Pant, L. A. Mcginty, H. Yasaei, et al. (2016). "A mechanistic evaluation of the Syrian hamster embryo cell transformation assay (pH 6.7) and molecular events leading to senescence bypass in SHE cells". In: *Mutation Research/Genetic Toxicology and Environmental Mutagenesis* 802, pp. 50–58.

Plöttner, S., H. U. Käfferlein, and T. Brüning (2013). "Miniaturization of cytotoxicity tests for concentration range-finding studies prior to conducting the pH 6.7 Syrian hamster embryo cell-transformation assay". In: *Mutation Research/Genetic Toxicology and Environmental Mutagenesis* 755.2, pp. 108–114.

Poburski, D. and R. Thierbach (2016). "Improvement of the BALB/c-3T3 cell transformation assay: a tool for investigating cancer mechanisms and therapies". In: *Scientific Reports* 6.32966.

Poth, A. (2009). "Cell transformation assay -past-present-future". In: *ALTEX: Abstracts 7th World Congress Rome 2009* 26.

Pott, P. (1775). "Chirurgical Observations Relative to the Cataract. The Polypus of the Nose, the Cancer of the Scrotum, the Different Kinds of Ruptures, and the Mortification of the Toes and Feet. Chapter III." In: Hawes, W. Clarke, and R. Collins, London, UK., pp. 60–68.

Priya, S., A. Nigam, P. Bajpai, and S. Kumar (2013). "Dysregulation of pathways involved in the processing of cancer and microenvironment information in MCA + TPA transformed C3H/10T1/2 cells". In: *In Vitro Cellular & Developmental Biology - Animal* 49.4, pp. 295–305.

Procaccianti, C., F. M. Stefanini, and C. Urani (2011). "The cell transformation assay: toward a statistical classification of mixed and intermediate foci images". In: *Alternatives to laboratory animals: ATLA* 39.1, pp. 23–36.

Reznikoff, C. A., D. W. Brankow, and C. Heidelberger (1973). "Establishment and characterization of a cloned line of C3H mouse embryo cells sensitive to postconfluence inhibition of division". In: *Cancer Research* 33.12, pp. 3231–3238.

Ridder, G. M., S. B. Stuard, G. A. Kerckaert, D. B. Cody, et al. (1997). "Computerized image analysis of morphologically transformed and nontransformed Syrian hamster embryo (SHE) cell colonies: application to objective SHE cell transformation assay scoring". In: *Carcinogenesis* 18.10, pp. 1965–1972.

Rieswijk, L., K. J. J. Brauers, M. L. J. Coonen, D. G. J. Jennen, et al. (2016). "Exploiting microRNA and mRNA profiles generated in vitro from carcinogen-exposed primary mouse hepatocytes for predicting in vivo genotoxicity and carcinogenicity". In: *Mutagenesis* 31.5, pp. 603–615.

Rodríguez-Sastre, M. A., E. Rojas, and M. Valverde (2014). "Assessing the impact of As-Cd-Pb metal mixture on cell transformation by two-stage Balb/c 3T3 cell assay". In: *Mutagenesis* 29.4, pp. 251–7.

Rohrbeck, A., G. Salinas, K. Maaser, J. Linge, et al. (2010). "Toxicogenomics applied to in vitro carcinogenicity testing with Balb/c 3T3 cells revealed a gene signature predictive of chemical carcinogens". In: *Toxicological Sciences* 118.1, pp. 31–41.

Rovida, C. (2014). "Integrated Testing Strategies (ITS) for safety assessment". In: *ALTEX-Alternatives to Animal Experimentation* 32.1, pp. 25–40.

Russel, W. and R. Burch (1959). *The Principles of Humane Experimental Technique.*

Sakai, A., K. Sasaki, D. Muramatsu, S. Arai, et al. (2010). "A Bhas 42 cell transformation assay on 98 chemicals: The characteristics and performance for the prediction of chemical carcinogenicity". In: *Mutation Research/Genetic Toxicology and Environmental Mutagenesis* 702.1, pp. 100–122.

Sasaki, K., S. Bohnenberger, K. Hayashi, T. Kunkelmann, et al. (2012b). "Photo catalogue for the classification of foci in the BALB/c 3T3 cell transformation assay". In: *Mutation Research* 744.1, pp. 42–53.

Sasaki, K., S. Bohnenberger, K. Hayashi, T. Kunkelmann, et al. (2012a). "Recommended protocol for the BALB/c 3T3 cell transformation assay". In: *Mutation Research/Genetic Toxicology and Environmental Mutagenesis* 744.1, pp. 30–35.

Sasaki, K., M. Umeda, A. Sakai, S. Yamazaki, and N. Tanaka (2015). "Transformation assay in Bhas 42 cells: a model using initiated cells to study mechanisms of carcinogenesis and predict carcinogenic potential of chemicals". In: *Journal of Environmental Science and Health. Part C, Environmental Carcinogenesis & Ecotoxicology Reviews* 33.1, pp. 1–35.

Serafimova, R., M. Fuart Gatnik, and A. Worth (2010). *Review of QSAR Models and Software Tools for Predicting of Genotoxicity and Carcinogenicity*. Publications Office of the European Union.

Smith, M. T., K. Z. Guyton, C. F. Gibbons, J. M. Fritz, et al. (2016). "Key Characteristics of Carcinogens as a Basis for Organizing Data on Mechanisms of Carcinogenesis". In: *Environmental Health Perspectives* 124.6, pp. 713–721.

Smyth, D. (1978). *Alternatives to animal experiments*. London: Scholar Press.

Snyder, R. D. (2009). "An update on the genotoxicity and carcinogenicity of marketed pharmaceuticals with reference to in silico predictivity". In: *Environmental and Molecular Mutagenesis* 50.6, pp. 435–450.

Stefanini, F. M. (2013). "Comment: Bayesian Network Integrated Testing Strategy and beyond". In: *ALTEX-Alternatives to Animal Experimentation* 30, pp. 386, 390.

Stewart, B. W. and C. P. Wild (2014). *World Cancer Report 2014*. OCLC: 908606220. Lyon: International Agency for Research on Cancer/World Health Organization.

Tanaka, N., S. Bohnenberger, T. Kunkelmann, B. Munaro, et al. (2012). "Prevalidation study of the BALB/c 3T3 cell transformation assay for assessment of carcinogenic potential of chemicals". In: *Mutation Research/Genetic Toxicology and Environmental Mutagenesis* 744.1, pp. 20–29.

Teegarden, D., E. J. Taparowsky, and C. Kent (1990). "Altered phosphatidylcholine metabolism in C3H10T1/2 cells transfected with the Harvey-ras oncogene." In: *Journal of Biological Chemistry* 265.11, pp. 6042–6047.

Thomson, J. P., J. G. Moggs, C. R. Wolf, and R. R. Meehan (2014). "Epigenetic profiles as defined signatures of xenobiotic exposure". In: *Mutation Research/Genetic Toxicology and Environmental Mutagenesis*. Epigenetics and chemical safety 764–765, pp. 3–9.

Tice, R. R., C. P. Austin, R. J. Kavlock, and J. R. Bucher (2013). "Improving the Human Hazard Characterization of Chemicals: A Tox21 Update". In: *Environmental Health Perspectives* 121.7, pp. 756–765.

Urani, C., F. M. Stefanini, L. Bussinelli, P. Melchioretto, and G. F. Crosta (2009). "Image analysis and automatic classification of transformed foci". In: *Journal of microscopy* 234.3, pp. 269–279.

Vaccari, M., M. G. Mascolo, F. Rotondo, E. Morandi, et al. (2015). "Identification of pathway-based toxicity in the BALB/c 3T3 cell model". In: *Toxicology in Vitro* 29.6, pp. 1240–1253.

Vasseur, P. and C. Lasne (2012). "OECD Detailed Review Paper (DRP) number 31 on "Cell Transformation Assays for Detection of Chemical Carcinogens": main results and conclusions". In: *Mutation Research/Genetic Toxicology and Environmental Mutagenesis* 744.1, pp. 8–11.

Verma, R., J. Ramnath, F. Clemens, L. C. Kaspin, and J. R. Landolph (2004). "Molecular biology of nickel carcinogenesis: Identification of differentially expressed genes in morphologically transformed C3H10T1/2 Cl 8 mouse embryo fibroblast cell lines induced by pecific insoluble nickel compounds". In: *Molecular and Cellular Biochemistry* 255.1, pp. 203–16.

Waters, M. D., M. Jackson, and I. Lea (2010). "Characterizing and predicting carcinogenicity and mode of action using conventional and toxicogenomics methods". In: *Mutation Research/Reviews in Mutation Research*. This issue includes the special issue section: Omics: Tools for Understanding and Studying Systems Toxicology 705.3, pp. 184–200.

Yamagiwa, K. and K. Ichikawa (1915). "Experimentelle studie uber die pathogenese der Epithelialgeschwulste." In: *Mitt. Med. Fak. Kaiserl Univ. Tokio* 15, pp. 295–344.

Yamasaki, H. (1995). "Non-genotoxic mechanisms of carcinogenesis: studies of cell transformation and gap junctional intercellular communication". In: *Toxicology Letters* 77.1, pp. 55–61.

Yang, R. S., R. S. Thomas, D. L. Gustafson, J. Campain, et al. (1998). "Approaches to developing alternative and predictive toxicology based on PBPK/PD and QSAR modeling." In: *Environmental Health Perspectives* 106 (Suppl 6), pp. 1385–1393.

2

Objectives of the thesis

Considering the need to implement alternative methods for the assessment of chemical carcinogenicity, the project developed during the three years of my PhD aimed at further improving and refining the *in vitro* Cell Transformation Assay.

This goal was addressed working simultaneously on two of the weak and mainly criticised points of CTAs, previously delineated in paragraph 1.2.2:

1. the possible subjectivity arising from the final phase of CTAs protocol, namely the visual scoring of transformed *foci*;
2. the lack of understanding of the molecular mechanisms underlying *in vitro* transformation.

The first concern, was addressed by taking advantage of tools of digital image analysis, in order to quantitatively evaluate transformed *foci* morphologies. Specifically, we focused on the translation of the coded morphological features used for *foci* classification (Type I, II and III) into statistical image descriptors, with the final aim of building a classification model of transformed *foci*, to support the visual scoring.

To disclose mechanisms of transformation (the second concern), it is crucial the evaluation of the biological process through a temporal approach. To this end, we performed the biochemical characterization of samples from subsequent phases of CTA protocol in order to get insights into the mechanisms underlying the *in vitro* transformation. In addition, this approach can increase the comprehension of the links between the transformed phenotype of *foci* and the biochemical fingerprint.

The two approaches were addressed focusing on CTAs performed through two different, but very similar, cell systems. Digital image analysis was applied to *foci* from BALB/c 3T3 CTAs, performed during a prevalidation study by EURL ECVAM, JRC (Tanaka et al., 2012), and by ARPA-ER. The availability of a large number of *foci* and the high quality of the experiments, performed following standard protocols and in qualified laboratories, favoured the choice of this cell system. On the other hand, *foci* from a C3H10T1/2 CTA were analysed to investigate the process of chemical-induced *in vitro* transformation, as C3H10T1/2 cell system has been indicated as a useful model to elucidate the molecular mechanisms of cell transformation at the genomic and transcriptomic levels (Vasseur and Lasne, 2012). However, both cell systems are based on immortalized aneuploid cell lines which measure later stages of carcinogenesis (OECD, 2007), hence we expect that the approaches and methods would be indeed adaptable to both cell systems.

Therefore, the long term goal is to join this two approaches, the first one based on quantification of *foci* morphologies, the second aiming at disclosing biochemical fingerprint underlying the transformed phenotypes, in order to provide an improved CTA. This advancement will also meet specific recommendations of EURL ECVAM in view of future formal acceptance of these assays.

2.1 Overview of the presented work

The project can be organized into two branches, and the presented thesis follows this organization, being divided into two main Parts: i) quantification of foci morphologies and ii) biochemical profiling of foci phenotypes.

Chapter 3 sets the basis for the Part I approach, defining the first three morphological descriptors used in the subsequent analyses. This Chapter presents the results obtained before the starting of the

PhD period, still very important as it put the basis for the project itself. In CHAPTER 4 the descriptors of morphologies formulated in Chapter 3 are applied to a model for the classification of morphologies obtained with CTA performed with the positive control (MCA). In CHAPTER 5 another application is presented, aiming at evaluating the influence of concentrations of two different compounds on the transformed morphologies. These findings gave the stimulus to a further improvement of the classification model previously proposed (Chapter 4), by extending the number of descriptors used and training the model with several different compounds and concentrations (CHAPTER 6).

In order to improve the understanding of the processes underlying *in vitro* transformation (Part II) we focused on the transforming potential of a well known carcinogen, $CdCl_2$ (Cd^{2+}), but whose mechanisms of action are still not completely unraveled. We chose this setup in order to accomplish a secondary effect, that os use CTA to study new mechanisms involved in chemical-induced *in vitro* carcinogenesis. Thus firstly, we assessed transforming properties of Cd^{2+} in CTA, and defined an experimental setup in order to study the transformation process (CHAPTER 7). Then we focused on the proliferative behaviours and activated pathways of different transformed *foci* obtained from Cd^{2+} treatment in a CTA. Proliferation behaviours influence the degree of several morphological features observed in the visual scoring phase (CHAPTER 8). We found indeed variability of proliferative behaviours, upon the same stimulus (Cd^{2+} treatment). We then decided to focus on the early events of Cd-induced transformation, considering the variability arising from the same stimulus, to identify specific pathway-based profiles that can be considered early markers of adverse outcomes related to the carcinogenesis process. (CHAPTER 9).

Finally, in CHAPTER 10, general conclusions are drawn, as well as future perspectives.

Part I

Quantification of foci morphologies

3

From morphological features to image descriptors

In this Chapter the concepts dealing with the transition from qualitative morphological features to quantitative statistical descriptors are presented, as well as the first three descriptors developed to mimic three coded morphological features used for foci classification.

Abstract

In vitro cell transformation assays (CTAs) have been shown to model important stages of *in vivo* carcinogenesis and have the potential to predict carcinogenicity in humans. The endpoint of the CTA is *foci* formation, and requires classification under light microscopy based on morphology. Thus current limitations for the wide adoption of the assay partially depend on a fair degree of subjectivity in *foci* scoring. An objective evaluation may be obtained after separating *foci* from background monolayer in the digital image, and quantifying values of statistical descriptors which are selected to capture eye-scored morphological features. The aim of this Chapter was to develop statistical descriptors to be applied to transformed *foci* of BALB/c 3T3, which cover *foci* size, multilayering and invasive cell growth into the background monolayer.

This Chapter is an extract of the published paper "Objective scoring of transformed foci in BALB/c 3T3 cell transformation assay by statistical image descriptors", Urani, C., Corvi, R., Callegaro, G., Stefanini, F.M., Toxicology in Vitro, 27, 1905–1912, 2013. The paper was published before the PhD project started, but it covers very important basis of the following research. Therefore a synopsis is included in the thesis.

3.1 Introduction

The prediction of the carcinogenic potential for humans still relies, at regulatory level, on life-time bioassays in rodents (OECD, 2009), but they are costly in terms of time, animal used and trained personnel hours. Among the proposed alternatives to the animal bioassay for human carcinogenicity prediction (Combes et al., 1999), the *in vitro* Cell Transformation Assays (CTA) have the potential to detect both genotoxic and non-genotoxic carcinogens (OECD, 2007).

CTAs are considered to provide additional useful information to more routinely employed genotoxicity tests for assessing carcinogenic potential and are therefore listed in various recent guidelines and testing strategies for such purposes (EC, 2003; Jacobson-Kram and Jacobs, 2005; ECHA, 2008; Pfuhler et al., 2010; SCCS, 2010).

The *in vitro* cell transformation is a staged process that closely mimics some stages of the multistep process of *in vivo* carcinogenesis. *In vitro* cell transformation has been related to morphological, biochemical and molecular features such as changes in cell morphology, structural and functional changes in the expression of genes involved in cell cycle control, proliferation and differentiation, acquisition of immortality, anchorage-independent growth and tumourigenicity when injected in suitable host animal (LeBoeuf et al., 1999).

A widely used assay is one based on BALB/c 3T3 cells. In this assay, the phenotypic changes induced by chemicals can be detected in mammalian cell cultures and rely on *focus* formation as the end-point of transformation. Mechanisms involved in *focus* formation include, for example, the loss of contact inhibition, uncontrolled cell growth and morphological changes of transformed cells. More recently, two-stage BALB/c 3T3 protocols have been developed, that have the potential to distinguish between tumour initiators and promoters (Asada et al., 2005; Sakai et al., 2011). Rules for the scoring and classification of a transformed *focus* are based on

microscopy observation of morphological features. The number and the Type of *foci* observed by microscopy are used to determine the carcinogenic potential of the test compound. An EURL ECVAM (European Union Reference Laboratory for Alternatives to Animal Testing) coordinated prevalidation study focusing on reproducibility and protocol standardization of the BALB/c 3T3 CTA has just been published (Tanaka et al., 2012), thus representing a great improvement for the applicability and acceptance of this assay. However, despite the good correlation of CTAs with rodent bioassay, concerns have been raised regarding the possible subjectivity of using arbitrary morphological criteria for the identification and classification of transformed cells, thus limiting their routine use and throughput. As recently proposed (Poth, 2009), the ideal CTA would be one which utilizes, among others, image analysis to avoid subjectivity in scoring of *foci*. Research is currently ongoing to improve the objectivity of CTAs (Urani et al., 2009; Procaccianti et al., 2011; Creton et al., 2012).

The aim of this study was to develop statistical descriptors which represent eye-scored morphological features adopted to classify transformed *foci* of BALB/c 3T3 CTA in a quantitative way through digital image processing.

3.2 Materials and Methods

3.2.1 *Foci* dishes

BALB/c 3T3 Cell Transformation Assays (CTAs) for assessment of carcinogenic potential of selected chemicals were previously performed within a prevalidation study coordinated by EURL ECVAM (Joint Research Centre, Ispra, Italy). Details of experimental procedures for these CTA experiments are found in Tanaka et al., 2012.

CTA dishes from the above mentioned study, obtained in the EURL ECVAM laboratory, were used to create the library of digital images subsequently used to perform the image analysis and the extraction of statistical descriptors of the present work.

The prevalidation study comprised both uncoded and coded chemicals, and the dishes considered here were treated with, among others, dimethylsulfoxide, 3-methylcholanthrene, Benzo[a]Pyrene, as elsewhere detailed (Corvi et al., 2012).

3.2.2 Standard criteria for morphological classification

Criteria for the morphological classification of *foci* from BALB/c 3T3 transformed cells have long been established (Kakunaga, 1973), and reviewed (IARC/NCI/EPA Working Group, 1985; Sasaki et al., 2012a). A photo catalogue of *foci* from BALB/c 3T3 cells has recently been published as a reference tool for the visual classification process (Sasaki et al., 2012b). The correct scoring of the transformed *foci* is performed under a microscope by trained experts. A *focus* with a diameter less than about 2 mm is considered too small to be scored. Three different categories of *foci* are recognized and divided into Type I, II, and III, although only those with Type III features are scored and classified as transformed such that cells from the *foci* induce tumours when injected into host animals, and recorded for assessment of carcinogenic potential of the test chemicals. Type I *foci* are small, non invasive and exhibit a weak basophilic staining. Type II *foci* are dense multilayered, and show less basophilic staining than Type III, contain spindle-shaped cells, exhibit some cell piling up and criss-crossing, although to a limited extent. Type III *foci* are densely multilayered (piling up), display deep basophilic staining of spindle-shaped cells which differ morphologically from normal cells of the background monolayer, random cell orientation, and invasive cell growth into the normal monolayer at the *focus* edge.

3.2.3 Experimental workflow

The experimental workflow (Figure 3.1) comprises a first step of image acquisition of *foci* from Petri dishes provided by the Joint Research Centre (Ispra, VA, Italy), in which they were originally obtained and analyzed by visual scoring, for the creation of a library of digital images. Image segmentation follows, consisting in the isolation of the *focus* area by means of a specifically developed algorithm (Figure 3.2). The segmented region of interest (ROI) includes the *focus* that will be analyzed for the extraction of statistical descriptors. Descriptors applied to the segmented *focus* provide numerical data reflecting its morphological features. The numerical data are further processed by means of statistical methods. Details of the different steps are provided below.

3.2.4 Image acquisition (Figure 3.1 Box B1)

Images were acquired under a stereomicroscope (Zeiss, Stemi SV6) equipped with 6,3× lens (Carl Zeiss, Arese, Italy), as suggested by the recommended protocol for the BALB/c 3T3 CTA (Sasaki et al., 2012a). Images of *foci* were acquired with a digital camera (AxioCam Mrc5, 36 bit) under the following experimental conditions: exposure time of 23 ms was chosen, images were white interactively balanced so that Red Channel resulted increase of the factor 1.02, likewise Green Channel was multiply by 1.37 and Blue Channel was decrease of the factor 0.61. Temperature of the light was 5000 K. Gain factor was set to 1. Images were saved in TIFF-48bit RGB format and had a size of 2572 × 1928 pixels, where 1 pixel is equivalent to a real size of 6.7842×10^{-3} mm (1cm=1474 pixels).

A total of 407 digital images were acquired and analyzed. All *foci* recognized by the segmentation algorithm in all Petri dishes were

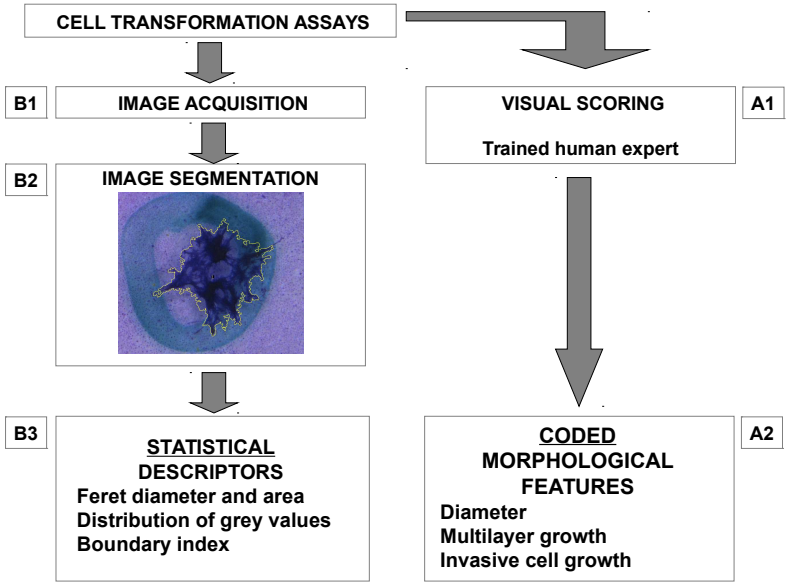

Figure 3.1: Experimental workflow. Cell Transformation Assays: CTA were performed within a previous prevalidation study (Sasaki et al., 2012a). **B1.** Image acquisition: images of *foci* coming from the prevalidation study are acquired, according to suggested methods, for the creation of a digital library, as detailed in par. 3.2.4. **B2.** Image segmentation: the *focus* area is isolated by means of an originally developed algorithm, and segmented as regions of interest (ROI) for further analysis. See par. 3.3.1 for methodological details. **B3.** Statistical descriptors: they are extracted from the ROI to quantitatively capture coded morphological features (Sasaki et al., 2012b). See par. 3.3.2 for methodological details. **A1**, **A2** Visual scoring and coded morphological descriptors: standard criteria for classification of Type III *foci* are based on visual scoring by a trained human expert (Sasaki et al., 2012b).

selected for the analysis, even when a *focus* partially grew on the vertical wall of a Petri dish. Overlapped-confluent *foci* were excluded from the analysis.

3.2.5 Computation (Figure 3.1 Boxes B2 and B3)

Foci images were processed using the Fiji open-source platform for image analysis (Schindelin et al., 2012), which has a user friendly graphical interface that makes available almost all the procedures we exploited. Fiji also allows extensions and plugins to be written in several different programming languages, and our own code was written in the Jython language (Python Language Reference, version 2.7, 2012) to perform automated reading-storing of pixels colour into a database. In Figure 3.2 a flowchart summarizes the main steps of image processing, from a raw image to descriptors. Statistical calculations on values of image descriptors were performed with the open-source platform R (R Core Team, 2012). Both R and Fiji are equipped with extensive manuals and documentation. Our collection of digital images comprises 407 *foci* generated by different experiments undertaken in two subsequent years in one laboratory. Treatments included several chemicals (see par. 3.2.1) at different concentrations.

3.3 Methodological Proposals and Results

3.3.1 Image segmentation

Within a Petri dish, several *foci* may be present and the expert in visual scoring typically considers one *focus* at a time by operationally

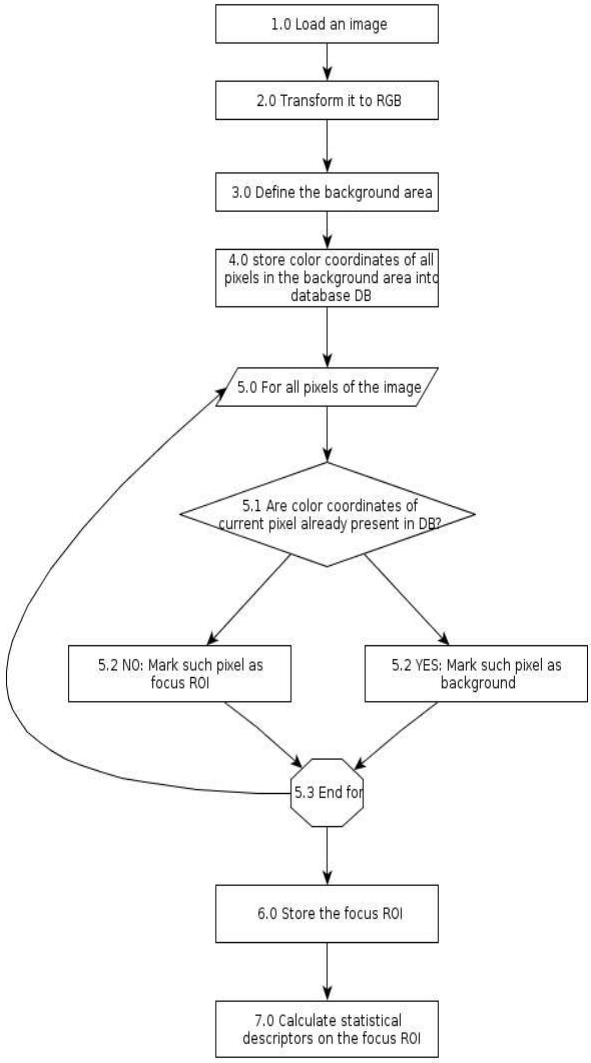

Figure 3.2: Image processing flowchart. Flowchart representing key steps of image processing to obtain numerical values of statistical descriptors.

separating a *focus* from the monolayer of normal cells surrounding it. While *foci* exhibit a quite large polymorphism of phenotypes (Sasaki et al., 2012b), cells of the surrounding normal monolayer are homogeneous in image texture and staining, and display an epithelial-like morphology of contact-inhibited cells (Kakunaga, 1973), which is easily recognized by a trained expert.

We implemented a subtractive algorithm that takes a colour image (8 bits for each colour) of a *focus* and its surrounding monolayer, then the *focus* image is segmented by recognizing pixels belonging to the background. Notwithstanding the mentioned background regularity, minor variability in saturation and brightness characterizes images of cell monolayers growing on different Petri dishes, as a result of differences in staining and/or other protocol procedures. It follows that the best reference monolayer for a *focus* is to be found in the same Petri dish. Recognition is made possible by an example of the background which is selected by the expert, for each *focus* to be segmented. Note that the expert is asked to indicate a region in the image which is indeed cell monolayer but it is not asked to precisely delimit a *focus*, a task automatically performed by the algorithm. A segmented *focus* is a region of the image whose pixels carry information about the *focus*.

Our collection of Petri dishes presented *foci* located near the border, and eventually some *foci* grew on the vertical wall of the dish. In this case the segmentation of the *focus* was partial, due to the impossibility of including the *focus* located on such orthogonal plane into the image. It could be questioned whether these partial *foci* should be considered in the scoring and consequently in the library, in any case assessment of their features, although partially achieved, may be useful in exploratory studies like this one.

Typical image artifacts were caused by rings on the bases of Petri dishes. A substantial fraction of the 407 images were overlapped by coloured hand marks (red, green, blue) produced during the original visual scoring, which made harder the work of our algorithm in delimiting the *focus* region. Artifacts were included into the selected

background area to make our algorithm able of recognizing and considering them as (corrupted) background to be removed. In a limited number of *foci* images, the elimination of artifacts failed and therefore those images were removed from the final database.

3.3.2 Formulation of statistical descriptors

After segmenting a *focus*, image pixels are split into two groups: the first one is made by pixels located within the *focus* (the region of interest, ROI), the second one collects pixels from background cell monolayer and artifacts. The statistical descriptors introduced below are all calculated on the ROI.

3.3.2.1 *Focus* diameter

In visual scoring, a necessary feature for declaring a *focus* is a diameter of more than about 2 mm (Sasaki et al., 2012b, pag. 33, right column). The diameter is a descriptor well defined for a perfectly circular *focus*, because any two points of its perimeter, which are also located on a straight line crossing the center of the *focus*, are good reference points to measure the diameter. For ellipsoidal *foci*, the length of the major axis may be taken as diameter under the assumption that the ratio major/minor axes is quite constant and well known to experts in this field. Nevertheless, *foci* typically show a high degree of shape polymorphism so that the generic term 'diameter' is not precisely defined. The unqualified diameter could correspond to the largest distance of two points located on the *focus* perimeter, in order to be easily found without uncertainty (the so called Feret diameter, FD), a task which is easy to perform through an image analysis software.

In Figure 3.3 (A, B, C, D), some *foci* images taken from our digital library are displayed showing examples of polymorphic shapes: FD

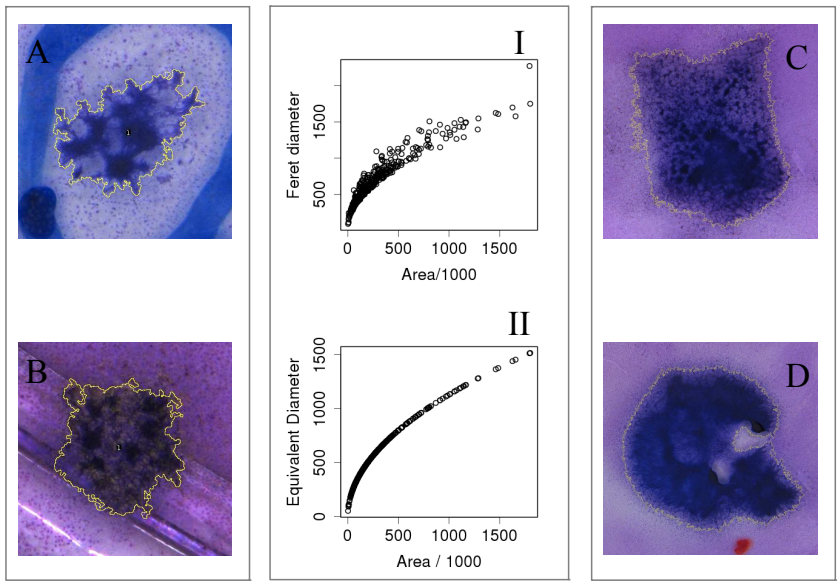

Figure 3.3: The size of a *focus*. The relation between Feret Diameter and rescaled area (panel I) and Equivalent Diameter and rescaled area (panel II) are shown in the mid panels. In A, B, C, and D the lines surrounding the *focus* define the Region of Interest (ROI) in each image. Examples of artifacts are shown: in A, coloured hand marks around the *focus* area; in B, rings on the base of Petri dish. All the images make clear how difficult is to define the diameter, even the Feret one, by visual inspection. In any case, differences of FD may exist for a given value of area (panel I), a variability that disappears if the ED is calculated (panel II).

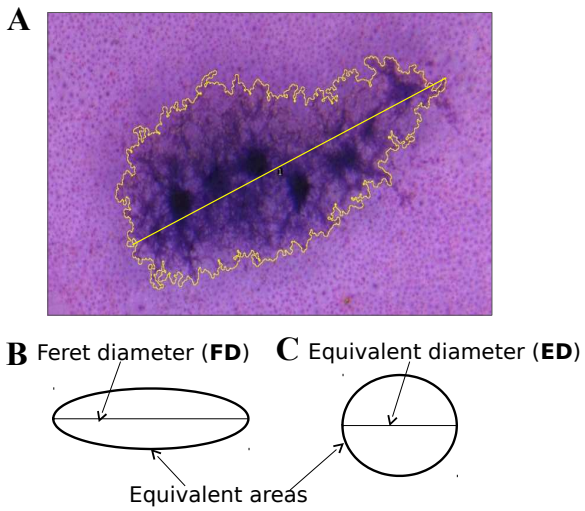

Figure 3.4: *Focus* diameters. In A, an actual long and thin *focus* is shown just after segmentation, after finding the ROI; the segment represents the largest distance between two points of the ROI (the Feret diameter, FD). A *focus* of elipsoidal shape (B) has a Feret diameter corresponding to its major axis (black segment). In (C) a circle whose area is equal to the area of (B) is shown with one of its diameters: this is the equivalent diameter (ED) of *focus* (B).

values of *foci* in A and B are small (left tail of its distribution), while FD values of *foci* in Figure C and D are large (right tail of the distribution). Examples in Figure 3.3 suggest that FD may be misleading as a descriptor of *focus* size, a feature which is better captured by the area of the segmented ROI and easily calculated by image processing tools. The relation between FD and area descriptors is illustrated by the scattergram in the Figure 3.3 (panel I): where it is clear that for a given *focus* area, say equal to 500 on the x axis, the value of FD ranges from about 700 pixels to about 1200 pixels. This variability remains substantial down to the origin of the x axis and it is maintained up to the maximum value of about 1700.

An extreme hypothetical shape may be devised in which the area is

very small but the FD value is high, for example as is the case of a very thin and long *focus* (Figure 3.4, A and Sasaki et al., 2012b, Figure 30).

The diameter feature adopted in the BALB/c catalogue could still be usefully maintained as a descriptor after suitable reformulation. An hypothetical *focus* which equally grows along all directions would show a perfectly circular shape, and this geometrical shape may be taken as reference. The extension, the size, of a *focus* F is captured by the diameter of the circle whose area is equal to the area of F. It follows that, after measuring the area, the here so called equivalent diameter (ED) is: $ED = 2\sqrt{\frac{area}{\pi}}$ where π is the trigonometric constant.

The advantages in the adoption of ED are substantial because no misinterpretation is possible (e.g. Figure 3.3 panel II) due to the lack of variability in ED given a value of area. In Figure 3.4, B, C a diagram illustrates an example of FD and ED in the same *focus*.

3.3.2.2 Multilayering

Cells within a *focus* grow piled up in several strata due to the absence of contact-inhibition and uncontrolled cell growth of transformed cells, leading to a multilayer morphology. In this case, after Giemsa staining within the ROI, multilayered regions within a *focus* will be highly stained. Thus, the gray image of a ROI will be darker than the gray image of the cells in the monolayer (background), and a strongly multilayered *focus* (ROI) will be darker than a *focus* with less stratified cells. A statistical descriptor which summarizes the distribution of gray values due to pixels in the ROI captures the degree of multilayering of the considered *focus*. The arithmetic mean is the obvious candidate for such summary but other choices are available. The segmentation algorithm is affected by noise, for example: from time to time the ROI may contain small portions of the surrounding area; the cell culture may contain small artifacts

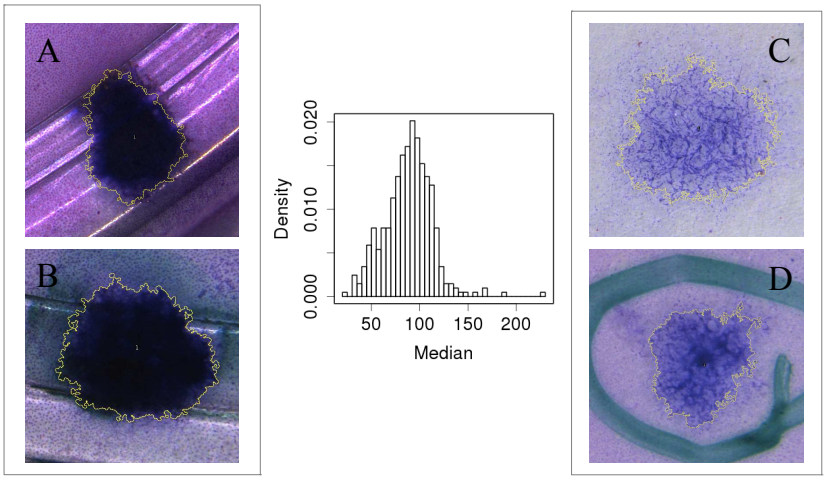

Figure 3.5: Multilayer growth. In the mid panel the histogram of the MD descriptor is shown for our database of 407 *foci*. On the left, two images (A, B) are shown among those characterized by a small MD value (high multilayering, dark). On the right, two images (C, D) are shown among those characterized by a high MD value (low multilayering, light).

eventually due to hand Petri manipulation; staining may be partially inhomogeneous. The arithmetic mean is highly sensitive to outliers, therefore we suggest the use of the median, indicated as MD, as a descriptor of multilayering. It is a robust descriptor with respect to extreme pixel values (close to black and close to white) and it is easy to obtain because it is the value that splits the ordered list of pixel values in two equal parts.

In Figure 3.5, the histogram of median values is shown. Small MD values refer to heavy multilayered (dark) *foci* (Figure 3.5, A and B), while large MD values are obtained under reduced multilayering (light *foci*, Figure 3.5 C and D).

Although we did not calculate values of MD on the catalogue images,

some considerations are in order. In Picture (Pic) 43 of the BALB/c catalogue (Sasaki et al., 2012b) the authors assign M++ to the *focus* to indicate strong multilayering. Nevertheless, visual inspection of Pic 43 reveals that about 30% of the *focus* area is indeed strongly layered. As such our descriptor based on the median would result in a higher value than needed to match the catalogue classification M++. Upon general agreement among experts in visual scoring, there would be the possibility of choosing a minimal area needed to declare a *focus* (strongly) multilayered, for example 25% of the whole area: in this case the first quartile would become a better descriptor, instead of the median, because it would get small values when just the 25% of *focus* pixels are dark.

The above considerations depend on the existence of heterogeneity within the *focus*, thus it is convenient to quantitatively assess the degree of heterogeneity in the pixel distribution within a *focus* by means of summaries based on quantiles, or by a more common summary like the standard deviation. In the Figure 3.6, the median is plotted against the standard deviation. Overall Figure 3.6 shows that *foci* characterized by the same value of multilayering (as captured by the median) may substantially differ as regards the homogeneity in "thickness": the cloud of points in the above Figure covers a range of standard deviation from 10 to 50 (fivefold increase). We expect *foci* with standard deviation above 30 (Figure 3.6, B) to be heterogeneous regarding multilayering (assuming the lack of artifacts and/or segmentation failure). Smaller degrees of heterogeneity correspond to lower values of standard deviation (Figure 3.6, A).

3.3.2.3 Invasiveness

A usual feature of a Type III *focus* is the random orientation and criss-cross pattern at the *focus* edge, typical of an invasive growth on the surrounding epithelial-like monolayer (Tanaka et al., 2012). Despite the above definition, high polymorphism is present in actual

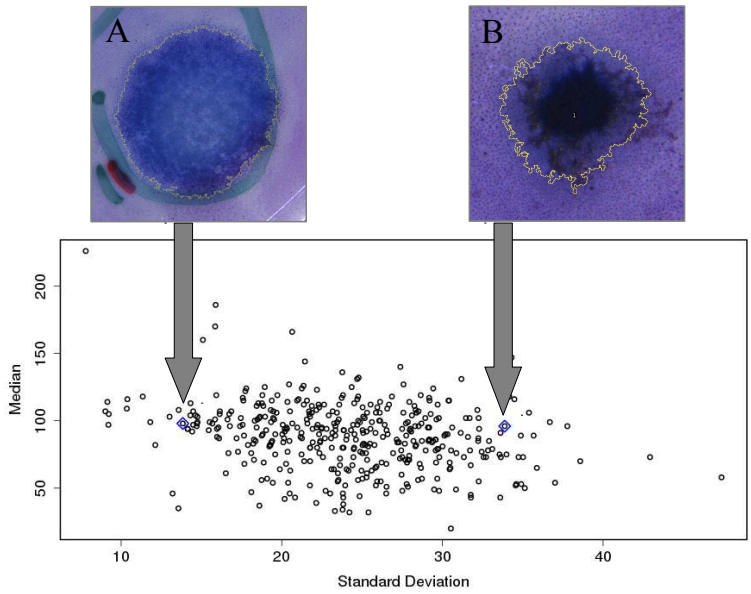

Figure 3.6: Distribution of MD values and standard deviations between *foci* images. In the bottom panel, MD values are plotted against standard deviations for each segmented *focus*. The same value of multilayering may substantially differ as regards the homogeneity in "thickness": MD values equal to a given value, say 100, may be obtained on *foci* in which the standard deviation is small, say 15, but also when the standard deviation is high, say 35 or more. An example of an heterogeneous *focus* as regard multilayering with standard deviation above 30 is shown (B). Smaller degrees of heterogeneity correspond to lower values of standard deviation (A).

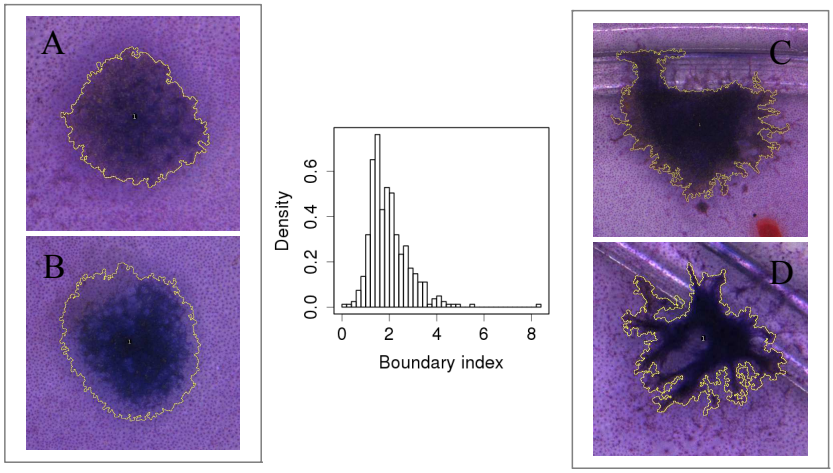

Figure 3.7: Distribution of boundary index (BD) values. In the mid panel the histogram of the BD descriptor is shown for our database of 407 *foci*. On the left (A, B), two images are shown among those characterized by a small BD value, thus their shape is close to be circular. On the right (C,D), two images are shown among those characterized by a high BD value: the shape is relatively far from a circle and the invasion onto the surrounding monolayer is more evident.

cultures. Ramifications of invasive growth range from short and straight to curved and prolonged onto the monolayer even to the point that vortexes with an almost white center may be seen, as displayed by the pictures recently published (Sasaki et al., 2012b).

The invasive growth on the surrounding epithelial-like monolayer may be captured by a statistical descriptor which takes as a reference an hypothetical perfectly circular *focus*, under the assumption that invasiveness often implies preferential directions of *focus* growth. For a given *focus* area, the circular shape is associated to a perimeter which is considered as the quantitative reference point for a general *focus* of the same area but of different shape. We propose to capture this trait of invasiveness by the boundary index (BD), which is a

statistical descriptor defined as $BD = (FP/EFP) - 1$, where FP is the perimeter of a *focus* whose area is A, EFP is the perimeter of the circle of equivalent area (i.e. equal to A). It follows that if the *focus* is a perfect circle then BD = 0, otherwise BD will be greater than zero. In Figure 3.7, the histogram of relative frequencies is shown for the variable BD. On the left tail, small values of BD are associated to *foci* whose shape is close to be circular (Figure 3.7, A and B). On the contrary, the right tail collects high values of BD which are related to high departures from circularity (Figure 3.7, C and D) where invasiveness is present.

3.4 Discussion

In March 2012 the EURL ECVAM published a Recommendation on three CTAs for assessment of the carcinogenic potential of chemical substances (EURL ECVAM, 2012). The authors recognized that CTA requires high skills in scoring which should also be supported by appropriate training of personnel and the use of photo catalogues. Nevertheless, suggested follow-up activities recommended by EURL ECVAM included the automation of the visual scoring to increase throughput and reliability of the CTA (EURL ECVAM, 2012).

The aim of this study was to build a numerical framework inspired by the published catalogue of BALB/c images (Sasaki et al., 2012b), by turning coded eye-scored features into quantitative statistical descriptors. The proposed descriptors are clearly related to coded morphological features although they depend on some operational choices strictly connected to the quantitative nature of the assessment. For example, the diameter feature of a Type III *focus* is not a self-definitional quantitative descriptor due to the polymorphic shape of *foci* which are almost always not circular. We operationally proposed the statistical descriptor called equivalent diameter (ED) which served well in our database of images, but further discussion

among experts is welcome, especially after collecting feedback from actual end users. The discussion about the value of the threshold to define a cell aggregate as *focus* is well behind the level of operational choices because a wrongly calibrated descriptor would probably lead to the underestimate (or overestimate) of the carcinogenic potential of test compounds, thus the statistical design of experiments devoted to calibration is an issue to be considered.

The translation of morphological features into quantitative descriptors posed a number of issues which are not preeminent in qualitative scoring. In our database of 407 *foci* images a high degree of polymorphism was found, well above what published in the BALB/c catalogue, reflecting the multi-step and complexity of the carcinogenic process. As regards invasiveness, the complex nature of such process seems to require several descriptors to obtain a full characterization, so our boundary index (BD) is just one among those currently under study. The most promising candidates include descriptors of criss-crossing and of vortexes, which characterize the morphology of fully transformed cells within a *focus*.

Operational choices mentioned above also stimulated theoretical considerations which deserve further attention from experts. For example, multilayer growth was here captured by the median of pixels grey level distribution, therefore at least half of the total number of pixels within a ROI (*focus*) are darker (indicating a thicker multilayer) than the median value. Different threshold areas to declare multilayering, like 30% (sensitive) or 90% (conservative), are open to consideration but they should be selected with care for the potential consequences on consumers due to the assignment of a chemical to a wrong carcinogenicity class.

The quantitative procedure here described is based on summary statistics applied to a segmented image. It follows that the quality of segmentation determines, among other factors, the accuracy of obtained ROI. While the analysis of standardized images without artifacts may produce optimal results, we proposed a protocol in which an inner control is adopted for each *focus*, where inner means

within the same Petri dish in which the *focus* is located. In this way, a fair degree of robustness is expected against the presence of artifacts, of colour shift and other changes and/or fluctuations which typically occur within and between experiments. In this regard, further descriptors might be introduced upon agreement among experts, for example to quantify multilayering as a comparison between the *focus* median and the median of the surrounding monolayer. The comparative approach to the formulation of descriptors could improve the estimate of the signal-to-noise ratio.

The statistical descriptors here introduced do not cover the full list of features described in the BALB/c catalogue, neither they do summarize well all the patterns observed in our database of *foci* images. Coded features for BALB/c do not address the presence of vortexes, although in our database they are often associated to Type III *foci*. We also found vortexes in cases of extreme criss-cross configurations. We believe that vortexes are related to a tight aggregation of spindle shaped cells, a feature not easily evaluated by means of a stereomicroscope: a higher magnification is typically needed to assess the presence of this peculiar shape in single cells.

Within this Chapter we have started the translation of coded morphological features as those in the BALB/c catalogue into quantitative statistical descriptors. Further work was performed to provide a tool for automatic and objective classification, and it is described in next Chapters.

3.5 Bibliography

Asada, S., K. Sasaki, N. Tanaka, K. Takeda, et al. (2005). "Detection of initiating as well as promoting activity of chemicals by a novel cell transformation assay using v-Ha-ras-transfected BALB/c 3T3 cells (Bhas 42 cells)". In: *Mutation Research* 588.1, pp. 7–21.

Combes, R., M. Balls, and R. Curren (1999). "Cell Transformation Assay as Predictor of human carcinogenicity, ECVAM Workshop Report 39". In: *Alternatives to laboratory animals: ATLA* 27, pp. 745–767.

Corvi, R., M. J. Aardema, L. Gribaldo, M. Hayashi, et al. (2012). "ECVAM prevalidation study on in vitro cell transformation assays: General outline and conclusions of the study". In: *Mutation Research/Genetic Toxicology and Environmental Mutagenesis* 744.1, pp. 12–19.

Creton, S., M. J. Aardema, P. L. Carmichael, J. S. Harvey, et al. (2012). "Cell transformation assays for prediction of carcinogenic potential: state of the science and future research needs". In: *Mutagenesis* 27.1, pp. 93–101.

EC (2003). "Directive 2003/15/EC of the European Parliament and of the Council of 27 February 2003 amending Directive 78/786/EEC on the approximation of the laws of the member states relating to cosmetic products". In: *Official Journal of the European Union* 66, pp. 26–35.

ECHA (2008). *Guidance on information requirements and chemical safety assessment.*

EURL ECVAM (2012). *EURL-ECVAM -Recommendation on three Cell Transformation Assays.*

IARC/NCI/EPA Working Group (1985). "Cellular and Molecular Mechanisms of Cell Transformation and Standardization of Transformation Assays of Established Cell Lines for the Prediction of Carcinogenic Chemicals: Overview and Recommended Protocols". In: *Cancer Research* 45, pp. 2395–2399.

Jacobson-Kram, D. and A. Jacobs (2005). "Use of genotoxicity data to support clinical trials or positive genetox findings on a candidate pharmaceutical or impurity .... now what?" In: *International Journal of Toxicology* 24.3, pp. 129–34.

Kakunaga, T. (1973). "A quantitative system for assay of malignant transformation by chemical carcinogens using a clone derived from BALB-3T3". In: *International journal of cancer* 12.2, pp. 463–473.

LeBoeuf, R. A., K. A. Kerckaert, M. J. Aardema, and R. J. Isfort (1999). "Use of Syrian hamster embryo and BALB/c 3T3 cell transformation for assessing the carcinogenic potential of chemicals". In: *IARC scientific publications* 146, pp. 409–425.

OECD (2007). *Detailed Review Paper on Cell Transformation Assays for detection of chemical carcinogens - series on testing and assessment Number 31.*

– (2009). *Test Guideline 451 – Carcinogenicity studies. OECD Guidelines for the Testing of Chemicals.*

Pfuhler, S., A. Kirst, M. Aardema, N. Banduhn, et al. (2010). "A tiered approach to the use of alternatives to animal testing for the safety assessment of cosmetics: Genotoxicity. A COLIPA analysis". In: *Regulatory Toxicology and Pharmacology* 57.2, pp. 315–324.

Poth, A. (2009). "Cell transformation assay -past-present-future". In: *ALTEX: Abstracts 7th World Congress Rome 2009* 26.

Procaccianti, C., F. M. Stefanini, and C. Urani (2011). "The cell transformation assay: toward a statistical classification of mixed and intermediate foci images". In: *Alternatives to laboratory animals: ATLA* 39.1, pp. 23–36.

Python Language Reference, version 2.7 (2012). *Jython*. URL: http://www.jython.com/.

R Core Team (2012). *R: A Language and Environment for Statistical Computing*. URL: http://www.R-project.org/.

Sakai, A., K. Sasaki, K. Hayashi, D. Muramatsu, et al. (2011). "An international validation study of a Bhas 42 cell transformation assay for the prediction of chemical carcinogenicity". In: *Mutation Research/Genetic Toxicology and Environmental Mutagenesis* 725.1, pp. 57–77.

Sasaki, K., S. Bohnenberger, K. Hayashi, T. Kunkelmann, et al. (2012b). "Photo catalogue for the classification of foci in the BALB/c 3T3 cell transformation assay". In: *Mutation Research* 744.1, pp. 42–53.

Sasaki, K., S. Bohnenberger, K. Hayashi, T. Kunkelmann, et al. (2012a). "Recommended protocol for the BALB/c 3T3 cell transformation assay". In: *Mutation Research/Genetic Toxicology and Environmental Mutagenesis* 744.1, pp. 30–35.

SCCS (2010). *The SCCS's notes of guidance for the testing of cosmetic ingredients and their safety evaluation - Scientific Committee on Consumer Safety, 7th revision*.

Schindelin, J., I. Arganda-Carreras, E. Frise, V. Kaynig, et al. (2012). "Fiji: an open-source platform for biological-image analysis". In: *Nature Methods* 9.7, pp. 676–682.

Tanaka, N., S. Bohnenberger, T. Kunkelmann, B. Munaro, et al. (2012). "Prevalidation study of the BALB/c 3T3 cell transformation assay for assessment of carcinogenic potential of chemicals". In: *Mutation Research/Genetic Toxicology and Environmental Mutagenesis* 744.1, pp. 20–29.

Urani, C., F. M. Stefanini, L. Bussinelli, P. Melchioretto, and G. F. Crosta (2009). "Image analysis and automatic classification of transformed foci". In: *Journal of microscopy* 234.3, pp. 269–279.

4

A classifier of foci based on statistical image descriptors

In this Chapter methods and descriptors introduced in the previous Chapter are exploited to build a foci classifier to improve the scoring phase of foci in the Cell Transformation Assay. In addition, a new method for the segmentation of foci images is presented.

Abstract

Carcinogenesis is a multi-step process involving genetic alterations and non-genotoxic mechanisms. The *in vitro* cell transformation assay (CTA) is a promising tool for both genotoxic and non-genotoxic carcinogenesis.

Herewith we provide a promising approach based on image analysis to support the scoring of malignant *foci* in BALB/c 3T3 CTA.

The image analysis system is a quantitative approach, based on measuring features of malignant *foci*: dimension, multilayered growth, and invasivity into the surrounding monolayer of non-transformed cells. A logistic regression model was developed to estimate the probability for each *focus* to be transformed as a function of three statistical image descriptors. The estimated sensitivity of the derived classifier (untransformed against Type III) was 0.9, with an Area Under the Curve (AUC) value equal to 0.90 under the Receiver Operating Characteristics (ROC) curve.

This Chapter is adapted from the published paper "An improved classification of foci for carcinogenicity testing by statistical descriptors", Callegaro, G., Stefanini, F.M., Colacci, A., Vaccari, M., Urani, C. Toxicology in Vitro, 29, 1839–1850, 2015.

4.1 Introduction

Not all the chemicals on the market have been adequately tested for their carcinogenic potential in humans and, more importantly, very little is known about the carcinogenic activity of single compounds in complex mixtures (Mascolo et al., 2010; Rodríguez-Sastre et al., 2014). To fulfil all the requirements of the current regulations to test the carcinogenicity of so many chemicals, following the standard test guidelines for animal studies, would require a huge number of animals, lengthy process and corresponding large investments (OECD, 2009a,b). The adoption of Integrated Testing Strategies (ITS), including both *in silico* and *in vitro* techniques, may contribute to the goal of further implementation of the 3R-principles in chemical safety assessment (Russel and Burch, 1959; Jaworska and Hoffmann, 2010).

Among the *in vitro* methods for carcinogenicity, the Cell Transformation Assay (CTA) seems to offer several advantages, including the possibility to highlight non-genotoxic compounds. For a complete description of CTAs, see section 1.2.2.

The aim of the present study is to develop and implement an automated imaging tool to support the scoring of malignant *foci* in the BALB/c 3T3 CTA.

BALB/c 3T3 CTA is a well-known model that has been used since 1965. Initially developed to study the virus-induced cell transformation, it was the first transformation assay to be set up to examine the tumour promotion *in vitro* (Schechtman, 1985). Contrary to other established cell lines (Jacobs et al., 2013), BALB/c 3T3 cells still retain enough metabolic activity to support both phase-1 and phase-2 metabolic activation of carcinogens (Colacci et al., 2011). The exposure to transforming agents leads to the formation of malignant *foci*, which can induce tumours when injected into suitable host animals (Melchiori et al., 1992; Adatia et al., 1993; Colacci

et al., 1993). BALB/c 3T3 CTA has been chosen in this study as the reference assay to highlight the efficiency of statistical descriptors to identify Type III *foci*. Our aim is to provide assistance in the *foci* scoring and support the use of this assay in ITS for carcinogenicity.

4.2 Material and Methods

4.2.1 Cells

The BALB/c 3T3 A31-1-1 cell line was purchased from the Health Science Research Resource Bank (Osaka, Japan). The cells were grown in Minimum Essential Medium (MEM) with 10% Fetal Bovine Serum (FBS) and routinely maintained in a humidified incubator with an atmosphere of 5% CO_2 in air at 37 °C. The cell cultures were cryoconserved in MEM 10% FBS solution containing 5% dimethyl sulfoxide (DMSO) and used for the CTAs at passage 3-5 from the initial stock. For the transformation assays, only sub-confluent cells (about 70% confluence) were used. The target cells were not maintained in culture beyond the third passage after thawing.

4.2.2 Cell Transformation Assay

The *foci* were obtained in the BALB/c 3T3 CTA performed according to the experimental protocol shown in Figure 4.1.

Cells were seeded at a density of 2 x 10^4 cells/100-mm plate in MEM 10% FBS containing 1% 10,000 U/ml penicillin 10 mg/ml streptomycin (M10F) and incubated at 37 °C in a 5% CO_2 humidified atmosphere for 24 h. Then, cells were exposed to the well-known carcinogen 3-methylcholanthrene (MCA, CAS number 56-49-5, Sigma-Aldrich, purity 98%), at the concentration of 4 μg/ml. Untreated

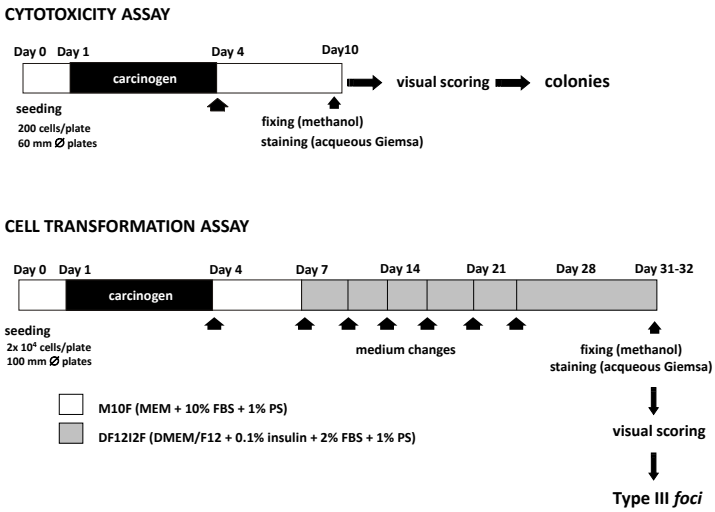

Figure 4.1: BALB/c 3T3 CTA experimental protocol.

BALB/c 3T3 A31-1-1 cells and solvent-treated (0.1% DMSO) cells were used as negative controls. After 72 h, the treatment medium was removed and replaced with M10F medium. At Day 7, M10F medium was replaced with DF2I2F medium (DMEM/F12 containing 2% FBS, 0.1% 2 mg/ml bovine insulin, 1% PS). Thereafter, DF2I2F medium was changed twice a week until Day 25. At Day 31-32, cells were fixed with methanol, stained with 10% aqueous Giemsa and scored for *foci* formation. The concurrent cytotoxicity assays were performed by seeding exponentially growing BALB/c 3T3 A31-1-1 cells at 200 cells/60-mm plate, in five replicates for each treatment. Cells were incubated and treated as for the CTA. At day 8-10, plates were fixed with methanol, stained with 10% aqueous Giemsa and scored for colony formation. Only colonies containing more than 50 cells were counted.

To create the digital image library from which statistical descrip-

tors were extracted, 18 plates treated with MCA coming from two different experiments were used. In the first experiment two different batches of Fetal Bovine Serum (FBS, Gibco Life Technologies catalogue number 10270-098, batch 41Q201K and 41A1119K) were tested in order to select the best experimental conditions to meet the acceptance criteria for the CTA. The selected serum (batch # 41Q201K) was used in the second experiment (n=10). Results were reported as: *i)* the number of positive plates (plates with *foci*/scored plates); *ii)* the mean number *foci*/plate ± standard error (SE); and *iii)* the transformation frequency (TF). TF is expressed as a function of the total number of *foci* for treatment divided by the number of surviving cells estimated from the clonal efficiency observed in the cytotoxicity assay performed in parallel with the transformation test (Schechtman, 1985).

The statistical significance of the results obtained in the CTA was assessed by applying the statistical tests, as previously reported (Mascolo et al., 2010). The percentage of plates with *foci* with respect to scored plates was calculated according to the Fisher–Yates test of significance in 2 x 2 contingency tables. The statistical analysis of the *foci* distribution was performed by the Mann–Whitney unpaired t-test. The Relative Clonal Efficiency (RCE) was analyzed by the Chi-square test of significance in 2 x 2 contingency tables. The TF significance was analyzed by the comparison of the Poisson rates, after verifying that the TF values fit a Poisson distribution.

4.2.3 Standard procedure for foci scoring

The scoring of the transformed *foci* was performed under an inverted microscope (40× magnification, Leitz DM-IL, Wetzlar, Germany), according to the following standard procedure: *i)* a trained expert performed the first scoring, taking into account the morphological criteria, as described below (Kakunaga, 1973; IARC/NCI/EPA Working Group, 1985; Sasaki et al., 2012a); *ii)* a second trained

expert reviewed the findings of the first trained expert; *iii)* for each *focus* which has different scoring between the first and the second reviewer, a third expert would make the final classification. The tabulated values represented the final product of this standard operating procedure.

4.2.4 Standard criteria for morphological classification

On the basis of morphological characteristics it is possible to distinguish three different categories of *foci*: Type I, II, and III. Type I *foci* are small, non invasive and weak basophilic. Type II *foci* are dense, multilayered, and show less basophilic staining than Type III, contain spindle-shaped cells, exhibit some cell piling-up and criss-crossing, although to a limited extent. Type III *foci* are densely multilayered (piling up), display deep basophilic spindle-shaped cells, which differ morphologically from normal cells of the background monolayer. Cells of Type III *foci* are randomly oriented and invade into the normal monolayer at the *focus* edge. Only Type III *foci* are included in the scoring. *Foci* whose diameter was less than about 2 mm are not included in the scoring.

4.2.5 Experimental workflow

The experimental workflow (Figure 4.2) is organized into two different but parallel paths, i.e. visual scoring and automatic scoring, providing two separate classifications which are eventually compared.

The visual scoring procedure performed by the experts, according to standard morphological criteria (Box A1), resulted in the classification of Type III *foci* or non-Type III *foci* (Box A2). See section 4.2.2 for details of the experimental procedures.

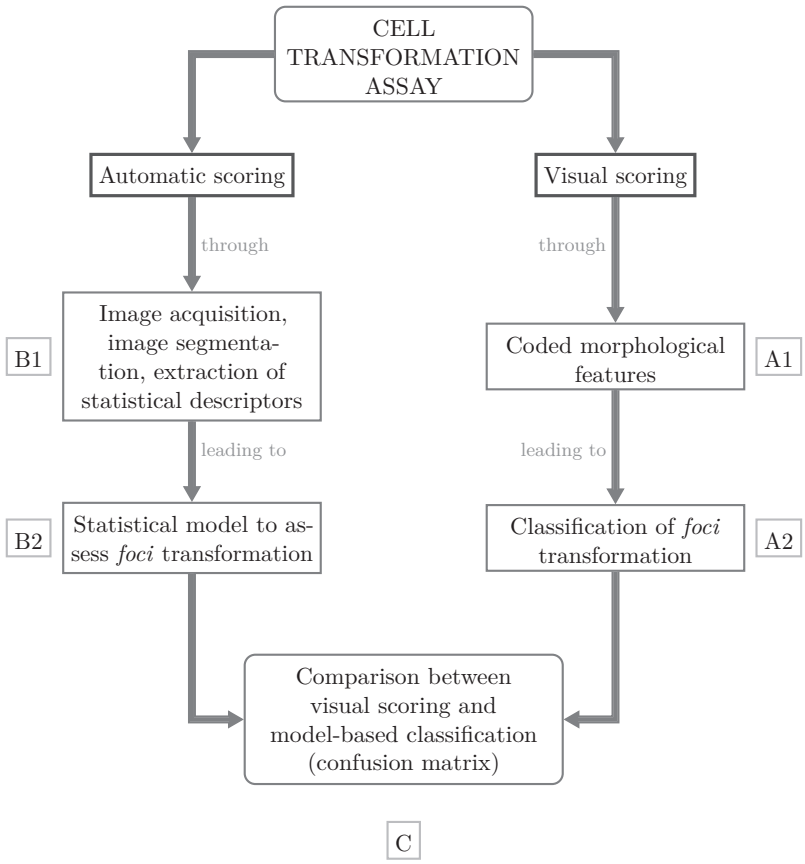

Figure 4.2: Experimental workflow. Standard CTA analysis (A) is shown on the right, while quantitative CTA analysis (B) based on statistical descriptors is on the left. CTA plates were visually scored using coded morphological descriptors (A1) leading to a classification of transformed *foci* (A2). B1: Images of *foci* coming from the BALB/c 3T3 CTA are acquired and *focus* area is isolated by means of an originally developed algorithm. From each region, specifically developed descriptors are extracted, in order to capture coded morphological features (par. 4.2.6). B2: Descriptors are used to build a statistical model to assess *foci* transformation, as detailed in par. 4.2.7. The results obtained from the expert visual scoring (A) and model-based classification (B) are compared and the model performance is evaluated (C).

Dishes were then acquired under a stereomicroscope equipped with a digital camera and organized in a digital library of images of *foci*. From each digital image the region whose pixels are representative of the *focus* was isolated by originally developed segmentation algorithm. Statistical summaries of pixels distribution and descriptors referring to each *focus* were then evaluated (Box B1) in order to build a statistical model able to assess the probability of transformation of each *focus* (Box B2). In sections 4.2.6 and 4.2.7 details on all these methodologies are provided.

A confusion matrix, finally, summarized the level of agreement between visual and automatic classifications (Box C).

4.2.6 Image processing

Images were acquired under a stereomicroscope (Zeiss, Stemi SV6) equipped with 6.3× lens (Carl Zeiss, Arese, Italy), as suggested by the recommended protocol for the BALB/c 3T3 CTA (Sasaki et al., 2012b). Images of *foci* were acquired with a digital camera (AxioCam Mrc5, 36 bit) under exposition of 23 ms and with an interactive balancing of white. Temperature of light was 5000 K while a gain factor was set to 1.

Images were saved in TIFF-48bit RGB format and had a size of 2572 × 1928 pixels, where 1 pixel is equivalent to a real size of 6.7842 $\times 10^{-3}$ mm (1 cm = 1474 pixels). A total of 306 digital images were acquired.

Foci images were processed using the Python programming language (Python Software Foundation, 2016): images were stored in a database created with the package PyTables and a segmentation algorithm based on the skimage library (Walt et al., 2014) was developed to separate the region corresponding to the *focus*, called region of interest (ROI), from the surrounding monolayer of normal cells.

During the visual scoring step, the experts are asked to identify the

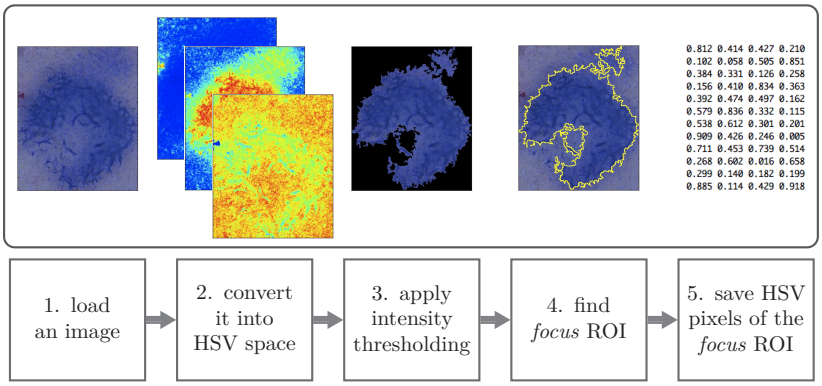

Figure 4.3: Flowchart of the segmentation algorithm. Flowchart of the main steps performed by the segmentation algorithm.

region corresponding to the *focus* and to characterize it. The properties of the *focus* region are compared to those of the surrounding monolayer with respect to all morphological features, in order to classify *foci* into different Types (I, II or III) (Sasaki et al., 2012a).

We implemented an algorithm that acquires a RGB colour space image, with 8 bit for each colour channel, converts it into HSV space and by appropriate intensity thresholding, separates the pixels belonging to the *focus* from the surrounding monolayer of untransformed cells (Figure 4.3).

HSV is a phenomenal colour space (Tkalcic and Tasic, 2003), characterized by three components: Hue, Saturation and Value of brightness. Hue is the quality of colour that distinguishes between red, yellow, green, blue, purple, and so on. Saturation characterises a colour as being pale or vivid; that means it measures the amount of white that has been added to a colour. Brightness is a measure of the intensity of light. This property of a colour allows to describe something as bright or dim. Each component of HSV colour space is a linear transformation of the three components of RGB space (Red, Green and Blue). The exact transformation functions depend on the equipment adopted, for our study we used the specific Python

package in matplotlib. HSV space is very close to mind's representation of colours, meaning the way human brain tends to organize colours. The perception of brightness is regulated in human eyes by the amount of light entering in the pupil. The retina light sensitive cells, rods and cones, perceive the amount of white (Saturation) and support the process to discriminate between different regions of wavelengths (Hue) (Cotton, 1996; Ford and Roberts, 1998; Tkalcic and Tasic, 2003).

A subset of 40 images was discarded because of failures in segmentation step. The remaining 266 ROIs, one for each distinct *focus*, were considered in the analysis, including also those *foci* which had partially grew on the edge of the Petri dish.

From each region identified by the segmentation process, we gathered statistical summaries of the distribution of images gray-levels and the descriptors previously developed (Urani et al., 2013). Details about these descriptors are reported in Table 4.1.

Table 4.1: Statistical descriptors collected. Statistical descriptors collected from each region segmented.

Variable collected	Definition
Median (MD)	the median value of the distribution of the image gray-levels of the *focus*
Weighted Perimeter Difference (WPD)	a measure of the invasiveness of the *focus* into the surrounding normal monolayer
Equivalent Diameter (ED)	diameter of the circle whose area is equal to the area of the *focus*

In summary, the statistical descriptors applied to a ROI (*focus*) included the median value (MD) of the distribution of gray values within a ROI, a measure of the level of multilayered growth. The gray level image displays the amount of light in the image, which means that the regions in the *focus* where cells piled up (multilayered) will correspond to darker pixels. On the other hand less multilayered regions will be brighter and will correspond to lighter pixels.

The descriptor called Equivalent Diameter (ED) is defined as the diameter of the circle whose area is equal to the area of the *focus*: $ED = 2\sqrt{\frac{area}{\pi}}$, where π is the trigonometric constant (3.1415). A *focus* is scored when the size of its diameter is more than about 2 mm. However, the shape of a *focus* is never a perfect circle. ED captures the size of the *focus* by taking into account the polymorphic shape of *foci*.

We suggest another statistical descriptor, instead of the previously defined Boundary Index (Urani et al., 2013), to take into account the ability of a transformed colony to invade the surrounding monolayer of not transformed cells. The third descriptor applied to the collected images was therefore the newly defined Weighted Perimeter Difference:

$$WPD = (FP - EFP) * \frac{(area - area_{min})}{(area_{max} - area_{min})} \tag{4.1}$$

where $area_{min}$ and $area_{max}$ are, respectively, the minimum and the maximum values of *focus* area observed in the collected data. Weight $(area - area_{min})/(area_{max} - area_{min})$ was calculated using a subset of the original values covered by the area summary, in which potential outliers were discarded, namely values lower than the 10% percentile and higher than the 90% percentile of the area distribution (trimmed subset). The gap between the actual perimeter of the region corresponding to the *focus* (FP) and the perimeter of a circle whose area is equal to the area of the *focus* (EFP) is itself an index of the invasivity of the colony: branches and ramifications of *focus* into the monolayer, as a consequence of directional growth, make the real perimeter exceeding the EFP.

Weighting the *focus* area highlights the difference between Type III and non-Type III *foci*: small non-Type III *foci* are usually not invasive, while large and fully transformed *foci* often show a high degree of invasiveness. By weighting the area, which corresponds to the *focus* size, a better descriptor was obtained to discriminate Type III *foci* from non-Type III *foci*.

4.2.7 Statistical models

All segmented ROIs were stored into a database together with summary information, visual scores, and values of the statistical descriptors.

We used binary logistic regression models, which describe the relationship between a dependent binary variable and one or more independent variables. Here the response variable Y_i, with $i = 1, 2, \ldots, n$, took value 1 if the *i-th focus* was classified as Type III, otherwise it was set to 0. The set of independent variables included statistical descriptors calculated on digital ROIs.

In the logistic regression model, the probability π_i that *focus* i is Type III is modeled on a transformed scale as a linear function of statistical descriptors x_1, x_2, x_3, namely Median (x_1), Equivalent Diameter (x_2) and Weighted Perimeter Difference (x_3):

$$ln\left(\frac{\pi_i}{1-\pi_i}\right) = \beta_0 + \beta_1 x_{1,i} + \beta_2 x_{2,i} + \beta_3 x_{3,i} \tag{4.2}$$

where $\beta_0, \beta_1, \beta_2, \beta_3$ are the unknown regression coefficients (model parameters); in equation (4.2) symbol ln indicates the natural logarithm. On the original scale, the probability π_i is:

$$\pi_i = \frac{exp(\beta_0 + \beta_1 x_{1,i} + \beta_2 x_{2,i} + \beta_3 x_{3,i})}{1 + exp(\beta_0 + \beta_1 x_{1,i} + \beta_2 x_{2,i} + \beta_3 x_{3,i})} \tag{4.3}$$

where exp indicates the exponential function. The likelihood function is defined as:

$$\mathcal{L}(\beta_0, \beta_1, \beta_2, \beta_3) = \prod_{i=1}^{n} (1-\pi_i)^{(n-\sum_i y_i)} \pi_i^{\sum_i y_i} \tag{4.4}$$

where π_i is defined in equation (4.3).

The space of models defined by the three statistical descriptors and by their interactions was enlarged by including into the linear predictor

(unknown) smooth functions of one or more explanatory variables, for example:

$$ln\left(\frac{\pi_i}{1-\pi_i}\right) = \beta_0 + h_1(x_{1,i}) + h_2(x_{2,i}, x_{3,i}) \tag{4.5}$$

where $h_1(), h_2()$ are unknown smooth functions to be estimated. Note that, in equation (4.5), the smooth function $h_2()$ takes two variables as argument, thus their interaction is automatically considered while estimating $h_2()$. The smooth functions $h_1(), h_2()$ were assumed to belong to the class of Thin Plate splines and model fitting was performed by penalized maximum likelihood estimation (Wood, 2006). Model selection was performed by minimizing the UBRE score (Wood, 2006).

Contour plots are graphs representing model response as a function of a pair of variables, here statistical descriptors. The 2D surface is the estimated probability of being a Type III *focus*. Each line of a contour plot is characterized by the same value of estimated probability (isoline), therefore it represents all the couples of values of the two descriptors that determine the same probability value. Contour plots can be shown for two descriptors at time, keeping a fixed value for the value of the third descriptor.

Given a fitted model, the probability of being Type III *focus* for an unknown *focus* may be estimated, when the value of statistical descriptors is determined. If the estimated probability of being a Type III is not less then 0.5 then the decision is taken to consider the unknown *focus* as Type III. Otherwise, it is assigned to a non-Type III. Thresholds different from 0.5 might be chosen, as it used in the calculation of AUC (see below).

A *focus* scored as Type III would be a positive instance, a non-Type III *focus* would define a negative instance. The resulting classifier applied to the original data could match or not match the visual scoring (see Table 4.2), in the following way:

- True positive (TP): Type III *foci* correctly classified;
- False positive (FP): non-Type III *foci* classified as positive;

- True negative (TN): non-Type III *foci* correctly classified;
- False negative (FNO): Type III *foci* classified as negative.

Table 4.2: Confusion matrix of a binary classification. Confusion matrix of a binary classification, giving an agreement between the output of the classification and the visual scoring.

		Visual scoring	
		Type III	non-Type III
classification	Type III	True positive	False positive
	non-Type III	False negative	True negative

The classification performance is summarized by the Accuracy (ACC), Sensitivity (SNS) and Specificity (SPC) indexes. SNS and SPC are related to the metrics False Positive rate (FP rate) and True Positive rate (TP rate), used to evaluate model-based classification performance using Receiver Operating Characteristics (ROC) curves. Definitions of the above mentioned metrics follow:

$$\text{ACC} = \frac{TP + TN}{P + N} \tag{4.6}$$

$$\text{SNS} = \frac{TP}{P} = \text{TP rate} \tag{4.7}$$

$$\text{SPC} = \frac{TN}{N} = 1 - \text{FP rate} \tag{4.8}$$

ROC curves are two-dimensional graphs that visually depict the performance of a classification model: TP rate is plotted on the Y axis and FP rate is plotted on the X axis. A ROC graph shows trade-offs between benefits (true positives) and costs (false positives). In particular, the ROC algorithm computes FP rate and TP rate through different thresholds, including the selected value 0.5. The diagonal line from the bottom left corner to the top right corner denotes the performances of a random classifier using no information, thus it is a reference to judge the performances of the investigated

classifier (Fawcett, 2004). The Area Under the ROC curve (AUC) was also calculated, to consider in a single scalar value the ability of the classifier to differentiate between the distributions of the two classes (Hand and Till, 2001). ROC analysis was conducted using ROCR toolkit for the R computing language (Sing et al., 2005).

4.3 Results

4.3.1 Cell transformation assay

The overall results from the CTAs experiments were reported in Table 4.3. Only Type III *foci* were used for data reporting and statistical comparisons. As shown in Table 4.3, no spontaneous malignant transformation was observed in the BALB/c A31-1-1 cells. The positive control (MCA, 4 μg/ml) induced a significant increase of the transformation frequency, while the negative control (DMSO, 0.1%) did not induce any significant increase of the cell transformation. In Table A1 in Appendix 1, the results of the visual scoring of MCA-treated plates are reported, together with the number of digital images that were correctly acquired from each scored plate.

4.3.2 Segmentation

In order to gather statistical descriptors related to each *focus*, a segmentation step was performed to isolate the ROI corresponding to the *focus* from each image. We developed a segmentation algorithm, able to separate pixels belonging to the *focus* from pixels belonging to the surrounding monolayer, by defining appropriate thresholding in the HSV colour space (see paragraph 4.2.6 for detailed references).

Table 4.3: CTA results. Effects of the treatment with MCA on the transformation rate of BALB/c 3T3 A31-1-1 cells.

Treatment	Plates with *foci*/ plates scored	Mean n° of transformed *foci*/plate ± SE	Total *foci* number	RCE (%)	TF ($\times 10^{-4}$)
		Experiment 1 - FBS 1			
UC	0/4	0.00±0.00	0	100	0
DMSO 0.1%	0/4	0.00±0.00	0	100	0
MCA 4μg/ml	4/4[a]	9.25±1.70[b]	37	12[c]	72.55[d]
		Experiment 1 - FBS 2			
UC	0/4	0.00±0.00	0	100	0
DMSO 0.1%	0/4	0.00±0.00	0	100	0
MCA 4μg/ml	4/4[a]	18.00±2.16[b]	71	19[c]	75.79[d]
		Experiment 2 - FBS 1			
UC	0/10	0.00±0.00	0	100	0
DMSO 0.1%	2/10	0.20±0.13	2	100	0.22
MCA 4μg/ml	10/10[a]	12.10±1.30[b]	121	23[c]	59.31[d]

UC = untreated cells
RCE = relative clonal efficiency
TF = transformation frequency
FBS 1 = Fetal Bovine Serum, Gibco Life Technologies catalogue number 10270-098, batch 41Q201K.
FBS 2 = Fetal Bovine Serum, Gibco Life Technologies catalogue number 10270-098, batch 41A1119K.
[a] Significantly different from control (solvent-treated plates) for the Fisher-Yates test of significance in 2x2 contingency tables ($p < 0.01$)
[b] Significantly different ($p < 0.01$) from controls (solvent-treated cells) for the Mann-Whitney unpaired t test
[c] Significantly different ($p < 0.01$) from controls (solvent-treated cells) for the Chi-square test of significance in 2x2 contingency tables
[d] Significantly different ($p < 0.01$) from controls (solvent-treated cells) for the Poisson test

A threshold in the Saturation component (Figure 4.3, Box 3), representing the level of non-whiteness of the image, was found able to discriminate the monolayer area from the *focus* area, which was

characterized by an intense tone of colour, due to the high proliferation rate of the transformed cells and to their increased sensitivity to basophilic dyes.

In the following step (Figure 4.3, Box 4), the ROI corresponding to the *focus* was finally identified, excluding regions corresponding to some artefacts in the *foci* images, which were due to the presence of rings at the bottom of the plastic Petri dishes (see for example Figure 4.4d), or hand marks produced during the visual scoring (see Figure 4.6a).

All the pixels in the selected region were stored in the database, together with the informations related to the dish in which the *focus* had been found (Figure 4.3, Box 5).

4.3.3 Model-based classification

At the end of the segmentation process, the final database was composed of 266 ROIs, corresponding to 266 properly segmented *foci*. According to the expert visual scoring, our dataset was arranged as follows:

- 77 non-Type III *foci*, comprehending Type I and Type II *foci*;
- 189 Type III *foci*.

Among the non-Type III *foci*, there were 14 structures identified by the trained experts as “ambiguous”, showing some properties of Type III *foci* but not fulfilling all the requirements for the classification. “Ambiguous" *foci* were excluded from the training set for the model fitting and included in the test set for later prediction (see paragraph 4.3.4). Table 4.4 provides a general view of the dataset.

We developed a model to estimate the probability that a transformed structure would be a Type III *focus*, on the basis of the information collected from digital image analysis, including the three descriptors selected. The explanatory variables were: the Median (MD) of the

Table 4.4: Organization of the dataset. Dishes were previously scored and degree of transformation assessed for each *focus*. Last column shows the final abundances of the classes. Note that for model fitting a total of 252 *foci* (189 Type III and 63 non-Type III) were considered, having excluded the 14 "ambiguous" *foci*.

Visual scoring	# of *foci*	"Ambiguous" *foci*	# of total *foci*
Type III	189	0	189
Non-Type III	77	14	63

distribution of gray levels of the ROI, the Equivalent Diameter (ED) and Weighted Perimeter Difference (WPD), which is considered an invasiveness index. For further details about the structure of the descriptors and of the model see sections 4.2.6 and 4.2.7.

Contour plots in Figures 4.4 and 4.5 are built by overlaying values of image descriptors of *foci* on the probability surface (visually represented through iso-probability lines and background colours), that is the probability of being a Type III *focus* as a function of image descriptors. Values corresponding to image descriptors are shown in contour plots by circles and stars representing, respectively, *foci* visually scored as Type III and non-Type III. The probability surface is shown according to the variation of the two descriptors ED and WPD, plotted in x and y axes. The three graphs differ as regards the value taken by the independent MD descriptor. Note that the fitted model does not include interactions between MD and the other two descriptors. MD was calculated on the basis of the distribution taken from the ROI of each *focus* by transforming the original colour images into gray level images. To understand the information carried by the MD, the distribution of MD values over all the collected *foci* was examined. If the value of MD was close to the first quartile (e.g. the 25^{th} percentile, defining the smallest 25% of collected values) then the *foci* showed a high degree of multilayering. There is an inverse relationship between the MD value and the colour saturation of the *focus* region (the lower the MD value, the darker was the *focus* region).

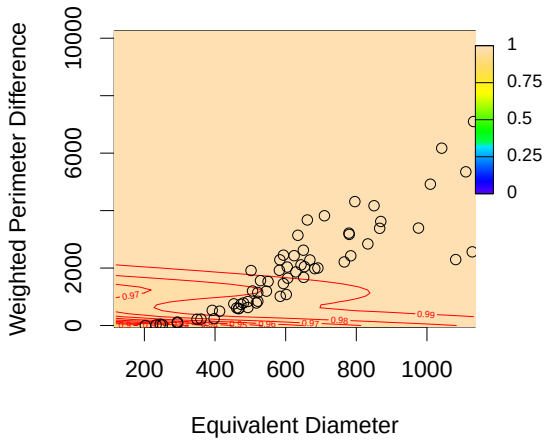

(a) Contour plot given MD= 1^{st} quartile, overlaid *foci* having MD values lower than its first quartile.

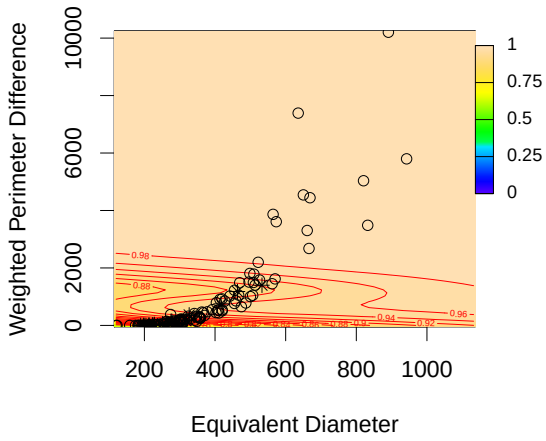

(b) Contour plot given MD= 2^{nd} quartile, overlaid *foci* having MD values between its first and third quartile.

Figure 4.4: Model response. Contour plots of model response (contour levels), and of the descriptors ED (x-axis), and WPD (Y-axis). Panels a and b show responses of the same model, given two different values of the independent descriptor Median (MD). Circles correspond to Type III *foci*, while stars represent non-Type III *foci*. Each contour line indicates the probability of being Type III *focus* as a function of image descriptors. Background colours emphasize changes of probability values, ranging from deep blue (close to 0) to orange-pink (close to 1).

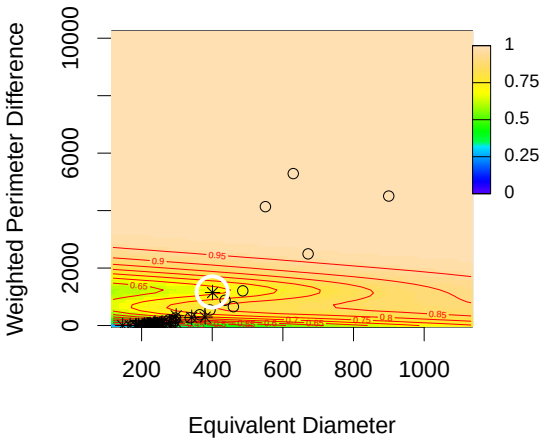

(a) Contour plot given MD= 3^{rd} quartile, overlaid *foci* having MD values higher than its third quartile. The white circle shows a non-Type III *focus* influential for the response.

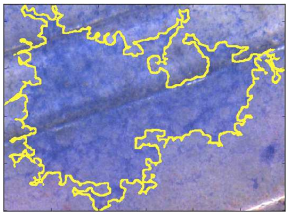

(b) Non-Type III *focus* highlighted in panel c by a white circle.

Figure 4.5: Model response. Contour plots of model response (contour levels), and of the descriptors ED (x-axis), and WPD (Y-axis). Panel a shows responses of the model, given MD= 3^{rd} quartile. Circles correspond to Type III *foci*, while stars represent non-Type III *foci*. Each contour line indicates the probability of being Type III *focus* as a function of image descriptors. Background colours emphasize changes of probability values, ranging from deep blue (close to 0) to orange-pink (close to 1). Panel b shows a non-Type III *focus*, driving the response of the model to lower values of probability to be a Type III *focus*.

In Figure 4.4a a contour plot is shown considering MD value equal to the first quartile of the distribution of MD values. To better understand the influence of descriptor values on the probability surface, we overlaid ED and WPD values of *foci* having MD value lower than its first quartile, representing the subset of collected *foci* involved in the current plot. Note that *foci* belonging to the above mentioned subset of dataset were all scored as Type III (circles). The model effectively was able to classify with high probability (higher than 0.9) a *focus* as Type III even if the other two descriptors had low values.

In Figure 4.4b a contour plot is shown considering MD value equal to the median of the distribution over *foci* (second quartile), in which the model-based estimated probability to be a Type III *focus* acquired lower values. In the same plot, observations characterized by an MD value between the first quartile and the third quartile are overlaid and showed a higher frequency of non-Type III *foci* (star points) compared to plotted values in Figure 4.4a.

Finally, in Figure 4.5a a contour plot of ED and WPD descriptors conditioned to the third quartile of MD distribution is shown. The subset of values of ED and WPD here overlaid collects *foci* having MD value higher than the third quartile of its distribution. Note that the frequency of non-Type III *foci* (star points) here is furthermore increased, compared to the previously described plots.

In these circumstances, the descriptors ED and WPD seemed to have a monotonic increasing relationship with the probability of a structure to be a Type III *focus*. Small *foci* with poor invasive properties have high probability to be non-Type III *foci*, with the presence of high MD values (indicative of reduced multilayering). For *foci* displaying lower multilayering, the probability to be classified as malignant *foci* was determined by the size and the level of invasiveness. In our model ED and WPD had enough information associated with these morphological characteristics.
A non-Type III *focus*, showed in Figure 4.5b, was characterized by average value of WPD (1147.94), a high value ED (400.79) and a

high value of MD descriptor (0.664). The estimated probability of being Type III *focus* for this *focus* was 0.55. Its digital image (Figure 4.5b) shows a quite jagged boundary and a large size that strongly influenced the shape of the probability surface in a region surrounding the coordinates of this *focus* (see contour lines in Figure 4.5a).

Given the fitted model and its estimated parameters, it is possible to estimate the probability of an unclassified *focus* to be classified as Type III. Choosing a threshold equal to 0.5, if the estimated probability of being a Type III is not less than 0.5 then the decision is taken to consider the unknown *focus* as Type III, otherwise it is assigned to a non-Type III class. Note that using this approach, it is possible to tune the threshold in the attempt to cope with borderline *foci*, whose probability of being Type III is near the threshold.

The resulting classifier was then applied to original data from the expert visual scoring to estimate the accuracy of classification. The confusion matrix and measures of the performance of the classification are shown in Figure 4.6.

Foci not correctly classified corresponded to very small Type III *foci* that probably have a very low value of the descriptor Equivalent Diameter compared to the other Type III *foci* (see for example Figure 4.6d). On the other side, non-Type III *foci*, which were overestimated by the model-based classification, were characterized by high values of the WPD descriptor, assigning to them higher probability to be Type III *foci* (see Figure 4.6b). An example is shown in Figure 4.5a, where one of these misclassified non-Type III *foci* (displayed in Fig 4.5b) was able to modify the contour level lines in the surrounding region, affecting the probability distribution shape but not at the point to increase the probability of being a Type III *focus*, at a 0.5 probability value.

A SNS index equal to 0.910 means that less than the 10% of the Type III *foci* have been misclassified and assigned to the class of lower transformation (Table 4.5). A SNS index remarkably high assures a good ability of the model to correctly classify Type III *foci* into

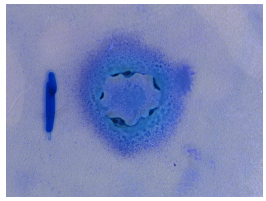

(a) Type III *focus* correctly classified.

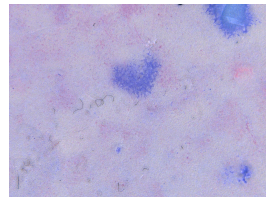

(b) Non-Type III *focus* classified as Type III (overestimated).

		Reference	
		Type III	non-Type III
predicted	Type III	172	20
	non-Type III	17	43

(c) Confusion matrix.

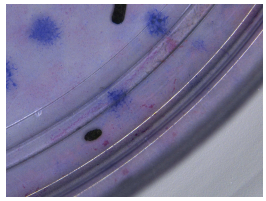

(d) Type III *focus* classified as non-Type III (underestimated).

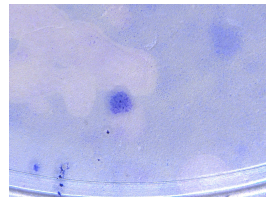

(e) Non-Type III *focus* correctly classified.

Figure 4.6: Model-based classification. Confusion matrix of the classification and examples of the predicted classes (the *focus* of interest is the one in the center of each image). The classification performed an ACC index equal to 0.853, SNS index equal to 0.910, while SPC was found to be equal to 0.683.

the corresponding positive class. This property is consistent with the reasonable requirement of avoiding misclassification of positive carcinogens.

Table 4.5: Classifier performances. SNS, SPC and ACC indexes of the model-based classification, using the two thresholds 0.5 and 0.6.

	0.5 threshold	0.6 threshold
Sensitivity index	0.910	0.868
Specificity index	0.683	0.794
Accuracy index	0.853	0.849

The SPC index, related to the ability of the classifier to recognize the negative class (non-Type III *foci*), was found to be equal to 0.683, meaning more that 30% of the non-Type III *foci* were misclassified (Table 4.5). An evaluation of the model-based classifier ability to identify both positive and negative instance is supplied by the ACC index. For the proposed model-based classification the accuracy index was found to be equal to 0.853 (Table 4.5).

To better evaluate the performance of our classifier, in Figure 4.7 we reported the ROC curve, which was built by setting different decision thresholds, in addition to the 0.5 threshold. This graph was intended to depict relative trade-offs between benefits (true positives) and costs (false positives) and provides a general and more balanced picture of the classification performance. Note that increasing the decision threshold from 0.5 to 0.6, the FP rate significantly decreased, while TP rate decreased to a smaller extent. With a decision threshold equal to 0.6, the performance indexes were more balanced, with sensitivity equal to 0.868 and specificity to 0.794, but the ACC index decreased (0.849), as compared to the performance at 0.5 threshold (Table 4.5).

In an applied context the threshold value should be selected according to the expected value of an utility function, a procedure considering decision-making criteria. Further work should address the elicitation of an utility function, taking into account the trade-off between

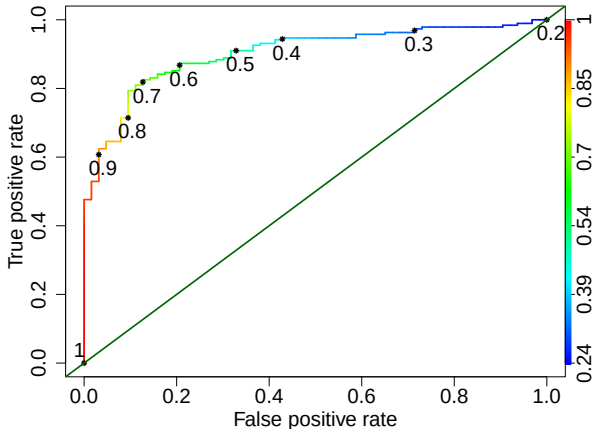

Figure 4.7: ROC curve. ROC curve with decision threshold values showed in rainbow colours. Labels for classifiers built with decision thresholds from 0.2 to 1 in steps of 0.1 are reported. The Area Under the Curve (AUC) was found to be equal to 0.903.

true positive and true negative recognition. Finally, the AUC index calculated from the ROC curve was found to be equal to 0.903.

4.3.4 Classification of "ambiguous" *foci*

Since several morphologically altered structures from Experiment 1 were difficult to discriminate as Type III or Type II *foci*, we reported them as "ambiguous" *foci*. These *foci* were not included in the model fitting because considered by the trained experts as "ambiguous". Therefore, their probability of being a Type III *focus* was estimated by using the model built with the complete dataset setting the probability threshold at 0.5.

Among 14 "ambiguous" *foci*, 11 were classified by the model as belonging to the class of the fully transformed Type III *foci*, while 3 of them were recognized to have a lower probability of being Type III *foci*, and eventually assigned to the not transformed class. These

foci were characterized by average values of the two descriptors MD and WPD, but showed very low values of the descriptor ED. When converting the pixel diameter into a real diameter (1 pixel=6.7810^{-3} mm) these *foci* appear to have a diameter smaller than 2 mm, which was the chosen cut-off for the classification as a fully transformed *focus* (Sasaki et al., 2012a).

The ED descriptor appeared to be very useful to support the classification of *foci* whose size is around the 2 mm cut-off. It allowed a more conservative approach than visual scoring, which is affected by the difficulty to correctly evaluate the size of small *foci*. Conversely, *foci* which exceeded the 2 mm cut-off, and that had been classified as "ambiguous" because showing a mixed phenotype, were cautiously identified as Type III *foci*, with the use of the model.

In Table A2 in Appendix 2, the number of "ambiguous" *foci* for each dish is reported, together with the model classification.

4.4 Discussion and Conclusions

This study focused on developing an automated imaging tool to support the scoring of malignant *foci* in BALB/c 3T3 CTA in the aim of addressing the subjectivity of scoring, one of the technical issue limiting its use.

It is agreed that the CTA should not be considered as a stand-alone assay for regulatory purposes but should be used as part of a Weight of Evidence approach or Integrated Testing Strategies in the context of the testing and assessment of substances for carcinogenic potential. However, CTA represents a promising tool for the prediction of carcinogenic properties, provided that some limitations could be overcome. The subjectivity in identifying morphologically transformed *foci* or colonies has often indicated as one of the main limitation of the CTAs (EURL ECVAM, 2011).

To address this problem, we started our investigation with a seminal work on C3H10T1/2 CTA, where first statistical descriptors were defined, providing a classifier of intermediate and mixed *foci* (Procaccianti et al., 2011). Shifting to BALB/c 3T3 CTA, by using the plates from the pre-validation study, we developed a more suitable methodology and extracted more informative descriptors (Urani et al., 2013 and Chapter 3), now applied, with some necessary fine tuning, and used to build a classifier in different CTAs.

The plates for digital imaging described in the present paper were provided by a laboratory, which has been working with BALB/c 3T3 CTA since 1989 (Colacci et al., 1990; Perocco et al., 1993; Mascolo et al., 2010; Colacci et al., 2014) and did not take part into the validation study. Plates were obtained from experiments performed with the A31-1-1 subclone to assess the carcinogenic potential of chemicals.
For the purpose of this study, we used *foci* induced by the treatment with MCA, a well known carcinogen, which is used as a reference chemical in the CTA. We are confident that the descriptors we developed on the basis of transformed *foci* induced by MCA could be applied to CTA results performed with other chemicals, belonging to different chemical classes. We cannot exclude, however, that adjustments of the model would be required in case of different morphologies as the consequence of chemical-induced transformation. At the current level of knowledge, and from a qualitatively point of view, the malignant phenotype is related to the cell type or target tissue, and surrounding microenvironment, rather than the kind of chemical, which, indeed, is responsible for the molecular initiating events and affects key biological features related to cancer onset and progression (Melchiori et al., 1992; Adatia et al., 1993; Colacci et al., 1993).

Starting from results obtained in a previous work (Urani et al., 2013, Chapter 3), a statistical model was developed to assign a probability value for every unclassified morphologically transformed structure to be a Type III *focus*. For this purpose *foci* images were acquired and

then regions of interest corresponding to each *focus* were isolated in a proper segmentation step. The segmentation algorithm we described here is able to recognize the region corresponding to the *focus* by using information carried by the HSV colour space. The boundaries of the *focus* are automatically identified without any intervention by the operator. The here described algorithm easily recognizes dense multilayered, fast growing Type III *foci* but also the thinner and not invasive non-Type III *foci*.

The probability model built with the calculated descriptors, using the decision threshold adjusted at 0.5, revealed a good ability to correctly classify Type III *foci* with high sensitivity index, but it was less effective in the recognition of negative instances. When adopting a decision threshold equal to 0.6, the performance became more balanced in terms of specificity and sensitivity but accuracy decreased. Finally, the value of AUC index suggested an overall good performance of the classifier, considering different possible decision thresholds. To this end, a decision rule could be established, requiring the expert intervention each time the probability value is very close to the 0.5 assigned value.

The plates from Experiment 1 and 2 had been visually scored, using the established classification criteria (Mascolo et al., 2010; Sasaki et al., 2012a). Some structures from Experiment 1, which showed borderline characteristics for the inclusion in the classification as Type III *foci*, such as mixed Type II/Type III morphological features or a size very close to the 2 mm cut-off, were marked as "ambiguous" and were not reported in Table 4.3. This conservative approach was routinely followed in order to reduce the risk of overestimating the transforming ability of chemicals (false positives). No *foci* were classified as "ambiguous" in the Experiment 2 since the photo-catalogue was very useful to reduce the uncertainties in the *foci* scoring.

Moreover, the combination of the digital image analysis and the photo catalogue can drastically reduce the subjectivity in the identification of fully malignant *foci*. However, even with the help of these tools, a certain level of subjectivity still remains in the assessment of

structures, showing all the hallmarks of morphological transformation, but whose diameter is around 2 mm. In this case, as showed by the results, the low value of the ED statistical descriptor of the automated system does not allow the classification of these structures as Type III *foci*. However, it is still possible to classify these structures as Type III *foci* on the basis of the expert judgement, after ruling out the possibility that they are daughter *foci*, stemming from the mother *focus*.

Our classifier has been built using statistical descriptors, that were defined on *foci* obtained from different laboratories, using different coded and uncoded chemicals.
As we reported before, the transformed cells acquire the same malignant properties after the treatment with different chemicals. For this reason we expect that this classifier would be applicable to BALB/c 3T3 CTAs carried out in different laboratories and will reveal good performance in terms of interlaboratory reproducibility. Moreover, it could be easily adapted to the classification of Bhas 42 *foci*.

The proposed automated approach could also help in the re-evaluation of results from experiments performed in different laboratories in order to establish inter-laboratories concordance and support the reliability of old existing data.

The level of accuracy of this approach may be enhanced by increasing the number of descriptors according to other reported features for the classification of malignant transformation (Kakunaga, 1973; IARC/NCI/EPA Working Group, 1985; Sasaki et al., 2012a), and by arranging them in a new model structure, trying to best use all the information encoded in the *foci* digital image. More exploration in this direction is presented in next Chapters.

In conclusion, we developed an automated imaging tool to support the scoring of *foci*, exploiting non conventional source of information, like morphological descriptors from microscope images, for carcinogenicity testing.

4.5 Bibliography

Adatia, R., A. Albini, A. Colacci, C. De Giovanni, et al. (1993). "Induction of chemotactic and invasive phenotype in BALB/c 3T3 cells by 1,2-dibromoethane transformation". In: *Invasion & Metastasis* 13.5, pp. 234–243.

Colacci, A., A. Albini, A. Melchiori, P. Nanni, et al. (1993). "Induction of a malignant phenotype in BALB/c 3t3 cells by 1,1,2,2-tetrachloroethane". In: *International Journal of Oncology* 2.6, pp. 937–945.

Colacci, A., M. G. Mascolo, S. Perdichizzi, D. Quercioli, et al. (2011). "Different sensitivity of BALB/c 3T3 cell clones in the response to carcinogens". In: *Toxicology in Vitro* 25.6, pp. 1183–1190.

Colacci, A., P. Perocco, M. Vaccari, M. Mazzullo, et al. (1990). "In vitro transformation of BALB/c 3T3 cells by 1,1,2,2-tetrachloroethane". In: *Japanese Journal of Cancer Research: Gann* 81.8, pp. 786–792.

Colacci, A., M. Vaccari, M. Mascolo, F. Rotondo, et al. (2014). "Alternative Testing Methods for Predicting Health Risk from Environmental Exposures". In: *Sustainability* 6.8, pp. 5265–5283.

Cotton, S. D. (1996). *Colour, Colour Spaces and the Human Visual System*. Technical Report B15-2TT. School of Computer Science, University of Birmingham, England.

EURL ECVAM (2011). *ESAC Working Group Peer Review Consensus Report on an ECVAM-coordinated prevalidation study concerning three protocols of the Cell Transformation Assay (CTA) for in vitro carcinogenicity testing*.

Fawcett, T. (2004). "ROC Graphs: Notes and Practical Considerations for Researchers". In: *Machine Learning* 31, pp. 1–38.

Ford, A. and A. Roberts (1998). "Colour space conversions". In: *Westminster University, London* 1998, pp. 1–31.

Hand, D. J. and R. J. Till (2001). "A Simple Generalisation of the Area Under the ROC Curve for Multiple Class Classification Problems". In: *Machine Learning* 45.2, pp. 171–186.

IARC/NCI/EPA Working Group (1985). "Cellular and Molecular Mechanisms of Cell Transformation and Standardization of Transformation Assays of Established Cell Lines for the Prediction of Carcinogenic Chemicals: Overview and Recommended Protocols". In: *Cancer Research* 45, pp. 2395–2399.

Jacobs, M. N., S. C. Laws, K. Willett, P. Schmieder, et al. (2013). "In vitro metabolism and bioavailability tests for endocrine active substances: what is needed next for regulatory purposes?" In: *ALTEX-Alternatives to Animal Experimentation* 30.3, pp. 331–351.

Jaworska, J. and S. Hoffmann (2010). "Integrated Testing Strategy (ITS) - Opportunities to better use existing data and guide future testing in toxicology". In: *ALTEX-Alternatives to Animal Experimentation* 27.4, pp. 231–242.

Kakunaga, T. (1973). "A quantitative system for assay of malignant transformation by chemical carcinogens using a clone derived from BALB-3T3". In: *International journal of cancer* 12.2, pp. 463–473.

Mascolo, M. G., S. Perdichizzi, F. Rotondo, E. Morandi, et al. (2010). "BALB/c 3T3 cell transformation assay for the prediction of carcinogenic potential of chemicals and environmental mixtures". In: *Toxicology in Vitro* 24.4, pp. 1292–1300.

Melchiori, A., A. Colacci, P. L. Lollini, C. De Giovanni, et al. (1992). "Induction of invasive and experimental metastasis potential in BALB/c 3T3 cells by benzo(a)pyrene transformation". In: *Invasion & Metastasis* 12.1, pp. 1–11.

OECD (2009a). *Test Guideline 451 – Carcinogenicity studies. OECD Guidelines for the Testing of Chemicals.*

– (2009b). *Test Guideline 453 - Combined Chronic Toxicity/Carcinogenicity Studies. OECD Guidelines for the Testing of Chemicals.*

Perocco, P., A. Colacci, and S. Grilli (1993). "In vitro cytotoxic and cell transforming activities exerted by the pesticides cyanazine, dithianon, diflubenzuron, procymidone, and vinclozolin on BALB/c 3T3 cells". In: *Environmental and Molecular Mutagenesis* 21.1, pp. 81–86.

Procaccianti, C., F. M. Stefanini, and C. Urani (2011). "The cell transformation assay: toward a statistical classification of mixed and intermediate foci images". In: *Alternatives to laboratory animals: ATLA* 39.1, pp. 23–36.

Python Software Foundation (2016). *Python Language Reference, version 2.7*. Python.org. URL: https://www.python.org/.

Rodríguez-Sastre, M. A., E. Rojas, and M. Valverde (2014). "Assessing the impact of As-Cd-Pb metal mixture on cell transformation by two-stage Balb/c 3T3 cell assay". In: *Mutagenesis* 29.4, pp. 251–7.

Russel, W. and R. Burch (1959). *The Principles of Humane Experimental Technique.*

Sasaki, K., S. Bohnenberger, K. Hayashi, T. Kunkelmann, et al. (2012a). "Photo catalogue for the classification of foci in the BALB/c 3T3 cell transformation assay". In: *Mutation Research* 744.1, pp. 42–53.

Sasaki, K., S. Bohnenberger, K. Hayashi, T. Kunkelmann, et al. (2012b). "Recommended protocol for the BALB/c 3T3 cell transformation assay". In: *Mutation Research/Genetic Toxicology and Environmental Mutagenesis* 744.1, pp. 30–35.

Schechtman, L. M. (1985). "BALB/c 3T3 cell transformation: protocols, problems and improvements". In: *IARC scientific publications* 67, pp. 165–184.

Sing, T., O. Sander, N. Beerenwinkel, and T. Lengauer (2005). "ROCR: visualizing classifier performance in R". In: *Bioinformatics* 21.20, pp. 3940–3941.

Tkalcic, M. and J. F. Tasic (2003). *Colour spaces: perceptual, historical and applicational background*. Vol. 1. IEEE.

Urani, C., R. Corvi, G. Callegaro, and F. Stefanini (2013). "Objective scoring of transformed foci in BALB/c 3T3 cell transformation assay by statistical image descriptors". In: *Toxicology in Vitro* 27.6, pp. 1905–1912.

Walt, S. v. d., J. L. Schönberger, J. Nunez-Iglesias, F. Boulogne, et al. (2014). "scikit-image: image processing in Python". In: *PeerJ* 2, e453.

Wood, S. (2006). *Generalized additive models: an introduction with R*. CRC press.

5

Effects of carcinogens concentration on foci morphology

In this Chapter another elaboration based on the methodology presented in previous Chapters is developed to estimate the effect of two carcinogens on foci morphology.

Abstract

Cell Transformation Assays (CTAs) have long been proposed for the identification of chemical carcinogenicity potential, but they are affected by potential subjectivity in the scoring phase. An objective evaluation of morphological features has been previously obtained through automated digital processing of *foci* images to extract the value of three statistical image descriptors. In this study a further potential of the CTA using BALB/c 3T3 cells is addressed by analysing the effect of increasing concentrations of two known carcinogens with different mode of action (benzo[a]Pyrene and $NiCl_2$) on *foci* morphology.

The main result of our quantitative evaluation shows that the concentration of the considered carcinogens has an effect on *foci* morphology that is statistically significant for the mean of two among the three selected descriptors. Statistical significance also corresponds to visual relevance. Therefore, it has the potential of providing new quantitative parameters in CTAs, and of exploiting all the information encoded in *foci*.

This Chapter is adapted from the published paper "Relationship between increasing concentrations of two carcinogens and statistical image descriptors of foci morphology in the Cell Transformation Assay", Callegaro, G., Corvi, R., Salovaara, S., Urani, C., Stefanini, F.M. Journal of Applied Toxicology, 5 December 2016.

5.1 Introduction

The Cell Transformation Assays (CTAs) have long been proposed for the identification of chemical carcinogenicity potential. For a complete description of CTAs, see section 1.2.2.

Despite the wide fields of applications and the numerous advantages of CTAs, their use in regulatory toxicology has been limited in part due to concerns about the reproducibility of the results between different laboratories in relation to the subjective nature of using morphological features for the identification of transformed cells, and the lack of understanding the mechanisms underlying the process of transformation (EURL ECVAM, 2012).

Recently several efforts have been undertaken to standardize and validate this test method, as well as to improve and refine different aspects of these assays. In particular, work is underway to respond to concerns that have been raised, such as the need for an objective scoring of transformed *foci*. This was addressed in the prevalidation and validation studies coordinated by the European Reference Laboratory on Alternative Methods (EURL ECVAM) and the Japanese Centre for the Validation of Alternative Methods (JaCVAM), which led to the publication of standardized protocols in combination with photo catalogues to support the researchers during the scoring procedure (Bohnenberger et al., 2012; Maire et al., 2012; Sasaki et al., 2012a; 2015; OECD, 2016 Annex 2). In the framework of this study, a new statistical method to improve the analysis of BALB/c 3T3 CTA data was developed (Hoffmann et al., 2012). Moreover, efforts addressed at the automation of the visual scoring and of *foci* classification by means of image analysis are ongoing in our group and several approaches based on extraction of statistical descriptors have already been published (Ridder et al., 1997; Urani et al., 2009; Procaccianti et al., 2011; Urani et al., 2013; Callegaro et al., 2015). In these studies, digital images of *foci* were acquired and regions of

interest corresponding to every single *focus* were identified. Statistical descriptors reflecting the coded morphological features, which are at the basis of visual scoring of *foci*, were developed with the aim of building a quantitative *foci* classifier. For more details about the aforementioned statistical descriptors, see Chapters 3 and 4.

The goal of this study is to provide the means to further exploit CTA results in order to consider the information encoded in *foci* morphology. To this aim, the effect of different concentrations of two known carcinogens, benzo[a]Pyrene (B[a]P) and nickel chloride ($NiCl_2$) on *foci* morphology is assessed in the CTA using BALB/c 3T3, as captured by three selected *foci* descriptors. As far as we are aware, this is the first attempt to quantitatively evaluate the role played by different concentrations of carcinogens on the morphological endpoint in the transformation process. The two carcinogens were selected based on their different modes of action, (B[a]P) which exerts its effects through genotoxic mechanisms, and $NiCl_2$ as it is known to act through indirect interactions with DNA.

5.2 Material and Methods

5.2.1 CTA experiments

The BALB/c 3T3 CTA experiments were previously performed by EURL ECVAM within two studies. The first study aimed at evaluating the transforming properties of different forms of nickel (Salovaara et al., in preparation) and the other one assessed the transforming potential of B[a]P as part of a broader study aimed at prevalidating the BALB/c 3T3 CTA (Corvi et al., 2012; Sasaki et al., 2012b). The assays were carried out according to the experimental protocol used in the EURL ECVAM prevalidation study (Corvi et al., 2012; Sasaki et al., 2012b). A concentration of 4 μg/ml of 3-methylcholanthrene

(MCA, CAS number # 56-49-5) was chosen as the positive control as this concentration was reported to induce positive transformation responses (Tanaka et al., 2012). In the present work we focused on the dishes treated with different concentrations of $NiCl_2$ (CAS number # 7718-54-9), more precisely the tested concentrations were 250, 275, 300, 350 and 400 μM. (CAS number # 50-32-8) Tested concentrations for B[a]P (CAS number # 50-32-8), were 0.0005, 0.005, 0.001, 0.05, 0.125, 0.625, 3.125, 15 μg/ml.

As described in the recommended protocol and in the photo catalogue, the scoring of transformed *foci* was performed under a stereomicroscope according to predefined criteria related to morphological characteristics, which allowed to assign the *foci* into three categories: Type I, Type II and Type III (Sasaki et al., 2012a; Tanaka et al., 2012). Only Type III *foci* were considered as transformed, and thus scored as positive. According to the recommended protocol, a *focus* with a diameter of less than 2 mm is too small to be considered as transformed.

Type I *foci* are small, non-invasive and weakly basophilic. Type II *foci* are multilayered, contain basophilic spindle shape cells, and exhibit some cell piling up and criss-crossing, although to a limited extent. Type III *foci* show dense multilayering (piling up) and display deep basophilic spindle-shape cells, which differ from the non-transformed monolayer of background cells, that shows contact-inhibition, and upon confluence is composed of flat, epithelial-like cells.

5.2.2 Workflow

The effect of different concentrations of two carcinogens on *foci* morphology was investigated through image analysis, as described by the workflow in Figure 5.1.

After performing the experiments (Box 1), *foci* images were acquired under a stereomicroscope equipped with a digital camera (Box 2), and

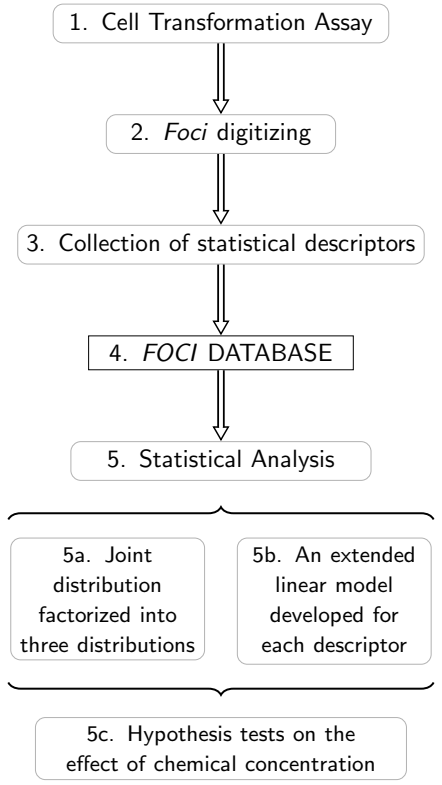

Figure 5.1: Experimental workflow. Main steps of the workflow: following the CTA experiments (1), *foci* images were acquired (2) and from each image three statistical descriptors were selected to represent distinct morphological features used in visual scoring (3). The *foci* datasets of the two carcinogens were analyzed by factorizing the joint probability distribution into three conditional distributions (5a), each one subsequently modeled in the class of extended linear mixed-effects models (5b). The final models including the concentration were selected according to the BIC value, then they were exploited to test the effect of carcinogen concentration on each image descriptors by likelihood ratio tests (5c).

statistical image descriptors were calculated for each *focus* (Box 3). A selection of three previously developed descriptors (Urani et al., 2013 and Chapter 3) was used to summarize the morphological features that are recognized as relevant in visual scoring (Sasaki et al., 2012a). As a result, a database comprising descriptors of *foci* morphology was built (Box 4), in which each collected *focus* is stored together with the value taken by its three descriptors, the carcinogen concentration and further auxiliary information represented by the label of the Petri dish in which the *focus* was acquired. The methodologies used in these steps, shown in Figure 5.1 by Boxes 2, 3, and 4, are detailed by Callegaro et al. (2015) and in Chapter 4 and summarized in section 5.2.3. The effect of concentration on *foci* morphology, as captured by selected image descriptors, was studied by developing extended linear mixed-effects models (Pinheiro and Bates, 2000, p.202 eq. 5.1) in which the correlation existing among *foci* collected from the same Petri dish was also taken into consideration. In each final model (3 descriptors times 2 carcinogens = 6 final models), a statistical test of the hypothesis stating the null effect of carcinogen concentration on *foci* morphology was performed. Further details about the statistical analysis in Boxes 5b and 5c of Figure 5.1 are provided in section 5.2.4.

5.2.3 *Foci* digitizing and data acquisition

Foci images were acquired by adopting the procedure previously developed by Callegaro et al. (2015), extensively described in Chapter 4 and briefly described below. Acquisition was performed under a stereomicroscope (Zeiss, Stemi SV6) equipped with 6.3× lens (Carl Zeiss, Arese, Italy) and a digital camera (AxioCam Mrc5, 36 bit). Images were saved in TIFF-48bit RGB format and had a size of 2572 × 1928 pixels, where 1 pixel is equivalent to a real size of 6.7842 $\times 10^{-3}$ mm (1 cm = 1474 pixels). Only fully transformed Type III *foci* were considered for the acquisition. *Foci* images com-

prised both the region corresponding to the transformed *focus* and a fraction of the surrounding monolayer of non-transformed cells. An original segmentation algorithm coded in Python (Python Software Foundation, 2016) was developed by Callegaro et al. (2015) in order to isolate the *focus* regions from the surrounding monolayer. The algorithm acquires a RGB colour space *focus* image, converts it into the HSV colour space and separates the region corresponding to each *focus* from the surrounding monolayer by setting appropriate intensity thresholds.

Table 5.1: The number of dishes and *foci* included in the final database following the segmentation process are shown for each $NiCl_2$ concentration. The initial number of dishes available for each concentration was 10. The symbol # stands for "number of".

Dose (μM)	# dishes containing Type III *foci* at the end of CTA	# dishes considered after segmentation	Total # of *foci* (III) before segmentation	# *foci* (III) after segmentation
250	7	4	10	6
275	10	10	33	23
300	10	10	73	40
350	10	10	137	78
400	9	9	29	18
Total	46	43	282	165

During the segmentation process a subset of all images (around 30% for $NiCl_2$ dataset, around 40% for B[a]P dataset) was discarded, mainly due to pen marks used in the visual scoring process. The derived $NiCl_2$ dataset comprised a collection of 165 Type III *foci* images, obtained from dishes tested with all the five $NiCl_2$ concentrations specified in section 5.2.1. While the B[a]P derived dataset comprised 224 Type III *foci* images, obtained from dishes tested with all eight B[a]P concentrations (see section 5.2.1).

The experiment has a balanced layout as regards the number of Petri dishes: ten Petri dishes were available for each treatment (i.e.

Table 5.2: The number of dishes and *foci* included in the final database following the segmentation process are shown for each B[a]P concentration. The initial number of dishes available for each concentration was 10. The symbol # stands for "number of".

Dose (μM)	# dishes containing Type III *foci* at the end of CTA	# dishes considered after segmentation	Total # of *foci* (III) before segmentation	# *foci* (III) after segmentation
0.0005	4	4	6	4
0.001	2	2	2	2
0.005	7	7	15	13
0.05	10	10	70	38
0.125	10	10	92	44
0.625	10	10	111	73
3.125	10	10	74	41
15	8	7	12	9
Total	46	43	382	224

$NiCl_2$ or B[a]P concentration). Nevertheless, a different number of Type III *foci* was observed in Petri dishes treated at different concentrations of the same carcinogen, therefore the resulting sample size is not constant over concentrations. The change in the number of segmented *foci* at each concentration was also due to the pen marks on Petri dishes, but no appreciable changes in the trend of number of *foci* depending on concentration are produced, as can be seen in the graphs of Figure 5.2 and Figure A3 in Appendix 3. See Table 5.1, Table 5.2 and Figure 5.2 for details on the structure of the two datasets after segmentation. Additional information about the number of *foci* observed at different concentrations before segmentation is shown in Figure A3 in Appendix 3.

For each image region corresponding to a Type III *focus* included in the final database after segmentation, the three previously developed statistical descriptors were calculated (Urani et al., 2013 and Chapter 3). These descriptors summarize three morphological features among those coded and visually scored in BALB/c 3T3 CTA (Sasaki et al.,

2012a), which are:

- Equivalent Diameter (ED);
- Median (MD);
- Boundary Index (BD).

The descriptor ED is defined as the diameter of the circle whose area is equal to the area of the *focus*: $\mathrm{ED} = 2\sqrt{\frac{\mathrm{area}}{\pi}}$, where π is the trigonometric constant. We selected the ED descriptor to evaluate the size of the *focus*, taking into account the *foci*'s shape polymorphism.

The descriptor MD is the median of the distribution made by image grey-levels in the region corresponding to a *focus*. The median

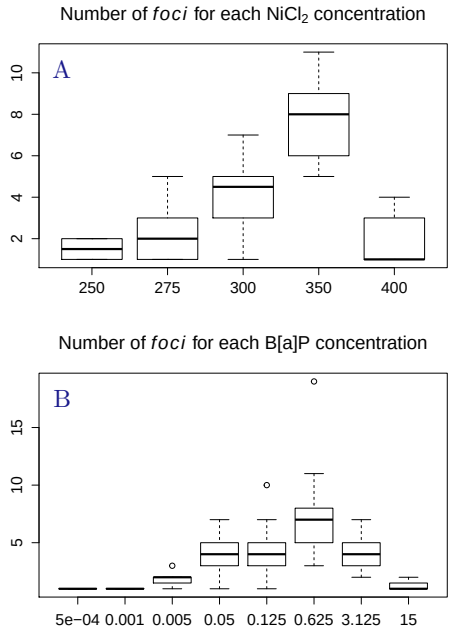

Figure 5.2: Boxplots of the number of *foci*. Boxplots of the number of Type III *foci* per dish given the carcinogen concentration. In A the number of *foci* from $NiCl_2$ dataset are shown, while in B the number of *foci* from B[a]P dataset are displayed. Empty circles in B represent candidate outliers.

value of this distribution depends on the degree of multilayer growth. Given that the intensity of light source is constant, image grey-levels mostly depend on the amount of light passing through the *focus* region: regions with dense piling up will correspond to darker image pixels, while regions that are less multilayered will correspond to lighter pixels.

Finally, the BD descriptor takes high values when invasive growth in the surrounding monolayer is pronounced, a typical feature of fully transformed cells belonging to Type III *foci*. Invasiveness often implies boundary heterogeneity of *foci*, thus the BD index compares the actual perimeter of the *focus* (FP) with the perimeter of the circle of equivalent area (EFP): $\mathrm{BD} = \frac{\mathrm{FP}}{\mathrm{EFP}} - 1$.

The above three descriptors were previously developed and applied to the analysis of *foci* images obtained from the prevalidation study coordinated by EURL ECVAM (Tanaka et al., 2012; Urani et al., 2013), which included a large amount of experiments conducted with coded and uncoded chemicals.

5.2.4 Statistical analysis

A generic Type III *focus* in a given Petri dish x_{PD} is characterized by the random variables Y_{ED} , Y_{MD} , Y_{BD} describing the value taken by statistical descriptors ED, MD and BD. The joint distribution of Y_{ED} , Y_{MD} , Y_{BD} given the Petri dish x_{PD} and the concentration x_C was considered at the start of model building. The factorization of the joint distribution function into univariate conditional distributions also allowed to study the dependence existing among statistical descriptors:

$$\begin{aligned} p(y_{ED}, y_{MD}, y_{BD} \mid x_{PD}, x_C, \theta) = {} & p(y_{ED} \mid y_{MD}, y_{BD}, x_{PD}, x_C, \theta_{ED}) \\ & * p(y_{MD} \mid y_{BD}, x_{PD}, x_C, \theta_{MD}) \\ & * p(y_{BD} \mid x_{PD}, x_C, \theta_{BD}) \end{aligned} \tag{5.1}$$

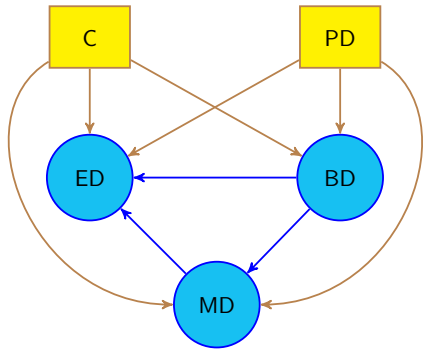

Figure 5.3: The dependence relationships between descriptors and concentration. The descriptors (ED, BD, MD) are displayed in blue circles, while nodes for concentration of a carcinogen (C) and Petri dish, both conditioning variables, are shown in yellow. Details of dependencies are provided in section 5.2.4.1.

where $\theta = (\theta_{ED}, \theta_{MD}, \theta_{BD})^T$ is the partitioned vector of model parameters. In Figure 5.3, the initial factorization for one single *focus* is shown by a Directed Acyclic Graph (details in Buntine, 1994) in which model parameters are omitted. Each conditional distribution on the right of equation 5.1 was parameterized assuming a Normal response explained by conditioning variables. Thus the starting model was in the class of linear mixed-effects models (Pinheiro and Bates, 2000) for each statistical descriptor. The concentration values were rescaled in the range [1,3] for the B[a]P carcinogen. The class of investigated extended linear mixed-effects models included linear predictors made by low degree polynomials of explanatory variables and their interactions, while the variance of the response was modelled as a function of the (rescaled) concentration. Model fitting was performed by Maximum Likelihood, after considering *foci* as conditionally exchangeable. A preliminary selection of reasonable models was performed looking for models with a small value of the Bayesian Information Criterion (BIC), while a Likelihood ratio test (Cox and Hinkley, 1979) for the effect of concentration was performed by comparing models with/without the explanatory variable concentration.

The final model of each descriptor belongs to the class of extended linear models (Pinheiro and Bates, 2000, p.202 eq. 5.1). The within group correlation existing among values of a descriptor assessed on *foci* located in the same Petri dish was computed by exploiting an R object in the class corCompSymm (nlme package, Pinheiro et al., 2015): we considered the Petri dishes as separate environments, characterised by micro-fluctuations of experimental conditions shared by all *foci* in each dish.

Residuals calculated from the final model of each image descriptor were graphically inspected to check model assumptions. Details about model diagnostic are provided Appendices 4 and 5, e.g. quantile-quantile plots of residuals for each model (Figures A4 and A5).

All statistical computations were performed in R (R Core Team, 2012), using nlme (Pinheiro et al., 2015) and effects packages (Fox, 2003). In Appendix 6 the code of the statistical analyses performed is detailed.

5.2.4.1 The factorization of the joint distribution

The statistical image descriptors ED, MD and BD carry information about morphological features jointly used for *foci* scoring, as previously shown by Urani et al. (2013) and in Chapter 3, therefore the correlation among them was expected. The configuration of considered dependencies is represented in Figure 5.3. The blue directed arrows shown in the graph represent dependence between the considered descriptors (details in Buntine, 1994). The influence of carcinogen concentration on the selected statistical descriptors is represented by yellow directed arrows starting in node C (Figure 5.3), while yellow arrows leaving node PD and reaching BD, ED and MD indicate the effect of Petri dish environment on *foci* morphology.

The factorization shown in equation 1 (section 5.2.4) was selected by taking into account the specific features of each descriptor before

looking at the data. A *focus* can expand in the x-y space of the Petri dish, determining its size, but it also grows in the third direction, the z axis of the Petri dish. Hence, it is expected that the MD descriptor would be also informative for the ED descriptor, which describes the dimension of a *focus*. Furthermore, the ability to invade the surrounding monolayer of non-transformed cells can be considered as influencing the growth process in the two-dimensional space of the Petri dish. Accordingly, the dependence relationship between ED and BD descriptors has to be taken into account (blue arrows in Figure 5.3).

Transformed BALB/c 3T3 cells in a *focus* exhibit different growth characteristics from those of non-transformed cells of the surrounding monolayer, primarily represented by a loss of contact-inhibition and uncontrolled proliferation due to complex molecular mechanisms. In a *focus* displaying these properties, the invasion on the monolayer of non-transformed cells can be observed, often by means of prolonged arms and vortexes of polarized cells (see for example figure 7D of Urani et al., 2013 and in Chapter 3). This behaviour of uncontrolled growth and invasiveness influences the *in vitro* three-dimensional growth (multilayering) of *foci*. Thus we developed a model for the response of the MD descriptor in which BD is an explanatory variable.

In addition, each Petri dish represents a separate environment in which *foci* are exposed to the same micro-environmental fluctuations and experimental errors, in contrast to *foci* observed in different dishes. For this reason, we have included into the model an intra-class correlation parameter (Pinheiro and Bates, 2000) which describes the degree of resemblance of *foci* in the same Petri dish for a given descriptor, as detailed in section 5.2.4. Note that, in the final model, we did not estimate the effects of Petri dishes since not relevant for the estimate of the effect of concentration on *foci* morphology, thus reducing the number of model unknowns.

5.2.4.2 Models

The estimated expected values of the three conditional distributions for the $NiCl_2$ and B[a]P carcinogens are shown respectively in Tables 5.3 and 5.4, just before testing for the contribution of concentration, therefore the concentration is included as explanatory variable.

Table 5.3: Point estimates from the $NiCl_2$ dataset. Expected value functions of each univariate conditional distribution for the final models including $NiCl_2$ concentration before testing the null hypothesis of no effect by means of likelihood ratio tests. The estimated value of intraclass correlation parameter is indicated as $\hat{\rho}$. The variance was modelled as a function of the rescaled concentration $\tilde{x_C}$. In particular, the estimated conditional variance function in all models is defined by the following equation: $\sigma^2{}_y = \sigma^2(\tilde{x_c}^{2\delta})$, where y is the descriptor considered as a response variable.

	Expected value	Variance function	Correlation
N1: $\hat{Y}_{ED} =$	$51993.62 - 141843 \cdot y_{MD} + 97223.63 \cdot y^2{}_{ED} + 1437.82 \cdot y_{BD} - 108.02 \cdot x_C - 1848.83 \cdot y_{MD} y_{BD}$	$\hat{\sigma} = 242.08$ $\hat{\delta} = 0.42$	$\hat{\rho} = 0.15$
N2: $\hat{Y}_{MD} =$	$0.72 + 0.013 \cdot y_{BD} - 0.13 \cdot x_C + 0.13 \cdot x_{C^2}$	$\hat{\sigma} = 0.024$ $\hat{\delta} = -0.16$	$\hat{\rho} = 0.01$
N3: $\hat{Y}_{BD} =$	$1.25 + 1.28 \cdot x_C$	$\hat{\sigma} = 0.94$ $\hat{\delta} = 0.16$	$\hat{\rho} = 0.006$

Note that $\hat{Y}_{ED} = E[Y_{ED} \mid y_{MD}, y_{BD}, x_{PD}, x_C, \theta_{ED}]$

5.3 Results

5.3.1 Conditional models of statistical descriptors

Considering the factorization of equation 5.1 also represented in Figure 5.3, in this section the final models of each image descriptor

given a specific carcinogen are described and commented. For details about model fitting, see sections 5.2.4.1 and 5.2.4.2.

Table 5.4: Point estimates from the B[a]P dataset. Expected value functions of each univariate conditional distribution for the final models including B[a]P concentration before testing the null hypothesis of no effect by means of likelihood ratio tests. The estimated value of intraclass correlation parameter is indicated as $\hat{\rho}$. The variance was modelled as a function of the rescaled concentration $\tilde{x_C}$. In particular, the estimated conditional variance function in all models is defined by the following equation: $\sigma^2{}_y = \sigma^2(\tilde{x_c}^{2\delta})$, where y is the descriptor considered as a response variable.

	Expected value	Variance function	Correlation
B1: $\hat{Y}_{ED} =$	$3232.74 - 4405.34 \cdot y_{MD} + 247.31 \cdot y_{BD} - 38.68 \cdot y^2{}_{BD} - 0.81 \cdot x_C$	$\hat{\sigma} = 228.7$ $\hat{\delta} = 0.06$	$\hat{\rho} = 0.15$
B2: $\hat{Y}_{MD} =$	$0.67 + 0.0003 \cdot y_{BD} - 0.001 \cdot x_C$	$\hat{\sigma} = 0.016$ $\hat{\delta} = 0.03$	$\hat{\rho} = 0.06$
B3: $\hat{Y}_{BD} =$	$1.60 + 0.08 \cdot x_C$	$\hat{\sigma} = 0.72$ $\hat{\delta} = -0.06$	$\hat{\rho} = 0.16$
Note that $\hat{Y}_{ED} = E[Y_{ED} \mid y_{MD}, y_{BD}, x_{PD}, x_C, \theta_{ED}]$			

5.3.1.1 The ED does not depend on carcinogen concentration

Models built to test the dependence of the expected value of ED on carcinogen concentration are indicated as model N1 ($NiCl_2$ dataset) and model B1 (B[a]P dataset) and they both include the other two descriptors, MD and BD, as explanatory variables. The model equations are shown in Table 5.3 and 5.4, first row. A remarkable feature of both models is that the effect of concentration on ED after including MD and BD was not found statistically significant. For model N1, the likelihood ratio test did not lead to the rejection of the hypotheses stating the null effect of concentration, with a p-value equal to 0.2427. Likewise, for model B1, the likelihood ratio test did not lead to the rejection of the hypothesis stating the

null effect of concentration, with a p-value equal to 0.8781. It is worth noticing that, although the expected value of ED does not depend on concentration, the value of variance does. Therefore, the conditional distribution of ED of both models indeed depends on concentration.

In practical terms, the average size of a *focus* does not depend on the concentration of a carcinogen when the comparison is performed among *foci* with the same values of BD and of MD.

Graphical summaries from the fitted models are shown in Figure 5.4, panels C and H, where linear relationships between the *focus* size and the concentration of the treatment can be observed. While the expected values for model B1 vary with B[a]P concentration according to a straight line whose slope is close to zero (panel H), for model N1 ($NiCl_2$ carcinogen) the correspondent slope is negative instead (panel C). Still, testing for the partial contribution exerted by concentration as explanatory variable led to the conclusion that concentration is not significant, as suggested also by the overlapping confidence intervals in Figure 5.4C. For each model, in Figure 5.4, are provided four examples of *foci* whose values of ED can be found in the extreme regions of the graph: for model N1 in Figure 5.4, panels A, B, D and E, for model B1 in the same Figure, panels F, G, I, J. Regardless the carcinogen concentration, small *foci* having low values for the ED descriptor (Figures 5.4, panels A and D, F and I) or bigger *foci* showing higher values for the ED descriptor (Figure 5.4, panels B and E, G and J) can be observed.

The dependence relationship between ED and MD descriptors was further explored by elaboration from fitted models. Considering the models presented here (see Table 5.3 and 5.4), a general large *focus* is characterized by a substantial ability to grow into multilayers, as shown by the *focus* in Figure 5.4, panels B and E, G and J. A reduced multilayer growth, in contrast, can be found in small *foci*, as the four provided in Figure 5.4, panels A and D, F and I.

Keeping in mind that MD is directly proportional to the amount of light in the *focus* grey-level image, low values for the MD descriptor

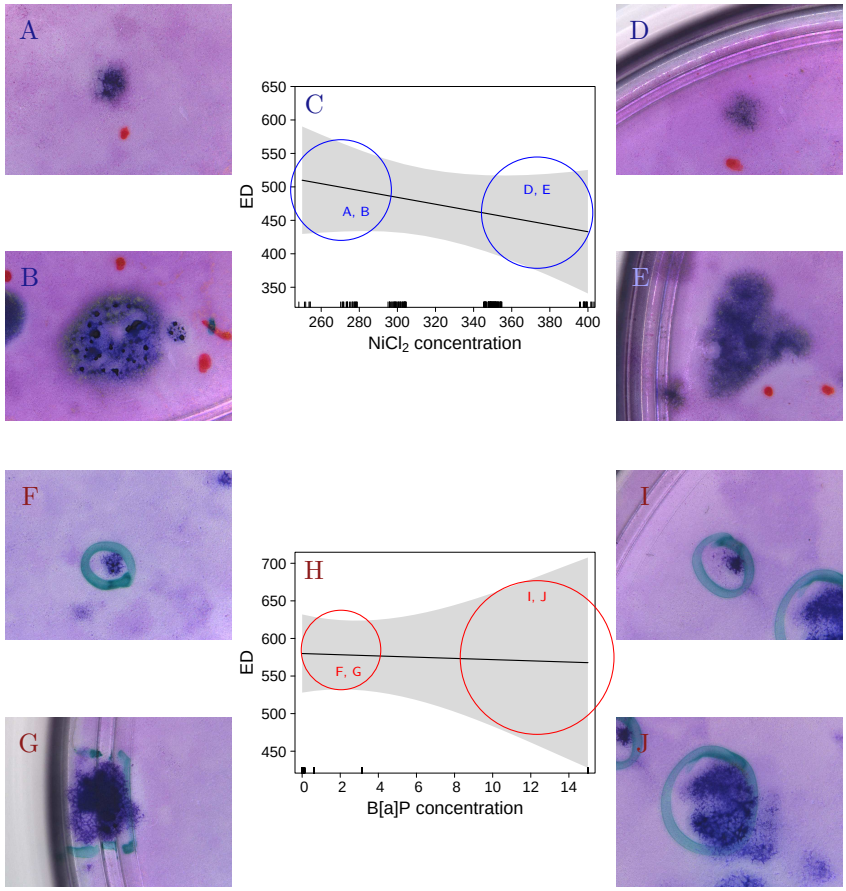

Figure 5.4: Plot of expected value functions for the Equivalent Diameter (ED) given the carcinogen concentration. In C and H, expected value functions of ED in models N1 ($NiCl_2$) and B1 (B[a]P) are plotted given the concentration. The grey shaded area represents pointwise confidence limits, on the scale of the linear predictor. Examples of *foci* showing ED values that can be found in the extreme regions of the graph are displayed in the panels A, B, D and E for model N1, and in F, G, I and J for model B1. The boxes on the x axis represent conditioning values of the carcinogen concentration.

will correspond to darker *foci*, thus *foci* characterised by several layers of cells. While high values for the MD descriptor will be associated with less multilayered *foci*.

Indeed, an inverse relationship can be found plotting the fitted values of ED versus MD descriptor, as provided in Appendix, Figures A4 and A5, panels G. A remarkable result from our analyses is that we found the same qualitative relationships among descriptors and of the concentration on descriptors, despite that models were fitted to data from two different types of carcinogen, one genotoxic and one non-genotoxic. Thus it will be interesting in the future to perform similar studies on additional carcinogens to test the general validity of such qualitative features.

5.3.1.2 The MD is dependent on carcinogen concentration

Models built to test the dependence of the expected value of Median descriptor (MD) on carcinogen concentration are indicated as Model N2 ($NiCl_2$ dataset) and Model B2 (B[a]P dataset) and they both include BD as explanatory variable (see Figure 5.3). The model equations are shown in Table 5.3 and 5.4, second rows.

In both models, the partial contribution of concentration after including BD into the model is statistically significant: for model N2, the likelihood ratio test for the hypothesis of no effect of concentration was rejected with a p-value lower than 0.005 (p-value 0.0025). Likewise, for model B2, the likelihood ratio test for the hypothesis of no effect of concentration was rejected with a p-value lower than 0.001 (p-value 0.0007). Hence for the average *focus*, multilayered growth changes with the carcinogen concentration when the comparison is performed among *foci* characterized by the same value of BD. With $NiCl_2$, the best model (N2) includes a second-degree polynomial in the concentration, thus the change of MD's average is not linear with respect to the increase of concentration (Figure 5.5, panel B).

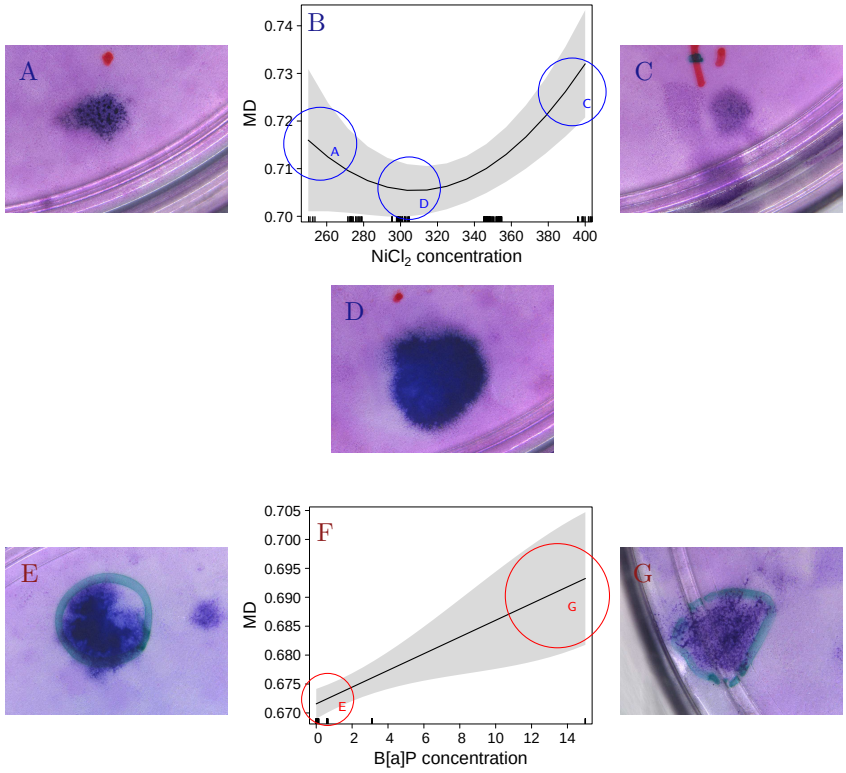

Figure 5.5: Plot of expected value functions of Median (MD) given the carcinogen concentration. In B and F expected values of MD in model N2 ($NiCl_2$) and B2 (B[a]P), respectively are plotted given the concentration. The grey shaded area represents pointwise confidence limits, on the scale of the linear predictor. Examples of *foci* showing MD values corresponding to the area inside the blue circles are displayed in panels A, C and D, while examples of *foci* showing MD values corresponding to the area inside the red circles are displayed in panels E and G. The boxes on the x axis represent conditioning values of carcinogen concentration.

Figure 5.5B describes the U-shaped non-linear behaviour of the MD descriptor obtained in Petri dishes treated with increasing concentrations of $NiCl_2$. A U-shaped trend can be observed with a minimum located at about 310 μM.

As MD is directly proportional to the amount of light in the *focus* grey-level image, high values for the MD descriptor will thus correspond to lighter *foci*, characterised by a reduced multilayering (Figure 5.5C). It follows that low values for the MD descriptor will be associated to *foci* characterized by a significant multilayer growth, as the one presented in Figure 5.5D. In the bounded range of considered concentrations, a first relative maximum, corresponding to 250 μM $NiCl_2$, is related to medium MD values, corresponding to *foci* not markedly and/or uniformly multilayered (see as example *focus* in Figure 5.5A); moderately higher MD values can be observed corresponding to the highest concentration (400 μM $NiCl_2$), as illustrated by the *focus* in Figure 5.5C. In between, corresponding to intermediate $NiCl_2$ concentrations (275-350 μM), the absolute minimum of the curve plotted in Figure 5.5B is located, suggesting the presence of multilayered *foci* (as e.g. Figure 5.5D). The best model for MD is not monotonic with the increase of concentration: higher and lower concentrations induce the formation of *foci* displaying a reduced multilayer growth, while *foci* obtained from intermediate $NiCl_2$ concentrations show an increase in this feature.

By contrast, in the best model built for B[a]P, the linear predictor is a straight line with respect to the concentration (Figure 5.5, panel F). Considering again that MD is directly proportional to the amount of light in the *focus* grey-level image, at low B[a]P concentrations *foci* having small MD values are found (Figure 5.5E), in contrast to the higher MD values observed in *foci* at the highest concentration.

Even if the two models differ in the shape of the curve representing the expected values in relation to the concentrations, they partially share a similar feature, which is that the expected value of MD is high at very high concentrations of carcinogens. We conjecture that the trend at very high concentrations, shared by both carcinogens,

could be due to a combination of three factors. Firstly, these very high concentrations might have cytotoxic effects, dampening the multilayer growth of the transformed *foci* in these Petri dishes. This conclusion is supported by the fact that these Petri dishes had fewer *foci*, when compared to lower doses (Tables 5.1 and 5.2, Figure 5.2). Secondly, in *foci* induced by the highest concentrations used, a remarkable heterogeneity, a hallmark of both intermediate and mixed *foci*, was found as shown in Figure 5G. The MD descriptor applied to such a variable region, could have underestimated the overall multilayer growth of *foci* found in Petri dishes treated with high doses. From the statistical point of view, the presence of cytotoxic effects of carcinogens possibly responsible for the decreased number of *foci* observed at high concentrations, could in turn have caused a reduced precision (and statistical power) of parameter estimates.

The expected value of MD with respect to the concentration differs in the two models, in particular in the low range of concentration, which could be due to specific differences of the carcinogens mode of action. Nonetheless, the concentration range of B[a]P was experimentally designed to be equally spaced on the logarithmic scale, hence a quite large part of the inner range has no observations on the original scale by design. Thus, there is a certain degree of uncertainty related to the estimate at intermediate range of concentrations, therefore the apparent linear shape could not be confirmed in specifically designed experiments with more distinct concentrations. Still, the concentration exerts a statistically significant effect on the MD descriptor.

In Figures A4 and A5 Appendices 4 and 5, further elaborations based on the fitted models (Model N2 and Model B2) show the dependence relationship of MD from BD, in particular a monotonic relationship was found in both cases. From these models, we expect that highly multilayered *foci* will be less invasive than less multilayered *foci*.

5.3.1.3 The BD is dependent on carcinogen concentration

Models built to test the dependence of Boundary Index (BD) on carcinogen concentration are indicated as Model N3 and Model B3, respectively for $NiCl_2$ and B[a]P datasets. The effect of concentration on BD was statistically significant in both models, and the expected value of BD is linear in the concentration (see Figures 5.6B and 5.6E): high values of BD result from high concentrations. In particular, for model N3, the likelihood ratio test for the hypothesis of no effect of concentration was rejected with a p-value lower than 0.001 (p-value 0.0004), while for model B3, the p-value of the test was lower than 0.0001. It is noteworthy to remember that the BD index is related to the degree of departure of the *focus* shape from that of a perfect circle with an equivalent area. Finger-like protuberances can be seen at the edge of the *focus*, as a result of the criss-cross growth at its edges (Sasaki et al., 2012a). The BD descriptor captures a trait of invasive growth that is characterized by heterogeneous growth at a *focus* boundary (Urani et al., 2013), therefore at higher concentrations of carcinogen more pronounced finger-like protuberances of *foci* are expected.

After treatment with the lower concentrations of both carcinogens (250-300 μM of $NiCl_2$ and from 0.0005 to 3.125 μg/ml of B[a]P), as described in section 5.3.1.2, fairly multilayered *foci* can be frequently observed: this phenotype is often associated with a circle-like growth (see as examples Figures 5.6A and 5.6D).
At higher concentrations, 350-400 μM $NiCl_2$ and 15 μg/ml of B[a]P, *foci* showing a more fragmented morphology can be found, such as those presented in Figures 5.6C and 5.6F. Within the same *foci*, distinct regions of aggregation can be observed, characterized by tightly packed spindle-shaped cells.

We remark, once more, that despite the different nature of the two carcinogens, qualitatively similar models for BD as a function of concentration were obtained.

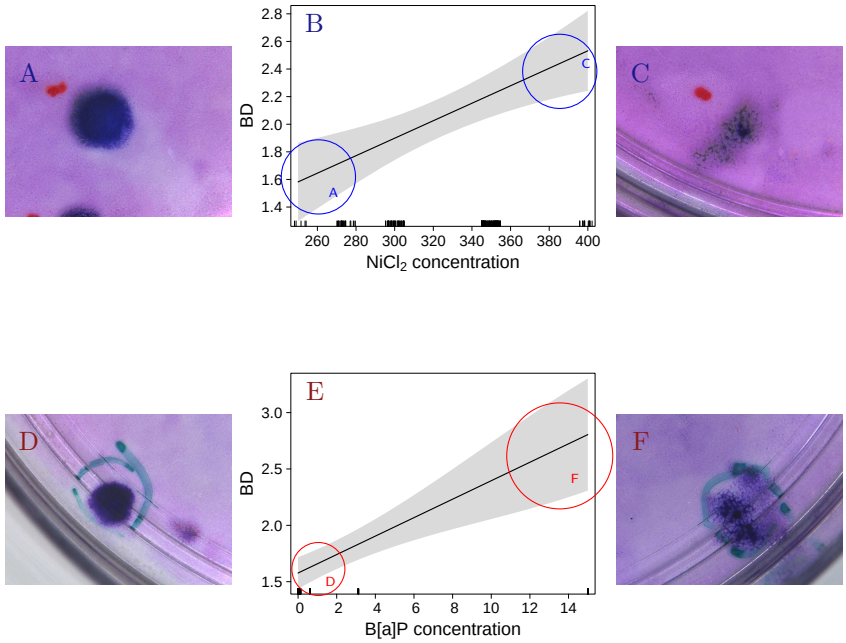

Figure 5.6: Plot of expected value functions of Boundary Index (BD) given the carcinogen concentration. In B and E, expected values of BD in model N3 ($NiCl_2$) and B3 (B[a]P), respectively are plotted given the concentration. The grey shaded area represents pointwise confidence limits, on the scale of the linear predictor. Examples of *foci* showing BD values corresponding to the area inside the blue circles are displayed in panels A and C, while D and F show *foci* having BD values corresponding to the area inside the red circles. The boxes on the x axis represent conditioning values of carcinogen concentration.

5.4 Discussion

In previous studies (Urani et al., 2013 and Chapter 3) three statistical descriptors of *foci* morphology were developed with the aim of mimicking those features that are assessed in visual scoring in CTAs for chemical carcinogenicity testing. In this work, we selected $NiCl_2$ and B[a]P *foci* images from previously performed CTAs, and we developed statistical models to test the effect of concentration on morphology. The joint distribution of all three statistical descriptors (ED, MD and BD) was factored into the product of three conditional distributions, after recognizing the statistical dependences existing among descriptors. Furthermore, we also considered that *foci* in the same Petri dish could be much more similar than *foci* located in different Petri dishes, due to the shared micro-environment.

This study suggests that the statistically significant effects of carcinogen concentration on some features of *foci* morphology, as represented by two of the three selected descriptors, are also coupled to visual relevance. *Foci* images obtained by testing two carcinogens with different mode of action were analyzed with the same method, and similar results in the structure of the dependencies with the concentration were obtained. Indeed, by inspecting the morphology of the *foci* obtained for each carcinogen at different concentrations, an appreciable degree of visual dissimilarity has been observed. At lower concentrations of both carcinogens (250-300 μM $NiCl_2$ and 0.0005-3.125 μg/ml B[a]P) analyzed *foci* seem to grow on average in multilayers and in a circle-like shape. While at higher concentrations (300-400 μM $NiCl_2$ and 15 μg/ml B[a]P) the *foci* show a fragmented morphology characterized by less uniform multilayer growth. It must be pointed out that the ranges of $NiCl_2$ and B[a]P were preliminarily selected by dose-range finding tests, as dictated by the CTA standard protocol, and qualitative similar shapes of boxplots for the number of *foci* in the concentration ranges were observed. By contrast, no

clear differences can be seen in *foci* dimension in relation to the concentrations when the comparison is performed among *foci* with the same values of BD and of MD. In fact, as demonstrated by our statistical analyses, the concentration does not exert a direct effect on ED when MD and BD are already taken into account. In other terms, the expected value of ED does not change with concentration if *foci* of similar MD and BD are compared. It must be remarked that the carcinogen concentration has a significant effect on some aspects of *foci* morphology even if the concentration is included into the model as a qualitative factor, that is without imposing a specific shape on the concentration-to-descriptor relationship. This is true for both the carcinogens considered. Note also that the variance of ED depends on the concentration, thus the variability changes with concentration. In the models developed here, the dependence among descriptors and of a descriptor on concentration is not always linear. This may reflect the inherent biological complexity of the carcinogenic process. In particular, such non-linearity was evidenced in the $NiCl_2$ model. Nickel compounds and B[a]P are classified as Group I carcinogens (IARC, 2012a,b) affecting human health through occupational and environmental exposure. While B[a]P is known to act through a genotoxic mechanism that involves biotransformation to highly reactive metabolites that form covalent adducts to DNA and other genotoxic effects, carcinogenicity induced by nickel compounds is characterized by the induction of oxidative stress through generation of reactive oxygen species and by the interference with DNA repair pathways, thus leading to genetic instability. Furthermore, nickel interferes with DNA methylation and histones acetylation, and activates hypoxic signaling. These mechanisms taken together cause deregulation of cell proliferation (Cameron et al., 2011; Magaye et al., 2012; Sun et al., 2013). As suggested by Haber et al. (2000), the indirect interaction with DNA in soluble nickel-induced *in vitro* transformation could imply a non-linear dose-response relationship. However, the authors also remarked that the overall available data are insufficient to determine the doses at which such non-linearity

occurs. Nonetheless, they also underline that the suggestion of such non-linearity is consistent with the negative animal carcinogenicity studies for soluble nickel, despite this negative results could also be due to a different bioavailability and clearance of nickel ions after exposure to soluble nickel compounds, as recently published (Goodman et al., 2011). As far as we are aware, no major developments have occurred in this direction. In our dataset the effect of $NiCl_2$ on one image descriptor (MD) was here estimated to be non-linear as a function of concentration. Widening the study of statistical descriptors to a broader concentration range might support the non-linearity hypothesized by Haber et al. (2000), and in such expanded range they could be studied in a quantitative way, thus possibly defining the concentration range at which non-linearity occurs.

In vitro cell transformation is considered to be a result of stepwise genotypic alterations, which underlie the corresponding phenotypical ones (Smets, 1980; Keshava, 2000). Increasing concentrations of carcinogens may lead to an accumulation of genetic changes (or different steps of the global process of transformation), resulting in a variety of phenotypes which reflect different molecular alterations. Quantitative morphological descriptors discriminate between the variety of morphologies that can be visually appreciated but not precisely determined, leading to a detailed evaluation of transformed *foci*. This may be especially useful to reduce the uncertainty in the classification of mixed or intermediate *foci*.

Our analysis showed for the first time the dependence of Type III *foci* morphology on concentration, thus it enabled the possibility of further distinctions inside the usual classification scheme, as previously suggested by other authors (Lu et al., 1986; Keshava, 2000). Further applicative relevance of our approach includes the possibility to predict the values of the three descriptors summarizing the morphological features of *foci* in the CTA for other concentrations comprised in the tested range but not actually experimentally assessed.

Additional improvements of the proposed method can be envisaged. The fraction of all *foci* images lost in the segmentation step could be

reduced in part by specific experimental precautions, for instance by limiting the use of pen marks outside the area of *foci*. In addition, improvements of the proposed descriptors might extract further quantitative information which is possibly relevant for the assessment of transformed *foci*. For example, the proposed Boundary Index (BD) captures just one of the aspects of invasive growth, in particular the degree of departure of the *focus* shape from that of an exact circle. Low values for the BD index seem to be related to *foci* composed of separated regions of cellular aggregates, rather than a unique *focus* body. A descriptor taking into account the heterogeneity within the same *focus* could improve both the assessment of invasiveness and the characterization of *foci* with mixed or intermediate morphology. Finally, large screening tests are needed for a detailed characterization of the effect of concentration on *foci* morphology, given that we provided positive evidence for just one compound for each major class of carcinogens (genotoxic and non-genotoxic).

The method presented in this study and applied to the BALB/c 3T3 CTA, could be potentially useful also in the CTA with Bhas 42 cells, for which an OECD Guidance Document has recently been published to support its use in regulatory applications (Sakai et al., 2011; OECD, 2016). The Bhas 42 cell line is in fact derived from BALB/c 3T3 cells transfected with the *v-Ha-ras* proto-oncogene, consequently its transformed *foci* are characterized by same morphological features which are similar to those of BALB/c 3T3 *foci*.

In conclusion, our quantitative evaluations mainly show that the concentration of the considered carcinogens exerts an effect on *foci* morphology. We believe that statistical descriptors of *foci* morphology have the potential of mimicking trained human scorers very well, but with the advantage of being both objective and quantitative. In this way, additional information can be extracted from CTAs to be exploited in the application of more reliable *in vitro* procedures when assessing carcinogenicity through an integrated testing strategy, either in a full probabilistic (Stefanini, 2013) or a Weight of Evidence approach (ECHA, 2010).

5.5 Bibliography

Bohnenberger, S., S. W. Bruce, T. Kunkelmann, K. Pant, et al. (2012). "Photo catalogue for the classification of cell colonies in the Syrian hamster embryo (SHE) cell transformation assay at pH 6.7". In: *Mutation Research* 744.1, pp. 82–96.

Buntine, W. L. (1994). "Operations for learning with graphical models". In: *Journal of Artificial Intelligence Research: JAIR* 2, pp. 159–225.

Callegaro, G., F. M. Stefanini, A. Colacci, M. Vaccari, and C. Urani (2015). "An improved classification of foci for carcinogenicity testing by statistical descriptors". In: *Toxicology in Vitro* 29.7, pp. 1839–1850.

Cameron, K., V. Buchner, and P. Tchounwou (2011). "Exploring the Molecular Mechanisms of Nickel-Induced Genotoxicity and Carcinogenicity: A Literature Review". In: *Reviews on Environmental Health* 26.2, pp. 81–92.

Corvi, R., M. J. Aardema, L. Gribaldo, M. Hayashi, et al. (2012). "ECVAM prevalidation study on in vitro cell transformation assays: General outline and conclusions of the study". In: *Mutation Research/Genetic Toxicology and Environmental Mutagenesis* 744.1, pp. 12–19.

Cox, D. R. and D. V. Hinkley (1979). *Theoretical Statistics*. Boca Raton: Chapman and Hall/CRC.

ECHA (2010). *Practical guide 2: How to report weight of evidence.*

EURL ECVAM (2012). *EURL-ECVAM -Recommendation on three Cell Transformation Assays.*

Fox, J. (2003). "Effect Displays in R for Generalised Linear Models". In: *Journal of Statistical Software* 8.15, pp. 1–27.

Goodman, J. E., R. L. Prueitt, S. Thakali, and A. R. Oller (2011). "The nickel ion bioavailability model of the carcinogenic potential of nickel-containing substances in the lung". In: *Critical Reviews in Toxicology* 41.2, pp. 142–174.

Haber, L. T., L. Erdreicht, G. L. Diamond, A. M. Maier, et al. (2000). "Hazard Identification and Dose Response of Inhaled Nickel-Soluble Salts". In: *Regulatory Toxicology and Pharmacology* 31.2, pp. 210–230.

Hoffmann, S., L. A. Hothorn, L. Edler, A. Kleensang, et al. (2012). "Two new approaches to improve the analysis of BALB/c 3T3 cell transformation assay data". In: *Mutation Research/Genetic Toxicology and Environmental Mutagenesis* 744.1, pp. 36–41.

IARC (2012a). *IARC Monograph: arsenic, metals, fibres, and dusts (volume 100 C). A review of human Carcinogens. Lyone, France.*

– (2012b). *IARC Monograph: chemical agents and related occupations (volume 100 F). A review of human Carcinogens. Lyone, France.*

Keshava, N. (2000). "Tumorigenicity of morphologically distinct transformed foci induced by 3-methylcholanthrene in BALB/c-3T3 cells". In: *Mutation Research/Fundamental and Molecular Mechanisms of Mutagenesis* 447.2, pp. 281–286.

Lu, Y.-P., C. Lasne, and I. Chouroulinkov (1986). "Use of an orthogonal design method to study two-stage chemical carcinogenesis in BALB/3T3 cells". In: *Carcinogenesis* 7.6, pp. 893–898.

Magaye, R., J. Zhao, L. Bowman, and M. Ding (2012). "Genotoxicity and carcinogenicity of cobalt-, nickel- and copper-based nanoparticles". In: *Experimental and Therapeutic Medicine* 4.4, pp. 551–561.

Maire, M.-A., C. Rast, and P. Vasseur (2012). "Photo catalogue for the classification of cell colonies in the Syrian hamster embryo (SHE) cell transformation assay at pH 7.0". In: *Mutation Research/Genetic Toxicology and Environmental Mutagenesis*. International Prevalidation Study on Cell Transformation Assays 744.1, pp. 97–110.

OECD (2016). *Guidance Document on the in vitro Bhas 42 Cell Transformation Assay - Series on Testing & Assessment No. 231*.

Pinheiro, J. C. and D. M. Bates (2000). *Mixed-effects models in S and S-PLUS*. Springer Science & Business Media.

Pinheiro, J. C., D. M. Bates, S. DebRoy, D. Sarkar, and R Core Team (2015). *nlme: Linear and Nonlinear Mixed Effects Models*. Version R package version 3.1-120.

Procaccianti, C., F. M. Stefanini, and C. Urani (2011). "The cell transformation assay: toward a statistical classification of mixed and intermediate foci images". In: *Alternatives to laboratory animals: ATLA* 39.1, pp. 23–36.

Python Software Foundation (2016). *Python Language Reference, version 2.7*. Python.org. URL: https://www.python.org/.

R Core Team (2012). *R: A Language and Environment for Statistical Computing*. URL: http://www.R-project.org/.

Ridder, G. M., S. B. Stuard, G. A. Kerckaert, D. B. Cody, et al. (1997). "Computerized image analysis of morphologically transformed and nontransformed Syrian hamster embryo (SHE) cell colonies: application to objective SHE cell transformation assay scoring". In: *Carcinogenesis* 18.10, pp. 1965–1972.

Sakai, A., K. Sasaki, K. Hayashi, D. Muramatsu, et al. (2011). "An international validation study of a Bhas 42 cell transformation assay for the prediction of chemical carcinogenicity". In: *Mutation Research/Genetic Toxicology and Environmental Mutagenesis* 725.1, pp. 57–77.

Sasaki, K., S. Bohnenberger, K. Hayashi, T. Kunkelmann, et al. (2012a). "Photo catalogue for the classification of foci in the BALB/c 3T3 cell transformation assay". In: *Mutation Research* 744.1, pp. 42–53.

Sasaki, K., S. Bohnenberger, K. Hayashi, T. Kunkelmann, et al. (2012b). "Recommended protocol for the BALB/c 3T3 cell transformation assay". In: *Mutation Research/Genetic Toxicology and Environmental Mutagenesis* 744.1, pp. 30–35.

Sasaki, K., M. Umeda, A. Sakai, S. Yamazaki, and N. Tanaka (2015). "Transformation assay in Bhas 42 cells: a model using initiated cells to study mechanisms of carcinogenesis and predict carcinogenic potential of chemicals". In: *Journal of Environmental Science and Health. Part C, Environmental Carcinogenesis & Ecotoxicology Reviews* 33.1, pp. 1–35.

Smets, L. A. (1980). "Cell transformation as a model for tumor induction and neoplastic growth". In: *Biochimica et Biophysica Acta (BBA) - Reviews on Cancer* 605.1, pp. 93–111.

Stefanini, F. M. (2013). "Comment: Bayesian Network Integrated Testing Strategy and beyond". In: *ALTEX-Alternatives to Animal Experimentation* 30, pp. 386, 390.

Sun, H., M. Shamy, and M. Costa (2013). "Nickel and Epigenetic Gene Silencing". In: *Genes* 4.4, pp. 583–595.

Tanaka, N., S. Bohnenberger, T. Kunkelmann, B. Munaro, et al. (2012). "Prevalidation study of the BALB/c 3T3 cell transformation assay for assessment of carcinogenic potential of chemicals". In: *Mutation Research/Genetic Toxicology and Environmental Mutagenesis* 744.1, pp. 20–29.

Urani, C., R. Corvi, G. Callegaro, and F. Stefanini (2013). "Objective scoring of transformed foci in BALB/c 3T3 cell transformation assay by statistical image descriptors". In: *Toxicology in Vitro* 27.6, pp. 1905–1912.

Urani, C., F. M. Stefanini, L. Bussinelli, P. Melchioretto, and G. F. Crosta (2009). "Image analysis and automatic classification of transformed foci". In: *Journal of microscopy* 234.3, pp. 269–279.

6

New descriptors for a comprehensive model of foci classification

In this Chapter an extended classifier is presented, by means of new descriptors, and trained on a dataset composed of different compounds and concentrations. Performances of previous classifier were outstanded, thus strengthening its application as a support for visual scoring.

Abstract

The identification of the carcinogenic risk of chemicals is currently mainly based on animal studies. The *in vitro* Cell Transformation Assays (CTAs) are a promising alternative to be considered in an integrated approach. Despite their favourable features, CTAs can be further improved, especially reducing the possible subjectivity arising from the last phase of the protocol, namely visual scoring of *foci* using coded morphological features. By taking advantage of digital image analysis, the aim of our work is to translate morphological features into statistical descriptors of *foci* images, and to use them to mimic the classification performances of the visual scorer to discriminate between transformed and non-transformed *foci*. Here we present a classifier based on five descriptors trained on a dataset of 1364 *foci*, obtained with different compounds and concentrations. Our classifier showed accuracy, sensitivity and specificity equal to 0.77 and an area under the curve (AUC) of 0.84. The presented classifier outperforms a previously published model.

This Chapter is adapted from the paper "A comprehensive statistical classifier of foci in the Cell Transformation Assay for carcinogenicity testing", Callegaro, G., Malkoc, K., Corvi, R., Urani, C., Stefanini, F.M., submitted in December 2016.

6.1 Introduction

Carcinogenicity evaluation of chemicals usually requires a battery of *in vitro* and *in vivo* genotoxicity tests that can be followed by the life-time cancer rodent bioassay (OECD, 2009a,b). Acknowledging the several limitations and concerns of the *in vivo* bioassays (Knight et al., 2006a,b; Paules et al., 2011), Cell Transformation Assays (CTAs) represent a promising *in vitro* alternative for carcinogenicity testing to be considered as a component of an Integrated Approach (Jaworska and Hoffmann, 2010; Benigni, 2014; Jacobs et al., 2016). An exhaustive description of CTAs is provided in section 1.2.1.

Further improvements of CTAs may promote their wider implementation for regulatory purposes. In particular, the mechanisms underlying *in vitro* morphological transformation necessitate in-depth analysis, and the possible subjectivity arising from the final phase of the protocol (the visual scoring of *foci* of transformed cells) needs to be completely dealt with (EURL ECVAM, 2012; Combes, 2012).

By taking advantage of digital image analysis, in recent years we have worked on the translation of morphological features used for visual scoring (Urani et al., 2013, and Chapter in 3) into statistical descriptors of *foci* images, with the final aim of mimicking the performances of a visual scorer with an unbiased and quantitative approach. We previously applied a set of statistical descriptors of *foci* morphologies to built a classifier for *foci* obtained with exposure to methylcholanthrene (Callegaro et al., 2015, and in Chapter 4). Another innovative aspect and application of our approach was the identification of a dependence between morphologies of transformed colonies (*foci*) and the carcinogen concentrations (Callegaro et al., 2016, and in Chapter 5).

Here we present a comprehensive automated and objective classifier, trained with *foci* images obtained testing different compounds. In addition to the previously developed descriptors (Urani et al., 2013,

Chapter 3), we translated two more morphological features of *foci* (spindle-shape of transformed cells and texture heterogeneity of *foci*) into statistical descriptors. Texture heterogeneity is a key feature that could help to the identification of mixed and intermediate *foci*, that still represents an open problem in visual classification (Landolph, 1985). We combined all of them into a classifier supporting visual scoring of malignant *foci* in the BALB/c 3T3 CTA in current applications.

6.2 Material and Methods

6.2.1 Cell Transformation Assays: from plates to images

The plates used for image analysis of transformed *foci* were obtained from CTAs performed by EURL ECVAM within the prevalidation study of BALB/c 3T3 CTA (Corvi et al., 2012; Sasaki et al., 2012a). At the end of the experimental phase, *foci* being more than about 2mm in diameter were evaluated by stereomicroscopy according to predefined morphological features, as detailed in the recommended protocol and photo catalogue (Sasaki et al., 2012b; Tanaka et al., 2012). According to the protocol, only Type III *foci* were considered as fully transformed, thus scored as positive. Type III *foci* are characterized by the following morphological features: *foci* cells are deeply basophilic stained, spindle-shaped and morphologically different from the background monolayer of non-transformed cells. Type III *foci* show dense multilayering (piling up), random orientation and invasive growth of cells at the edge of *foci* (criss-cross pattern). *Foci* images were acquired by adopting the procedure previously developed by Callegaro et al. (2015), detailed in Chapter 4, and briefly described below.

Acquisition was performed under a stereomicroscope (Zeiss, Stemi

SV6) equipped with 6.3× lens (Carl Zeiss, Arese, Italy) and a digital camera (AxioCam Mrc5, 36 bit). Images were saved in TIFF-48bit RGB format and had a size of 2572 × 1928 pixels, where 1 pixel is equivalent to a real size of 6.7842×10^{-3} mm (1 cm = 1474 pixels). Both fully transformed Type III *foci* and non-Type III *foci* (Type I and II) were considered for the acquisition, as well as *foci* obtained from various coded and uncoded compounds and concentrations, as detailed in Table 6.1. A segmentation algorithm coded in Python (Python Software Foundation) was applied to each *focus* image in order to isolate the *focus* region from the surrounding monolayer (Callegaro et al., 2015). The algorithm acquires a RGB *focus* image, converts it into the HSV colour space and separates the Region of Interest (ROI) corresponding to each *focus* from the surrounding monolayer by setting appropriate intensity thresholds.

At the end of the process of segmentation, the final dataset comprised a total of 2046 *foci* images, including both Type III and non-Type III *foci*, in the proportion detailed in Table 6.1.

Table 6.1: Dataset composition. Dataset composition is detailed for compound and number of Type III *foci* and non-Type III *foci*. For each compound, the number of concentrations tested is shown. Compounds tested were: dimethyl sulfoxide 0.5% (DMSO, # 67-68-5), 3-methylcholanthrene (MCA, # 56-49-5), from 0.01 to 10 µg/ml, 2-acetylaminofluorene (A, # 53-96-3), from 0.05 to 35 µg/ml, benzo[a]pyrene (B[a]P, # 50-32-8), from 0.0005 to 15 µg/ml, anthracene (HB, # 120-12-7), from 0.1 to 40 µg/ml, o-toluidine (TB, # 636-21-5), from 20 to 1750 µg/ml, and $NiCl_2$ (# 50–32-8), from 50 to 400 µM.

	Concentrations tested	Number of Type III *foci*	Number of non-Type III *foci*
Control	-	11	9
DMSO	-	16	11
MCA	7	487	330
A	8	150	61
B[a]P	9	224	174
HB	6	47	15
TB	8	84	23
$NiCl_2$	8	369	6
Total	-	1416	630

6.2.2 Quantifying morphological features: ED, MD, BD

From each *focus* ROI the set of previously developed descriptors was calculated (described in detail in Urani et al., 2013 and Chapter 3). These three descriptors are related to three of the morphological features used for visual scoring in BALB/c 3T3 CTA (Sasaki et al., 2012a). Specifically, the Equivalent Diameter (ED) is the diameter of the circle having the same area of the *focus*, then calculated as: $ED = 2\sqrt{\frac{area}{\pi}}$, where π is the trigonometric constant. ED measures *foci* dimensions, taking into account their shape polymorphism. The median of the gray-scale image pixels distribution (MD) was selected as a proxy of *focus* ability to grow into multilayers, as image gray levels (or saturation) depend on the amount of light passing through *focus* region. The more a *focus* is multilayered, the darker will be its grayscale image. Finally, the descriptor called Boundary Index (BD) was developed in order to capture a trait of *foci* invasiveness. Invasiveness often implies boundary heterogeneity of *foci*, thus BD compares the actual *focus* perimeter (FP) and the perimeter of the circle having the same *focus* area (EFP): $BD = (\frac{FP}{EFP}) - 1$.

6.2.3 The multicellular-Spindle Detector (SD)

BALB/c 3T3 cells originate from mesenchimal fibroblastic cells; at the early stage of culture they are spindle-shaped, while they exhibit an epithelial-like morphology (cobble-stones) when they are at the contact-inhibited confluent stage. In the CTA, malignantly transformed cells change morphology from epithelial-like (as the cells growing in the background monolayer) to rather spindle-shaped, probably because of rearranged structures and functions in the transformation process, which lead to *focus* formation. The "spindle-shape" is among the coded morphological features for *foci* visual scoring (Sasaki et al.,

2012b). However, at the recommended magnification (50×, Sasaki et al., 2012b), single cell shapes are not always observable. Nonetheless, spindle-shaped cells tend to pack into macro-segments that are clearly visible and detectable at the magnification suggested. See as examples the aggregate regions of pictures 41, 42 and 47 provided in the photo catalogue for the classification of *foci* (Sasaki et al., 2012b).

We therefore applied a Line Segment Detector, LSD (Grompone von Gioi et al., 2012) to each gray-scale *focus* image (step 2a, Figure 6.1). LSD is a linear-time Line Segment Detector aiming at detecting locally straight contours, or line segments, on images. The algorithm, described in details by Grompone von Gioi and co-authors (2012), starts with the computation of a level-line field for the *focus* image; it then segments the field into connected regions called line-supporting regions, each one representing a candidate for a line segment. Candidates are finally subjected to a validation step based on a contrario approach (step 3a, Figure 6.1). ROI perimeter of *focus* image was discarded as naturally segment-rich, since sharply separated by the background monolayer of untransformed cells (step 4a, Figure 6.1).

The number of segments were then automatically counted for each *focus* image (step 5a, Figure 6.1), and normalized with respect to the *focus* size, in particular considering the Equivalent Diameter (ED) defined in the previous section. We finally stretched the range of values in the lower range intervals by a log-transformation: $SD = ln(\frac{\#(segments)}{ED}) + 1$ (step 6a, Figure 6.1). See the workflow in Figure 6.1 for a detailed pipeline of the calculus of SD descriptor.

6.2.4 The Heterogeneity Detector (HD)

Foci's texture heterogeneity can lead to ambiguity in *foci* scoring, as it can be a confounding factor when classifying the fully transformed morphology. *Foci* can display intermediate and mixed degrees of

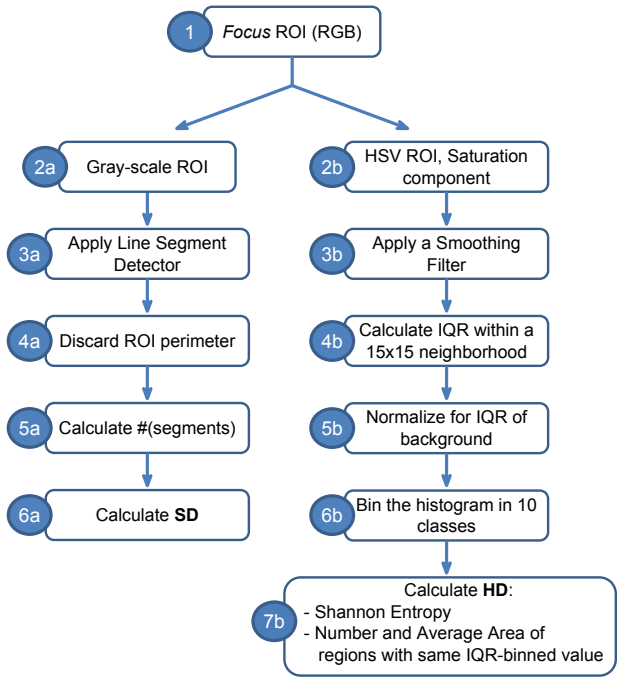

Figure 6.1: Pipeline of Multicellular-Spindle Detector (SD) and Heterogeneity Detector (HD). Steps of the calculus of descriptors SD and HD are shown. Starting from RGB images of *foci* (step 1), SD is calculated on the gray-scale image (step 2a): through the application of a Line Segment Detector (LSD, step 3a), the number of segments in the inner *focus* area is calculated (steps 4a-5a) and SD obtained (step 6a). HD is obtained from the smoothed Saturation component of HSV *foci* images (steps 2b-3b), where the Inter Quartile Range is calculated on a mobile window of 15-15 pixels neighborhood (step 4b). On the binned distribution of background-normalized IQR (steps 5b-6b), HD indexes are calculated (step 7b). For details see paragraphs 6.2.3 and 6.2.4.

coded morphological criteria, as a result of their texture heterogeneity.

In order to capture texture heterogeneity of *foci* we developed a specific image descriptor based on the algorithm described in the "b" series of boxes of Figure 6.1, step by step. We first transformed RGB images of *foci* into the HSV colour space, then we selected Saturation component for further analysis (step 2b, Figure 6.1); a smoothing filter (a Bilateral Filter; Gonzalez and Woods, 2009) was applied in order to smooth out the variability arising from micro fluctuations in the experimental conditions (step 3b, Figure 6.1).

With the image Saturation component, we then calculated the Inter-Quartile Range (IQR) referred to each pixel in the ROI. Given an image pixel s, the IQR of s is calculated over a 15×15 neighbourhood of pixels around pixel s as the difference between the third quartile and the first quartile of the resulting distribution (step 4b, Figure 6.1). The neighbourhood size was selected after appreciating the scale at which visual scoring is performed, which is indeed related to the human eye resolution. The output of the algorithm consisted in pseudo-images that were normalized through the average median of the IQR values calculated within selections of pixels taken from the monolayer of untransformed cells, so that differences due to the background texture (without artifacts) are taken into account (step 5b, Figure 6.1). The distribution of IQR values was binned into 10 intervals of equal size. Finally, Heterogeneity Detector (HD), defined as a collection of indexes shown in box (7b), was calculated. Firstly, the Shannon Entropy, defined as $-\sum_i p_i \ln(p_i)$, with p_i the absolute frequencies of *focus* IQR distributions, using a dedicated function in SciPy library (Jones et al., 2001). Then, further indexes were computed on pixels falling into the same bin of the partitioned IQR. Over each of the 10 slices, enclosed areas were identified, counted and their average area was calculated. For a graphical representation of these indexes, see the Figure 6.3.

6.2.5 Statistical analysis

In the BALB/c 3T3 CTA only Type III *foci* are considered fully transformed (Sasaki et al., 2012a). Thus, we performed the classification of *foci* in two classes, Type III (Y=1) and non-Type III (Y=0) *foci* using classification trees. These are models developed to partition the statistical units in groups according to the value taken by a collection of variables $(X_1, X_2, ..., X_k)$, here represented by statistical image descriptors. The sample space $\Omega(X_1, X_2, ..., X_k)$ is therefore decomposed into the union of non-overlapping regions $(R_1, R_2, ..., R_w)$, each one defined by the intersection of one interval for every variable, thus

$$\Omega(X_1, X_2, ..., X_k) = \bigcup_{1}^{w} R_i = \bigcup_{1}^{w} [I_{1,i} \cap ... \cap I_{j,i} \cap ... I_{k,i} \cap] \qquad (6.1)$$

where $I_{j,i}$ is an interval of values for variable X_j that may have finite or infinite as well as including or excluding endpoints. The partition into regions is typically represented by a tree, where each branch is associated to an endpoint of the above described intervals. The probability of observing a Type III *focus* given that its statistical image descriptors take value in R_i is typically estimated by the relative frequency of Type III *foci* in that class. Several algorithms exist to estimate the best tree's structure and they typically optimize an objective function like Gini index, miss-classification error or cross-entropy (details in Hastie et al., 2009). The classification performances are often improved by extending the model through several classification trees (ensemble models). A BART model (Chipman and McCulloch, 2016) is a Bayesian model where the classification is performed by adding predictions performed by several trees:

$$h(x_1, x_2, ..., x_k) = \sum_{j=1}^{m} g_j(x_1, x_2, ..., x_k) \qquad (6.2)$$

$$P[Y = 1 \mid x_1, x_2, ..., x_k] = F_\Phi(h(x_1, x_2, ..., x_k)) \tag{6.3}$$

where each $g_j(x_1, x_2, ..., x_k)$ denotes a regression tree and $F_\Phi(z)$ indicates the standard normal cumulative distribution function (also known as probit link). Each tree is constrained by a prior distribution in order to contribute in a small amount to the overall classification (details in Chipman and McCulloch, 2016).

Classification performances were summarized by accuracy, sensitivity and specificity indexes, related to the false positive and the true positive rates, finally used to evaluate model-based classification performances using Receiver Operating Characteristics (ROC) curves. The Area Under the ROC curve (AUC) was also calculated, as a single scalar value to evaluate the ability of the classifier to differentiate between the distributions of the Type III and non-Type III *foci* classes (Hand and Till, 2001).

All the analysis were performed in R (R Core Team, 2012), using the packages BayesTree (Chipman and McCulloch, 2016), mgcv (general additive models, Wood, 2006), ROCR (Sing et al., 2005).

6.3 Results

Two new image descriptors, one univariate (SD) and the other one multivariate (HD), were formulated with the aim of extending the ongoing conversion of morphological features assessed during visual scoring into quantitative statistical summaries. Then, a new automated classifier was built, and its performances to discriminate between Type III and non-Type III *foci* were assessed.

6.3.1 Descriptors of *foci* spindle-shape and heterogeneity

We developed a descriptor called SD to measure the spindle-shape morphology at the *focus* level, which is among the features used

to visually classify transformed *foci*. One good reason to evaluate this feature at the *focus* level, rests on the difficulty of recognizing the shape of single cells at the recommended magnification (50×). Nevertheless, spindle-shaped cells tend to pack into macro-structures, namely segments, which are visible at the suggested magnification. SD descriptor precisely captures line segments detectable in the *focus* area, as described in detail in paragraph 6.2.3 and Figure 6.1.

In Figure 6.2 (first row), some examples of SD performances in describing spindle-shape feature are shown. Note that Figure 6.2B represents the same *focus* shown in Figure 6.2A, but cropped at the region corresponding to the *focus*. The same applies to Figure 6.2D and 6.2C. The different magnified image regions of the same *focus* provide information on *foci* size.
Low SD values correspond to *foci* in which few segments related to packed spindle-shaped cells are visible (*focus* in Figure 6.2A,B). While high SD values correspond to *foci* displaying several aggregated regions of cells, finally organized into detectable segments, as in the case of *focus* shown in Figure 6.2C,D. Note that low values of SD descriptor can correspond to *foci* composed of round-shaped cells, eventually low multilayered: in this case few segments could be detectable since round-shaped cells would not tend to pack into marco-segments. In addition, as it can be seen in Figure 6.2A,B, also deeply multilayered *foci* can show low values of SD, as segments can be visible only in the perimeter region. Indeed, a visual scorer would come to the same conclusion, considering information about the spindle-shape feature just from the perimeter region.

Part of the difficulties related to *foci* scoring rely on the fact that transformed morphologies do not group clearly into distinct categories, but are generated from a continuous distribution, so that frequently doubtful cases occur. *Foci* intermediate between Type III and non-Type III morphologies, as well as *foci* composed of heterogeneous regions assignable each one to different categories can affect the scoring of *foci* (Landolph, 1985; Procaccianti et al., 2011; Urani et al., 2013). Hence, in order to reduce the ambiguity in *foci* scoring,

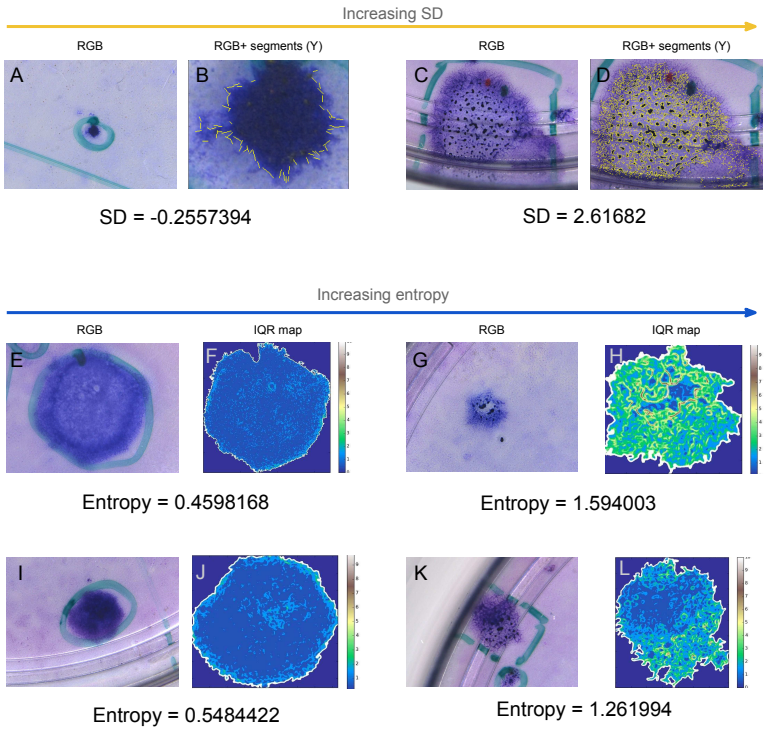

Figure 6.2: Multicellular-Spindle Detector and entropy index (Heterogeneity Detector): examples. *Foci* images having increasing values of SD descriptor and entropy index are shown. The first row presents two examples of *foci*, for each one RGB full image and the same *focus*, but cut at the region corresponding to the *focus* and overlayed segments found by the LSD algorithm (in yellow). In A and B a *focus* having a low value of SD descriptor is shown, while in C and D a *focus* having high value of SD descriptor is provided. The second and the third rows, present 4 examples of *foci*, E, F and I, J showing low values of entropy index, G, H and K, L showing high values of entropy index. For each *focus*, RGB full image is shown, followed on its side by the IQR map of the same *focus*, but cropped at the region corresponding to the *focus*.

we centred our attention on the degree of texture heterogeneity that can be found inside each *focus* area. Texture was measured by evaluating the IQR for each pixel of the *focus* region within a 15×15 neighbourhood, and summarizing the resulting gray-level texture image with a collection of indexes (see paragraph 6.2.4 for details). Examples of the first index, the entropy of the IQR map images, are provided in Figure 6.2, second and third rows. Again, Figure 6.2F represents the same *focus* shown in Figure 6.2E, but cropped at the region corresponding to the *focus*. The same applies to Figure 6.2H and 6.2G, 6.2J and 6.2I, 6.2L and 6.2K.
Low values of the entropy index correspond to overall homogeneous texture of *foci*, as the two presented on the left (Figure 6.2E,F and I,J). Note that entropy index do not discriminate between highly multilayered (Figure 6.2I,J) or poorly multilayered *foci* (Figure 6.2E,F), feature that is already taken into account by the previously developed MD descriptor (Urani et al., 2013). When entropy index acquires high values, *foci* showing different levels of heterogeneity can be detected: the *focus* in Figure 6.2G,H, shows regions of complex spatial organization, but overall constant over the whole *focus* area. While the *focus* in Figure 6.2K,L, again characterized by a high value of entropy index, exhibits two distinct regions of organization, one where the multilayer feature is more expressed, the other one characterized by a more complex organization, similar to the *focus* in Figure 6.2G,H.

Finally, other two indexes were collected from the IQR map images of each *focus*, described in Figure 6.3. The IQR map obtained from the RGB *foci* images, was divided into 10 intervals (from blue to brown in Figure 6.3, IQR map). As a consequence, the IQR map can be divided in slices, each one considering just pixels taking value in the selected interval. So, for example, the first interval included just pixels represented in dark blue inside the *focus* area in the IQR map (Figure 6.3). Hence, the first slice, will consider just those blue pixels, as depicted in the corresponding image in Figure 6.3.

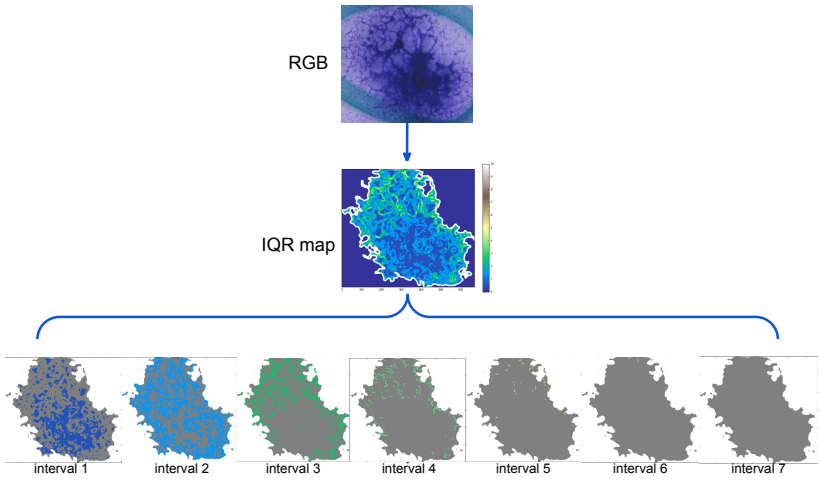

Number of regions having the same IQR value						
277	202	395	276	111	19	4
Average area of regions having the same IQR value						
265	495	89	35	15	14	9

Figure 6.3: Number and average area of regions (HD descriptor). Starting from RGB *foci* images, a IQR map is obtained for every *focus*: steps are detailed in paragraph 6.2.4. The IQR map was divided into 10 intervals (from blue to brown in IQR map bar). As a consequence, the IQR map can be divided into slices, each one considering just pixels taking values in the selected interval. Here are just presented 7 slices because the higher IQR levels were not populated. For every slice of the IQR map, enclosed regions are identified: then they are counted ("Number of regions having the same IQR value") and their average area is calculated ("Average area of regions having the same IQR value"). For the example *focus* provided in the figure, these indexes of HD descriptor are listed in a table.

Over each of the 10 slices, enclosed areas were identified: they were automatically counted ("Number of regions having the same IQR value" in Figure 6.3) and their average area was calculated ("Average area of regions having the same IQR value", Figure 6.3). In Figure 6.3, just slices from 1 to 7 are displayed, since the higher intervals were not populated. As it can be seen from the table in Figure 6.3, both the number and the average area of regions can provide additional information, since they are not following the exact same trend (see the values for interval 2, as an example).

6.3.1.1 A classifier of *foci* based on statistical descriptors

The aim of the visual scoring is to classify each *focus* arising from Petri dishes treated with a suspected carcinogen as being a Type III *focus*, thus fully transformed and scored as positive, or non-Type III *focus*, scored as negative.

To obtain a quantitative and objective classification, we built a Bayesian Tree Classification model, where our statistical image descriptors were used to reach the final classification of the collected *foci* into the two defined classes. All the variables (in our case, the descriptors), were used by the simulated trees with the same frequencies: apparently no single image descriptor stood out as regards the classification power while discriminating between Type III and non-Type III *foci*. See paragraph 6.2.5 for additional details. Note that we built the model using a training set composed of a randomly drawn set of 1364 *foci*, where $\frac{2}{3}$of images were scored as positive and $\frac{1}{3}$ as negative. We subsequently evaluated the performance on a test set of 682 additional samples, with the same ratio of positive/negative *foci* of the training set. The results presented are therefore from a cross-validated model, trained and tested on sets of *foci* obtained with different chemicals and different concentrations (Table 6.1). After model fitting, the probability of being a Type III *focus* was estimated for all *foci* in the testing dataset. Nevertheless,

to assign the *focus* to a class, a threshold t has to be defined, for example if $t = 0.65$ then all *foci* with estimated probability equal or greater than 0.65 will be assigned to the Type III class.
The performances on the test set of the proposed model, called *BT1* (Bayesian Tree 1) are presented in Table 6.2 and Figure 6.4. Depending on the threshold t selected, the ability of the classifier to discriminate between the two classes varies (Figure 6.4).

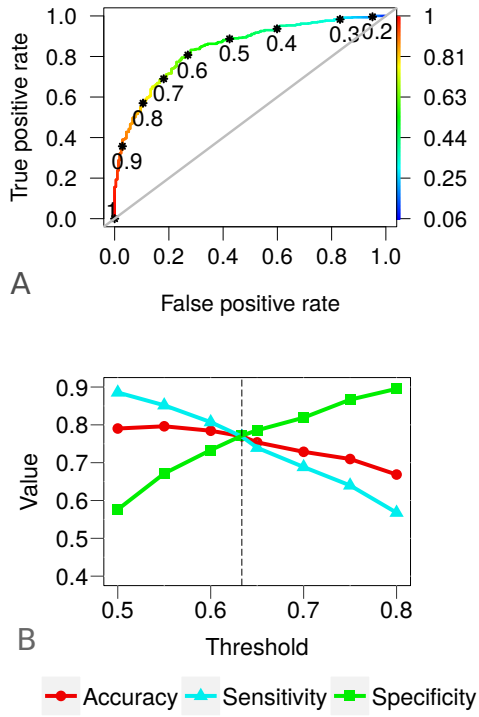

Figure 6.4: ROC curve and performance indexes. In A, the ROC curve of BT1 model is shown, where True positive rate is plotted versus False positive rate, depending on the threshold selected (in rainbow colours). The diagonal line denotes the performance of a random classifier, to be used as a reference. In B, accuracy, sensitivity and specificity are plotted depending on the threshold selected (x-axis). The vertical dashed line refers to the threshold maximizing all three values (0.6335).

The ROC curve (Figure 6.4A) shows the relationship between True positive rate and False positive rate, depending on the threshold selected (rainbow colours). The Area under the curve (AUC), a summary of the inherent ability of the classifier to discriminate between positive and negative instances, was found to be equal to 0.84. An AUC equal to 1 denotes a perfect classifier, while an AUC equal to 0.5 indicates a random classifier.

Indeed in Figure 6.4B, that shows the variation of accuracy, sensitivity and specificity depending on the threshold selected, it is more clearly visible that the standard threshold (0.5) slightly penalizes the recognition of negative instances, as shown by the low value of specificity. It should be remembered that specificity measures the proportion of negatives that are correctly identified as such, while sensitivity measures the proportion of positives that are correctly identified as such. The threshold that maximizes all the three performances indexes to the value of 0.77 was found to be equal to 0.6335 (the dashed vertical line in Figure 6.4B), and led to the confusion matrix in Table 6.2, that compares the performances of the visual and of the automatic classifiers. To further prove the general validity of our classification model, we expanded our analysis with other models, here briefly presented. This analysis has the double aim to make a comparison with the classification model presented in Chapter 4, based on three descriptors on a methylcholanthrene-dataset (Callegaro et al., 2015), and to stress the importance of the newly defined descriptors. In Table 6.3, the performances of different models are presented. In the first row, models built using Bayesian Tree

Table 6.2: Confusion Matrix of best threshold. Using the selected threshold 0.6335, accuracy, sensitivity and specificity were found to be equal to 0.77.

		Observed	
		Type III	non-Type III
Predicted	Type III	363	48
	non-Type III	109	162

methods are listed. *BT1*, the model already presented, was built considering all the descriptors (ED, MD, BD, SD and HD indexes); while *BT2* was built using just the three previously developed and presented (Urani et al., 2013, Chapter 3) descriptors (ED, MD and BD). As it can be seen, the use of the three previous descriptors only, reduces the performances (AUC is equal to 0.74), thus stressing the importance of the additional information conveyed by the newly presented descriptors (SD and HD indexes). The optimal threshold (0.64), maximizing the performances indexes, was found to be very similar to the one of *BT1*.

Table 6.3: Comparison between different models. The first row shows the performances indexes of Bayesian Tree models (*BT1* and *BT2*): the left cell refers to the model presented in this work; in the right cell the same model is built using just three variables (the descriptors ED, MD and BD). The second row shows the performances related to the two models built accordingly to the results in Callegaro et al. (2015) and Chapter 4, namely adapting binary logistic regression models (*BLR1* and *BLR2*) but using the extended dataset here presented. The left cell refers to the model built with all the variables presented in this work (*BLR1*), while the right cell refers to the model having the same structure of the one presented in Callegaro et al. (2015), but using the full dataset (*BLR2*).

	All descriptors	Three descriptors
Bayesian trees models	*BT1*	*BT2*
	AUC = 0.84 accuracy = 0.77 sensitivity = 0.77 specificity = 0.77 (threshold = 0.6335)	AUC = 0.74 accuracy = 0.67 sensitivity = 0.67 specificity = 0.67 (threshold = 0.64)
Binary logistic regression models	*BLR1*	*BLR2*
	AUC = 0.82 accuracy = 0.37 sensitivity = 0.09 specificity = 0.99 (threshold = 0.5)	AUC = 0.74 accuracy = 0.41 sensitivity = 0.15 specificity = 0.99 (threshold = 0.5)

In the second row of Table 6.3, models adapted on the complete dataset here presented, and following the methods used in Chapter 4 (Callegaro et al., 2015), namely binary logistic regression models (BLR), are presented. In the first column, model *BLR1*, was adapted using all the here presented descriptors. Using the standard threshold 0.5 the recognition of Type III *foci* is heavily penalized (sensitivity index is very low, 0.09), thus it is intuitive that probably a threshold lower than 0.5 would perform better. Still, the best threshold (0.3) able to maximize performances indexes results in a classification less performing than the one provided by *BT1* (accuracy = 0.75, sensitivity = 0.75, specificity = 0.74). In addition, the AUC value is lower than the one of *BT1*. *BLR2* model in the second column is, on the contrary, a binary logistic regression model adapted using the same descriptors as Chapter 4 (Callegaro et al., 2015), namely ED, MD and Weighted Perimeter Difference (WPD). WPD was preferred to BD because more efficient in discriminating between Type III and non-Type III *foci* in the binary regression model presented in Chapter 4 (Callegaro et al., 2015). As for *BLR1* model, performances with standard threshold (0.5) penalize the recognition of Type III *foci*, and using a lower threshold just partially recovers its performances. Again, AUC value is much lower than the one of the presented model *BT1*. For more details about *BLR1* and *BLR2* models structures see the Table in A7 in Appendix 7.

6.4 Discussion

We here proposed a further step towards an objective and automated classification of Type III *foci* in BALB/c 3T3 CTA, by extending the collection of descriptors referred to morphological features currently used in visual scoring. We achieved a general classifier with respect to the considered substances and their concentrations. We consider this step as a major achievement since the original recommendation on CTAs formulated by EURL ECVAM (2012).

The actual performances of our *BT1* classifier indeed depend on the selection of threshold value t. A threshold slightly higher than 0.5 was found to produce the top value of specificity and sensitivity. This is not completely unexpected given that Type III *foci* represent the predominant type of *foci* observed, while Type I and II *foci* occur less often (see Table 6.1 frequencies, and Sasaki et al., 2012b), then a higher probability of occurrence needs to be considered through the selection of a specific threshold t. We conjecture that *BT1* stands out in performances because of the inherent non-linearity characterizing Bayesian Additive Trees classifiers. Remarkably, the BART algorithm does not need special tuning from the user, thus end users of CTA ranging from the regulatory to the industrial areas may use it confidently, even without extensive statistical training.

Note that *BT1* classifier strongly outperforms the previously developed logistic regression classifier *BLR1* (Callegaro et al., 2015; Chapter 4), which was surprisingly quite weak in recognizing Type III *foci*, at least without performing model re-elaboration. This result is confirmed both using all the variables as well as using just original descriptors. In addition, when looking for the best threshold to be used, a non-intuitive value needs to be selected (lower than 0.5), not consistent with the actual occurrence of Type III *foci*. The model presented in Chapter 4 (Callegaro et al., 2015) was highly performing being adapted to one type of chemical, at a single concentration (MCA, 4 μg/ml). Note that the model here presented is built using a full dataset resulting from exposure to several chemicals acting through different modes of action, genotoxic and non-genotoxic (see Table 6.1), several concentrations of these chemicals, and positive and negative controls. The fact that the logistic regression classifier is not yet so performant is another evidence confirming that different compounds and different concentrations exert a specific effect on *foci* morphology, as demonstrated in Chapter 5 (Callegaro et al., 2016) for two known carcinogens, benzo[a]pyrene and $NiCl_2$. Remarkably, the effect of different compounds and concentrations on *foci* morphology turned out to be relevant for *foci* classification.

We strongly believe in the robustness of our results, because the training and the testing datasets were obtained by (stratified) random sampling from the whole dataset, thus compounds and concentrations were randomly distributed in the two sub-datasets. In addition, when adapting other ensemble methods, like Random Forest (Breiman, 2001), they provided slightly inferior performances very close to BART results. Even when smaller training sets were considered to achieve an equal number of *foci* in the Type III and non-Type III classes, (see par 6.2.5), classification performances on the test set were quite close to BART. Nevertheless, given the importance of the training dataset in determining classifier performances, the inclusion of a larger variety of compounds at different concentrations in the dataset has to be recommended. We conjecture that upon consideration of a sufficiently large sample of compounds and concentrations and an expansion of the set of coded morphological features (Sasaki et al., 2012b), the resulting Bayesian Tree classifier could reach the optimal performances without further training.

On a more methodological side, the comparison of classifiers depends on false positive and false negative rates, but the importance of the two types of error may be differently judged among users of CTA. Different goals inherently characterize regulatory hazard assessors and industrial safety assessors, hence different types of concerns are expected (Benigni, 2014). Our classifier addressed the probability of being Type III *foci* as the key quantity in classification, but consequences of a wrong classification (false positive and false negative) could, and maybe should, be properly considered, for example in relation to the priorities of the CTA user involved. False positive instances in screening programmes performed by the industry can be detrimental, since they preclude further development in a future product. On the contrary, hazard assessors from regulatory agencies stress the need of avoiding false negatives, since these occurrences can expose the population to hazardous compounds. These different purposes of the test should be addressed before selecting a specific threshold for the parameter representing the classification probability,

given the existence of such heterogeneous purposes. In addition, prior information from other *in vitro* and/or non-testing methods about the expected carcinogenic effect of the considered compound could be at the core of an utility-based classifier, following an Integrated Testing Strategy (ITS) approach. Research is ongoing on this issue and we plan to address this in a dedicated paper.

In conclusion, we are here presenting a comprehensive, automated classifier of malignant *foci* in the BALB/c 3T3 CTA, which may be considered as a valid support to the human scoring and provide a valuable improvement to the yet mostly standardized available and validated *in vitro* methods for the carcinogenicity evaluation of chemicals.

6.5 Bibliography

Benigni, R. (2014). "Predicting the carcinogenicity of chemicals with alternative approaches: recent advances". In: *Expert Opinion on Drug Metabolism & Toxicology* 10.9, pp. 1199–1208.

Breiman, L. (2001). "Random Forests". In: *Machine Learning* 45.1, pp. 5–32.

Callegaro, G., R. Corvi, S. Salovaara, C. Urani, and F. M. Stefanini (2016). "Relationship between increasing concentrations of two carcinogens and statistical image descriptors of foci morphology in the cell transformation assay". In: *Journal of applied toxicology: JAT* Dec, 2016.

Callegaro, G., F. M. Stefanini, A. Colacci, M. Vaccari, and C. Urani (2015). "An improved classification of foci for carcinogenicity testing by statistical descriptors". In: *Toxicology in Vitro* 29.7, pp. 1839–1850.

Chipman, H. and R. McCulloch (2016). *BayesTree: Bayesian Additive Regression Trees*. Version 0.3-1.4. URL: https://cran.r-project.org/web/packages/BayesTree/index.html (visited on 12/02/2016).

Combes, R. (2012). "Cell transformation assays: are we barking up the wrong tree?" In: *Alternatives to laboratory animals: ATLA* 40.2, pp. 115–130.

Corvi, R., M. J. Aardema, L. Gribaldo, M. Hayashi, et al. (2012). "ECVAM prevalidation study on in vitro cell transformation assays: General outline and conclusions of the study". In: *Mutation Research/Genetic Toxicology and Environmental Mutagenesis* 744.1, pp. 12–19.

EURL ECVAM (2012). *EURL-ECVAM -Recommendation on three Cell Transformation Assays*.

Gonzalez, R. C. and R. E. Woods (2009). *Digital Image Processing*. Pearson Education. 978 pp.

Grompone von Gioi, R., J. Jakubowicz, J.-M. Morel, and G. Randall (2012). "LSD: a Line Segment Detector". In: *Image Processing On Line* 2, pp. 35–55.

Hand, D. J. and R. J. Till (2001). "A Simple Generalisation of the Area Under the ROC Curve for Multiple Class Classification Problems". In: *Machine Learning* 45.2, pp. 171–186.

Hastie, T., R. Tibshirani, and J. Friedman (2009). *The Elements of Statistical Learning*. Second Edition. Data Mining, Inference, and Prediction. Springer.

Jacobs, M. N., A. Colacci, K. Louekari, M. Luijten, et al. (2016). "International regulatory needs for development of an IATA for non-genotoxic carcinogenic chemical substances". In: *ALTEX-Alternatives to Animal Experimentation* 33.4, pp. 359–392.

Jaworska, J. and S. Hoffmann (2010). "Integrated Testing Strategy (ITS) - Opportunities to better use existing data and guide future testing in toxicology". In: *ALTEX-Alternatives to Animal Experimentation* 27.4, pp. 231–242.

Jones, E., O. Travis, P. Peterson, et al. (2001). *SciPy: Open Source Scientific Tools for Python*. URL: http://www.scipy.org/.

Knight, A., J. Bailey, and J. Balcombe (2006a). "Animal carcinogenicity studies: 1. Poor human predictivity". In: *Alternatives to laboratory animals: ATLA* 34.1, pp. 19–27.

– (2006b). "Animal carcinogenicity studies: 2. Obstacles to extrapolation of data to humans". In: *Alternatives to laboratory animals: ATLA* 34.1, pp. 29–38.

Landolph, J. R. (1985). "Chemical transformation in C3H 10T1/2 Cl 8 mouse embryo fibroblasts: historical background, assessment of the transformation assay, and evolution and optimization of the transformation assay protocol". In: *IARC scientific publications* 67, pp. 185–203.

OECD (2009a). *Test Guideline 451 – Carcinogenicity studies. OECD Guidelines for the Testing of Chemicals.*

– (2009b). *Test Guideline 453 - Combined Chronic Toxicity/Carcinogenicity Studies. OECD Guidelines for the Testing of Chemicals.*

Paules, R. S., J. Aubrecht, R. Corvi, B. Garthoff, and J. C. Kleinjans (2011). "Moving forward in human cancer risk assessment". In: *Environmental health perspectives* 119.6, pp. 739–743.

Procaccianti, C., F. M. Stefanini, and C. Urani (2011). "The cell transformation assay: toward a statistical classification of mixed and intermediate foci images". In: *Alternatives to laboratory animals: ATLA* 39.1, pp. 23–36.

Sasaki, K., S. Bohnenberger, K. Hayashi, T. Kunkelmann, et al. (2012b). "Photo catalogue for the classification of foci in the BALB/c 3T3 cell transformation assay". In: *Mutation Research* 744.1, pp. 42–53.

Sasaki, K., S. Bohnenberger, K. Hayashi, T. Kunkelmann, et al. (2012a). "Recommended protocol for the BALB/c 3T3 cell transformation assay". In: *Mutation Research/Genetic Toxicology and Environmental Mutagenesis* 744.1, pp. 30–35.

Sing, T., O. Sander, N. Beerenwinkel, and T. Lengauer (2005). "ROCR: visualizing classifier performance in R". In: *Bioinformatics* 21.20, pp. 3940–3941.

Tanaka, N., S. Bohnenberger, T. Kunkelmann, B. Munaro, et al. (2012). "Prevalidation study of the BALB/c 3T3 cell transformation assay for assessment of carcinogenic potential of chemicals". In: *Mutation Research/Genetic Toxicology and Environmental Mutagenesis* 744.1, pp. 20–29.

Urani, C., R. Corvi, G. Callegaro, and F. Stefanini (2013). "Objective scoring of transformed foci in BALB/c 3T3 cell transformation assay by statistical image descriptors". In: *Toxicology in Vitro* 27.6, pp. 1905–1912.

Wood, S. (2006). *Generalized additive models: an introduction with R*. CRC press.

PartII

Biochemical profiling of foci phenotypes

7

Cadmium induces in vitro transformation

This Chapter wants to provide a guide to understand the following Chapters, clarifying the design of the experiments and explaining the rationale.

Abstract

Cell Transformation Assays (CTAs) allow to evaluate the carcinogenic potential through the study of morphological changes induced by chemical compounds in mammal cell systems. One of CTA recommended usage is for mechanistic studies of carcinogenicity induced by chemicals (e.g. in academia and industry). Nonetheless, CTAs have been questioned for the lack of understanding of the molecular mechanisms underlying the chemical-induced *in vitro* transformation. For these reasons, the aim of the second part of the here presented PhD project is to improve the understanding of the mechanisms of *in vitro* transformation. We decided to pursue this goal while studying the mechanisms involved in *in vitro* transformation induced by a specific chemical. We focused on the study of cadmium, a human carcinogen, whose mechanisms of action are still not completely understood.

By taking advantage of the protocol of CTA, we isolated cell samples from subsequent phases of the process of *in vitro* transformation, and applied transcriptomic and biochemical analyses to investigate the mechanisms involved.

For the experiments presented in this Chapter and partially in Chapter 8, I acknowledge Dr Claudio Procaccianti and Pasquale Melchioretto for the contribution in the CTAs assessment and isolation of cell clones.

7.1 Introduction

Cell Transformation Assays (CTAs) are *in vitro* methods aiming at evaluating *in vitro* carcinogenesis induced by both genotoxic and some non-genotoxic compounds (Smets, 1980; Vanparys et al., 2012; Vasseur and Lasne, 2012). CTAs allow to evaluate the carcinogenic potential through the study of morphological changes induced by chemical compounds in mammalian cell systems. For more details about CTAs, see the extensive description in section 1.2.2. One of CTA recommended usage is for mechanistic studies of carcinogenicity induced by chemicals, performed both in academia and in industry (EURL ECVAM, 2012). To this end, we exploited CTA to study the mechanisms involved in cadmium-induced *in vitro* transformation.

Cadmium and its inorganic compounds are classified by the International Agency for Research on Cancer (IARC) in Group 1, that is carcinogenic to humans, basing on the evidence of carcinogenicity in humans and experimental animals (IARC, 2012; Hartwig, 2013a).

Cadmium (Cd) is a rare naturally occurring element. Most of the mobilization of Cd in the environment is due to anthropogenic activities, mainly for its production for industrial applications, encompassing nickel-cadmium batteries, pigments, coatings, paints, and stabilizers for plastics. With respect to the general population, relevant exposure occurs *via* food, water and – less important – *via* inhalation of ambient air. Also, due to an accumulation of Cd in tobacco plants, smoking contributes considerably to Cd exposure. Occupational exposure occurs predominantly *via* inhalation, and additionally, there may also be incidental ingestion of dust from contaminated hands and food (Hartwig, 2013a).

Cd can be solubilized in biologically relevant environments, such as water or lipids, after coordination by biologically compatible ligands. This largely depends on its electronic characteristics: Cd outer electronic configuration fills shells like zinc and mercury (Moulis et al.,

2014). Cd exposure to humans can occur via inhalation (mostly for occupational exposure and recreational tobacco smoking): in this case Cd can be found as a component of airborne particles, and may be assimilated by endocytosis. When Cd is ingested, or dissolved in water or lipids, most chemical forms of the metal are therefore ionic, which prevents passive diffusion through biological membranes. A variety of transmembrane molecules have been proposed to mediate Cd cellular uptake, export and intracellular traffic. In particular Cd can enter mammalian cells, *via* the intestinal ferrous ion transporter MNT1 (SLC11A2), or *via* members of the ZIP family, zinc transporters. Intracellular trafficking of Cd can be regulated, among others, by glutathione (GSH) or metallotioneins (MTs) (Urani et al., 2007; Moulis et al., 2014).

After long-term intoxication of laboratory animals, a large majority of Cd resides in the cytosol with 10% to 15% found in organelles. Bound forms of Cd, such as Cd-MT, can release Cd in endosomes of cells such as those of the proximal tubules of the kidney. Cd crosses the endosomal membrane through the constitutive and non-iron-regulated form(s) of divalent metal transporter 1 (DMT1). Apoptosis, autophagy and endoplasmic reticulum stress are triggered by Cd exposure. This strongly suggests interaction of the metal ion with organelles (Moulis et al., 2014).

Cd, as other metals with the exception of chromium (VI), shows low mutagenicity, but rather exerts clastogenic activity in mammalian cells (Hu et al., 2002; Tapisso et al., 2009; IARC, 2012). Indeed, Cd carcinogenicity is likely mediated by non-genotoxic mechanisms of action. The most well characterized include:

Induction of oxidative stress. Transition metal ions play an important role in the induction of oxidative DNA damage. Cd increase the production of Reactive Oxygen Species (ROS) not *via* Fenton-like reactions, but due to an inhibition of the antioxidant defense by Cd, such as the antioxidant enzymes catalase, superoxide dismutase, glutathione reductase, and glutathione peroxidase. One other mechanism proposed consists in the

displacement of redox active metal ions, e.g., Fe^{2+} , for example in metallothioneins, giving rise to Fenton-like reactions (Hartwig, 2013a,b).

Interactions with the DNA Damage Response System. Cd has been shown to impair almost all major DNA repair pathways, e.g. nucleotide excision repair, base excision repair, and mismatch repair (Hartwig, 2010; Koedrith and Seo, 2011; Hartwig, 2013a).

Interaction with p53 Tumor Suppressor Functions. Cd has been shown to interfere with structure and function of p53, but opposite effects have been reported (IARC, 2012; Hartwig, 2013a; Urani et al., 2014).

Impact on Gene Expression and Deregulation of Cell Proliferation Cd has been shown to interfere with several signaling pathways in a complex manner. This includes Ca^{2+}-signaling, cAMP-signaling, NO-signaling, as well as Ca^{2+}- and cAMP-independent protein kinase signaling. Furthermore, Cd interacts with the oxidative stress response, such as the activation of nuclear factor kB (NF-kB) and NF-E2-related factor (Nrf2) (Joseph et al., 2001; Gebraël and Jumarie, 2015).

Cadmium interplay with zinc and calcium. Cd, calcium and zinc (Zn) show similar chemical properties. The similar sizes of Cd and calcium ions are of biological importance. Calcium is a major biological messenger, which dynamically, and often transiently, binds to specific targets to transmit signals. Cd interference in calcium regulatory processes changes the kinetics of metal exchange, and this should perturb signal transmission. Zn is an essential ion present as a cofactor in many proteins and involved in processes like signal transduction, gene expression, stabilization of DNA (Frassinetti et al., 2006). The chemical differences between Cd and zinc (ionic radii, favoured coordination numbers, polarizability) do not always allow biological systems to discriminate between the essential (Zn) and the toxic (Cd) elements (Moulis et al., 2014; Choong et al., 2014;

Urani et al., 2015).

Still, many mechanisms of actions in Cd-induced carcinogenicity remain unraveled. We are therefore using CTAs as a tool to study the signals and the pathways involved in Cd-induced carcinogenicity.

In addition, CTAs have been questioned for the lack of understanding of the molecular mechanisms underlying the transformation (point number (3) listed in paragraph 1.2.2). Our aim is finally to improve the understanding of the mechanisms of *in vitro* transformation, while providing new insights in the mechanisms involved in carcinogenicity induced by a specific chemical, namely Cd.

7.2 Preliminary results

C3H10T1/2 CTAs were performed to assess the *in vitro* carcinogenic potential of Cd ($CdCl_2$), following the protocol set by OECD (2007). A wide range of $CdCl_2$ concentrations was tested; in particular the dose 1 μM $CdCl_2$, which is below the cytotoxicity threshold (IC50 of 2.4 μM), was able to induce the formation of transformed *foci* (Urani et al., 2009).

We expanded our analysis, by designing and performing a two-stage C3H10T1/2 CTA to evaluate the ability of 1 μM of $CdCl_2$ (24 hours of treatment) to induce *in vitro* carcinogenesis. As detailed in Chapter 8, Cd was found to be an inducer of *in vitro* carcinogenesis, with the administration of the promoter TPA. Specifically, dishes exposed to 1μM Cd (inducer)+TPA (promoter) showed a high number (20) of transformed *foci* leading to a high Transformation Frequency (TF=0.78). The TF is expressed as (OECD, 2007):

$$TF = \frac{(\text{average number of tranformed } \textit{foci} \text{ per plate})}{(\text{number of surviving cells})} \tag{7.1}$$

Surviving cells are calculated in a preliminary cytotoxicity test, according to standard protocols (OECD, 2007).

On the contrary, both negative control groups, CTR (samples with medium only) and TPA, never showed any Type II or Type III *focus*, thus resulting in a TF=0.

For experimental details about the followed protocol, see sections 8.2.1, 8.2.2, 8.2.3, 8.2.4 in Chapter 8.

7.3 Rationale and experimental setup

Considering the starting point of the ability of Cd to induce *in vitro* carcinogenicity in the CTA system, we started a project aiming at dissecting the biochemical and molecular events taking place during Cd-induced *in vitro* carcinogenicity.

For a graphical representation of the project outline, see Figure 7.1.

At the end of CTA, Cd-induced *foci* were identified by microscopy examination, were scrape-harvested and re-seeded in 35 mm ∅ Petri dishes for future biochemical characterization ("Transformed foci" in Figure 7.1). Also all needed controls (monolayers from treated and control plates) were collected and reseeded for further analyses. We focused our analysis of the link between transformed morphologies and biochemical profiling of *foci* induced by the same compound at the same concentration (1 μM of $CdCl_2$). In Chapter 8 results related to this part are detailed.

In order to further investigate the process of Cd-induced *in vitro* transformation, we also collected samples simulating the initial phases of the analysed process. We then collected samples of C3H10T1/2 cells treated with 1 μM of $CdCl_2$ for 24 hours, right after the treatment ("$CdCl_2$ 1 μM 24h" in Figure 7.1). In the performed CTA, after Cd treatment, cells were let recovered for four days before the addition of TPA (medium change): then we also collected samples of C3H10T1/2 cells treated with 1 μM of $CdCl_2$ for 24 hours, followed

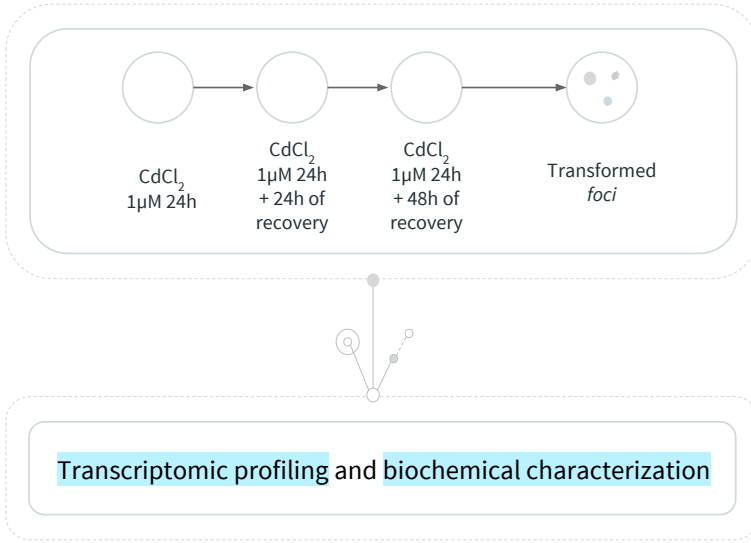

Figure 7.1: Experimental setup.

by other additional 24 hours of recovery ("$CdCl_2$ 1 µM 24h + 24h of recovery" in Figure 7.1) and followed by other total additional 48 hours of recovery ("$CdCl_2$ 1 µM 24h + 48h of recovery" in Figure 7.1). All needed controls were also considered. In Chapter 9 the above mentioned samples were analysed for their transcriptomic profiling, providing a conjectural framework of the initial phases of response after Cd insult. Note that the same experimental setup is maintained through all the experiments, thus the conclusions can be considered together, as summarizing different steps of the same process.

7.4 Bibliography

Choong, G., Y. Liu, and D. M. Templeton (2014). "Interplay of calcium and cadmium in mediating cadmium toxicity". In: *Chemico-Biological Interactions* 211, pp. 54–65.

EURL ECVAM (2012). *EURL-ECVAM -Recommendation on three Cell Transformation Assays.*

Frassinetti, S., G. Bronzetti, L. Caltavuturo, M. Cini, and C. D. Croce (2006). "The role of zinc in life: a review". In: *Journal of Environmental Pathology, Toxicology and Oncology: Official Organ of the International Society for Environmental Toxicology and Cancer* 25.3, pp. 597–610.

Gebraël, C. and C. Jumarie (2015). "Cadmium interference with ERK1/2 and AhR signaling without evidence for cross-talk". In: *Toxicol. Res.* 4.6, pp. 1488–1497.

Hartwig, A. (2010). "Mechanisms in cadmium-induced carcinogenicity: recent insights". In: *BioMetals* 23.5, pp. 951–960.

– (2013a). "Cadmium and Cancer". In: *Cadmium: From Toxicity to Essentiality.* Ed. by A. Sigel, H. Sigel, and R. K. Sigel. Vol. 11. Dordrecht: Springer Netherlands, pp. 491–507.

– (2013b). "Metal interaction with redox regulation: an integrating concept in metal carcinogenesis?" In: *Free Radical Biology and Medicine* 55, pp. 63–72.

Hu, J., Y. Mao, K. White, and The Canadian Cancer Registries Epidemiology Research Group (2002). "Renal cell carcinoma and occupational exposure to chemicals in Canada". In: *Occupational Medicine* 52.3, pp. 157–164.

IARC (2012). *IARC Monograph: arsenic, metals, fibres, and dusts (volume 100 C). A review of human Carcinogens. Lyone, France.*

Joseph, P., T. K. Muchnok, M. L. Klishis, J. R. Roberts, et al. (2001). "Cadmium-induced cell transformation and tumorigenesis are associated with transcriptional activation of c-fos, c-jun, and c-myc proto-oncogenes: role of cellular calcium and reactive oxygen species". In: *Toxicological sciences* 61.2, pp. 295–303.

Koedrith, P. and Y. R. Seo (2011). "Advances in carcinogenic metal toxicity and potential molecular markers". In: *International Journal of Molecular Sciences* 12.12, pp. 9576–9595.

Moulis, J.-M., J. Bourguignon, and P. Catty (2014). "Cadmium". In: *Binding, Transport and Storage of Metal Ions in Biological Cells.* RSC Metallobiology 2. The Royal Society of Chemistry.

OECD (2007). *Detailed Review Paper on Cell Transformation Assays for detection of chemical carcinogens - series on testing and assessment Number 31.*

Smets, L. A. (1980). "Cell transformation as a model for tumor induction and neoplastic growth". In: *Biochimica et Biophysica Acta (BBA) - Reviews on Cancer* 605.1, pp. 93–111.

Tapisso, J. T., C. C. Marques, M. d. L. Mathias, and M. d. G. Ramalhinho (2009). "Induction of micronuclei and sister chromatid exchange in bone-marrow cells and abnormalities in sperm of Algerian mice (Mus spretus) exposed to cadmium, lead and zinc". In: *Mutation Research* 678.1, pp. 59–64.

Urani, C., P. Melchioretto, C. Canevali, F. Morazzoni, and L. Gribaldo (2007). "Metallothionein and hsp70 expression in HepG2 cells after prolonged cadmium exposure". In: *Toxicology in vitro* 21.2, pp. 314–319.

Urani, C., P. Melchioretto, M. Fabbri, G. Bowe, et al. (2014). "Cadmium Impairs p53 Activity in HepG2 Cells". In: *ISRN toxicology* 2014.

Urani, C., F. M. Stefanini, L. Bussinelli, P. Melchioretto, and G. F. Crosta (2009). "Image analysis and automatic classification of transformed foci". In: *Journal of microscopy* 234.3, pp. 269–279.

Urani, C., P. Melchioretto, M. Bruschi, M. Fabbri, et al. (2015). "Impact of Cadmium on Intracellular Zinc Levels in HepG2 Cells: Quantitative Evaluations and Molecular Effects". In: *BioMed Research International* 2015.949514.

Vanparys, P., R. Corvi, M. J. Aardema, L. Gribaldo, et al. (2012). "Application of in vitro cell transformation assays in regulatory toxicology for pharmaceuticals, chemicals, food products and cosmetics". In: *Mutation Research/Genetic Toxicology and Environmental Mutagenesis* 744.1, pp. 111–116.

Vasseur, P. and C. Lasne (2012). "OECD Detailed Review Paper (DRP) number 31 on "Cell Transformation Assays for Detection of Chemical Carcinogens": main results and conclusions". In: *Mutation Research/Genetic Toxicology and Environmental Mutagenesis* 744.1, pp. 8–11.

8

Cadmium triggers different proliferative behaviours

In this Chapter proliferation patterns are analysed in cells from transformed foci induced by Cd through CTA, and their relationship with foci phenotypes is studied.

Abstract

The *in vitro* Cell Transformation Assay (CTA) is a powerful tool for mechanistic studies of carcinogenesis. The endpoint is the classification of transformed colonies (*foci*) by means of standard morphological features. To increase throughput and reliability of CTAs, a better comprehension of the mechanisms underlying cell transformation is recommended. To this end, we have performed CTAs testing $CdCl_2$, a widespread environmental contaminant classified as a human carcinogen with the underlying mechanisms of action not completely understood. We have isolated and re-seeded the cells at the end (6 weeks) of *in vitro* CTAs to further identify the biochemical pathways underlying the transformed phenotype of *foci*. Morphological evaluations, proliferative assays and biochemical analysis of EGFR pathway revealed that, despite the same initial carcinogenic stimulus (1 μM $CdCl_2$ for 24 hours), transformed clones are different. Our preliminary results on molecular characterization of cell clones from different *foci* could be exploited for CTAs improvement, supporting the comprehension of the *in vivo* process and complementing the morphological evaluation of *foci*.

This Chapter is adapted from the published paper "Cadmium-transformed cells in the in vitro cell transformation assay reveal different proliferative behaviours and activated pathways", Forcella M., Callegaro G., Melchioretto P., Gribaldo L., Frattini M., Stefanini F.M., Fusi P., Urani C. Toxicol in Vitro, 36, 71–80, 2016.

8.1 Introduction

Cadmium (Cd) is a widespread environmental contaminant that has been shown to cause adverse health effects. The non-occupational exposure arises mainly from the diet, the ingestion of contaminated drinking-water, the inhalation of ambient air, and from contaminated soil or dust. Other possible sources of exposure are represented by phosphate-based fertilizers, and cosmetic products, in which Cd is used for its colour properties. In addition, in the general population, cigarettes represent a significant source due to a natural Cd accumulation by tobacco leaves. Once it has entered the human body, Cd accumulates in various organs with a long biological half-life (10-30 years) due in part to its low excretion rate (see for a comprehensive description the report of U.S. Department of Health and Human Services, 2012; Bocca et al., 2014; IARC, 2012; Choong et al., 2014). This metal has been classified as a human carcinogen by the International Agency for Research on Cancer (IARC), but the underlying mechanisms of action are complex and not completely known to date (IARC, 2012; Hartwig, 2013). A powerful tool for mechanistic studies of carcinogenesis is represented by the Cell Transformation Assays (CTAs). The CTAs are the most advanced *in vitro* test for the prediction of human carcinogenicity induced by chemicals, in terms of standardization and validation (Vanparys et al., 2012), and have been used for decades as *in vitro* methods for screening the potential carcinogenicity and for investigating the mechanisms of action of hazardous compounds (Combes et al., 1999; Corvi et al., 2012). In addition, these assays have been shown to closely model some key stages of the conversion of normal cells to malignant phenotypes, like the *in vivo* carcinogenic process (Landolph, 1985). In this regard, the CTA based on the use of C3H10T1/2Cl8 mouse embryo fibroblasts, which are among the suitable cells suggested by standard protocols (OECD, 2007), has been indicated as a useful model to

elucidate the molecular mechanisms of cell transformation at the genomic and transcriptomic levels (Vasseur and Lasne, 2012). Upon chemical exposure, these cells undergo morphological transformation visualized by the formation of transformed cell colonies (*foci*). The *foci* are recognized under a microscope and classified by standard features, such as deep basophilic staining, multilayered growth, random cell orientation at the edge of the *focus*, and invasiveness of the surrounding monolayer of normal cells (Landolph, 1985; OECD, 2007). These morphological features are related to molecular changes leading the cells to acquire fully malignant characteristics, which were demonstrated by their ability to yield tumours when injected into susceptible host animals (Reznikoff et al., 1973). The CTAs are a relatively simple technique, in comparison to the two-year bioassay with rodents (OECD, 2009, TG451), and have the potential to analyse both genotoxic and some non-genotoxic chemicals, and support the 3Rs principles of Replacement, Reduction and Refinement of experimental animals. Furthermore, they provide a tool for the comprehension of the mechanisms underlying the *in vitro* carcinogenic processes, which is still to be exploited. The latter represents a specific follow-up request of the European Union Reference Laboratory for Alternatives to Animal Testing, along with the automation of *foci* scoring, in order to increase throughput and reliability of CTAs, and to possibly include these assays in the regulatory carcinogenicity testing battery (EURL ECVAM, 2012; Creton et al., 2012).

The activation of the epidermal growth factor receptor (EGFR) pathway is one of the best characterized molecular mechanisms so far identified in the cell transformation process (Baselga, 2001; Venook, 2005; Immervoll et al., 2006), and has a central role in the pathogenesis and progression of different carcinoma types (Normanno et al., 2006). EGFR is a member of the tyrosine kinase ErbB receptor family, playing an important role in the regulation of cell growth, proliferation, and differentiation (Zhen et al., 2003; Liu et al., 2011). Upon binding of the epidermal growth factor (EGF) to its receptor (EGFR), two main downstream pathways can be activated: 1) the

Ras/Raf/mitogen-activated protein kinase (MAPK) signalling cascade (activated when the Erk protein is hyperphosphorylated), that drives pro-proliferative gene expression, cytoskeletal rearrangement, and increased cell proliferation, and 2) the phosphoinositide-3-kinase (PI3K)/PTEN/AKT cascade (activated when Akt protein is hyperphosphorylated), which is involved in cell survival and motility (Jorissen et al., 2003). The identification of possible EGFR pathways alterations may open the door to new therapies for the early phases in the development of several cancer types. Of high relevance, several drugs directly targeting either EGFR or a member of its downstream pathways have been developed or are under evaluation in clinical trials (www.clinicaltrials.gov). The aim of the present study is the characterization of proliferative and survival behaviours in C3H10T1/2 Cl8 cells transformed upon Cd exposure. Although it has been studied in depth in many cancer cell lines, EGFR activation has not been investigated in C3H10T1/2 Cl8 mouse embryo fibroblasts so far, nor in other cell lines suitable for CTAs. Therefore, we focused on EGFR pathway as a starting point to identify the biochemical alterations underlying the morphological changes exploited in *foci* recognition and classification.

8.2 Materials and Methods

8.2.1 Cells culture and conditions

The experiments were performed using contact-sensitive C3H10T1/2 clone 8 (C3H from here on) mouse embryonic fibroblasts (cell line ATCC, CCL 226 lot. n. 58078542). This cell line was chosen for its high sensitivity to carcinogenic compounds, its low spontaneous transformation rates, and because it represents one of the cell models suggested to be used in CTAs (OECD, 2007). The cells were stored in

ampoules, frozen at −80°C with 10% sterile DMSO as a preservative. Cells at passages from 9 to 12 were used for cell transformation studies (OECD, 2007). Cells were cultured in Basal Medium Eagle (BME, Sigma Chemical Co., St. Louis, MO, USA) enriched with 10% heat-inactivated fetal bovine serum (FBS, Euroclone, Pero, Italy), 1% glutamine, 0.5% HEPES 2M and 25 μg/mL gentamicin (all purchased from Sigma) at37°C in a humidified incubator supplied with a constant flow of 5% CO_2 in air throughout each experiment. Cells were routinely seeded in 100 mm ∅ Petri dishes, the medium was changed every 3 days and cells were grown until 80% confluence maximum was reached.

8.2.2 Chemicals

The stock solution (1 mM) of $CdCl_2$ (97% purity BDH Laboratory, Milan, Italy) was prepared in ultra-pure water (0.22 μm filtered Milli-Q water, Millipore, Vimodrone, Milan, Italy) and stored at 4°C. Stock solution of 12-O-tetradecanoylphorbol-13-acetate (TPA) (Sigma) was prepared in DMSO to a final concentration of 1 μg/μl. TPA was chosen as a well-known promoter agent (OECD, 2007).

8.2.3 CTA and isolation of the cells

C3H were seeded at a density of 800 cells/dish in 100 mm diameter Petri dishes, and exposed 24 h after seeding to 1 μM $CdCl_2$ for 24 hours. Previous Cell Transformation Assays performed by our group (Urani et al., 2009) on a wide range of $CdCl_2$ concentrations demonstrated that 1 μM $CdCl_2$, which is below the cytotoxicity threshold (IC50 of 2.4 μM), is able to induce the formation of transformed *foci*. Therefore, in the present work we have used a single concentration with the only aim to obtain transformed cells to be further isolated and characterized. Samples treated with

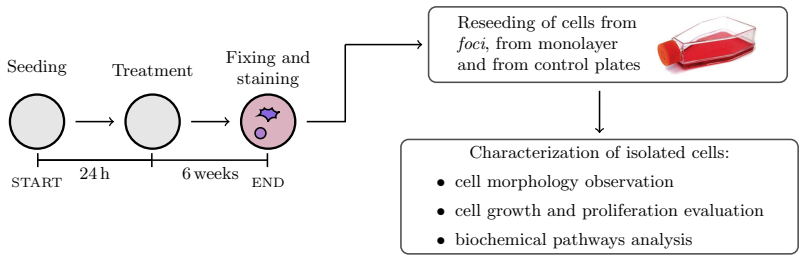

Figure 8.1: Outline of the experimental design. A C3H10T1/2 CTA was performed and clones of transformed and untransformed cells were isolated and characterized. Briefly, C3H cells were seeded at a density of 800 cells/dish in Petri dishes, and exposed, 24 hours after seeding to 1 µM $CdCl_2$ for 24 hours. After 4 days cells were exposed to 0.1 µg/ml 12-O-tetradecanoylphorbol-13-acetate (TPA), a known tumour promoter. Controls were the cells exposed to DMSO, or to TPA alone. At the end of CTA (6th week) some Cd-transformed *foci* and all needed controls were observed under microscope, scrape-harvested and re-seeded in 35 mm ∅ Petri dishes for future biochemical characterization. Then, all Petri dishes were methanol-fixed and Giemsa-stained for the assessment of the transformation frequency.

$CdCl_2$, were exposed 4 days after the treatment to 0.1 µg/ml TPA in DMSO. TPA addition was maintained throughout all the experiments. Cells exposed to 0.1 µg/ml TPA alone were used as controls. The negative controls consisted in the medium alone or the medium containing DMSO at the final concentration below the 0.1% (v/v) set by the OECD (OECD, 2007). After 24 hours of treatment, the cells were rinsed twice with phosphate buffered saline (PBS) and fresh medium was added. The medium was changed weekly. Upon confluence (around the 3rd week), high serum (10% FBS) medium was substituted with low (5% FBS) serum medium. The samples were observed weekly under a light microscope throughout the duration of the assay (6 weeks) to check healthy cells status and *foci* formation. At the end of CTAs (6th week), Cd-transformed *foci* and all necessary controls were identified by microscopy examination, were scrape-harvested and re-seeded in 35 mm ∅ Petri dishes for future biochemical characterization. All Petri dishes were then rinsed with PBS, fixed in absolute methanol for 10 min, and stained with

10% Giemsa solution (v/v in distilled water), rinsed three times with distilled water and observed by light microscopy for *foci* scoring and classification, according to standard procedures. All methodological details of CTAs with C3H cells are elsewhere described (Reznikoff et al., 1973; Landolph, 1985; OECD, 2007; Urani et al., 2009). In Figure 8.1, an outline of the experimental design is provided. The following cell samples were collected at the end of CTAs and re-seeded (from here on cell clones) for a further characterization:

- CTR: cells from a normal monolayer of sample exposed to complete medium only;
- TPA: cells from a monolayer exposed to TPA alone;
- F1: cells from a fully transformed *focus* (Type III) after exposure to 1μM $CdCl_2$;
- F2: cells from a *focus* classified as intermediate between Type II and III after exposure to 1μM $CdCl_2$;
- F3: cells from a fully transformed *focus* (Type III) after exposure to 1μM $CdCl_2$;
- MN3: cells from the contact-inhibited monolayer in the Petri dish where F3 was collected.

8.2.4 Morphological criteria for cell transformation

The CTA rely on the evaluation of morphological changes in cell colonies (*foci*) through optical microscopy observation performed by a trained expert (Landolph, 1985; OECD, 2007). In the C3H CTA, Type II and III *foci* are considered fully transformed and scored for the estimate of the transformation frequency (TF). When reinjected into syngenic animals, cells from Type II and Type III *foci* form tumours with a frequency of 50% and 80-90% respectively (Reznikoff et al., 1973; Male et al., 1987). The scoring is based on standard morphological criteria (Reznikoff et al., 1973; Landolph, 1985): Type

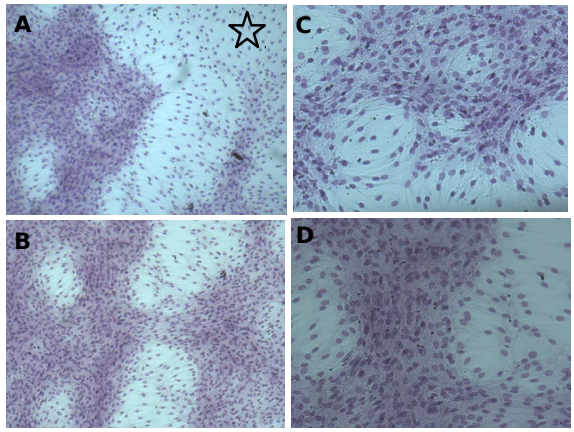

Figure 8.2: Type III *focus*. Example of different areas of a Type III *focus* formed at the end of a CTA (6^{th} weeks) induced by 1 μM $CdCl_2$ exposure, followed by TPA addition. The *focus* shows the typical morphological features of transformation: deep basophilic staining and multilayering of transformed cells, the invasiveness into the surrounding monolayer of normal contact-inhibited cells (upper right part of A, star) and vortexes formation (B) with polarized and spindle shaped cells with flattened nuclei (C, D). Magnification: A, B 32 ×; C, D 100×.

II are *foci* with extensive cellular piling into multilayers and mildly polar cells; Type III are *foci* with highly polar, fibroblastic and multilayered crisscrossed cells. Examples of a Type III *focus* obtained upon Cd exposure at the end of CTAs, and further morphological features are shown and described in Figure 8.2. Type I *foci*, although showing highly packed cells, are excluded from the estimate of the TF being characterized by a normal morphology.

8.2.5 Proliferation assays

Proliferation activity of each clone was assessed through two different assays, the first one aiming at the evaluation of the proliferation activity in terms of cell count at consecutive time points, the second one focused on the morphological analysis of different clones at

confluence. In the first assay, cell clones (CTR, TPA, MN3, F3, F1 and F2) were seeded (100.000 cell/35 mm ∅ Petri dishes, 50.000 cells/ml) and harvested by trypsinization at 24, 48 and 72 hours after seeding. Aliquots (40 µl) of the cell suspensions were diluted in isotonic solution and counted in a Coulter counter (Z1, Beckman Coulter Inc, CA, USA). All counts were expressed as number of cells/ml. In the second assay, all cell clones were seeded at 100.000 cells/35 mm ∅ Petri dishes (50.000 cells/ml) and left in culture until confluence was reached to test for their contact-inhibition properties. All dishes were then fixed in methanol for 10 min at room temperature, washed in distilled water, stained with 10% Giemsa for 10 min at room temperature and finally washed again in distilled water. All samples were viewed under a Zeiss Axioskop 40 microscope (5× objective magnification) and photographed with Axiovision 4.6 software (Zeiss, Oberkochen, Germany).

8.2.6 SDS-PAGE and Western Blotting

All cell clones were harvested by trypsinization at 80% confluence, washed with ice-cold PBS and lysed in RIPA buffer (50 mM Tris-HCl pH 7.5, 150 mM NaCl, 1% NP-40, 0.5% sodium deoxycholate, 0,1% SDS) containing protease and phosphatase inhibitors and 1 mM PMSF (phenylmethylsulfonyl fluoride). After lysis on ice, homogenates were obtained by passing 5 times through a blunt 20-gauge needle fitted to a syringe and then centrifuged at 15,000 g for 30 min. Supernatants were analysed for protein content by the BCA protein assay (Smith et al., 1985). SDS-PAGE and Western blotting were carried out by standard procedures (Laemmli, 1970). Sixty µg of proteins were separated on a 10% acrylamide/bis-acrylamide SDS-PAGE, transferred onto a nitrocellulose membrane (Millipore, Billerica, MA, USA), probed with the appropriated antibodies and visualized using ECL detection system (Millipore). Protein levels were quantified by densitometry of immunoblots using ScionImage software (Scion

Corporation, 2012). The following primary antibodies were used (all purchased by Cell Signaling Technology, Danvers, MA, USA): anti EGFR (dilution 1:1000), phospho-EGFR (Tyr1068; dilution 1:1000), p44/42 MAPK (Erk1/2; dilution 1:1000), phospho-p44/42 MAPK (P-Erk1/2) (Thr202/Tyr204; dilution 1:1000), Akt (dilution 1:1000), phospho-Akt (Ser 473; dilution 1:1000), PTEN (dilution 1:1000), vinculin (dilution 1:1000). IgG HRP-conjugated secondary antibodies (purchased by Cell Signaling Technology, Danvers, MA, USA) were diluted 1:10000.

8.2.7 Statistical analysis

Data from proliferation assays were analysed as follows. The maximum value over 3-4 technical replicates was calculated for each block/time/clone tuple after recognizing that experimental errors in technical replicates may only be negative. The two blocks were both full factorial designs with 6 clones tested at 3 times, but they differed in the number of biological replicates, 3 in the first block and 2 in the second block. The final dataset comprises 83 observations because 6 x 3 = 18 clone-time treatments got 3 biological replicates in the first block (54 observations) and 2 biological replicates in the second block (36 observations), but 7 values were missing, thus 54 + 36 - 7 = 83 observations were available at the end of the experiment. We decided to analyse count data fitting a general linear mixed-effects model (Pinheiro and Bates, 2000) to improve the estimate of variance and to better capture technical variability through a variance component. The sample size may be considered quite small for what regards the goal of estimating specific parameters for each time and each treatment. A joint model of all observations, by contrast, has the potential of reducing bias and of capturing further features of the data generating process, like technical variability, finally leading to more powerful tests. Then, observed counts $Y_{e,c,t,j}$ are decomposed

as follows:

$$Y_{e,c,t,j} = \mu + \alpha_e + \gamma_c + \beta_t + \theta_{c,t} + \varepsilon_{e,c,t,j} \tag{8.1}$$

where e indicates a block, c refers to a clone, t to time and j to biological replicate within clone-time. Residuals are assumed to be independent normal variables $\varepsilon_{e,c,t,j} \backsim N(0, {\sigma^2}_{e,c,t,j})$ with the variance a power function of the expected value of the response Y, precisely:

$${\sigma^2}_{e,c,t,j} = \sigma^2 {\mu^{2\delta}}_{e,c,t,j} \tag{8.2}$$

where δ is a model parameter to be estimated. Right side of equation 8.1, μ is the mean value of the TPA clone (considered as the reference control), α is a random effect associated to blocks in the experiment, thus $\alpha_e \backsim N(0, {\sigma^2}_{\alpha})$ are normally distributed and independent; gammas are fixed effects representing departure of other clones from the mean value of TPA; betas are fixed effects due to time with respect to the 24 hours; thetas are interactions between clone and time, therefore they capture specific behaviour of clones at different times (see supplementary material for details). Likelihood ratio test for the hypothesis of null interaction were also performed. Quantile-quantile plot of normalized residuals were checked out looking for evidences against the normality assumption of model residuals. Calculations were performed in R (R Core Team, 2012) using the nlme package (Pinheiro et al., 2015).

Densitometric data from Western blot analysis were analysed as follows. Each target (protein analysed) for each cell clone was analysed in triplicates. Densitometric values for each clone and each target were normalized to the loading control (vinculin); in the case of phosphorylated targets, densitometric values were normalized to the value obtained for the total target protein. Since values of Erk tot were missing in one replicate of Erk phosphorylation, model-based imputation was performed by regressing observed Erk tot on vinculin, then by estimating the expected value of Erk tot in the missing replicate given its observed values of vinculin. Robust estimates of

model parameters were obtained under the assumption that residuals followed a Student-t distribution with small degree of freedom, that is a heavy-tailed distribution. Values of fold change versus control, the TPA clone, were finally calculated after imputation of missing values TPA clone. All clone-to-control contrasts were tested by Dunnet multiple comparison procedure applied to log-transformed fold-change data. Calculations were performed in R (R Core Team, 2012) using the heavy package (Osorio, 2014) and multcomp package (Hothorn et al., 2008).

8.3 Results

8.3.1 Cadmium exposure leads to cell transformation

In our experiments, dishes exposed to 1μM Cd (inducer)+TPA (promoter) showed a high number (20) of transformed *foci* leading to a high TF (TF=0.78). On the contrary, both negative control groups, CTR (samples with medium only) and TPA, never showed any Type II or Type III *focus*, thus resulting in a TF=0. The TF is expressed as a function of the average number of transformed *foci* per plate divided by the number of surviving cells, as suggested by standard protocols (OECD, 2007). Surviving cells are calculated in a preliminary cytotoxicity test, according to standard protocols (OECD, 2007).

8.3.2 Transformed *foci* have different proliferation rates

Since changes in cell morphology and growth behaviour in culture represent typical features of transformed cells, morphological observation and cell proliferation rate estimates were carried out in

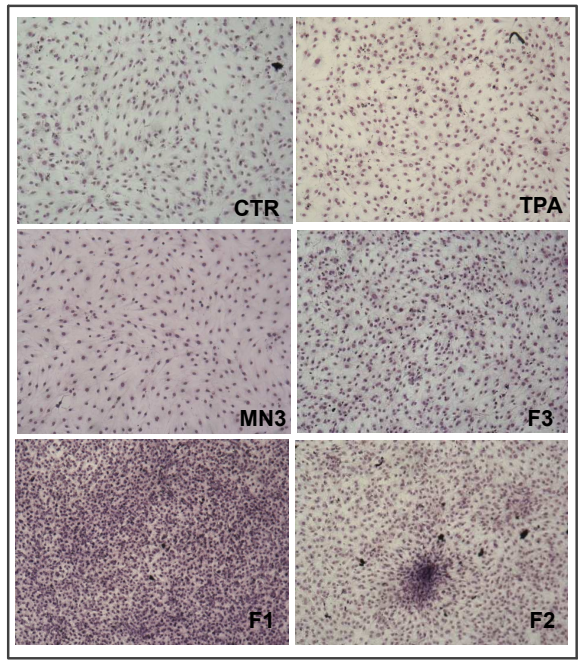

Figure 8.3: Cell morphology evaluation. Clones from normal cells (CTR, TPA, MN3) and transformed *foci* (F1, F2, F3) were observed by optical microscopy after fixing and Giemsa staining. The typical contact-inhibition at confluence is displayed by normal cells, although TPA shows a slighter increase of cell density. On the contrary, clones from transformed *foci* show a loss of contact-inhibition with tightly packed nuclei and the formation of highly dense and piled-up regions. Magnification 50×.

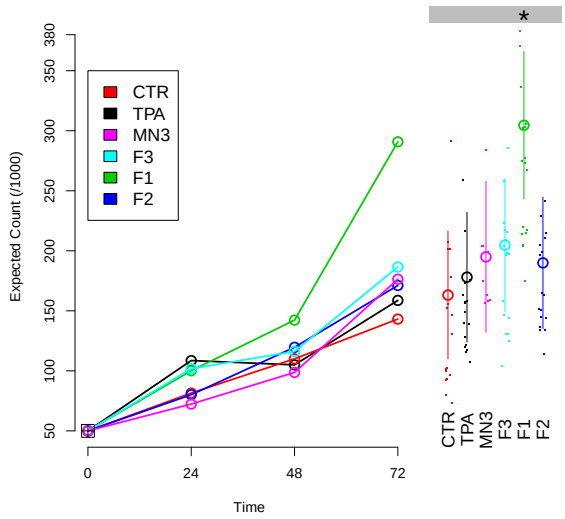

Figure 8.4: Cell proliferation evaluation. CTR, TPA, MN3, F3, F1 and F2 cell clones were seeded at 50.000 cells/ml and harvested by trypsinization at 24, 48 and 72 h after seeding. On the left, the expected values (empty circles) of clones at each time are estimated by a linear mixed-effects model. On the right, bars represent 95% confidence intervals of expected values for clones at time 72h ($*$ p-value <0.05), while small dots represent original counts at time 72h.

all isolated clones (transformed and untransformed). As expected, control samples (CTR) exhibited low cell density and the typical contact-inhibition of normal cells at confluence, when observed by optical microscopy (Figure 8.3, CTR). Normal cells from the contact-inhibited monolayer, harvested in Cd-treated plate (MN3), showed a morphology comparable to that of CTR with low density, and contact-inhibited cells (Figure 8.3, MN3). The TPA-treated samples (TPA) showed morphology comparable to CTR, although a slightly increased density could be observed (Figure 8.3, TPA). On the contrary, when cells from a fully transformed Type III *focus* (F3) were grown until confluence, they demonstrated a loss of contact-inhibition, and a dense growth, as shown by highly packed nuclei (Figure 8.3, F3). A dense growth was also observed in transformed cells of F1 and

F2 clones, the latter also evidencing the formation of multilayered, piled-up areas typical of cells with loss of contact-inhibition (Figure 8.3, F1 and F2). To quantify the proliferative behaviour, growth curves of all isolated clones were determined through cell counting, and subsequently analysed through a general linear mixed model specifically adapted. Results of model fitting are summarized in Figure 8.4, left, where expected values for different clones at different times are plotted. Clones collected from transformed *foci*, like F1 and F2, deviate from the linear growth otherwise observed. 95% confidence intervals for the expected value of the response and original count values for 72 hours are shown (Figure 8.4, right) and they are all similar except for F1 clone showing a higher proliferation rate at 72 hours. While the likelihood ratio test for the hypothesis of null interactions between variables time and treatment was rejected ($p < 0.005$), the only significant interaction term in the final model (t-test) was clone F1 by time 72 hours ($p<0.05$). Quantile-quantile plot of normalized residuals did not show relevant evidence against the assumption of normality for residuals.

8.3.3 Different *foci* activate proliferative or survival pathway

Since transformed cells are characterized by uncontrolled cell growth, we undertook the characterization of specific proliferative markers. The activation of EGFR pathways in different re-seeded cell clones was investigated. EGFR expression was found to be below the Western blot detection limit in all the cell clones. However, intracellular mediators of proliferation (Erk, belonging to the MAPK pathway) and survival (Akt, belonging to the PI3K/PTEN/AKT pathway) were seen to be deregulated nearly in all the transformed clones. Protein activation was assessed through Western blotting of crude extracts, and immunodecoration was performed with antibodies recognizing either the phosphorylated or the total form of each protein. As shown in Figure 8.5, F1 clone showed a significant

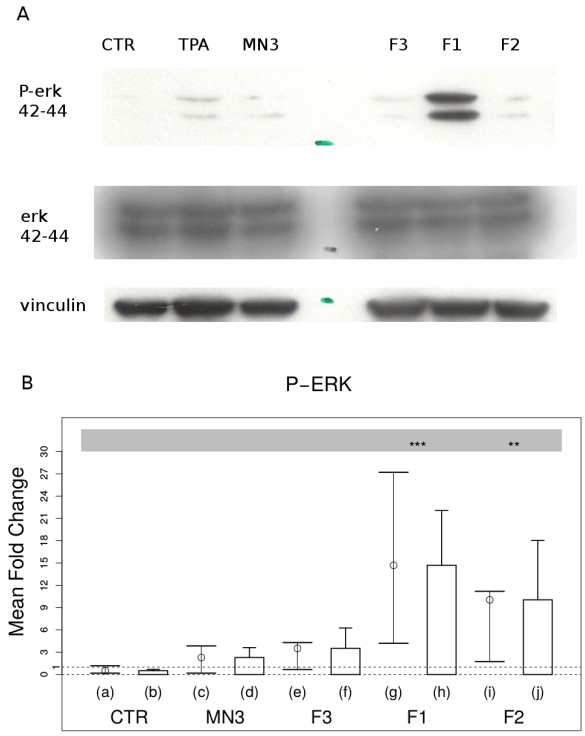

Figure 8.5: Western blotting analysis of Erk activation. A) Representative Western blotting performed on crude extracts, using anti-P-Erk and anti-Erk antibodies. Vinculin was used as a loading control. The experiments were performed in triplicate. B) Determination of phosphorylation rate by densitometric analysis was performed with Scion Image Software. Values are calculated as the P-Erk/total Erk ratio; each ratio is normalized on P-Erk/total Erk ratio of TPA treated control cells. Points and whiskers in (a), (c), (e), (g) and (i) represent respectively the means and confidence intervals for each fold ratio of each clone. In addition, bars and whisker in (b), (d), (f), (h) and (j) represent respectively means and standard errors for each fold ratio of each clone ($**$ p-value <0.005, $***$ p-value <0.001).

($p<0.001$) increase of Erk phosphorylation level compared to TPA clone, in agreement with its high proliferative activity. F2 clone showed a significant Erk phosphorylation level compared to TPA as well, although less marked than F1 ($p<0.05$). All other clones, including controls as well as F3 clone, did not show any significant and comparable phosphorylation levels. No significant differences in total Erk protein expression levels were found in all clones (Figure 8.5). On the other hand, as reported in Figure 8.6, we observed an increase in Akt phosphorylation level (P-Akt) only in the F3 clone, compared to TPA. Although not statistically significant, this suggests a different activation trend in comparison with other transformed clones and controls. No differences in total Akt protein expression levels were found in all clones (Figure 8.6). To further investigate the deregulation of the PI3K/PTEN/AKT signalling cascade, we analysed its negative regulator, PTEN. Its protein levels (Figure 8.7) showed no alterations in all the cell clones.

8.4 Discussion

With a long term aim of developing a quantitative and objective method of *foci* scoring and classification, our research group is working towards the automation of this step of the assay (Urani et al., 2009; 2013; Callegaro et al., 2015). Herewith we undertook a further step to meet EURL ECVAM recommendations, i.e. the molecular characterization of pathways involved in the complex process of cell transformation. Being the best characterized cancer activated pathway, EGFR and the activation of its downstream pathways were chosen as a starting point (Baselga, 2001; Venook, 2005; Immervoll et al., 2006). To the best of our knowledge, since the first pioneering study of Male and colleagues (1987), very few papers have addressed this issue; some authors have analysed the pathways involved in MCA+TPA-induced transformation in C3H10T1/2 cells (Priya et al., 2013), others have characterized gene expression profiles

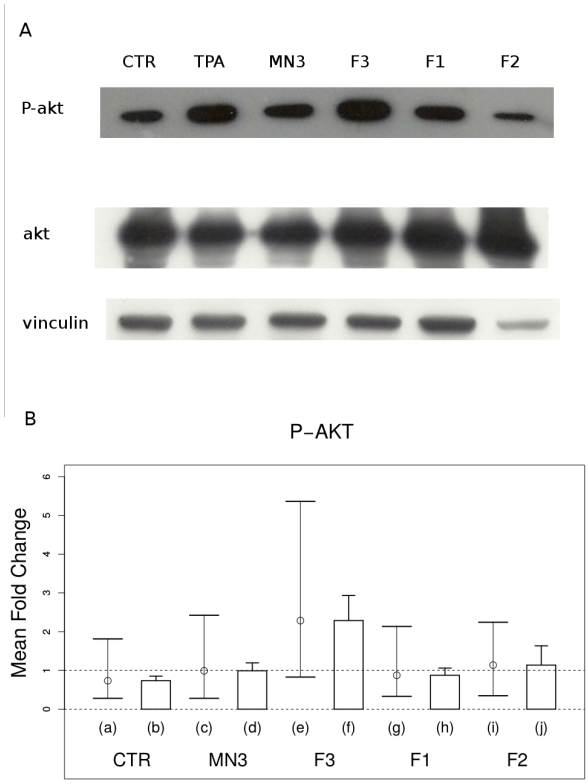

Figure 8.6: Western blotting analysis of Akt activation. A) Representative Western blotting performed on crude extracts, using anti-P-Akt and anti-Akt antibodies. Vinculin was used as loading control. The experiments were performed in triplicate. B) Determination of phosphorylation rate by densitometric analysis was performed with Scion Image Software. Values are calculated as the P-Akt/total Akt ratio; each ratio is normalized on P-Akt/total Akt ratio of TPA treated control cells. Points and whiskers in (a), (c), (e), (g) and (i) represent respectively the means and confidence intervals for each fold ratio of each clone. In addition, bars and whisker in (b), (d), (f), (h) and (j) represent respectively means and standard errors for each fold ratio of each clone.

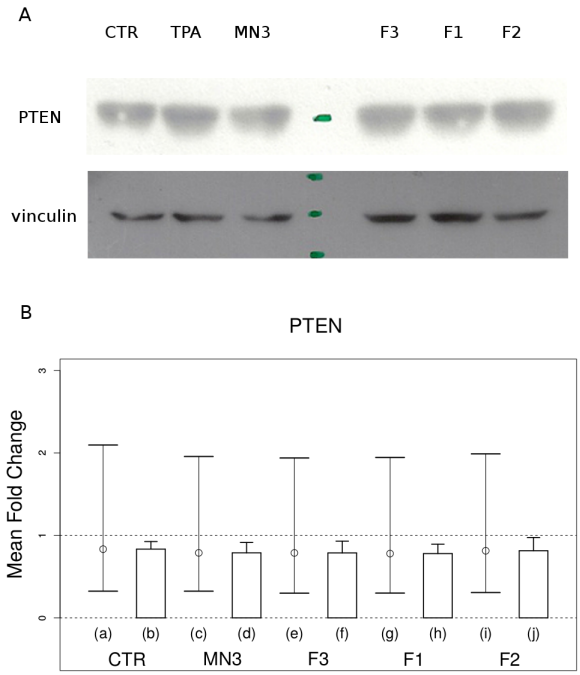

Figure 8.7: Western blotting analysis of PTEN protein level. A) Representative Western blotting performed on crude extracts, using anti-PTEN antibody. Vinculin was used as loading control. The experiments were performed in triplicate. B) Densitometric analysis of total protein content was performed with Scion Image Software. Data are expressed as fold changes compared to TPA treated control cells. Points and whiskers in (a), (c), (e), (g) and (i) represent respectively the means and confidence intervals for each fold ratio of each clone. In addition, bars and whisker in (b), (d), (f), (h) and (j) represent respectively means and standard errors for each fold ratio of each clone.

in BALB/c 3T3 transformed *foci* exposed to carcinogens or tumour promoting agents to identify a gene signature (Rohrbeck et al., 2010; Ao et al., 2010). Therefore, our work may significantly contribute to a knowledge advancement in this field.

It is noteworthy to remark that all fully transformed *foci* used herein for the biochemical characterization (F1, F2 and F3) were formed at the end of the CTAs (6 weeks) upon the same chemical inducer ($CdCl_2$ 1μM, 24 hours), selected in previously performed experiments aimed at the identification of the carcinogenic dose-response (Urani et al., 2009). Cadmium-induced carcinogenesis is still a matter of study, although different mechanisms have been proposed or identified: e.g., the involvement of reactive oxygen species (ROS), the deregulation of cell growth and resistance to apoptosis (see Hartwig, 2013,for a comprehensive review), and the interference with essential metals (Martelli et al., 2006; Urani et al., 2015). In the present study, the morphological analysis of *foci*-derived cell clones by optical microscopy showed in all instances a loss of contact-inhibition, as well as higher cell densities, compared to normal cells (Figure 8.3), all common features of transformed cells. However, proliferation rate analyses showed that only F1 clone displayed a significant increase, compared to control cells. The investigation of EGFR pathways, most commonly responsible for cell proliferation, confirmed these data. Our results indicate that EGFR itself does not seem to play any direct role in cadmium-induced *foci*: indeed, we were not able to detect EGFR protein expression levels neither in transformed nor in non-transformed clones, thus suggesting its marginal role in cadmium-induced transformation. This is in agreement with previously reported data in other cancer cells (Krasinskas, 2011). On the contrary, interesting considerations can be done on the analysis of EGFR downstream pathways, the MAPK axis (activated when Erk protein is hyperphosphorylated) and the PI3K/PTEN/AKT axis (activated when Akt is hyperphosphorylated). It is of high relevance that both these pathways have been found altered in cadmium-induced *foci*: either the ERK pathway, as in F1 cells and to a minor

extent also in F2 cells, or the AKT pathway, as in F3 cell clone, were found to be activated. In particular, for F3 cell clone, we observed a trend in Akt phosphorylation levels, even though not statistically significant (sample size is equal to 3). In our samples, the alteration of Akt phosphorylation can be ascribed to Akt itself or to an upstream deregulation, but not to PTEN, a negative regulator of the PI3K/PTEN/AKT pathway, since we did not observe any significant change (decrease) in PTEN expression, when compared to TPA samples. F2 cells showed an increase in Erk phosphorylation despite its proliferation being comparable to controls. At the end of the CTA, F2 *focus* was classified by microscopy observation as intermediate (Type II/III) and morphological assessment of cell proliferation of its derived clone revealed spatial heterogeneity, i.e. the formation of multilayered, piled-up areas of cells. Thus we can consider F2 cell clone as having an intermediate phenotype reflecting the intermediate biochemical fingerprint observed for proliferation behaviour. Moreover, it is worth noticing that an increase in Akt phosphorylation was also detected in F3 clone, when compared to its own control (MN3 clone), representing untransformed cells growing as a monolayer in the same plate.

On the whole, our data suggest that F1 cell growth is supported by the activation of the ERK pathway, leading to a high proliferation state. The same pathway is activated in F2 cell clone, although to a lower extent than in F1 cells. On the other hand, F3 cell clone shows a shift towards a survival mode, with the activation of the PI3K/PTEN/AKT pathway, paralleled by PTEN unaltered levels. The ability of cadmium to promote cell transformation through Erk and Akt signalling activation was recently reported in human lung epithelial cells, and was demonstrated to be mediated by ROS production (Jing et al., 2012). Further mechanisms of Erk and Akt signalling activation have been described and comprehensively reviewed (Choong et al., 2014). For instance, it is recognized that cadmium participates in many Ca^{2+}-dependent pathways in different cell types (e.g., skin fibroblasts, mesangial cells) due to its “ionic

mimicry". The central role of cadmium in calcium mobilization and the changes in calmodulin and Ca^{2+}/calmodulin-dependent protein kinase II activation and their regulation of downstream signalling cascades, such as the Erk and Akt, have been described. Thus, the interplay of calcium and cadmium in mediating the transformation of C3H10T1/2 cells is a mechanism that deserves further studies.

It has to be highlighted that in our work, although both F3 and F1 clones were collected from fully transformed *foci*, as assessed by previously described morphological procedures of optical microscopy (Landolph, 1985; Ao et al., 2010), we have observed an activation of two different EGFR downstream pathways at a molecular level.

Our data clearly show that transformed *foci* classified on the basis of standard morphological features, may display different molecular profiles. The discovery of molecular alterations and/or markers of the *in vitro* cell transformation process will open the way to a deeper molecular characterization of *foci* and will lead to the identification of a number of quantitative parameters to be applied in CTAs. This characterization will be useful for the improvement of the assay, the comprehension of the *in vivo* carcinogenic process, and to fulfil the specific requests of EURL ECVAM 2012.

A future expansion of the present study will be the molecular characterization of other receptor tyrosine kinase pathways: in fact, our data, showing a deregulation of the MAPK and of the PI3K/PTEN/AKT pathways (which are shared by a number of receptor tyrosine kinases) and the absence of EGFR deregulation, clearly indicate that other receptor tyrosine kinases (such as HER2, HER3, HER4), which are expressed at different levels in various cell lines (Normanno et al., 2006) may be involved in cadmium-induced *foci*.

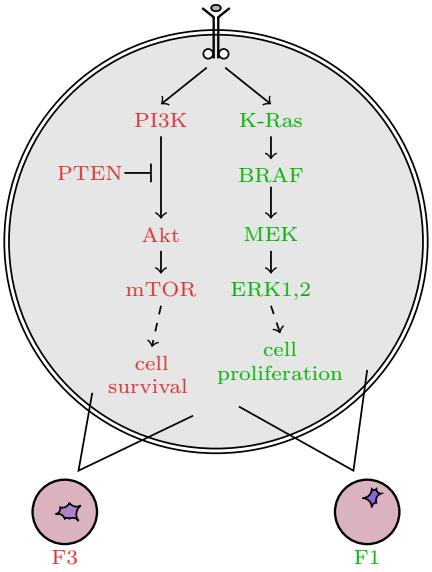

Figure 8.8: Graphical representation of the results. In two different clones of cadmium-induced transformed cells, two different pathways were found to be activated. Cells belonging to the clone called F3 showed an activation of the PI3K/Akt/mTOR pathway, known to be related to cell survival, while cells belonging to clone called F1 are supported by proliferative signals, due to the activation of MEK/ERK1,2 axis.

8.5 Conclusions

In conclusion, we suggest that cell clones derived from transformed *foci* obtained after the same treatment and classified by trained experts on the basis of standard morphological features (Ao et al., 2010), are characterized by different molecular pathways, survival or proliferation, both leading to uncontrolled cell growth (see Figure 8.8 for a summary of the results). As known, typical hallmarks of cancer include, among others, a sustained signalling for proliferation, immortalization, resistance to cell death, and evasion of growth suppression. Accumulated evidence suggests that the cellular and

molecular processes of the *in vivo* multistage carcinogenesis and the *in vitro* cell transformation are similar, and that the CTAs closely mimic the *in vivo* conversion of normal cells into the transformed phenotype (Combes et al., 1999; Sakai, 2007). Thus, the molecular characterization of cells from *foci* carrying a transformed phenotype is a key tool for CTAs improvement as well as crucial for the comprehension of the *in vivo* process, to investigate possible therapies and chemo-preventive properties of compounds. Our data along with those from the literature (Corvi et al., 2012; Urani et al., 2013; Annys et al., 2014) suggest that the CTAs should be further improved for their implementation in a regulatory context within a wider approach such as the Integrated Testing Strategy (ITS) for the prediction of carcinogenic potential in agreement with the 3Rs principles.

8.6 Bibliography

Annys, E., R. Billington, R. Clayton, K.-D. Bremm, et al. (2014). "Advancing the 3Rs in regulatory toxicology – Carcinogenicity testing: Scope for harmonisation and advancing the 3Rs in regulated sectors of the European Union". In: *Regulatory Toxicology and Pharmacology* 69.2, pp. 234–242.

Ao, L., J.-y. Liu, W.-b. Liu, L.-h. Gao, et al. (2010). "Comparison of gene expression profiles in BALB/c 3T3 transformed foci exposed to tumor promoting agents". In: *Toxicology in Vitro* 24.2, pp. 430–438.

Baselga, J. (2001). "The EGFR as a target for anticancer therapy–focus on cetuximab". In: *European Journal of Cancer (Oxford, England: 1990)* 37 (Suppl 4), S16–22.

Callegaro, G., F. M. Stefanini, A. Colacci, M. Vaccari, and C. Urani (2015). "An improved classification of foci for carcinogenicity testing by statistical descriptors". In: *Toxicology in Vitro* 29.7, pp. 1839–1850.

Choong, G., Y. Liu, and D. M. Templeton (2014). "Interplay of calcium and cadmium in mediating cadmium toxicity". In: *Chemico-Biological Interactions* 211, pp. 54–65.

Combes, R., M. Balls, and R. Curren (1999). "Cell Transformation Assay as Predictor of human carcinogenicity, ECVAM Workshop Report 39". In: *Alternatives to laboratory animals: ATLA* 27, pp. 745–767.

Corvi, R., M. J. Aardema, L. Gribaldo, M. Hayashi, et al. (2012). "ECVAM prevalidation study on in vitro cell transformation assays: General outline and conclusions of the study". In: *Mutation Research/Genetic Toxicology and Environmental Mutagenesis* 744.1, pp. 12–19.

Creton, S., M. J. Aardema, P. L. Carmichael, J. S. Harvey, et al. (2012). "Cell transformation assays for prediction of carcinogenic potential: state of the science and future research needs". In: *Mutagenesis* 27.1, pp. 93–101.

EURL ECVAM (2012). *EURL-ECVAM -Recommendation on three Cell Transformation Assays*.

Hartwig, A. (2013). "Metal interaction with redox regulation: an integrating concept in metal carcinogenesis?" In: *Free Radical Biology and Medicine* 55, pp. 63–72.

Hothorn, T., F. Bretz, and P. Westfall (2008). "Simultaneous inference in general parametric models". In: *Biometrical Journal. Biometrische Zeitschrift* 50.3, pp. 346–363.

IARC (2012). *IARC Monograph: arsenic, metals, fibres, and dusts (volume 100 C). A review of human Carcinogens. Lyone, France*.

Immervoll, H., D. Hoem, K. Kugarajh, S. J. Steine, and A. Molven (2006). "Molecular analysis of the EGFR-RAS-RAF pathway in pancreatic ductal adenocarcinomas: lack of mutations in the BRAF and EGFR genes". In: *Virchows Archiv: An International Journal of Pathology* 448.6, pp. 788–796.

Jing, Y., L.-Z. Liu, Y. Jiang, Y. Zhu, et al. (2012). "Cadmium increases HIF-1 and VEGF expression through ROS, ERK, and AKT signaling pathways and induces malignant transformation of human bronchial epithelial cells". In: *Toxicological Sciences* 125.1, pp. 10–19.

Jorissen, R. N., F. Walker, N. Pouliot, T. P. J. Garrett, et al. (2003). "Epidermal growth factor receptor: mechanisms of activation and signalling". In: *Experimental Cell Research* 284.1, pp. 31–53.

Krasinskas, A. M. (2011). "EGFR Signaling in Colorectal Carcinoma". In: *Pathology Research International* 2011.932932.

Laemmli, U. K. (1970). "Cleavage of structural proteins during the assembly of the head of bacteriophage T4". In: *Nature* 227.5259, pp. 680–685.

Landolph, J. R. (1985). "Chemical transformation in C3H 10T1/2 Cl 8 mouse embryo fibroblasts: historical background, assessment of the transformation assay, and evolution and optimization of the transformation assay protocol". In: *IARC scientific publications* 67, pp. 185–203.

Liu, Y.-C., H.-Y. Yen, C.-Y. Chen, C.-H. Chen, et al. (2011). "Sialylation and fucosylation of epidermal growth factor receptor suppress its dimerization and activation in lung cancer cells". In: *Proceedings of the National Academy of Sciences of the United States of America* 108.28, pp. 11332–11337.

Male, R., R. Bjerkvig, and J. R. Lillehaug (1987). "Biological and biochemical characterization of cell lines derived from initiation-promotion transformed C3H/1OT1/2 cells". In: *Carcinogenesis* 8.10, pp. 1375–1383.

Martelli, A., E. Rousselet, C. Dycke, A. Bouron, and J. M. Moulis (2006). "Cadmium toxicity in animal cells by interference with essential metals". In: *Biochimie*. Facets of Environmental Nuclear Toxicology 88.11, pp. 1807–1814.

Normanno, N., A. De Luca, C. Bianco, L. Strizzi, et al. (2006). "Epidermal growth factor receptor (EGFR) signaling in cancer". In: *Gene* 366.1, pp. 2–16.

OECD (2007). *Detailed Review Paper on Cell Transformation Assays for detection of chemical carcinogens - series on testing and assessment Number 31.*

– (2009). *Test Guideline 451 – Carcinogenicity studies. OECD Guidelines for the Testing of Chemicals.*

Osorio, F. (2014). *Heavy: Package for robust estimation using heavy-tailed distributions*. Version R Package Version 0, pp. 2–35.

Pinheiro, J. C. and D. M. Bates (2000). *Mixed-effects models in S and S-PLUS*. Springer Science & Business Media.

Pinheiro, J. C., D. M. Bates, S. DebRoy, D. Sarkar, and R Core Team (2015). *nlme: Linear and Nonlinear Mixed Effects Models*. Version R package version 3.1-120.

Priya, S., A. Nigam, P. Bajpai, and S. Kumar (2013). "Dysregulation of pathways involved in the processing of cancer and microenvironment information in MCA + TPA transformed C3H/10T1/2 cells". In: *In Vitro Cellular & Developmental Biology - Animal* 49.4, pp. 295–305.

R Core Team (2012). *R: A Language and Environment for Statistical Computing*. URL: http://www.R-project.org/.

Reznikoff, C. A., D. W. Brankow, and C. Heidelberger (1973). "Establishment and characterization of a cloned line of C3H mouse embryo cells sensitive to postconfluence inhibition of division". In: *Cancer Research* 33.12, pp. 3231–3238.

Rohrbeck, A., G. Salinas, K. Maaser, J. Linge, et al. (2010). "Toxicogenomics applied to in vitro carcinogenicity testing with Balb/c 3T3 cells revealed a gene signature predictive of chemical carcinogens". In: *Toxicological Sciences* 118.1, pp. 31–41.

Sakai, A. (2007). "BALB/c 3T3 cell transformation assays for the assessment of chemical car- cinogenicity". In: *Alternatives to Animal Testing and Experimentation: AATEX* 14.367.

Scion Corporation (2012). *Scion Image for Windows*.

Smith, P. K., R. I. Krohn, G. T. Hermanson, A. K. Mallia, et al. (1985). "Measurement of protein using bicinchoninic acid". In: *Analytical Biochemistry* 150.1, pp. 76–85.

Urani, C., R. Corvi, G. Callegaro, and F. Stefanini (2013). "Objective scoring of transformed foci in BALB/c 3T3 cell transformation assay by statistical image descriptors". In: *Toxicology in Vitro* 27.6, pp. 1905–1912.

Urani, C., F. M. Stefanini, L. Bussinelli, P. Melchioretto, and G. F. Crosta (2009). "Image analysis and automatic classification of transformed foci". In: *Journal of microscopy* 234.3, pp. 269–279.

Urani, C., P. Melchioretto, M. Bruschi, M. Fabbri, et al. (2015). "Impact of Cadmium on Intracellular Zinc Levels in HepG2 Cells: Quantitative Evaluations and Molecular Effects". In: *BioMed Research International* 2015.949514.

U.S. Department of Health and Human Services, Public Health Service Agency for Toxic Substances and Disease Registry (2012). *Toxicological Profile for Cadmium*.

Vanparys, P., R. Corvi, M. J. Aardema, L. Gribaldo, et al. (2012). "Application of in vitro cell transformation assays in regulatory toxicology for pharmaceuticals, chemicals, food products and cosmetics". In: *Mutation Research/Genetic Toxicology and Environmental Mutagenesis* 744.1, pp. 111–116.

Vasseur, P. and C. Lasne (2012). "OECD Detailed Review Paper (DRP) number 31 on "Cell Transformation Assays for Detection of Chemical Carcinogens": main results and conclusions". In: *Mutation Research/Genetic Toxicology and Environmental Mutagenesis* 744.1, pp. 8–11.

Venook, A. P. (2005). "Epidermal growth factor receptor-targeted treatment for advanced colorectal carcinoma". In: *Cancer* 103.12, pp. 2435–2446.

Zhen, Y., R. M. Caprioli, and J. V. Staros (2003). "Characterization of glycosylation sites of the epidermal growth factor receptor". In: *Biochemistry* 42.18, pp. 5478–5492.

9

Cadmium and the early response

In this Chapter the CTA model is further exploited to study early mechanisms of adverse outcome related to Cd-induced carcinogenicity.

Abstract

Cadmium (Cd) is a well recognized non-genotoxic carcinogen, but whose mechanisms of action are still not completely understood. In the effort to understand the early events responsible for Cd-induced carcinogenesis, we have used an *in vitro* biological system (the Cell Transformation Assay, CTA), that has been shown to closely model some key stages of the conversion of normal cells into malignant ones. Cd-triggered early responses in CTA were analyzed through microarray-based toxicogenomics, after 24 hours Cd administration and after 24 and 48 hours recovery. Results show that metallothioneines represent the earliest cell response, together with *Slc30a1* encoding for a ZnT-1 zinc exporter. Other genes were found to be upregulated in the first 24 hours following Cd administration: *Pip5k1a*, three isoforms of glutathione S-transferase (*Gsta 1-3*), and aldolase. In the recovery period, a number of genes expressing zinc proteins were found to be downregulated, amongst which many olfactory receptors (OR) coding genes. We also observed that Cd administration promotes massive Zn release inside the cell. On the whole our data suggest that, although early metallothionein and *GST* defense is effective in removing Cd, Zn release acts as signaling, leading to gene expression alterations which later induce metabolic alteration and eventually, transformation.

This Chapter is adapted from the submitted paper "Toxicogenomics applied to in vitro Cell Transformation Assay reveals mechanisms of early response to cadmium", Callegaro G., Forcella M., Melchioretto P., Frattini A., Gribaldo L., Fusi P., Fabbri M., Urani C.

9.1 Introduction

Cadmium (Cd) is a non-essential transition metal primarily released into the environment by anthropogenic activities. Approximately 30000 tons of Cd are released into the environment each year (Thévenod, 2009). Cd and Cd compounds find applications in the nickel-cadmium battery industry, in phosphate-based fertilizers, photovoltaic cells, nanomaterials (e.g. quantum dots) and cosmetic products for Cd's colour properties (Moulis et al., 2014; Bocca et al., 2014).

The human uptake of Cd is 5-10% in the gastrointestinal tract from ingestion of contaminated water, food crops (cereals and vegetables) and seafood, and 40-60% from inhaled particles in the respiratory tract (Maret and Moulis, 2013). The average Cd intake from food is generally between 8-25 µg/day, but could increase in certain Countries (Järup and Akesson, 2009). Inhalation of cigarette smoke is another way of heavy Cd exposure due to a natural Cd accumulation by tobacco leaves. Approximately 10% of inhaled cadmium oxide, generated during cigarette burning, is deposited in the lungs, and another 30-40% is absorbed into the systemic blood circulation (Talio et al., 2010). Most chemical forms of Cd are ionic, thus preventing passive diffusion through biological membranes. A variety of transmembrane proteins and mechanisms have been proposed to mediate Cd uptake. In mammals members of different transporters families (ZIP, NRAMP, voltage gated calcium channels) and endocytosis are considered ways for cellular Cd uptake (Moulis et al., 2014) thanks to its ability to mimic essential ions. Upon uptake in human tissues, Cd has a very long biological half-life, estimated to be of more than 26 years, partly because of its low excretion rate (U.S. Department of Health and Human Services, Public Health Service Agency for Toxic Substances and Disease Registry, 2012).

In 1993 and 2009, Cd and its inorganic compounds were recognized as

carcinogenic to humans by the International Agency for Research on Cancer (IARC, Group 1) mainly based on evidence for increased risks of lung cancer in occupationally exposed population (Hartwig, 2013). An updated literature on proposed and recognized mechanisms for Cd carcinogenesis is available (see for comprehensive reviews Hartwig, 2013; Thévenod, 2009). Cd genotoxicity is probably due to indirect mechanisms, mainly the induction of oxidative stress and interference with the DNA damage response and repair systems. For these reasons Cd is considered a co-mutagen and a non-genotoxic carcinogen. In addition, studies on signalling pathways alterations triggered by Cd revealed its ability to interfere with second messenger cascades, to affect gene transcription and microRNA regulation, to activate proliferative and survival signalling pathways that will promote carcinogenesis when not controlled by pro-apoptotic mechanisms (Thévenod, 2009; Fabbri et al., 2012; Forcella et al., 2016). Due to the multiple processes, pathways and cascades involved and altered by Cd, in 2009 Thévenod stressed the importance "to understand the chronology of signalling activation induced by Cd^{2+} because in general the first trigger determines subsequent events".

Stimulated by the scientific challenge of understanding early events responsible for Cd-induced carcinogenesis, we have used an *in vitro* biological system (the Cell Transformation Assay, CTA) that has been shown to closely model some key stages of the conversion of normal cells into malignant ones, like in the *in vivo* process (Landolph, 1985; OECD, 2007). The CTA is a powerful tool for mechanistic studies of carcinogenesis and it is the most advanced *in vitro* test for human carcinogenicity prediction induced by chemicals (Vanparys et al., 2012). Suitable cell lines are exposed to suspected carcinogens and, as a consequence of cell transformation, *foci* of transformed cells are formed after 4-6 weeks (Urani et al., 2009). We have previously performed CTA experiments to induce Cd cell transformation and to characterize different proliferative behaviours and activated pathways of Cd-transformed cells (Forcella et al., 2016, and Chapter 8). In this work, we exposed the same cell system (mouse embryo fibroblasts,

C3H10T1/2 Cl8 cells) to a low Cd concentration ($CdCl_2$ 1 μM, 24h) able to induce transformation. The analysis of early phases of response through microarray-based toxicogenomics allowed the identification of pathway-based toxicity profiles and the sequence of signalling activation that can be considered early markers of adverse outcomes related to the carcinogenesis process. In addition, mechanisms of Cd-triggered responses are analysed and discussed.

9.2 Materials and Methods

9.2.1 Cells culture and conditions

C3H10T1/2 clone 8 (C3H from here on) mouse embryonic fibroblasts (cell line ATCC, CCL 226 lot. n. 58078542) were selected for the experiments. This cell line was chosen as it represents one of the cell models suggested to be used in CTAs (OECD, 2007), for its high sensitivity to carcinogenic compounds and for its low spontaneous transformation rate. Hence, these cells are suitable models to study the mechanisms and early events of Cd-induced *in vitro* carcinogenicity. The cells were stored in ampoules, frozen at -80 °C with 10% sterile DMSO as a preservative. Cells were cultured in Basal Medium Eagle (BME, Sigma Chemical Co., St. Louis, MO, USA) enriched with 10% heat-inactivated fetal bovine serum (FBS, Euroclone, Pero, Italy), 1% glutamine, 0.5% HEPES 2 M and 25 μg/mL gentamicin (all purchased from Sigma) at 37 °C in a humidified incubator supplied with a constant flow of 5% CO_2 in air throughout each experiment. Cells were routinely seeded in 100 mm ∅ Petri dishes, the medium was changed every 3 days and cells were grown until 80% confluence maximum was reached to avoid an increase of the spontaneous transformation rate.

9.2.2 Treatments and samples preparation

For RNA extraction, the cells were seeded at a density of 10^6 cells/dish in 100 mm ∅ Petri dish, two Petri dish for each treatment. For SDS-PAGE and Western blotting, cells were seeded at a density of $2*10^6$ cells/flask in 162 cm^2 growth area flasks, three flasks for each treatment. The cells were exposed 24 hours after seeding to 1 μM $CdCl_2$ (Cd) for 24 hours, by changing the medium with an enriched medium with 1μM $CdCl_2$. Previous experiments performed by our group (Urani et al., 2009; Forcella et al., 2016) demonstrated that 1μM $CdCl_2$, which is below the cytotoxicity threshold (IC50 of 2.4 μM), is able to induce the formation of transformed colonies (*foci*) in the Cell Transformation Assay. The stock solution (1 mM) of $CdCl_2$ (97% purity BDH Laboratory, Milan, Italy) was prepared in ultrapure water (0.22 μm filtered Milli-Q water, Millipore, Vimodrone, Milan, Italy) and stored at 4 °C.

Controls, treated, and recovered samples were obtained as follows:

- CTR24: control samples exposed to complete medium only and harvested at the end of 24 hours of Cd treatment (control reference for Cd 24 hours);
- CTR48: control samples exposed to complete medium only and harvested at the end of all recovery times (control reference for Cd24R and Cd48R);
- Cd24h: samples harvested after 24 hours of Cd treatment;
- Cd24R: samples treated for 24 hours with Cd and collected after 24 hours of recovery in control medium;
- Cd48R: samples treated for 24 hours with Cd and collected after 48 hours of recovery in control medium.

9.2.3 RNA extraction and purification

Cells from each sample type were harvested by trypsinisation and lysed in 300 µl RLT buffer (Qiagen, Germantown, MD, USA) added with 1:100 β-mercaptoethanol. Homogenates were obtained by passing 5 times through a blunt 20-gauge needle fitted to a syringe. Samples were stored at -80°C until RNA extraction was carried out. Three independent replicates of sample Cd24h were performed. RNA was purified from C3H10T1/2 cells using the RNeasy Plus kit (Qiagen, Germantown, MD, USA). RNA was quantified using a ND-1000 UV-Vis Spectrophotometer (NanoDrop Technologies), and the integrity of the RNA was assessed with the Agilent 2100 Bioanalyzer (Agilent), according to the manufacturer's instructions. RNA samples used in this study all had a 260/280 ratio above 1.9 and a RNA Integrity Number (RIN) above 9.0.

9.2.4 Microarray expression profiling

In the microarray experiments, all sample-labeling, hybridization, washing, and scanning steps were conducted following the manufacturer's specifications. In brief, Cy3-labeled cRNA was generated from 500 ng input total RNA using Quick Amp Labeling Kit, One-color (Agilent). For every sample, 1.65 µg cRNA from each labeling reaction (with a specific activity above 9.0) was hybridized using the Gene Expression Hybridization Kit (Agilent) to the SurePrint G3 Mouse GE 8×60K Microarray (G4852, Agilent), which is a 8×60k 60mer slide format. After hybridization, the slides were washed and then scanned with the Agilent G2565BA Microarray Scanner (Agilent). The fluorescence intensities on scanned images were extracted and preprocessed by Agilent Feature Extraction Software (v10.5.1.1). Quality control and array normalization was performed in the R

statistical environment using the Agi4×44PreProcess package downloaded from the Bioconductor web site (Gentleman et al., 2004). The normalization and filtering steps were based on those described in the Agi4×44PreProcess reference manual.

In order to detect expression differences among different cell populations a moderate t test was applied. Moderated t statistics were generated by the Limma Bioconductor package. Modulated genes were chosen as those with a fold change greater than 1 or smaller than -1 and a false discovery rate (Benjamini and Hochberg's method) corrected p-value smaller than 0.05 (Smyth, 2004). Cd24R and Cd48R modulated genes were chosen as those with a fold change greater than 2 or smaller than -2. All of the above computations were conducted using the R statistics programming environment.

Differentially Expressed Genes (DEGs), namely up-regulated and down-regulated genes, were analyzed in the KEGG and GO databases to identify genes with similar functions. Enrichment analyses were conducted online using WebGestalt (J. Wang et al., 2013), selecting GO categories and KEGG pathways with a p-value lower than 0.05 in a hypergeometric test.

9.2.5 Preparation of cell extracts and MTs immunoblotting

Cells were harvested by trypsinisation at the end of treatment and recovery periods, washed with ice-cold PBS by centrifugation and lysed in 10 mM Tris-HCl buffer (pH 7), containing 5mM EDTA, 1 mM PMSF and protease inhibitors. The cell suspension was immediately frozen (-20°C) for 10-15 min for cell lysis and homogenisation. Samples were then ultracentrifuged (20000 ×g for 45 min.) to separate low molecular weight proteins, and a small aliquot of the supernatans (clarified samples) were analysed for protein content by the Bradford assay (Bradford, 1976). The remaining volume of clarified samples was resuspended 1:1 in sample buffer (0.25 M Tris-HCl, pH 6.8, 2%

SDS, 30% glycerol, 10% β-mercaptoethanol, 0.01% bromophenol blue) and stored at -20°C.

Proteins (20 µg) were separated by SDS-PAGE in 12% NuPage gels (Invitrogen), and gels of separated proteins were equilibrated for 20 min with transfer buffer (CAPS buffer: 10 mM 3-cyclohexylamino-1-propanesulfonic acid pH 10.8 in 10% methanol containing 2mM $CaCl_2$). Western blotting procedures were performed according to previously published protocols (Urani et al., 2007) using a mouse anti-metallothionein antibody (1:1000, Zymed, Invitrogen Corporation) that reacts with both MT-1 and MT-2 isoforms.

Densitometric data from Western blot were analysed as follows. Three biological replicates and at least four technical replicates were performed. Densitometric values for each sample were normalized to the loading control (tubulin). Samples were compared to their reference controls. Cd24h-CTR24 contrast was tested by Student's t-test, while all recovered sample-CTR48 contrasts were tested by Dunnet multiple comparison procedure. Calculations were performed in R (R Core Team, 2012) using the heavy package (Osorio, 2014) and multcomp package (Hothorn et al., 2008). The results are expressed as fold-change versus each control in a graphical summary.

9.2.6 Visualization of free Zn by fluorescent probe Zinquin

Cells were seeded in complete medium on sterile glass coverslips in 35 mm culture plates (60.000 cells/plate). The medium was changed 24 hours after seeding and substituted with 50 µM $ZnSO_4$ (Zn)- or 1 µM Cd-containing medium. At the end of treatment time (24 hours), all samples were processed according to Urani et al., (2015) for labile Zn intracellular visualization by Zinquin [ethyl (2-methyl-8-p-toluenesulphonamido-6-quinolyloxy)acetate] (Sigma Aldrich, Italy) a permeable probe, essentially non fluorescent until it complexes with Zn with a high selectivity. The cells were washed in warm PBS

and fixed (formaldehyde 3.7% in PBS, 30 min, 37°C). After removing the excess of fixative by PBS washing, the cells were incubated in the dark (30 min. 37°C) with Zinquin to a final concentration of 25 μM. The slides were then washed, air dried and mounted using glycerol and PBS (9:1). The presence of intracellular Zn was viewed under a fluorescent microscope (Zeiss Axioplan) equipped with UV filter set. Images were acquired by a digital camera (CoolSnap-ProColors Media Cybernetics, Bethesda, MA, USA) and stored by Image Proplus software (Media Cybernetics).

9.3 Results

9.3.1 Differentially expressed genes upon Cd exposure

Genes expression profiles of the three treatments and control group were analysed using an Agilent Mus musculus genome microarray. A summary of differentially expressed genes (DEGs) between treated and control samples is shown in the Venn Diagram in Figure 9.1A.

In the comparison between Cd24h and control samples, 13 DEGs were identified, interestingly all the genes are up-regulated. On the other hand, 47 DEGs were identified in the comparison Cd24R versus control and 49 DEGs for the Cd48R versus control. A different proportion of up- and down- regulated genes were identified in the two sets. Namely, in Cd24R sample 12 genes were found to be up-regulated, and 35 down-regulated, while in Cd48R the majority of DEGs were down-regulated (4 up- and 45 down-regulated). The Top 15 up-regulated genes (if present) and Top 15 down-regulated genes (if present) are shown in Table 9.1, 9.2 and 9.3 for the 24h treated sample and the recovered samples. Overlapping genes were found in different comparison, and showed consistent patterns (Figure 9.1A): Cd24h and Cd24R samples showed 3 up-regulated DEGs in common;

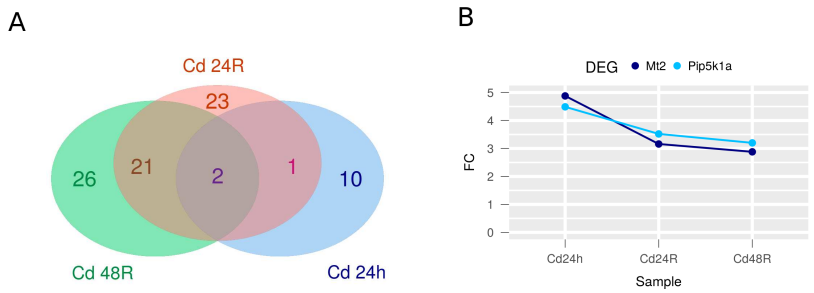

Figure 9.1: The Differentially Expressed Genes (DEGs) upon Cd exposure: the Venn Diagram and the two common DEGs. A. The Venn Diagram of DEGs in samples treated with $CdCl_2$ for 24h (in blue), and samples recovered after 24h treatment, respectively, other 24h (in salmon) and 48h (in green). The number of genes that are shared between different samples are showed in the overlapping regions of diagram. B. Graphs of the fold change values of the three genes deregulated in all three samples.

Cd24R and Cd48R samples shared 23 DEGs, all down-regulated ($R^2 = 0.983$ in a simple regression).

The three analyses shared two DEGs, namely *Mt2* and *Pip5k1a*, all up-regulated and with consistent descending trends: the highest up-regulation could be observed at the end of the Cd-treatment (Cd24h), dampened during recovery phases (Figure 9.1B). In addition, *Mt2* and *Pip5k1a* were found to be among the top up-regulated genes in all three samples. The 24h Cd-treated sample (Cd24h) also showed a remarkable *Mt1* up-regulation, together with three genes encoding for three isoforms of glutathione S-transferase (*Gsta1-3*), Gstα3 being still upregulated after 24 hours recovery. GSTs are a family of multifunctional proteins involved in phase II metabolism and detoxification of electrophilic xenobiotics, such as anti-cancer drugs, chemical carcinogens and environmental pollutants (Hayes et al., 2005). Overexpression of GSTs in mammalian tumour cells has also been implicated with resistance to various anticancer agents and chemical carcinogens. Furthermore, induction of GSTs expression is also an evolutionarily conserved response of cells to oxidative stress.

It appears that GSTs have evolved to eliminate many types of toxic compounds with the necessity of broad specificity resulting in low affinity for co-substrates, but compensated by a very high enzyme concentration in cell. GSTs work *in vivo* under unusual conditions of $[substrate] << [enzyme]$; since only deprotonated GSH is bound by the enzyme, GSTs lower GSH pK, and act as chemical machines increasing effective concentration of reactive GSH thiolate, speeding its interaction with many toxic compounds (Fabrini et al., 2011).

Table 9.1: List of Top 15 up- regulated genes in 24h Cd-treated samples (Cd24h). DEGs are listed in descending order of fold change compared to control. For each DEG, gene ID, the symbol and a description of the gene are provided. Only 13 DEGs were found in 24h treated samples, and all of them are up-regulated compared to control.

Top Gene	Gene ID	Symbol	Description	Fold Change
1	17750	Mt2	metallothionein 2	4.88
2	18720	Pip5k1a	phosphatidylinositol-4-phosphate 5-kinase, type 1 alpha	4.49
3	17748	Mt1	metallothionein 1	4.10
4	100042314	Gm10639	predicted gene 10639	3.30
5	14857	Gsta1	glutathione S-transferase, alpha 1 (Ya)	3.22
6	107849	Prl2c5	prolactin family 2, subfamily c, member 5	3.18
7	14858	Gsta2	glutathione S-transferase, alpha 2 (Yc2)	3.08
8	23886	Gdf15	growth differentiation factor 15	2.00
9	14859	Gsta3	glutathione S-transferase, alpha 3	1.83
10	12776	Ccr8	chemokine (C-C motif) receptor 8	1.82

Table 9.1: continues in next page

Table 9.1: continues from previous page

Top Gene	Gene ID	Symbol	Description	Fold Change
11	22782	Slc30a1	solute carrier family 30 (zinc transporter), member 1	1.52
12	11676	Aldoc	aldolase C, fructose-bisphosphate	1.42
13	319269	A130040M12Rik	RIKEN cDNA A130040M12 gene	1.29

Table 9.1: end of table

Together, these results indicate the importance of chelation of metals and response to oxidative stress processes in particular at the beginning of the response to Cd. See section 9.3.2 for a deeper description about the response of metallothioneins after Cd-induced insult.
The up-regulation of Phospatidylinositol-4-phospate 5-kinase alpha (*Pip5k1a*) can have a multifaceted interpretation. Pip5k1a catalyzes the phosphorylation of phosphatidylinositol 4-phosphate (PtdIns(4)P) to form phosphatidylinositol 4,5 bisphosphate (Ptdins(4,5)P_2). PtdIns(4,5)P_2 acts as a second messenger and is a substrate for several key reactions. e.g. PhospholipaseC (PLC) metabolizes it into inositol(1,4,5)triphosphate (IP_3), involved in the increase in intracellular Ca^{2+} levels (Gericke et al., 2013). PtdIns(4,5)P_2 as a second messenger can also interact with several proteins that regulate actin cytoskeleton (Bout and Divecha, 2009). In addition Pip5k1a has nuclear activities related to oxidative stress: the enzyme can interact with Star-PAP (PtdIns4,5P_2 -regulated nuclear poly(A) polymerase) in the nucleus and together they can control the stability of a subset of mRNAs regulated in response to oxidative stress (Li et al., 2013). Hence, the up-regulation of *Pip5k1a* can be relevant for the spatial/temporal regulation of PtdIns(4,5)P_2 pool and its downstream regulated activities, as for the role of the enzyme itself.

Table 9.2: List of Top 15 up- and Top 15 down-regulated genes in 24h Cd-treated 24h recovered samples (Cd24R). DEGs are listed in descending order of fold change compared to control. For each DEG, gene ID, the symbol and a description of the gene are provided.

Top Gene	Gene ID	Symbol	Description	Fold Change
1	22270	Upk3a	uroplakin 3A	3.91
2	18720	Pip5k1a	phosphatidylinositol-4-phosphate 5-kinase, type 1 alpha	3.52
3	627191	Tmem90a	transmembrane protein 90a	3.24
4	17750	Mt2	metallothionein 2	3.16
5	258291	Olfr1167	olfactory receptor 1167	2.87
6	234673	Ces2e	carboxylesterase 2E	2.87
7	630994	Gm9782	predicted pseudogene 9782	2.87
8	258377	Olfr654	olfactory receptor 654	2.69
9	51885	Tubgcp4	tubulin, gamma complex associated protein 4	2.33
10	83433	Trem2	triggering receptor expressed on myeloid cells 2	2.21
11	70362	1700007I08Rik	RIKEN cDNA 1700007I08 gene	2.12
12	14859	Gsta3	glutathione S-transferase, alpha 3	2.08
-15	319984	Jph4	junctophilin 4	-2.25
-14	271375	Cd200r2	Cd200 receptor 2	-2.29
-13	239618	Pdzrn4	PDZ domain containing RING finger 4	-2.3
-12	226154	Lzts2	leucine zipper, putative tumor suppressor 2	-2.36

Table 9.2: continues in next page

Table 9.2: continues from previous page

Top Gene	Gene ID	Symbol	Description	Fold Change
-11	56015	Olfr71	olfactory receptor 71	-2.37
-10	228543	Rhov	ras homolog gene family, member V	-2.42
-9	19014	Med1	mediator complex subunit 1	-2.45
-8	276950	Slfn8	schlafen 8	-2.47
-7	545192	Baiap3	BAI1-associated protein 3	-2.52
-6	100048534	Wdr96	WD repeat domain 96	-2.55
-5	103711	Pnpo	pyridoxine 5'-phosphate oxidase	-2.55
-4	244667	Disc1	disrupted in schizophrenia 1	-2.64
-3	105653	Phyhip	phytanoyl-CoA hydroxylase interacting protein	-3.02
-2	58176	Rhbg	Rhesus blood group-associated B glycoprotein	-3.09
-1	73744	Man2c1	mannosidase, alpha, class 2C, member 1	-5.3

Table 9.2: end of table

Finally, *Slc30a1*, encoding for the plasma membrane ZnT-1 zinc exporter (Hardyman et al., 2016), was found to be among the top 15 up-regulated genes in Cd24h sample (1.52 fold change), but not in the later phases of response. On the other hand, recovery phases were characterized by several downregulated, genes e.g. *Man2c1*, encoding for a mannosidase alpha, involved in the pathway of protein glycosilation and working with zinc as a cofactor (Kuntz et al., 2006). In the recovery period, 24 hours and 48 hours after cadmium administration, the expression of a number of olfactory receptors (ORs) was found to be altered. Two genes encoding ORs were found

upregulated, after 24 hours recovery, and five downregulated; this pattern was still evident after 48 hours recovery (Tables 9.2 and 9.3). Olfactory receptors are believed to be seven-helices transmembrane proteins, with an odorant binding site on the extracellular side and a G protein binding site on the cytoplasmic domain. Activation of the receptor by the odour ligand elicits a G protein-mediated increase in cAMP that triggers the opening of a cyclic nucleotide-gated channel (CNG) permeable to monovalent cations and calcium (Schild and Restrepo, 1998; Gold, 1999). Interestingly, the major role of the CNG channel is not to depolarize the cell, but rather to mediate a large increase in intracellular Ca^{2+}, leading to the opening of aCa^{2+}-activated Cl^{-} channel that causes cell depolarization.

Finally, the glycolytic enzyme aldolase was found to be upregulated after 24 hours treatment with cadmium, but not in the recovery period.

Table 9.3: List of Top 15 up- and Top 15 down- regulated genes in 24h Cd-treated 48h recovered samples (Cd48R). DEGs are listed in descending order of fold change compared to control. For each DEG, gene ID, the symbol and a description of the gene are provided.

Top Gene	Gene ID	Symbol	Description	Fold Change
1	18720	Pip5k1a	phosphatidylinositol-4-phosphate 5-kinase, type 1 alpha	3.2
2	17750	Mt2	metallothionein 2	2.88
3	234673	Ces2e	carboxylesterase 2E	2.2
4	75507	Pou5f2	POU domain class 5. transcription factor 2	2.13
-15	14810	Grin1	glutamate receptor, ionotropic, NMDA1 (zeta 1)	-2.22
-14	67320	Iqcf4	IQ motif containing F4	-2.27

Table 9.3: continues in next page

Table 9.3: continues from previous page

Top Gene	Gene ID	Symbol	Description	Fold Change
-13	258841	Olfr1107	olfactory receptor 1107	-2.27
-12	18363	Olfr62	olfactory receptor 62	-2.28
-11	18992	Pou3f2	POU domain, class 3, transcription factor 2	-2.32
-10	78795	Armc9	armadillo repeat containing 9	-2.33
-9	241116	Ccdc108	coiled-coil domain containing 108	-2.42
-8	103711	Pnpo	pyridoxine 5'-phosphate oxidase	-2.44
-7	234911	Mmp27	matrix metallopeptidase 27	-2.44
-6	100048534	Wdr96	WD repeat domain 96	-2.5
-5	226154	Lzts2	leucine zipper, putative tumor suppressor 2	-2.54
-4	214230	Pak6	p21 protein (Cdc42/Rac)-activated kinase 6	-2.68
-3	58176	Rhbg	Rhesus blood group-associated B glycoprotein	-3.15
-2	105653	Phyhip	phytanoyl-CoA hydroxylase interacting protein	-3.17
-1	73744	Man2c1	mannosidase, alpha, class 2C, member 1	-5.31

Table 9.3: end of table

9.3.2 MTs upregulation is the earliest response to Cd insult

Mammalian metallothioneins (MTs) are a family of intracellular low molecular weight proteins (approximately 6 kDa) mainly involved in metal detoxification and homeostasis (Babula et al., 2012). Our results clearly evidenced the early response of the cells after Cd insult by a primarily and immediate up-regulation the metallothioneins. As described by DEGs analysis (par. 9.3.1), *MTs* figure among the top regulated genes after 24 hours of Cd exposure, with a fold change of 4.10 and 4.88 for *MT-1* and *MT-2*, respectively (Table 9.1). Although *MTs* genes show a decreasing trend after Cd treatment (Figure 9.1B), high levels of *MTs* gene expression are maintained even after 48 hours of recovery (Cd48R), with *MT-2* being the second top up-regulated gene (2.88 fold change, Table 9.3). The microarray-based results on *MTs* expression were validated and confirmed by Western blot analyses (Figure 9.2) on metallothioneins protein (MT-1, -2) expression. MT-1 and -2 were highly and significantly (p-value <0.01) induced by exposure to Cd (Figure 9.2A, Cd24h sample). The protein levels, although decreased, were maintained significantly (p-value<0.01) above the constitutive levels of control (CTR48), even after 48 hours of recovery (Cd48R), as shown by protein expression (Figure 9.2A) and densitometric analysis (Figure 9.2B) .

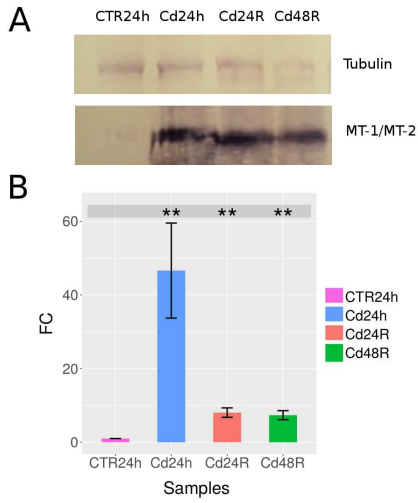

Figure 9.2: Western Blot analysis of Metallothioneins expression upon Cd exposure. A) Representative Western blotting performed on cell extracts, using anti-Metallothionein (reactivity MT1 and MT2). Tubulin was used as a loading control. The experiments were performed in three biological replicates and in, at least, four technical replicates. B) Quantification of protein expression rate was performed by densitometric analysis with Scion Image Software. Values are calculated as the MT/tubulin ratio; each ratio is normalized on MT/tubulin CTR: the 24h control (CTR24) for Cd24h sample, and the CTR48 control for recovered samples were used respectively. Bars and whiskers represent respectively means and standard errors for each fold ratio of each sample (** p-value <0.01).

9.3.3 Gene ontology and KEGG pathway analysis

WebGestalt was used to perform gene ontology (GO) term and KEGG pathway enrichment analysis. Our functional analysis revealed DEGs covering the three GO categories: biological process (BP), cellular component (CC), and molecular function (MF). We identified: 10 biological process (BP) terms and 4 molecular function (MF) terms significantly enriched in Cd24h; 10 biological process (BP) terms, 3 molecular function (MF) terms and 2 cellular com-

ponent (CC) terms significantly enriched in Cd24R, as well as 10 biological process (BP) terms, 10 molecular function (MF) terms and 10 cellular component (CC) terms significantly enriched in Cd48R (Figure 9.3).
GO terms related to ion homeostasis and to metal ion response were found to be particularly enriched in Cd24h (e.g. BP of zinc ion homeostasis, GO:0055069, and response to metal ion, GO:00100) whereas terms related to chemical homeostasis, to receptor activity and to microtubule cytoskeleton organization were most represented in Cd24R (e.g. BP of chemical and divalent inorganic cation homeostasis, GO:0048878, GO:0072507; MF of (olfactory) receptor activity GO:0004872, GO:0004984; and BP of microtubule skeleton organization, GO:0000226, and CC microtubule, GO:0005874). On the other hand, terms related to ion homeostasis, to signal transduction, to receptor activity were found in Cd48R (e.g. BP ion homeostasis, GO:0050801; MF signaling receptor/transducer activity GO:0038023, GO:0004871; and MF olfactory/G-protein coupled receptor activity, GO:0004984 and GO:0004930). Interestingly, we found that all GO terms identified in cells treated with cadmium for 24 hours (Cd24h) were significantly enriched by up-regulated genes.

GO terms were found to be enriched for both up- and down-regulated genes in Cd24R, whereas the most of GO terms identified in Cd48R were significantly enriched by down-regulated genes. Our data showed that overlapping GO terms between the three analysed samples are related to ion homeostasis, whereas Cd24R and Cd48R samples shared GO terms involved in receptor activity, particularly olfactory receptor activity (circles connected by a red line in Figure 9.3).

Our KEGG pathway enrichment analysis revealed that three pathways related to detoxification mechanisms, such as drug metabolism, metabolism of xenobiotics by cytochrome P450 and glutathione metabolism were significantly represented in Cd24h. In particular the two genes differentially expressed in KEGG glutathione metabolism pathway, are glutathione S-transferase alpha 2 and alpha 3 isoforms

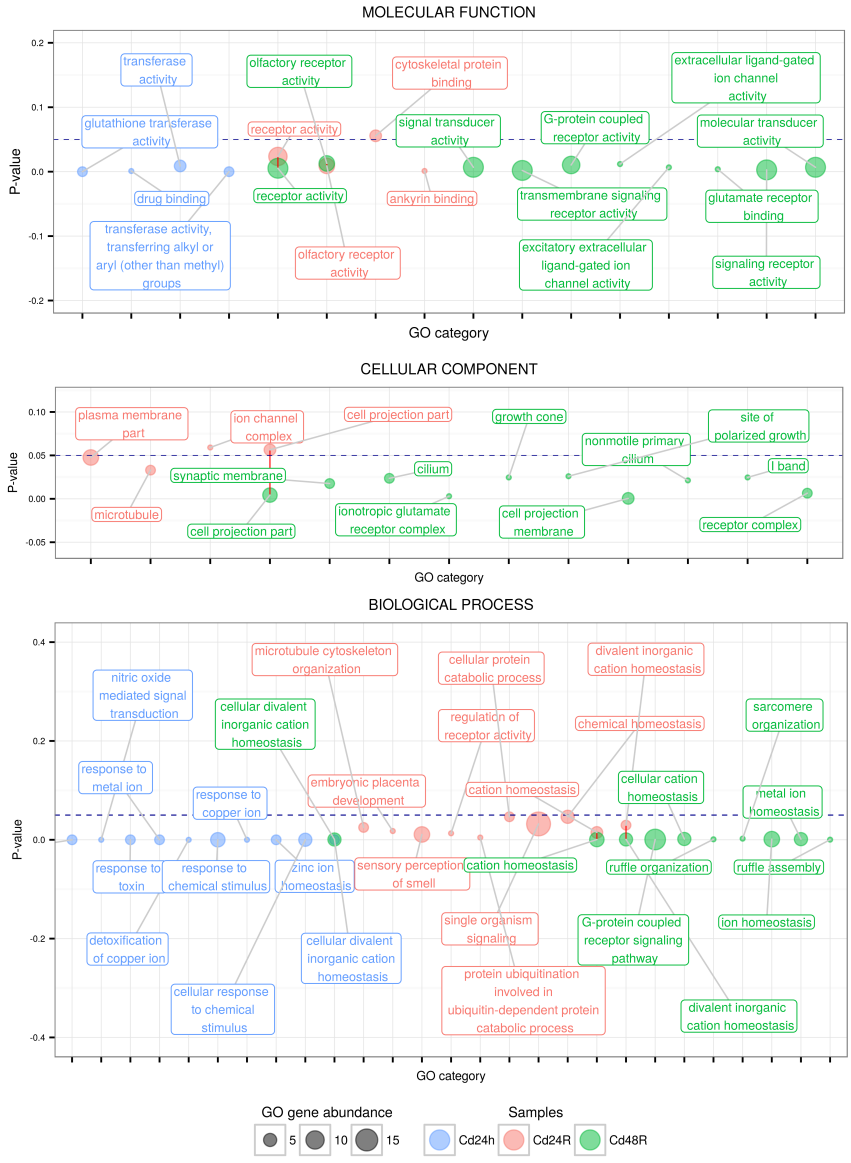

Figure 9.3: (Caption next page.)

Figure 9.3: (Previous page.) **Gene Ontology (GO) enriched categories in samples upon Cd exposure**. Gene Ontology enriched categories are shown in three panels, one for each sub-roots Molecular Function, Cellular Component and Biological Process. For each panel, enriched categories are displayed in circles: for each x unit a GO category is shown and its position on the y axis depends on its p-value from the hypergeometric test. The colour of circles reflect the sample type: blue for 24 hours treatment (Cd24h), salmon for 24 hours treatment followed by 24 hours of recovery (Cd24R), and green for 24 hours treatment followed by 48 hours of recovery (Cd48R). The size of circles is dependent on the abundance of DEGs in each category. The horizontal dashed line represents threshold value for significant p-values ($p < 0.05$). Overlapping GO between samples are connected by a red vertical line.

(Table 9.4).

Finally, only olfactory transduction pathway was significantly enriched in Cd24R, and a pathway related to neuroactive ligand-receptor interaction was found to be enriched in Cd48R.

Table 9.4: DEGs in KEGG pathways enriched in samples upon Cd exposure. For each enriched KEGG pathway are shown: the pathway ID, the pathway name, the number of total genes present in the KEGG pathway, the number of genes of the pathway differentially expressed in the considered samples. Asterisks next to DEGs number show p-values in the hypergometric test: *** $p < 0.001$, ** $p < 0.01$, . $p < 0.1$.

Pathway	Total genes	DEGs in Cd 24h	DEGs in Cd 24h+24R	DEGs in Cd 24h+48R
Drug metabolism - cytochrome P450 (ID 982)	66	2 (***)	0	0
Metabolism of xenobiotics by cytochrome P450 (ID 980)	58	2 (***)	0	0
Glutathione metabolism (ID 480)	45	2 (***)	0	0
Metabolic pathways (ID 1100)	1067	2	2	2

Table 9.4: continues in next page

Table 9.4: continues from previous page

Pathway	Total genes	DEGs in Cd 24h	DEGs in Cd 24h+24R	DEGs in Cd 24h+48R
Olfactory transduction (ID 4740)	903	0	7 (**)	5 (.)
Endocytosis (ID 4144)	203	0	2 (.)	2 (.)
Neuroactive ligand-receptor interaction (ID 4080)	268	0	0	4 (**)
Regulation of actin cytoskeleton (ID 4810)	209	0	0	2

Table 9.4: end of table

9.3.4 Increase of intracellular Zn in Cd-treated cells

Our toxicogenomics results and gene ontology analysis on differentially expressed genes revealed that ion homeostasis (zinc and divalent inorganic cation homostasis) represents one major biological process significantly activated in Cd and recovered samples (Figure 9.3). To investigate the effect of Cd on Zn homeostasis, we used the probe Zinquin. This fluorescent probe is extensively used as a chemosensor to study the role of intracellular Zn^{2+} in cellular biology, and provides also a tool to visualize the presence of free or labile zinc, where the term "labile" refers to all the Zn(II) freely available and sensed by Zinquin (Urani et al., 2015). In control cells (Figure 9.4), undetectable levels of free zinc were seen, as expected in well regulated biological systems. The exposure of the cells to 50 μM Zn, used as a positive control, showed the typical punctuate fluorescence of Zinquin-Zn binding, which has a decreasing trend at the longest recovery time. Interestingly, cells exposed to 1 μM Cd

show an increase of intracellular free zinc, still visible after 48 hours recovery.

9.4 Discussion

In the present work, we analysed by transcriptomic profiling the early phase of response (from right after the treatment, to 48 hours of recovery phase), to unravel pathways-based toxicity profiles that can be considered early markers of adverse outcomes related to cadmium-induced carcinogenicity.

By taking advantage of the experimental system of Cell Transformation Assay (CTA), we exposed C3H10T1/2 cells to a low Cd concentration able to induce the formation of *foci*, as previously assessed (Urani et al., 2009; Forcella et al., 2016). *Foci* are colonies of cells classified as fully transformed based on coded morphological features, and able to induce tumours when injected in suitable animal hosts (Reznikoff et al., 1973; LeBoeuf et al., 1999; OECD, 2007). Despite CTA regular use was limited, historically, to the detection of chemical-induced transformation, we believe that its usage could be improved including mechanistically-based information, related to both cellular and multicellular levels. CTA model shows the advantage of a strict relationship between adverse outcome (chemical-induced morphological transformation) and potential biomarker/molecular targets measurable during and at the end of transformation, thus reducing the risk of misinterpretation of ying/yang process involved both in tumorigenesis and cell defence e.g. cell death and immune system evasion (Khatami, 2008; Jacobs et al., 2016).

Transcriptomic profiling revealed sets of differentially expressed genes involved in several processes, that could be additionally grouped into two major categories: 1) processes related to metal ions trafficking and 2) processes associated with rearrangements of the cytoskeleton. Our transcriptome analysis also revealed that three members of the

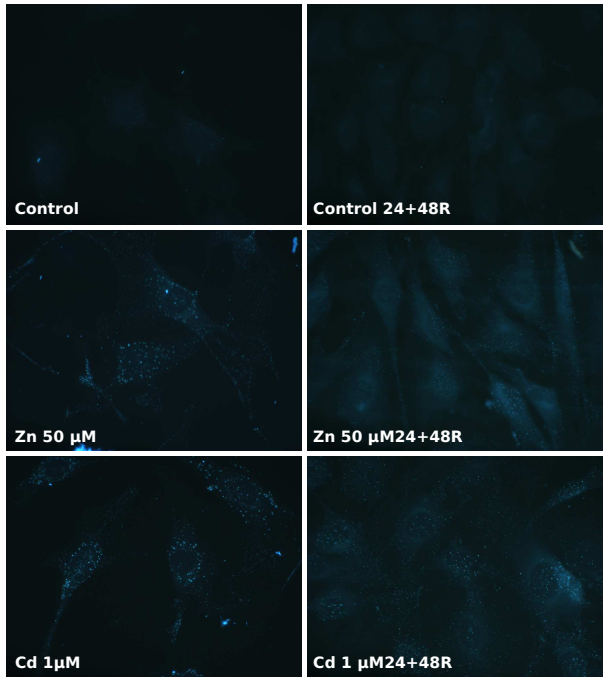

Figure 9.4: Visualization of labile zinc by the fluorescent probe Zinquin in C3H cells. Microscopy images show undetectable basal levels of loosely bound zinc in both control samples. Cells treated with 50 µM Zn after 24 hours and loaded with the zinc-specific fluorescent probe Zinquin show punctate intracellular fluorescence, that decreases after recovery, although still visible. The punctate pattern of the zinc-related fluorescence is highly evident also in Cd-treated cells, both at 24 hours of treatment and after recovery. Microscope magnification 400×.

GSTα family, *GSTα1*, *GSTα2* and *GSTα3* were upregulated after Cd administration. GSTs can metabolize a variety of xenobiotics, like cancer chemotherapeutic agents, insecticides, herbicides, carcinogens, and by-products of oxidative stress. In particular, type αGSTs also contribute, through their non-substrate binding activity, to intracellular transport, sequestration, and disposition of xenobiotics and hormones (Hayes et al., 2005). Moreover, GSTα2 has been reported to play a role in arsenic detoxification: GSTα2 upregulation was observed in wild type mice embryo cells, thus paralleling our data on cadmium (Qu and Waalkes, 2015).

In addition to protection towards oxidative stress and metal toxicity, other metal-related mechanisms are envisaged by our data. In our experimental system, *Pip5k1a*, *Mt1* and *Mt2*, *Slc30a1*, *Man2c1* and several olfactory receptors genes, were found to be regulated in response to 24 hours Cd treatment. Interestingly, *Pip5k1a*, human *Mt2* homologous genes and some human gene members of Slc30 transporters, Olfactory Receptors and mannosidases, are all predicted to be target of metal-responsive transcription factor 1 (MTF-1), by TRANSFAC Predicted Transcription Factor Targets dataset (Rouillard et al., 2016). MTF-1 is a zinc sensor and binds to the metal responsive element in target genes both as an activator and a repressor of their expression. Considering the relationship between Cd and MTF-1 activation, it is noteworthy to evidence that Cd was shown to regulate MTF-1 activity not by direct binding to the transcription factor, but through indirect mechanisms, e.g. by sensing the zinc displaced from Zn-binding proteins (Zhang et al., 2003; Waldron et al., 2009; Choi and Bird, 2014). Thus MTF-1 cannot be considered as a genuine Cd sensor (Moulis et al., 2014).
The *Slc30a1* gene, encoding for the zinc efflux protein ZnT-1, and the family members of MTs have been found to be directly regulated by MTF-1 (Hardyman et al., 2016). In addition, Zap1, a zinc-responsive transcription factor in *S.cerevisiae*, after Zn shock up-regulates the expression of ZRC1, the homologue mouse Slc30a1 gene. The regulation of this zinc transporter serves as a mechanism

to protect zinc-limited cells from a sudden exposure to high zinc (MacDiarmid et al., 2002). Very intriguingly, in a recently published work (Shusterman et al., 2017) the ZnT-1 transporter is described as a moonlighting protein, performing distinct and independent functions in zinc homeostasis: facilitates zinc efflux, and inhibits zinc (and calcium) influx through the L-type calcium channel, the latter probably mediated by the long cytoplasmic C-terminal of the protein. In addition, the C-terminal was shown to activate ERK proliferative signalling (Beharier et al., 2012), which is implicated in the carcinogenesis process (Krasinskas, 2011; Forcella et al., 2016). Considering the very narrow range of optimal zinc level for a cell, for which even a small deviation can trigger changes in genes expression to counter changes in cytosolic zinc level (Choi and Bird, 2014), and the above depiction on zinc transporters and the mechanisms of MTF-1 activation, we have hypothesized in C3H cells the involvement of zinc displacement in response to Cd treatment. Our microscopy results using the zinc-specific probe Zinquin clearly showed the presence of increased free zinc in Cd-treated cells. The mechanism of zinc-displacement and increase of labile-free zinc in Cd-treated cells was proposed in our previous works (Urani et al., 2010; Urani et al., 2015), and of other authors (Méplan et al., 1999; Babula et al., 2012). Overall, the fluorescence results along with our transcriptomic data strongly support the hypothesis of Cd-interference with zinc-proteins and of zinc-displacement from the zinc-proteome, leading to the increase of free zinc. Noteworthy, approximately 3200 proteins, that account for around 10% of the human proteome, require zinc to properly function, and among those zinc-proteins are transcription factors, tumour suppressor proteins, DNA repair proteins (Witkiewicz-Kucharczyk and Bal, 2006; Hartwig, 2013). In addition, zinc increase represents a second messenger, critical for cell growth that may play important roles in cancer etiology and outcome (Grattan and Freake, 2012). Recently, the involvement of zinc increase in cancer cells progression and aggressiveness has been demonstrated, in particular involving EGFR signalling activation

(Cheng et al., 2017; Pisano et al., 2017).

Another important result that suggests cadmium interference on zinc (divalent ions) homeostasis evidenced by our transcriptomic data is on the Olfactory receptors (ORs). ORs seem to play an important role in the recovery phases after Cd exposure in our cell system. Most of the genes appear to be downregulated, only two being upregulated, and there is a perfect correspondence between 24 hours and 48 hours recovery data, the same genes being upregulated and downregulated at both times. Although it may seem unlikely that C3H fibroblasts express olfactory receptors, these receptors have been found in a variety of cells other than olfactory neurons (Kang and Koo, 2012), like testis, blood, heart, pancreas, lung, kidney and brain cells. Moreover, while only one olfactory receptor (out of the 1000 and more coded in mouse) is expressed in each cell of the olfactory neuron in the olfactory epithelium, other tissues may violate this one cell-one receptor rule. It seems that more than one OR is expressed in one cell of testis and muscle, where they regulate cell adhesion (Fukuda and Touhara, 2006; Griffin et al., 2009).
Moreover, divalent metal ions, like Zn^{2+} and Cu^{2+} have been proposed to play a role in odorant recognition (J. Wang et al., 2003; Duan et al., 2012). According to Wang and colleagues (J. Wang et al., 2003), odorants binding to metal ion would disrupt the protein charge balance and lead to a structural rearrangement; this hypothesis accounts for the very high olfactory sensitivity for metal ion coordinating compounds, like thiol and amines. Technical difficulties in the expression and crystallization of olfactory receptors have so far hampered the elucidation of their molecular structure. However, copper has been recently reported to be required for robust ligand binding and activation of murine olfactory receptor MOR244-3 (Sekharan et al., 2014). Besides, clinical studies show that cadmium and nickel are the only metals whose compounds have been specifically associated with olfactory impairment (Sunderman, 2001). All our data on olfactory receptors and on perturbation of ions homeostasis triggered by Cd are in agreement with previously published

papers (see Moulis and Thévenod, 2010 for a review), although future studies should be devoted to investigate the direct mechanism.

Our results further evidence how Cd can influence the cytoskeletal organization. Low Cd^{2+} concentrations induce a fast transient increase of Ca^{2+} and Ins(1,4,5)P_3, mediated by binding to G-protein coupled receptors in the plasma membrane (Hartwig, 2013). *Pip5ka*, that was found in our samples to be upregulated in a time-dependent manner, is the major isoform responsible for the replenishment of PtdIns(4,5)P_2, after stimulation of G-protein coupled receptors in mice (Y. Wang et al., 2008). PtdIns(4,5)P_2 can also interact, as a second messenger, with several proteins that regulate actin cytoskeleton (Bout and Divecha, 2009).

Another interesting result found by our transcriptomic data is related to aldolase. This enzyme, the only one of the glycolytic pathway found to be upregulated after cadmium exposure, is also the only glycolytic enzyme whose knock-down leads to a decrease in cell proliferation (Ritterson and Tolan, 2012). This effect is not linked to aldolase activity within the glycolitic pathway. Aldolase has been implicated in several so called "moonlighting" functions, distinct from its role in glycolysis, including roles in signal transduction, vesicles trafficking and cell motility. Many of these functions involve interactions of aldolase with F-actin, a protein involved in cell division, where it is critical for formation of the cleavage furrow during cytokinesis. Data suggest that aldolase sustains cell proliferation through its actin-binding ability. In C3H cells, aldolase upregulation is likely related to the alteration of cytoskeletal organization which becomes apparent in the recovery period, with the upregulation of *Tubgcp4* and the downregulation of *Bicd2* and *Disc1*, all involved in the organization of microtubule cytoskeleton. The response of the cytoskeletal proteins to Cd insult deserves further investigation in consideration to the role of cytoskeletal rearrangements in the process of cell transformation (Albiges-Rizo et al., 2009).

9.5 Conclusions

The early response to cadmium exposure in our cell system accounts for a very limited number of genes (13, right after Cd treatment), and is characterized by mechanisms directly triggered by Cd^{2+} ions, but also involving interactions with the homeostasis of other divalent ions (Zn^{2+}, Ca^{2+}) and novel moonlighting activities of regulated genes (proteins), which in turn are again related to zinc homeostasis. Genes related to oxidative stress response and involved in rearrangements of cytoskeleton are other important players in the early response against cadmium treatment. As it could be expected, MTs and GST are the early responses activated in defence against cadmium, but these might not be sufficient to contrast side-effects of the metal. Among those side-effects we can highlight: 1) the recognised oxidative stress and interactions with the DNA damage response systems (see Hartwig, 2013 for a review), 2) the here demonstrated increase of free zinc, most likely due to displacement of zinc from zinc proteins and transcription factors and 3) the perturbation of zinc homeostasis as evidenced by our analyses on differentially expressed genes and gene ontology categories involved in early and recovered samples. All zinc-related functions and moonlighting functions evidenced in our work address the cells to signalling of uncontrolled growth and cytoskeletal rearrangements and to an environment favourable to transformation.

Considering that the dose investigated is able to induce a morphological transformation in the evaluated experimental system, an analysis of the early response could be representative of the general mechanisms activated by the cell as a protection from the insult. Failures in the evaluated response, as aberrations of protections systems, could be considered as the initial step of the adverse response.

9.6 Bibliography

Albiges-Rizo, C., O. Destaing, B. Fourcade, E. Planus, and M. R. Block (2009). "Actin machinery and mechanosensitivity in invadopodia, podosomes and focal adhesions". In: *Journal of Cell Science* 122.17, pp. 3037–3049.

Babula, P., M. Masarik, V. Adam, T. Eckschlager, et al. (2012). "Mammalian metallothioneins: properties and functions". In: *Metallomics* 4.8, pp. 739–750.

Beharier, O., S. Dror, S. Levy, J. Kahn, et al. (2012). "ZnT-1 protects HL-1 cells from simulated ischemia-reperfusion through activation of Ras-ERK signaling". In: *Journal of Molecular Medicine (Berlin, Germany)* 90.2, pp. 127–138.

Bocca, B., A. Pino, A. Alimonti, and G. Forte (2014). "Toxic metals contained in cosmetics: a status report". In: *Regulatory toxicology and pharmacology: RTP* 68.3, pp. 447–467.

Bout, I. van den and N. Divecha (2009). "PIP5K-driven PtdIns(4,5)P2 synthesis: regulation and cellular functions". In: *Journal of Cell Science* 122.21, pp. 3837–3850.

Bradford, M. M. (1976). "A rapid and sensitive method for the quantitation of microgram quantities of protein utilizing the principle of protein-dye binding". In: *Analytical Biochemistry* 72, pp. 248–254.

Cheng, X., L. Wei, X. Huang, J. Zheng, et al. (2017). "SLC39A6 Promotes Aggressiveness of Esophageal Carcinoma Cells by Increasing Intracellular Levels of Zinc, Activating Phosphatidylinositol 3-kinase Signaling, and Upregulating Genes That Regulate Metastasis". In: *Gastroenterology*.

Choi, S. and A. J. Bird (2014). "Zinc'ing sensibly: controlling zinc homeostasis at the transcriptional level". In: *Metallomics* 6.7, p. 1198.

Duan, X., E. Block, Z. Li, T. Connelly, et al. (2012). "Crucial role of copper in detection of metal-coordinating odorants". In: *Proceedings of the National Academy of Sciences of the United States of America* 109.9, pp. 3492–3497.

Fabbri, M., C. Urani, M. G. Sacco, C. Procaccianti, and L. Gribaldo (2012). "Whole genome analysis and microRNAs regulation in HepG2 cells exposed to cadmium". In: *ALTEX* 29.2, pp. 173–182.

Fabrini, R., A. Bocedi, K. F. Dawood, P. Turella, et al. (2011). "The extended catalysis of glutathione transferase". In: *FEBS letters* 585.2, pp. 341–345.

Forcella, M., G. Callegaro, P. Melchioretto, L. Gribaldo, et al. (2016). "Cadmium-transformed cells in the in vitro cell transformation assay reveal different proliferative behaviours and activated pathways". In: *Toxicology in Vitro* 36, pp. 71–80.

Fukuda, N. and K. Touhara (2006). "Developmental expression patterns of testicular olfactory receptor genes during mouse spermatogenesis". In: *Genes to Cells: Devoted to Molecular & Cellular Mechanisms* 11.1, pp. 71–81.

Gentleman, R. C., V. J. Carey, D. M. Bates, B. Bolstad, et al. (2004). "Bioconductor: open software development for computational biology and bioinformatics". In: *Genome Biology* 5.10, R80.

Gericke, A., N. R. Leslie, M. Lösche, and A. H. Ross (2013). "PtdIns(4,5)P2-mediated cell signaling: emerging principles and PTEN as a paradigm for regulatory mechanism". In: *Advances in Experimental Medicine and Biology* 991, pp. 85–104.

Gold, G. H. (1999). "Controversial issues in vertebrate olfactory transduction". In: *Annual Review of Physiology* 61, pp. 857–871.

Grattan, B. J. and H. C. Freake (2012). "Zinc and cancer: implications for LIV-1 in breast cancer". In: *Nutrients* 4.7, pp. 648–675.

Griffin, C. A., K. A. Kafadar, and G. K. Pavlath (2009). "MOR23 promotes muscle regeneration and regulates cell adhesion and migration". In: *Developmental Cell* 17.5, pp. 649–661.

Hardyman, J. E. J., J. Tyson, K. A. Jackson, C. Aldridge, et al. (2016). "Zinc sensing by metal-responsive transcription factor 1 (MTF1) controls metallothionein and ZnT1 expression to buffer the sensitivity of the transcriptome response to zinc". In: *Metallomics* 8.3, pp. 337–43.

Hartwig, A. (2013). "Cadmium and Cancer". In: *Cadmium: From Toxicity to Essentiality*. Ed. by A. Sigel, H. Sigel, and R. K. Sigel. Vol. 11. Dordrecht: Springer Netherlands, pp. 491–507.

Hayes, J. D., J. U. Flanagan, and I. R. Jowsey (2005). "Glutathione transferases". In: *Annual Review of Pharmacology and Toxicology* 45, pp. 51–88.

Hothorn, T., F. Bretz, and P. Westfall (2008). "Simultaneous inference in general parametric models". In: *Biometrical Journal. Biometrische Zeitschrift* 50.3, pp. 346–363.

Jacobs, M. N., A. Colacci, K. Louekari, M. Luijten, et al. (2016). "International regulatory needs for development of an IATA for non-genotoxic carcinogenic chemical substances". In: *ALTEX-Alternatives to Animal Experimentation* 33.4, pp. 359–392.

Järup, L. and A. Akesson (2009). "Current status of cadmium as an environmental health problem". In: *Toxicology and Applied Pharmacology* 238.3, pp. 201–208.

Kang, N. and J. Koo (2012). "Olfactory receptors in non-chemosensory tissues". In: *BMB reports* 45.11, pp. 612–622.

Khatami, M. (2008). "'Yin and Yang' in inflammation: duality in innate immune cell function and tumorigenesis". In: *Expert Opinion on Biological Therapy* 8.10, pp. 1461–1472.

Krasinskas, A. M. (2011). "EGFR Signaling in Colorectal Carcinoma". In: *Pathology Research International* 2011.932932.

Kuntz, D. A., H. Liu, M. Bols, and D. R. Rose (2006). "The role of the active site Zn in the catalytic mechanism of the GH38 Golgi alpha-mannosidase II: Implications from noeuromycin inhibition". In: *Biocatalysis and Biotransformation* 24.1, pp. 55–61.

Landolph, J. R. (1985). "Chemical transformation in C3H 10T1/2 Cl 8 mouse embryo fibroblasts: historical background, assessment of the transformation assay, and evolution and optimization of the transformation assay protocol". In: *IARC scientific publications* 67, pp. 185–203.

LeBoeuf, R. A., K. A. Kerckaert, M. J. Aardema, and R. J. Isfort (1999). "Use of Syrian hamster embryo and BALB/c 3T3 cell transformation for assessing the carcinogenic potential of chemicals". In: *IARC scientific publications* 146, pp. 409–425.

Li, W., R. S. Laishram, and R. A. Anderson (2013). "The novel poly(A) polymerase Star-PAP is a signal-regulated switch at the 3'-end of mRNAs". In: *Advances in Biological Regulation* 53.1, pp. 64–76.

MacDiarmid, C. W., M. A. Milanick, and D. J. Eide (2002). "Biochemical properties of vacuolar zinc transport systems of Saccharomyces cerevisiae". In: *The Journal of Biological Chemistry* 277.42, pp. 39187–39194.

Maret, W. and J.-M. Moulis (2013). "The bioinorganic chemistry of cadmium in the context of its toxicity". In: *Metal Ions in Life Sciences* 11, pp. 1–29.

Méplan, C., K. Mann, and P. Hainaut (1999). "Cadmium induces conformational modifications of wild-type p53 and suppresses p53 response to DNA damage in cultured cells". In: *The Journal of Biological Chemistry* 274.44, pp. 31663–31670.

Moulis, J.-M., J. Bourguignon, and P. Catty (2014). "Cadmium". In: *Binding, Transport and Storage of Metal Ions in Biological Cells*. RSC Metallobiology 2. The Royal Society of Chemistry.

Moulis, J.-M. and F. Thévenod (2010). "New perspectives in cadmium toxicity: an introduction". In: *BioMetals* 23.5, pp. 763–768.

OECD (2007). *Detailed Review Paper on Cell Transformation Assays for detection of chemical carcinogens - series on testing and assessment Number 31.*

Osorio, F. (2014). *Heavy: Package for robust estimation using heavy-tailed distributions.* Version R Package Version 0, pp. 2–35.

Pisano, A., M. F. Santolla, E. M. De Francesco, P. De Marco, et al. (2017). "GPER, IGF-IR, and EGFR transduction signaling are involved in stimulatory effects of zinc in breast cancer cells and cancer-associated fibroblasts". In: *Molecular Carcinogenesis* 56.2, pp. 580–593.

Qu, W. and M. P. Waalkes (2015). "Metallothionein blocks oxidative DNA damage induced by acute inorganic arsenic exposure". In: *Toxicology and Applied Pharmacology* 282.3, pp. 267–274.

R Core Team (2012). *R: A Language and Environment for Statistical Computing*. URL: http://www.R-project.org/.

Reznikoff, C. A., D. W. Brankow, and C. Heidelberger (1973). "Establishment and characterization of a cloned line of C3H mouse embryo cells sensitive to postconfluence inhibition of division". In: *Cancer Research* 33.12, pp. 3231–3238.

Ritterson, C. and D. R. Tolan (2012). "Targeting of several glycolytic enzymes using RNA interference reveals aldolase affects cancer cell proliferation through a non-glycolytic mechanism". In: *The Journal of Biological Chemistry* 287.51, pp. 42554–42563.

Rouillard, A. D., G. W. Gundersen, N. F. Fernandez, Z. Wang, et al. (2016). "The harmonizome: a collection of processed datasets gathered to serve and mine knowledge about genes and proteins". In: *Database: The Journal of Biological Databases and Curation* 2016.

Schild, D. and D. Restrepo (1998). "Transduction mechanisms in vertebrate olfactory receptor cells". In: *Physiological Reviews* 78.2, pp. 429–466.

Sekharan, S., M. Z. Ertem, H. Zhuang, E. Block, et al. (2014). "QM/MM model of the mouse olfactory receptor MOR244-3 validated by site-directed mutagenesis experiments". In: *Biophysical Journal* 107.5, pp. L5–8.

Shusterman, E., O. Beharier, S. Levy, R. Zarivach, et al. (2017). "Zinc transport and the inhibition of the L-type calcium channel are two separable functions of ZnT-1". In: *Metallomics*.

Smyth, G. K. (2004). "Linear models and empirical bayes methods for assessing differential expression in microarray experiments". In: *Statistical Applications in Genetics and Molecular Biology* 3, Article3.

Sunderman, F. W. (2001). "Nasal toxicity, carcinogenicity, and olfactory uptake of metals". In: *Annals of Clinical and Laboratory Science* 31.1, pp. 3–24.

Talio, M. C., M. O. Luconi, A. N. Masi, and L. P. Fernández (2010). "Cadmium monitoring in saliva and urine as indicator of smoking addiction". In: *The Science of the Total Environment* 408.16, pp. 3125–3132.

Thévenod, F. (2009). "Cadmium and cellular signaling cascades: to be or not to be?" In: *Toxicology and Applied Pharmacology* 238.3, pp. 221–239.

Urani, C., P. Melchioretto, C. Canevali, F. Morazzoni, and L. Gribaldo (2007). "Metallothionein and hsp70 expression in HepG2 cells after prolonged cadmium exposure". In: *Toxicology in vitro* 21.2, pp. 314–319.

Urani, C., P. Melchioretto, and L. Gribaldo (2010). "Regulation of metallothioneins and ZnT-1 transporter expression in human hepatoma cells HepG2 exposed to zinc and cadmium". In: *Toxicology in vitro* 24.2, pp. 370–374.

Urani, C., F. M. Stefanini, L. Bussinelli, P. Melchioretto, and G. F. Crosta (2009). "Image analysis and automatic classification of transformed foci". In: *Journal of microscopy* 234.3, pp. 269–279.

Urani, C., P. Melchioretto, M. Bruschi, M. Fabbri, et al. (2015). "Impact of Cadmium on Intracellular Zinc Levels in HepG2 Cells: Quantitative Evaluations and Molecular Effects". In: *BioMed Research International* 2015.949514.

U.S. Department of Health and Human Services, Public Health Service Agency for Toxic Substances and Disease Registry (2012). *Toxicological Profile for Cadmium*.

Vanparys, P., R. Corvi, M. J. Aardema, L. Gribaldo, et al. (2012). "Application of in vitro cell transformation assays in regulatory toxicology for pharmaceuticals, chemicals, food products and cosmetics". In: *Mutation Research/Genetic Toxicology and Environmental Mutagenesis* 744.1, pp. 111–116.

Waldron, K. J., J. C. Rutherford, D. Ford, and N. J. Robinson (2009). "Metalloproteins and metal sensing". In: *Nature* 460.7257, pp. 823–830.

Wang, J., Z. A. Luthey-Schulten, and K. S. Suslick (2003). "Is the olfactory receptor a metalloprotein?" In: *Proceedings of the National Academy of Sciences of the United States of America* 100.6, pp. 3035–3039.

Wang, J., D. Duncan, Z. Shi, and B. Zhang (2013). "WEB-based GEne SeT AnaLysis Toolkit (WebGestalt): update 2013". In: *Nucleic Acids Research* 41 (Web Server issue), W77–W83.

Wang, Y., X. Chen, L. Lian, T. Tang, et al. (2008). "Loss of PIP5KIbeta demonstrates that PIP5KI isoform-specific PIP2 synthesis is required for IP3 formation". In: *Proceedings of the National Academy of Sciences of the United States of America* 105.37, pp. 14064–14069.

Witkiewicz-Kucharczyk, A. and W. Bal (2006). "Damage of zinc fingers in DNA repair proteins, a novel molecular mechanism in carcinogenesis". In: *Toxicology Letters* 162.1, pp. 29–42.

Zhang, B., O. Georgiev, M. Hagmann, C. Günes, et al. (2003). "Activity of metal-responsive transcription factor 1 by toxic heavy metals and H2O2 in vitro is modulated by metallothionein". In: *Molecular and Cellular Biology* 23.23, pp. 8471–8485.

10

Conclusions and Outlook

This Chapter provides a perspective summary of the results obtained in this thesis, and describes future developments of the presented methods and results.

Contents

10.1 Summary

The assessment of chemical carcinogenesis for both chemical risk assessment and drug development is a key issue to be addressed in order to obtain a better knowledge on carcinogenesis induced by chemicals, and to ensure conditions of a more and more safe human life.

CTAs can provide useful information to the assessment of chemical carcinogenesis for what concerns the cell and tissue levels, are cost efficient and can be performed in a shorter period of time, compared to rodent bioassays. The results and the conclusions described in this thesis widen the body of evidence that CTAs are valuable techniques to be exploited for chemical carcinogenicity testing.

Results of the two parts of this thesis are now summarized respectively in two paragraphs, the first one analysing advancements in the scoring phase of CTA, obtained through digital image analysis of *foci* images, and subsequent applied models (*in silico* refinement). The second paragraph summarizes results pointing towards the improvement of *in vitro* carcinogenesis understanding, analysing processes occurring during subsequent phases of *in vitro* transformation induced by a recognized carcinogen (cadmium).

***In silico* refinement.** Digital image analysis is a powerful tool for cell biology studies, since it can provide objective and fully reproducible data related to cell morphology. The latter, is finally related to biochemical and molecular events.

CTA's final phase of *foci* scoring relies on coded morphological criteria, it is prone to subjectivity and it is not quantitative. We hence applied techniques of image analysis in order to obtain an automated and objective classification of *foci*.

We worked on a large and reliable database, comprising more than two thousand *foci* images, of high spatial and color resolution, and

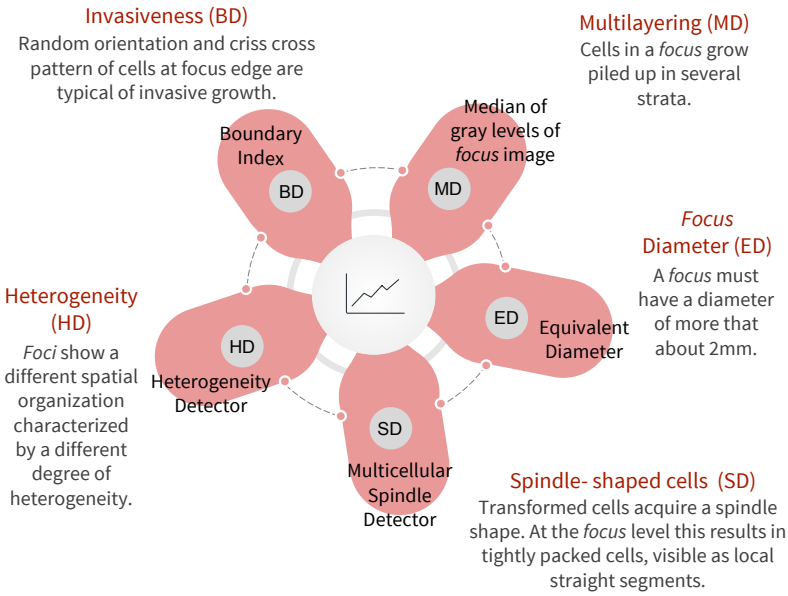

Figure 10.1: A graphical summary of statistical image descriptors. Statistical image descriptors developed in this thesis (the petals) and their relevance concerning morphological criteria used for visual scoring (in dark red).

obtained from standardized BALB/c 3T3 CTA experiments. We first developed a segmentation algorithm, able to isolate the region of interest, corresponding to each *focus*, from the surrounding monolayer. From these regions, we calculated a set of statistical image descriptors specifically designed to encompass the morphological features used for visual scoring. In this way, we decided to emulate the processes underlying visual scoring performed by an expert, in order to maintain a readable output of our analyses. See Figure 10.1 for a graphical representation of the descriptors and their morphological correspondences.

Finally, we exploited the obtained data related to *foci* morphology for further analyses and applications. We built classifiers of *foci* morphology in order to mimic the assessment of *in vitro* carcinogenicity power of a suspected compound obtained at the end of a CTA, and we compared the obtained classification with the visual scoring

performed by the expert, thus measuring classifiers performances. Two version of a classifier were built, the latter outstanding the performances of the initial one. The final classifier is able to score *foci* of unknown classification into the two main categories, Type III *foci* and the non-transformed classes Type II-Type I, with accuracy, sensitivity and specificity equal to 0.77 and an area under the curve (AUC) of 0.84. A remarkable feature of the aforementioned classifier is that it was trained with a large number of *foci* images, obtained from CTAs testing several compounds, at several concentrations.

In addition, we further exploited our original methods to analyse the dependence of morphology to the concentration of a compound, finding that they are related. In other words, the morphology of *foci* changes depending on the carcinogen concentration.

We presented an experimental setup based on one operator and one microscope-camera which is suited for exploring the numerical distributions of proposed statistical descriptors, and to incorporate them in a classifier able to score the number of transformed *foci*.

Improvement of *in vitro* carcinogenesis understanding. CTAs have been questioned for the lack of understanding of the molecular mechanisms underlying *in vitro* transformation, since these assays have been developed in order to mimic the multistage process of carcinogenesis and not based on a correlation with a particular mode of action.

We then devoted our analysis to contribute to the understanding of the *in vitro* transformation process by considering its different steps. We isolated clones from fully transformed *foci*, obtained with 1 μM of $CdCl_2$, and relative controls. We then analysed samples from initial phases of response after $CdCl_2$ treatment, in order to obtain a temporal framework of the processes involved.

Our main result is that after Cd treatment and during *in vitro* transformation many processes are involved and non-unique ways to the establishment of transformed cells can be covered.

The very initial phases seem to be governed by processes related to metal and chemical homeostasis, cytoskeleton rearrangements and signalling processes. In particular we hypothesized that the intracellular zinc and calcium increases may be the two main events driving Cd response, where the increase of the first ion could be the key player. On the contrary, established clones (hence isolated from transformed *foci*) show a great variety of biochemical patterns. Indeed, *foci* induced by the same stimulus, classified both as fully transformed Type III, show different proliferative behaviours (EGFR downstream pathways signalling), and different phenotypes. Very intriguingly, EGFR downstream pathways have been recently shown to be linked to intracellular zinc increase in cancer cells.
Hence, the different phenotypes found in transformed *foci* finally correspond to a specific biochemical/molecular cell clone fingerprint. *Foci* phenotypes are therefore indicative of processes underlying *in vitro* transformation, providing a link to be used to further improve the biological relevance of CTAs.
In addition, we achieved simultaneously a second, but not of secondary importance, aim: we contributed to a further characterization of the processes involved in Cd-induced transformation, exploiting CTA as model of chemical-induced carcinogenesis. CTA is remarkably strictly related to the adverse outcome (the chemical-induced morphological transformation), and at the same time it allows to measure potential biomarkers during, and at the end, of the process. We indeed further confirmed with our results the relevance and the advantages of using CTA for mechanistic understanding of chemical-induced carcinogenesis.

Finally, the developed methods are applicable to multiple protocols of CTAs. In particular, we are confident that the image analysis approach is applicable not only to the BALB/c 3T3 CTA, but with specific adaptations could be applicable to C3H10T1/2 CTA and also to the more recently developed Bhas 42 CTA. Similarly, the approach based on the biochemical and molecular characterization of cell samples from subsequent phases of chemical-induced transformation,

it is adaptable to other CTAs (e.g. BALB/3T3 and Bhas 42 CTA). Moreover, comparisons of results obtained with different CTAs could clarify the differences of performances between protocols, and further define the limitations and the applicability domain of each system.

In conclusion, the *in vitro* and *in silico* approaches can be joined together defining a complete panel of general and specific markers of transformation need to be defined, and considering them in a network, together with the coded morphologies.

10.2 Outlook

Our results showed that plenty of information than expected is available in CTA and that further data can be processed to contribute to the assessment of chemical carcinogenicity power of chemical compounds.

Our analysis showed for the first time the dependence of fully transformed *foci* morphology on concentration: increasing concentrations of carcinogens result in a variety of phenotypes which may reflect different molecular alterations (Chapter 5). In addition, we demonstrated that at different phenotypes of fully transformed *foci* correspond specific biochemical signatures (Chapter 8).

The standard classification of *foci* into two main categories (fully transformed and non-transformed) arises from an actual continuous distribution of morphologies. Our results, together, point towards the possibility of further distinctions inside the usual classification scheme. This distinctions, or subcategories of transformation, could finally correspond to specific molecular/biochemical profiles of transformation (Figure 10.2). As a consequence, a different classification scheme could be envisaged, where *foci* would be assigned to classes of transformation based on smaller differences in morphological features, that we can call shades of transformation, that would be finally related to distinct biochemical profiles. This new refined classification

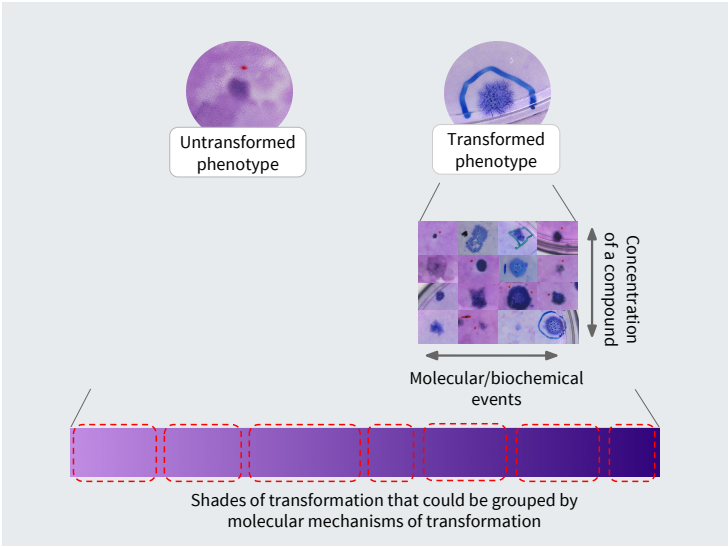

Figure 10.2: More distinctions inside the usual classification scheme. In this graphical representation, one of the consequences of our results is highlighted. Since the transformed morphology was found to be related to both carcinogen concentrations and molecular mechanisms of transformations, a different classification scheme can be envisaged. This new classification scheme could be more informative of the processes underlying the *in vitro* transformation induced by chemicals and improve CTA performances.

method of transformed *foci* would provide the desired link between the *in vitro* transformation process and the mechanisms underlying it. In addition, it would probably improve CTA performances in a tiered or integrated approach, as other tests could be triggered depending on CTA results.

It is still a matter of investigation if these detectable differences in *foci* phenotypes and their corresponding biochemical profiles, are attributable to final stages reached by different *foci*, that are then reasonably considerable as established clones, or are a result of intermediate stages of the transformation process by different *foci*. In the first scenario, the distinct morphological and biochemical profiles are imputable to different roads to transformation undertaken by each of the initiated cell of different *foci*. The second hypothesis,

acknowledges the possibility that in CTA the starting point of the transformation could not correspond to the administration of the compound, hence occurs in later stages of recovery phase.

In the presented thesis, we investigated the variability of *foci* phenotypes depending on the carcinogen concentrations (the columns in the matrix of *foci* images in Figure 10.2), and the relationship of *foci* phenotypes with some underlying processes (the rows in the matrix in Figure 10.2). It is planned, to expand the analyses taking into account more compounds and to expand the biochemical profiling of different *foci* phenotypes, taking into consideration more processes occurring in transformed clones, as well as analysing *foci* obtained from several different compounds. In such a way a panel of general and specific markers if *in vitro* transformations would become available.

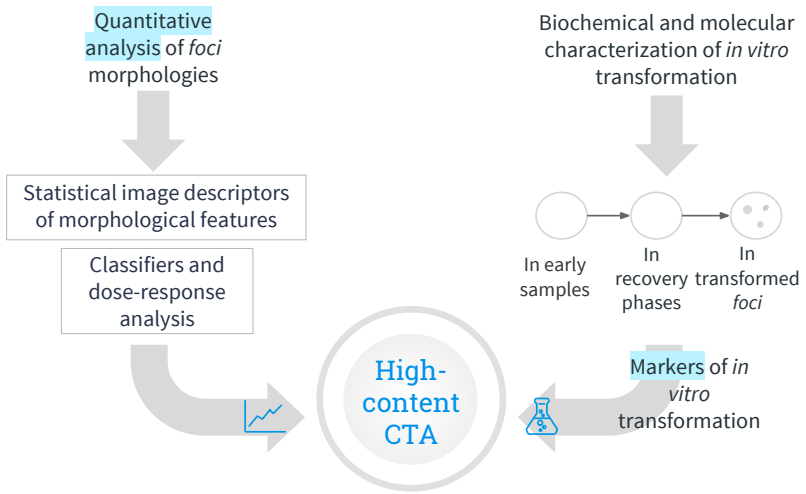

Figure 10.3: Summary of the perspectives envisaged following the results presented in this thesis.

In particular it would be challenging to evaluate the biochemical signatures depending also on the concentration of a carcinogen, in other words, the diagonal in the matrix in Figure 10.2. Quantitative morphological markers representative of specific molecular pathways and of specific classes of damages in transformed cells could be hence investigated for their relationship with the concentration.

Finally it is an open question whether *foci* phenotype may vary depending also on the type/class of carcinogen considered, and this issue indeed deserves further studies, exploiting the methods and the approaches that we have already developed and applied in conjunction and comparison with different tools, such as the QSAR analysis.

A so defined CTA, able to incorporate an objective analysis of transformed morphologies, and markers of specific and general processes of *in vitro* transformation could open the way towards an "High-content CTA" (Figure 10.3). As a final remark, the proposed improved CTA may be considered in the wider perspective of Integrated Testing Strategies, a promising framework to effectively pursue the goals of 3Rs (Reduce, Refine, Replace) in the context of carcinogenesis.

List of Papers

I Urani C., Corvi R., Callegaro G., Stefanini F.M.
Objective scoring of transformed foci in BALB/c 3T3 cell transformation assay by statistical image descriptors.
Toxicology in Vitro (**2013**), 27 (6), 1905-1912, DOI: 10.1016/j.tiv.2013.06.011.

II Callegaro G., Stefanini F.M., Colacci A., Vaccari M., Urani C.
An improved classification of foci for carcinogenicity testing by statistical descriptors.
Toxicology in Vitro (**2015**), 29 (7), 1839–1850, DOI: 10.1016/j.tiv.2015.07.013.

III Forcella M., Callegaro G., Melchioretto P., Gribaldo L., Frattini M., Stefanini F.M., Fusi P., Urani C.
Cadmium-transformed cells in the in vitro Cell Transformation Assay reveal different proliferative behaviours and activated pathways.
Toxicology in Vitro (**2016**), 36, 71–80, DOI: 10.1016/j.tiv.2016.07.006.

IV Callegaro G., Corvi R., Salovaara S., Urani C., Stefanini F.M.
Relationship between increasing concentrations of two carcinogens and statistical image descriptors of foci morphology in the Cell Transformation Assay.
Journal of Applied Toxicology (**2016**), DOI: 10.1002/jat.3419.

V Callegaro G., Malkoc K., Corvi R., Urani C., Stefanini F.M.
A comprehensive statistical classifier of foci in the Cell Transformation Assay for carcinogenicity testing. Toxicology in Vitro, Special Issue: *in vitro* Safety Assessment (submitted **2016**).

VI Callegaro G., Forcella M., Melchioretto P., Frattini A., Gribaldo L., Fusi P., Fabbri M., Urani C.
Toxicogenomics applied to in vitro Cell Transformation Assay reveals mechanisms of early response to cadmium. Metallomics (submitted **2017**).

International peer-reviewed conferences and proceedings

I Urani C., Callegaro G., Stefanini F.M.
Image Descriptors of Transformed Foci in BALB/c 3T3 Cell Transformation Assay: a Statistical Analysis.
In Vitro Cellular and Developmental Biology - Animal (Conference Proceedings) (**2013**), vol 49:557- 567(A-3008).

II Niemeijer M., Callegaro G., Van de Water B.
An Imaging-Based RNA-Interference Screen Reveals Novel Key Regulators of the Drug-Induced Endoplasmic Reticulum Stress Response.
The Toxicologist: Supplement to Toxicological Sciences, Society of Toxicology (**2016**), Abstract no. 2291. vol 150(1).

Oral communications and posters

I poster: Urani C.,Callegaro G., Stefanini F.M.
Image Descriptors of Transformed Foci in BALB/c 3T3 Cell Transformation Assay: a Statistical Analysis.
In Vitro Biology Meeting, held in Providence (RI, USA) in June 15-19 **2013**.

II poster: Malkoc K., Callegaro G., Urani C., Corvi R. and Stefanini F.M.
More than just transformed colonies: an integrated approach to the character- ization of foci in the Cell Transformation Assays.
IHCP Training on basic knowledge in modern toxicological sciences, Joint Research Centre, Ispra (VA), Italy, **2016**.

III poster: Niemeijer M., Callegaro G., Van de Water B.
An Imaging-Based RNA-Interference Screen Reveals Novel Key Regulators of the Drug- Induced Endoplasmic Reticulum Stress Response.
the Society of Toxicology 55th Annual Meeting and ToxExpo (**2016**), New Orleans, Louisiana.

IV ORAL COMMUNICATION: Callegaro G., Forcella M., Malkoc K., Melchioretto P., Gribaldo L., Corvi R., Fusi P., Stefanini F.M., Urani C.
Focusing on foci: beyond the standard use of Cell Transformation Assays to improve in vitro carcinogenicity testing.
ESTIV **2016** congress, "In Vitro Toxicology for Safety Assessment", Juan-les-Pins, France.

V POSTER: Niemeijer M., Callegaro G., Van de Water B.
An Imaging-Based RNA-Interference Screen Reveals Novel Key Regulators of the Drug- Induced Endoplasmic Reticulum Stress Response.
the Society of Toxicology 56th Annual Meeting and ToxExpo (**2017**), Baltimore, Maryland.

AWARDS

I ESTIV award bursaries for ESTIV 2016 congress, European Society of Toxicology In Vitro, 2016

A

Appendix

Contents:

Appendix 1: Table A1, Chapter 4

Table A1: Type III and non-Type III *foci*, the dataset.

	Visual scoring		Digitalized images		Automated classification	
Sample n°	Type III *foci*	Non Type III *foci*	Type III *foci*	Non Type III *foci*	Type III *foci*	Non Type III *foci*
Experiment 1 - FBS 1						
9	8	0	7	0	7	0
10	9	1	7	1	7	1
11	6	3	4	3	3 + **1**	2 + **1**
12	14	6	13	6	10	6 + **3**
Experiment 1 - FBS 2						
21	18	10	15	10	15 + **3**	7
22	14	8	11	8	11 + **1**	7
23	24	9	22	9	20 + **2**	7 + **2**
24	16	3	12	3	11 + **1**	2 + **1**
Experiment 2 - FBS 1						
21	6	1	6	1	4 + **1**	**2**
22	14	4	11	4	10 + **1**	3 + **1**
23	11	2	11	2	11 + **1**	1
24	17	2	15	2	13 + **1**	1 + **2**
25	17	1	12	1	12 + **1**	
26	13	2	10	2	10 + **1**	1
27	10	3	7	3	7 + **3**	
28	17	4	15	4	11 + **1**	3 + **4**
29	8	1	4	1	4	1
30	8	3	8	3	7	3 + **1**
Total	230	63	190	63	191	62

FBS 1 = Fetal Bovine Serum, Gibco Life Technologies catalogue number 10270-098, batch 41Q201K.
FBS 2 = Fetal Bovine Serum, Gibco Life Technologies catalogue number 10270-098, batch 41A1119K.

Appendix 2: Table A2, Chapter 4

Table A2: "Ambiguous" *foci* dataset.

	Visual scoring	Digitalized images	Automated classification	
Sample n°	"Ambiguous" *foci*	"Ambiguous" *foci*	Type III *foci*	Non Type III *foci*
Experiment 1 - FBS 1				
9	3	3	3	0
10	1	1	0	1
11	2	2	1	1
12	0	0	0	0
Experiment 1 - FBS 2				
21	1	1	1	0
22	1	1	0	1
23	5	4	4	0
24	3	2	2	0
Total	16	14	11	3

FBS 1 = Fetal Bovine Serum, Gibco Life Technologies catalogue number 10270-098, batch 41Q201K.
FBS 2 = Fetal Bovine Serum, Gibco Life Technologies catalogue number 10270-098, batch 41A1119K.

Appendix 3: Figure A3, Chapter 5

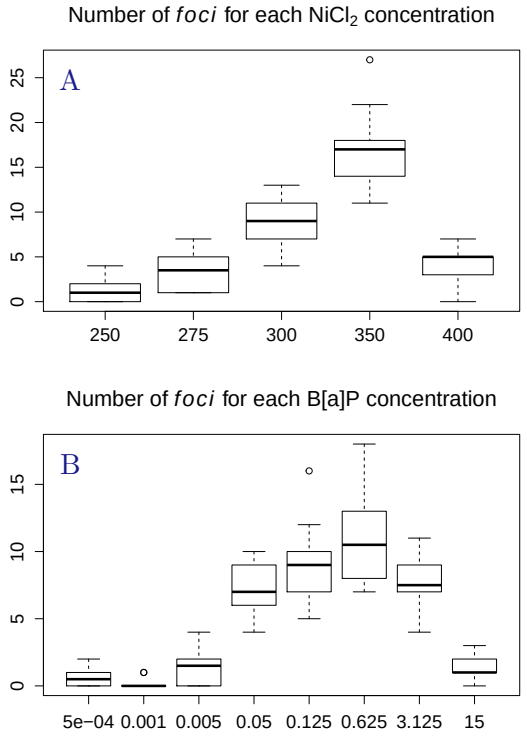

Figure A3: Boxplots of the number of *foci* before performing segmentation. Boxplots of the number of Type III *foci* per dish (y axes) before segmentation process and carcinogen concentrations (x axes). In A *foci* images from $NiCl_2$ database are considered, while in B *foci* images from B[a]P database are included. Empty circles represent candidate outliers.

Appendix 4: Figure A4, Chapter 5

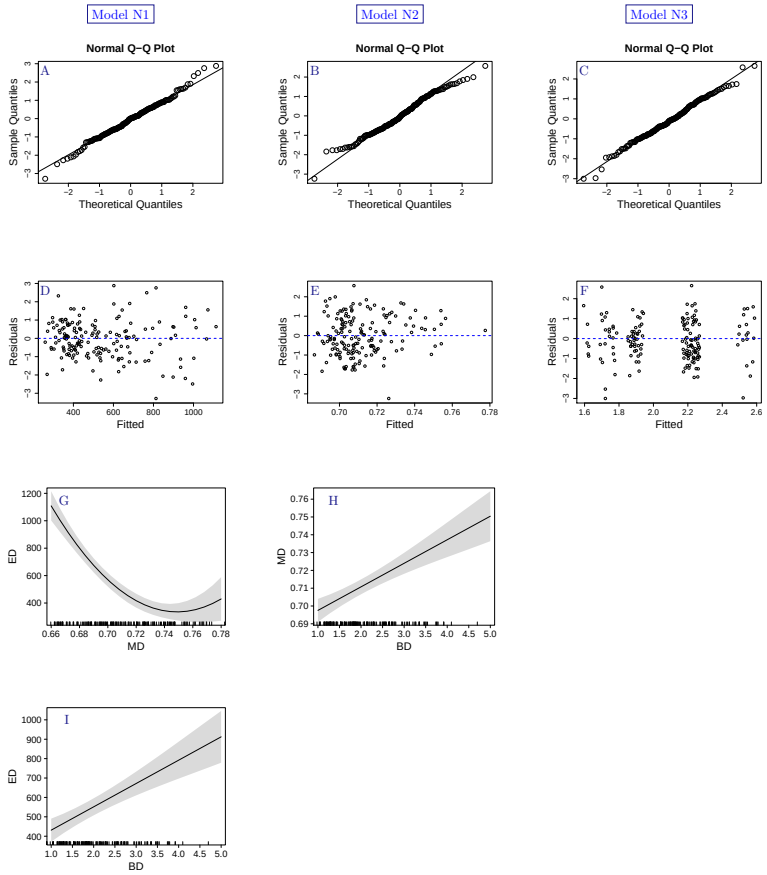

Figure A4: Diagnostics and additional plots of models of $NiCl_2$ dataset. Graphs are grouped according to model, by column: Model N1 (ED as the response variable), Model N2 (MD as the response variable) and Model N3 (BD as the response variable). In the first two rows diagnostic graphs are shown, quantile-quantile plots (A, B, C) and plot of fitted values versus residuals (D, E, F), respectively. In G and I are plotted fitted values (Model N1) of the descriptor ED compared, respectively, to the linear predictor MD and to the linear predictor BD. The bars on the x axis represent MD and BD actual values, in plot C and D, respectively. In H are plotted fitted values (Model N2) of the descriptor MD compared to the linear predictor MD (bars on the x axis represent BD actual values).

Appendix 5: Figure A5, Chapter 5

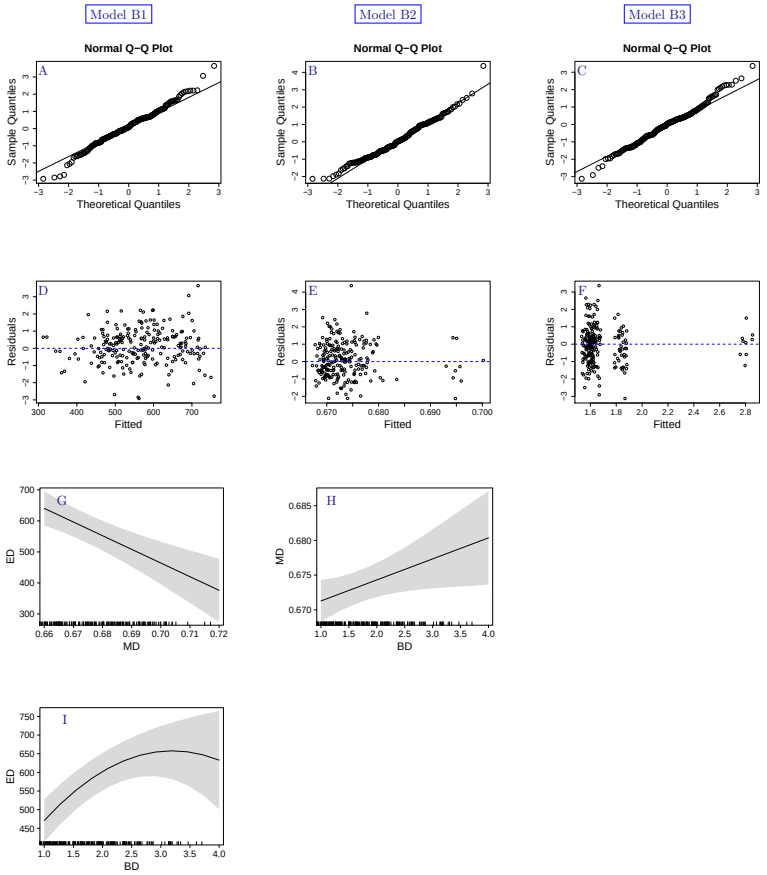

Figure A5: Diagnostics and additional plots of models of B[a]P dataset. Graphs are grouped according to model, by column: Model B1 (ED as the response variable), Model B2 (MD as the response variable) and Model B3 (BD as the response variable). In the first two rows diagnostic graphs are shown, quantile-quantile plots (A, B, C) and plot of fitted values versus residuals (D, E, F), respectively. In G and I are plotted fitted values (Model B1) of the descriptor ED compared, respectively, to the linear predictor MD and to the linear predictor BD. The bars on the x axis represent MD and BD actual values, in plot C and D, respectively. In H are plotted fitted values (Model B2) of the descriptor MD compared to the linear predictor MD (bars on the x axis represent BD actual values).

Appendix 6: Document A6, Chapter 5

In the following sections R code for the statistical analysis performed in Chapter 4 is detailed, as well as supplementary materials of the presented models.

First, the following packages have to be loaded:

```
library(nlme)
library(car)
library(nlme)
library(effects)
```

$NiCl_2$ dataset

First, models for each descriptor as a response variable are fitted with generalized least squares accounting for unequal variance, and including a correlation structure (object of class *CorCompSymm*).

```
mod.1N <- gls(equivalentDiameter~median
              +I(median^2)
              +boundaryIndex
              +median:boundaryIndex
              +dose,
              data=workDF,
              correlation = corCompSymm(0.1, form = ~ 1 | plate),
              method='ML')
mod.1N <- update(mod.1N, weights = varPower(form= ~ dose))

mod.2N <- gls(median~boundaryIndex
                +dose
                +I(dose^2),
                data=workDF,
                correlation = corCompSymm(0.1, form = ~ 1 | plate),
                method='ML')
mod.2N <- update(mod.2N, weights = varPower(form = ~dose))

mod.3N <- gls(boundaryIndex~dose,
                data=workDF,
                correlation = corCompSymm(0.1, form= ~1 |plate),
                method='ML')
mod.3N <- update(mod.3N, weights = varPower(form = ~ dose))
```

Then contribution of concentration on the expected value of descriptors was tested with reducted models:

```
mod.1N_r <- update(mod.1N, ~.-dose)
anova(mod.1N, mod.1N_r )
```

```
mod.2N_r <- update(mod.2N, ~.-dose - I(dose^2))
anova(mod.2N, mod.2N_r )

mod.3N_r <- update(mod.3N, ~.-dose)
anova(mod.3N, mod.3N_r )
```

Diagnostic graphs were created with the following code (mod.1N shown as example), and are provided in Figure S2.

```
myres <- residuals(mod.1N, type='normalized')
qqnorm(myres)
qqline(myres)

plot(myres~jitter(fitted(mod.1N), amount=.05), data=workDF)
abline(h=0, col=4, lwd=2, lty=2)
```

We here provide, as supporting materials, confidence intervals for estimated parameters and variance function for each fitted model:

```
intervals(mod.1N)
```

```
## Approximate 95% confidence intervals
##
##  Coefficients:
##                              lower         est.        upper
## (Intercept)            34516.6646   51993.6151  69470.56561
## median               -192036.6855 -141843.6447 -91650.60389
## I(median^2)            61201.4529   97223.6306 133245.80831
## boundaryIndex            609.1660    1437.8238   2266.48156
## doseNORM                -290.7646    -108.0184     74.72777
## median:boundaryIndex   -2990.1239   -1848.8325   -707.54106
## attr(,"label")
## [1] "Coefficients:"
##
##  Correlation structure:
##          lower      est.     upper
## Rho 0.03874005 0.1541243 0.3232199
## attr(,"label")
## [1] "Correlation structure:"
##
##  Variance function:
##           lower      est.     upper
## power 0.01743034 0.4164543 0.8154782
## attr(,"label")
## [1] "Variance function:"
```

```
##
##  Residual standard error:
##    lower     est.    upper
## 194.0061 242.0850 302.0790
```

```
intervals(mod.2N)
```

```
## Approximate 95% confidence intervals
##
##  Coefficients:
##                       lower        est.       upper
## (Intercept)    0.674492416  0.71539245  0.75629247
## boundaryIndex  0.008647398  0.01326386  0.01788032
## doseNORM      -0.262721928 -0.13779164 -0.01286134
## I(doseNORM^2)  0.032246221  0.12622566  0.22020509
## attr(,"label")
## [1] "Coefficients:"
##
##  Correlation structure:
##           lower        est.     upper
## Rho -0.04937754 0.009573488 0.1226112
## attr(,"label")
## [1] "Correlation structure:"
##
##  Variance function:
##            lower      est.     upper
## power -0.5023479 -0.159366 0.1836158
## attr(,"label")
## [1] "Variance function:"
##
##  Residual standard error:
##      lower       est.      upper
## 0.01972629 0.02402997 0.02927258
```

```
intervals(mod.3N)
```

```
## Approximate 95% confidence intervals
##
##  Coefficients:
##                 lower     est.    upper
## (Intercept) 0.8066259 1.249700 1.692775
## doseNORM    0.6118222 1.282781 1.953740
## attr(,"label")
## [1] "Coefficients:"
##
##  Correlation structure:
```

```
##          lower       est.     upper
## Rho -0.0687326 0.00572599 0.2066248
## attr(,"label")
## [1] "Correlation structure:"
##
##  Variance function:
##            lower      est.     upper
## power -0.1349208 0.1571835 0.4492878
## attr(,"label")
## [1] "Variance function:"
##
##  Residual standard error:
##     lower      est.     upper
## 0.7873429 0.9404370 1.1232993
```

Plots of fitted values of each descriptor as response variable for each model and concentration variable was obtained with the following code (mod.1N shown as example):

```
eff1N_dose <- Effect('dose', mod.1N,
                     xlevels = list(dose = unique(workDF$dose)),
                     vcov.=vcov, se = TRUE, confidence.level = 0.95,
                     transformation = NULL,
                     typical = mean)
plot(eff1N_dose)
```

B[a]P dataset

First, models for each descriptor as a response variable are fitted with generalized least squares accounting for unequal variance, and including a correlation structure (object of class *CorCompSymm*).

```
mod.1B <- gls(equivalentDiameter~median
               +boundaryIndex
               +I(boundaryIndex^2)
               +dose,
               data=workDF,
               correlation = corCompSymm(0.1, form = ~ 1 | plate),
               method='ML')
mod.1B <- update(mod.1B, weights = varPower(form= ~ dose))

mod.2B <- gls(median~boundaryIndex
              +dose,
              data=workDF,
              correlation = corCompSymm(0.1, form = ~ 1 | plate),
```

```
              method='ML')
mod.2B <- update(mod.2B, weights = varPower(form =~dose))

mod.3B <- gls(boundaryIndex~dose,
               data=workDF,
               correlation = corCompSymm(0.1, form= ~1 |plate),
               method='ML')
mod.3B <- update(mod.3B, weights = varPower(form = ~ dose))
```

Then contribution of concentration was tested with reducted models:

```
mod.1B_r <- update(mod.1B, ~.-dose)
anova(mod.1B, mod.1B_r)

mod.2B_r <- update(mod.2B, ~.-dose)
anova(mod.2B, mod.2B_r)

mod.3B_r <- update(mod.3B, ~.-dose)
anova(mod.3B, mod.3B_r)
```

Diagnostic graphs were created with the following code (mod.1B shown as example), and are provided in Figure S3.

```
myres <- residuals(mod.1B, type='normalized')
qqnorm(myres, main='q-q plot mod.1B')
qqline(myres)

plot(myres~jitter(workDF$doseSTD, amount=.05), data=workDF)
abline(h=0, col=4, lwd=2, lty=2)
```

We here provide, as supporting materials, confidence intervals for estimated parameters and variance function for each fitted model:

```
intervals(mod.1B)
```

```
## Approximate 95% confidence intervals
##
##  Coefficients:
##                           lower          est.        upper
## (Intercept)         1898.17101  3232.7439192  4567.316824
## median             -6406.81328 -4405.3403410 -2403.867401
## boundaryIndex         93.19703   247.3053228   401.413611
## I(boundaryIndex^2)   -72.20875   -38.6749767    -5.141206
## dose                 -11.28108    -0.8103561     9.660365
## attr(,"label")
```

```
## [1] "Coefficients:"
##
##  Correlation structure:
##         lower      est.     upper
## Rho 0.03737678 0.1450291 0.3018267
## attr(,"label")
## [1] "Correlation structure:"
##
##  Variance function:
##            lower        est.       upper
## power -0.1072438 -0.05933182 -0.01141989
## attr(,"label")
## [1] "Variance function:"
##
##  Residual standard error:
##    lower     est.    upper
## 203.7128 228.6996 256.7512
```

```
intervals(mod.2B)
```

```
## Approximate 95% confidence intervals
##
##  Coefficients:
##                       lower        est.       upper
## (Intercept)   0.6611820055 0.666215044 0.671248082
## boundaryIndex 0.0002813363 0.003027738 0.005774139
## dose          0.0006216444 0.001445237 0.002268830
## attr(,"label")
## [1] "Coefficients:"
##
##  Correlation structure:
##             lower       est.     upper
## Rho -0.007080117 0.06425425 0.1753773
## attr(,"label")
## [1] "Correlation structure:"
##
##  Variance function:
##              lower       est.      upper
## power -0.01543731 0.03072261 0.07688253
## attr(,"label")
## [1] "Variance function:"
##
##  Residual standard error:
##      lower       est.      upper
## 0.01459902 0.01628850 0.01817350
```

```
intervals(mod.3B)
```

```
## Approximate 95% confidence intervals
##
##  Coefficients:
##                  lower       est.     upper
## (Intercept) 1.44733940 1.58828135 1.7292233
## dose        0.04595192 0.07733259 0.1087133
## attr(,"label")
## [1] "Coefficients:"
##
##  Correlation structure:
##          lower      est.     upper
## Rho 0.05466433 0.1577961 0.3005583
## attr(,"label")
## [1] "Correlation structure:"
##
##  Variance function:
##            lower        est.      upper
## power -0.2263946 -0.06441809 0.09755844
## attr(,"label")
## [1] "Variance function:"
##
##  Residual standard error:
##     lower      est.     upper
## 0.6090554 0.7188179 0.8483614
```

Plots of fitted values of each descriptor as response variable for each model and concentration variable was obtained with the following code (mod.1B shown as example):

```
eff1B_dose <- Effect('dose', mod.1B,
                     xlevels = list(dose = unique(workDF$dose)),
                     vcov.=vcov, se = TRUE, confidence.level = 0.95,
                     transformation = NULL,
                     typical = mean)
plot(eff1B_dose)
```

Appendix 7: Table A7, Chapter 6

Table A7: Binary Logistic Regression models. Details of BRL1 and BLR2 models are listed.

Model	*BLR1*	*BLR2*
Formula	$\backsim s(MD) + s(ED, WPD) + LD + +entropy + num\_reg\_k2 + +s(num\_reg\_k1)$	$\backsim s(MD) + s(ED, WPD)$
Significance of terms	s(MD) p<0.001	s(MD) p<0.001
	s(ED,WPD) p<0.001	s(ED,WPD) p<0.001
	s(num_reg_k1) p<0.001	- -
	SD p<0.001	- -
	entropy p<0.001	- -
	num_reg_k2 p<0.001	- -
UBRE	-0.44179	-0.39